# Axisymmetric saturated granular column collapses at elevated gravitational accelerations

William O. Webb, MEng.

Thesis submitted to the University of Nottingham for the degree of

Doctor of Philosophy

March 2024

# Abstract

Debris flows represent a prevalent natural hazard, posing a significant threat to communities and infrastructure located in mountainous regions susceptible to intense precipitation events worldwide. Furthermore, the escalating impacts of climate change are poised to intensify both the frequency and severity of these events. The dynamics of debris flows, in contrast to other geophysical granular flows, exhibit heightened complexity owing to substantial fluid volumes and a broad spectrum of particle sizes present within the flow. The diverse composition of debris flows gives rise to highly heterogeneous flow states, wherein many contributing mechanisms, notably the interplay between the granular and fluid phases, remain inadequately understood within the wider scientific community. Consequently, there persists a lack of consensus on the optimal approach to incorporate the influence of grain-fluid interactions into numerical models which are essential for predicting debris flow behaviour and formulating effective mitigation strategies.

This study aims to shed light on grain-fluid interactions within debris flows through a programme of physical scaling analysis complemented by two numerical approaches, inspired by the classical granular column collapse experiment. Focus was given to the just-saturated case, where granular pores were filled with fluid up to the column's free surface. Crucially, a geotechnical centrifuge controlled the stress state within the granular-fluid flow, enabling experiments across a wide parameter space, including cases where force balances matched those in geophysical flows. The study's parameter space considered variables such as gravitational acceleration, inertial particle size, fluid viscosity, and the contribution of fine granular material, with different concentrations of fine kaolin clay particles suspended within the fluid phase. High-speed imaging and basal fluid pressure measurements were used to quantify characteristic acceleration stage flow outcomes as functions of dimensionless parameters defined from the initial column configuration.

The results from the physical experiments formed a substantial dataset applicable for calibrating or validating numerical models. Two numerical modelling schemes, a continuum-continuum (shallow water) approach, which was implemented within Mat-

lab, and a discrete-continuum (Discrete Element Method-Lattice Boltzmann Method) approach, were used to replicate the observed behaviour from the experiments and gain further insights into the nature of the grain-fluid interactions. The latter model was then employed to investigate how the dynamics of the column collapses were influenced by the rotation of the geotechnical centrifuge, focusing on the effects of centrifugal and Coriolis accelerations. Key takeaways include the development of a design criterion based on the log of the ratio of the centrifuge's radius and the height of the mounted model. It was found that when this ratio exceeds 4, it can be assumed that the centrifuge model is subjected to a constant gravitational field, where the influence of horizontal centrifugal and Coriolis accelerations are negligible.

This study emphasises that although complex experimental setups and numerical models are necessary to replicate the flow conditions observed in natural debris flows, simplicity is crucial for gaining insight into the specific mechanisms and processes that drive their dynamics.

# Acknowledgements

# Statement of authorship

I confirm that the submitted thesis contains published works. Written statements from each co-author, confirming my contribution to each paper, can be found below.

Webb, W., Heron, C., and Turnbull, B. (2023b). Inertial effects in just-saturated axisymmetric column collapses. *Granular Matter*. 25(2):40

**Statement from Author:** I confirm that I, as the lead author, was solely responsible for the design of the experimental configuration, the implementation of the experimental testing regime, and the collection and analysis of the data. The initial draft of the paper was independently composed by the lead author. Subsequent revisions by Drs. Heron and Turnbull were integrated into the manuscript prior to its submission.

**Statement of Contribution from Dr. Charles Heron:** I confirm as a co-author of this paper that my contribution was to support the experimental development and implementation, as well are providing feedback on the initial draft of the paper.

**Statement of Contribution from Dr. Barbara Turnbull:** I confirm that, as a co-author of this paper, lead the conceptualisation of the experiment and supported its implementation. I provided developmental feedback on the manuscript and review responses.

Webb, W., Heron, C., and Turnbull, B. (2023a). Fines-controlled drainage in just-saturated, inertial column collapses. *E3S Web of Conferences*. 415:01030

**Statement from Author:** I confirm that I, as the lead author, was solely responsible for the design of the experimental configuration, the implementation of the experimental testing regime, and the collection and analysis of the data. The initial draft of the paper was independently composed by the lead author. Subsequent revisions by Drs. Heron and Turnbull were integrated into the manuscript prior to its submission.

**Statement of Contribution from Dr. Charles Heron:** I confirm as a co-author of this paper that my contribution was to support the experimental development and implemen-

tation, as well are providing feedback on the initial draft of the paper.

**Statement of Contribution from Dr. Barbara Turnbull:** I confirm that, as a co-author of this paper, lead the conceptualisation of the experiment and supported its implementation. I provided developmental feedback on the manuscript and review responses.

Webb, W., Turnbull, B., and Johnson, C. G. (2024a). Continuum modelling of a just-saturated inertial column collapse: Capturing fluid-particle interaction. *Granular Matter*. 26(1):21

**Statement from Author:** I confirm that I, as the lead author, was solely responsible for the implementation of the numerical model within Matlab, and the collection and analysis of the data. The initial draft of the paper was independently composed by the lead author. Subsequent revisions by Drs. Turnbull and Johnson were integrated into the manuscript prior to its submission.

**Statement of Contribution from Dr. Barbara Turnbull:** I confirm that, as a co-author of this paper, supported the research process and assisted in the interpretation of results. I provided developmental feedback on the manuscript and review responses.

**Statement of Contribution from Dr. Chris Johnson:** I confirm that I, as co-author of this paper, suggested a set of shallow-water equations to model the system and numerical methods to solve these, and provided feedback on the manuscript and review responses.

Webb, W., Turnbull, B., and Leonardi, A. (2024b). Performance and limits of a geotechnical centrifuge: DEM-LBM simulations of saturated granular column collapse. *Granular Matter*. 26(2):32

**Statement from Author:** I confirm that I, as the lead author, was solely responsible for the design of the experimental configuration, the implementation of the experimental testing regime, designing and conducting the numerical simulation campaign, and the collection and analysis of the data. The initial draft of the paper was independently composed by the lead author. Subsequent revisions by Drs. Turnbull and Leonardi were integrated into the manuscript prior to its submission.

**Statement of Contribution from Dr. Barbara Turnbull:** I confirm that, as a co-author of this paper, supported the research process and assisted in the interpretation of results.

I provided developmental feedback on the manuscript.

**Statement of Contribution from Dr. Alessandro Leonardi:** I confirm that, as a co-author of this paper, supported the development of the numerical model, provided access to pre-existing software, and assisted in the calibration campaign and in the interpretation of the results. I provided developmental feedback on the manuscript.

# Changes to publications

In order to benefit the flow of the thesis, the published papers are not reproduced here in their published form. Instead, the constituents of the papers are reproduced within each chapter with the following amendments:

1. Section, figure, table and equation numbers are adjusted to include a chapter reference for consistency.

2. Figures, tables and equations have been adjusted and resized to better fit the page dimensions of the thesis. Figure colour maps have also been adapted.

3. The symbols used within the papers have been adjusted to allow for a single streamlined nomenclature to be developed for the thesis as a whole.

4. Reference to journal details, submission, revision and acceptance dates, and contact details for the corresponding authors have not been included.

5. Footnotes have been included to provide reference to other chapters of the thesis.

# Contents

CONTENTS

CONTENTS

XI

CONTENTS

# List of Figures

LIST OF FIGURES

XVII

# List of Tables

# Notation

## Latin script

| Symbol | Dimensions | Chapter | Description |
|---|---|---|---|
| $a_0$ | [ ] | 3, 5, 6 | Initial column aspect ratio |
| $a_p, b_p, c_p$ | [ ] | 5 | Constants of the three-parameter exponential curve |
| $a_r$ | $[LT^{-2}]$ | B | Resultant acceleration of the lifting system |
| $a_V$ | $[L^3T^{-1}I^{-1}]$ | A | Linear gradient used when calibrating the pressure sensors |
| $\boldsymbol{a}, a$ | $[LT^{-2}]$ | 6 | Acceleration vector field and scalar quantity |
| $\boldsymbol{a}_{cf}, a_{cf}$ | $[LT^{-2}]$ | 6 | Centrifugal acceleration vector and scalar quantities |
| $\boldsymbol{a}_{co}, a_{co}$ | $[LT^{-2}]$ | 6 | Coriolis acceleration vector and scalar quantities |
| $A_p$ | [ ] | 5 | Constant used for pressure signal processing |
| $b$ | [L] | C | Basal surface level |
| $B$ | [ ] | 5, 6 | Dimensionless group controlling the family of curves |
| $B_p$ | [ ] | 5 | Normalised pressure gradient threshold |
| Bo | [ ] | 3, 4, 5, 6, B | Column-scale Bond number |
| $Bo_k$ | [ ] | 4 | Grain-scale Bond number |
| $\boldsymbol{c}, c$ | $[LT^{-1}]$ | 6 | Mesoscopic fluid velocity vector and scalar quantities |
| $C$ | [ ] | 3 | Temperature constant used by Takamura et al. (2012) |

## Notation

| Symbol | Dimensions | Chapter | Description |
|---|---|---|---|
| $C_B$ | [ ] | 2 | Bulk sediment concentration |
| $C_{dd}$ | $[ML^{-3}T^{-1}]$ | C | Darcy drag coefficient |
| $C_f$ | [ ] | C | Chézy drag coefficient |
| $C_g$ | [ ] | 3 | Glycerol mass concentration |
| $C_k$ | [ ] | 4, A | Mass concentration of fines |
| $C_r$ | [ ] | 5 | Constant for the 'rainfall' scheme |
| Ca | [ ] | 3, 4, 5, 6, B | Column-scale Capillary number |
| $Ca_k$ | [ ] | 4 | Grain-scale Capillary number |
| $d_k$ | [L] | 4 | Reference length scale for kaolin clay particles |
| $d_p$ | [L] | 2, 3, 4, 5, 6, B, C | Coarse grain diameter |
| $D$ | [L] | 6 | Characteristic DEM particle diameter |
| $D_{v,L}$ | [ ] | B | Scale factor |
| $E$ | $[ML^{-1}T^{-2}]$ | 5 | Elastic bulk modulus |
| $f$ | [ ] | 6 | LBM density function |
| $f_1$ | $[LT^{-1}]$ | 3, 4 | Unknown function |
| $f_2$ | [ ] | 3, 4 | Unknown function |
| $f_3$ | [ ] | 3, 4 | Unknown function |
| $f_c$ | $[T^{-1}]$ | 3, 5 | Cutoff frequency |
| $f_d$ | $[MLT^{-2}]$ | 6 | Inter-phase drag force |
| $f^{eq}$ | [ ] | 6 | LBM density function at equilibrium |
| $\boldsymbol{f}$ | $[ML^{-2}T^{-2}]$ | C | Remaining interphase body force |
| $\boldsymbol{f}_B$ | $[ML^{-2}T^{-2}]$ | C | Buoyancy force contribution |
| $F^b$ | [L] | C | Function of the basal surface |
| $F_c$ | $[MLT^{-2}]$ | B | Weight of the steel mass |
| $F_m$ | $[MLT^{-2}]$ | B | Weight of the steel cylinder |
| $F_n, F_t$ | $[MLT^{-2}]$ | 6 | Surface normal and tangential contact forces |
| $F_r$ | $[MLT^{-2}]$ | B | Resultant force of the lifting system |
| $F^v$ | [L] | C | Function of the $v$ phase surface |
| $Fr_{m,L}$ | [ ] | 4 | Maximum flow front Froude number evaluated at $u_m$ |
| $Fr_{v,L}$ | [ ] | 3, 6 | Maximum $v$ phase front Froude number evaluated at $u_{v,m}$ |

# Notation

| Symbol | Dimensions | Chapter | Description |
|---|---|---|---|
| $g$ | $[LT^{-2}]$ | 2, 3, 4, 6, A, C | Earth's constant of gravitational acceleration |
| $\boldsymbol{g}$ | $[LT^{-1}]$ | 6, C | Gravitational acceleration vector |
| $G$ | $[LT^{-2}]$ | 3, 4, 5, A, B | Gravitational acceleration applied to the model |
| $h_0$ | $[L]$ | 3, 4, 5, 6, A, B | Initial column height |
| $h_c$ | $[L]$ | A | Height difference between the capillary rise and depression |
| $h_v$ | $[L]$ | 5, C | $v$ phase flow height |
| $h_{v,0}$ | $[L]$ | 5 | Initial $v$ phase height |
| $h_{v,1}$ | $[L]$ | 5 | Initial $v$ phase height of the reduced column configuration |
| $H$ | $[L]$ | 5, C | Characteristic flow depth scale |
| $\boldsymbol{I}$ | $[\ ]$ | C | Unit tensor |
| $k$ | $[L^2]$ | 2, 5, C | Granular phase permeability |
| $k_0$ | $[\ ]$ | 3 | Temperature constant used by Takamura et al. (2012) |
| $k_1$-$k_5$ | $[\ ]$ | 3, 4 | Constants in equation for $Q$ |
| $k_{act/pass}$ | $[\ ]$ | C | Lateral earth pressure coefficient |
| $k_n, k_t$ | $[MT^{-2}]$ | 6 | Surface normal and tangential contact stiffnesses |
| $K$ | $[LT^{-1}]$ | 5 | Hydraulic conductivity |
| $L$ | $[L]$ | C | Characteristic flow length scale |
| $L_c$ | $[L]$ | 6 | Base length of centrifuge model |
| $m_p$ | $[M]$ | 6 | Mass of a particle |
| $M_c$ | $[M]$ | B | Mass of the steel cylinder |
| $M_g$ | $[M]$ | 3 | Mass of glycerol |
| $M_m$ | $[M]$ | B | Mass of the mass used to lift up the steel cylinder |
| $M_p$ | $[M]$ | 3 | Mass of granular material |
| $M_r$ | $[ML^2T^{-2}]$ | 6 | Torque opposing particle rotation |
| $M_w$ | $[M]$ | 3 | Mass of water |
| $n$ | $[\ ]$ | 6 | Number of sectors used to obtain the average phase front position |

# Notation

| Symbol | Dimensions | Chapter | Description |
|---|---|---|---|
| $n_c$ | [ ] | 6 | Particle coordination number |
| $n_p$ | [ ] | 2, 6 | Number of grains |
| $n_w$ | [ ] | A | Number of interrogation windows |
| $\boldsymbol{n}$ | [ ] | C | Upward pointing $v$ phase surface normal vector |
| $N$ | [ ] | 2, 3, 4, 6, B | Constant reflective of the elevated gravitational acceleration |
| $N_{Bag}$ | [ ] | 2 | Bagnold number |
| $N_{Dar}$ | [ ] | 2 | Darcy number |
| $N_{Sav}$ | [ ] | 2 | Savage number |
| $p_f$ | $[ML^{-1}T^{-2}]$ | 6, C | Fluid pressure within the mixture |
| $P$ | $[ML^{-1}T^{-2}]$ | 3, 5, A, B | Basal fluid pressure at the centre of the column |
| $P_0$ | $[ML^{-1}T^{-2}]$ | 5 | Basal fluid prior to collapse initiation for the 'rainfall' scheme simulations |
| $P_F$ | $[ML^{-1}T^{-2}]$ | 3 | Residual basal fluid pressure |
| $P_p$ | [ ] | 6 | Percentage of grains |
| $P_p^{[0,1]}$ | [ ] | 6 | Percentage of grains with a coordination number of 0 or 1 |
| $\dot{P}$ | $[ML^{-1}T^{-3}]$ | 3 | Basal fluid pressure gradient at the centre of the column |
| $\dot{P}_m$ | $[ML^{-1}T^{-3}]$ | 3 | Basal fluid pressure gradient over the first significant pressure drop at the centre of the column |
| $\dot{P}^*$ | [ ] | 3 | The ratio between $\dot{P}$ and the equivalent hydrostatic pressure gradient down the initial height of the column |
| $\dot{P}_m^*$ | [ ] | 3 | The ratio between $\dot{P}_m$ and the equivalent hydrostatic pressure gradient down the initial height of the column |
| $P^*$ | [ ] | 5 | Normalised basal fluid pressure |
| $P_F^*$ | [ ] | 3 | Normalised residual basal fluid pressure |

# Notation

| Symbol | Dimensions | Chapter | Description |
|---|---|---|---|
| $P_r^*$ | [ ] | 5 | Averaged initial value of the reduced normalised pressure signal |
| $\mathcal{P}$ | $[\mathrm{ML}^{-1}\mathrm{T}^{-2}]$ | 5 | Hydrostatic pressure of the column prior to collapse |
| $q_v$ | $[\mathrm{LT}^{-1}]$ | 5 | Phase-specific volume flux per unit area |
| $Q$ | [ ] | 3, 4 | Quantities of interest |
| $r$ | [L] | 5, A, C | Radial spatial dimension |
| $r_0$ | [L] | 3, 4, 5, 6 | Radius of the column prior to collapse initiation |
| $r_c$ | [L] | A | Radius of the capillary |
| $r_{f,0}$ | [L] | 3 | Initial fluid phase front position |
| $r_v$ | [L] | 3, 5, 6, A, B | Instantaneous $v$ phase front position |
| $r_{v,F}$ | [L] | 3 | Final $v$ phase front position |
| $r^*$ | [ ] | 3, 4, B | System size |
| $r_v^*$ | [ ] | 5, 6, B | Normalised $v$ phase runout length |
| $\boldsymbol{r}_c$ | [L] | 6 | Coordinate direction aligned with the gravity vector |
| $R_c$ | [L] | 6 | Distance from the centre of the centrifuge |
| Re | [ ] | 3 | Reynolds number |
| $\mathrm{RMSE}_N$ | [ ] | 3, 4, 6 | Normalised root mean square error |
| $s^v$ | [L] | C | Surface level of the $v$ phase |
| $S$ | [ ] | C | Arbitrary scaler quantity |
| $S_v$ | $[\mathrm{L}^2\mathrm{T}^{-2}]$ | C | Summation of the $O(1)$ $v$ phase source terms |
| St | [ ] | 3 | Stokes number |
| $t$ | [T] | 3, 4, 5, 6, B, C | Time |
| $t_{col}$ | [T] | 3 | Cylinder lifting time scale |
| $t_{\mathrm{gap}}$ | [T] | B | Time required for the gap between the column and the horizontal plane to equal the inertial grain diameter |
| $t_{\mathrm{gap}}^*$ | [ ] | B | $t_{\mathrm{gap}}^*$ normalised by $t_I$ |

Notation

| Symbol | Dimensions | Chapter | Description |
|---|---|---|---|
| $t_m$ | [T] | 4 | Time after collapse initiation at which the maximum front velocity is achieved |
| $t_{\text{meet}}$ | [T] | B | Time at which point the free surface of the collapsing mixture is in line with the bottom of the steel cylinder |
| $t_{v,m}$ | [T] | 3 | Time after collapse initiation at which the maximum $v$ phase front velocity is achieved |
| $t_{v,ff}$ | [T] | 5 | Time related to the free-fall of the column $v$ phase |
| $t_F$ | [T] | 3, 5 | Time at the end of the recorded collapse period |
| $t_I$ | [T] | 3, B | Inertial column timescale |
| $t_L^*$ | [ ] | 3, 4, 5, 6, B | Ratio between $t$ and a characteristic inertial timescale $\sqrt{L/G}$ |
| $t_{m,L}^*$ | [ ] | 4 | Dimensionless time at which the maximum flow front Froude number is achieved |
| $t_{\text{meet}}^*$ | [ ] | B | $t_{\text{meet}}$ normalised by $t_I$ |
| $t_{v,L}^*$ | [ ] | 3 | Dimensionless time at which the maximum $v$ phase Froude number is achieved |
| $T$ | [K] | 3 | Fluid phase temperature |
| $T_c$ | [ML$^{-2}$T$^{-2}$] | 2 | Particle collision stress |
| $T_{fq}$ | [ML$^{-2}$T$^{-2}$] | 2 | Viscous shear stress |
| $T_T$ | [ML$^{-2}$T$^{-2}$] | 2 | Turbulent mixing stress |
| $u$ | [LT$^{-1}$] | 4 | Flow front velocity |
| $u_m$ | [LT$^{-1}$] | 4 | Maximum flow front velocity |
| $u_v$ | [LT$^{-1}$] | 3, 5, 6 | $v$ phase front velocity |
| $u_{v,m}$ | [LT$^{-1}$] | 3, 6 | Maximum $v$ phase front velocity |
| $u_v$, $w_v$ | [LT$^{-1}$] | C | $v$ phase down and perpendicular slope velocities |
| $\boldsymbol{u}$ | [LT$^{-1}$] | 6 | Arbitrary velocity vector |
| $\boldsymbol{u}_v$ | [LT$^{-1}$] | C | $v$ phase velocity vector |

Notation

| Symbol | Dimensions | Chapter | Description |
|---|---|---|---|
| $u^*$ | $[\mathrm{LT}^{-1}]$ | 5 | Viscous velocity scale |
| $u^*_{v,L}$ | [ ] | 3, 5, 6 | $u_v$ normalised by $\sqrt{LG}$ |
| $u^*_L$ | [ ] | 4 | $u$ normalised by $\sqrt{LG}$ |
| $\bar{u}_v, \bar{w}_v$ | $[\mathrm{LT}^{-1}]$ | 5, C | Depth averaged $v$ phase down and perpendicular slope velocities |
| $\bar{\boldsymbol{u}}_v$ | $[\mathrm{LT}^{-1}]$ | C | Depth averaged $v$ phase velocity vector |
| $U$ | $[\mathrm{LT}^{-1}]$ | C | Characteristic downslope speed |
| $V$ | $[\mathrm{ML}^2\mathrm{T}^{-3}\mathrm{I}^{-1}]$ | A | Voltage output |
| $V_0$ | $[\mathrm{ML}^2\mathrm{T}^{-3}\mathrm{I}^{-1}]$ | A | Voltage intercept |
| $V_v$ | $[\mathrm{L}^3]$ | 2, 3 | Volume of the $v$ phase |
| $x, y, z$ | $[\mathrm{L}]$ | 6, A, C | Planes of the Cartesian reference domain |
| $x_d, y_d, z_d$ | $[\mathrm{L}]$ | 6 | Length of the simulation domain in the three directions |
| $z_0, z_1$ | $[\mathrm{L}]$ | C | Arbitrary surfaces |

# Greek script

| Symbol | Dimensions | Chapter | Description |
|---|---|---|---|
| $\alpha, \beta, \gamma$ | [ ] | 3, 4, B | Constants in equation for $Q$ |
| $\alpha_n, \alpha_t$ | [ ] | 6 | Surface normal and tangential damping coefficients |
| $\alpha_v$ | [ ] | 6 | Proportion of the column's free-fall velocity attained by the $v$ phase |
| $\boldsymbol{\beta}_v$ | $[\mathrm{ML}^{-2}\mathrm{T}^{-2}]$ | C | Interaction force exerted on the $v$ phase by the other |
| $\dot{\gamma}$ | $[\mathrm{T}^{-1}]$ | 2, 4, A | Shear rate |
| $\gamma^*$ | [ ] | 5, 6, C | Grain-fluid density ratio |
| $\Delta_f$ | $[\mathrm{L}]$ | 6 | Fluid mesh size |
| $\Delta r$ | $[\mathrm{L}]$ | 5 | Cell width |
| $\Delta t$ | $[\mathrm{T}]$ | 5 | Time interval |
| $\epsilon$ | [ ] | C | Flow aspect ratio |

Notation

| Symbol | Dimensions | Chapter | Description |
|---|---|---|---|
| $\zeta$ | [L] | 6 | Elongation of a tangential spring |
| $\zeta_s$ | [ ] | C | Angle of inclination |
| $\eta_0$ | $[ML^{-1}T^{-1}]$ | 3 | Viscosity constant |
| $\eta_f$ | $[ML^{-1}T^{-1}]$ | 2, 3, 4, 5, 6, A, B, C | Fluid dynamic viscosity |
| $\eta_w$ | $[ML^{-1}T^{-1}]$ | 6 | Water dynamic viscosity |
| $\eta_f^*$ | [ ] | 6 | Normalised fluid dynamic viscosity |
| $\theta$ | [ ] | A | Angle axis |
| $\kappa$ | $[L^2]$ | C | Non-conservative flux term |
| $\mu_b$ | [ ] | 5, C | Basal friction coefficient |
| $\mu_r$ | [ ] | 6 | Rolling friction coefficient of the particles |
| $\mu_{rest}$ | [ ] | 6 | Coefficient of restitution |
| $\mu_s$ | [ ] | 6 | Static friction coefficient of particles |
| $\mu_{s,w}$ | [ ] | 6 | Particle-wall friction coefficient |
| $\xi$ | [L] | 6 | Particle overlap |
| $\rho$ | $[ML^{-3}]$ | 3, 4, 5, 6, A | Effective density of the granular-fluid column |
| $\rho_f$ | $[ML^{-3}]$ | 2, 3, 4, 5, 6, A, C | Fluid density |
| $\rho_g$ | $[ML^{-3}]$ | 3 | Glycerol density |
| $\rho_k$ | $[ML^{-3}]$ | A | Kaolin density |
| $\rho_p$ | $[ML^{-3}]$ | 2, 3, 4, 5, 6, C | Particle density |
| $\rho_w$ | $[ML^{-3}]$ | 3, A | Water density |
| $\rho^*$ | [ ] | 3, 4, B | Relative granular fluid density ratio accounting for acceleration scale buoyancy |
| $\sigma_f$ | $[MT^{-2}]$ | 3, 4, A | Fluid surface tension |
| $\sigma_g$ | $[MT^{-2}]$ | 3 | Glycerol surface tension |
| $\sigma_w$ | $[MT^{-2}]$ | 3 | Water surface tension |
| $\sigma'_{p,xx}, \sigma'_{p,zz}, \sigma'_{p,xy}$ | $[ML^{-1}T^{-2}]$ | C | Effective granular stress components |

# Notation

| Symbol | Dimensions | Chapter | Description |
|---|---|---|---|
| $\boldsymbol{\sigma}_v$ | $[\mathrm{ML^{-1}T^{-2}}]$ | C | $v$ phase symmetric stress tensor |
| $\boldsymbol{\sigma}'_p$ | $[\mathrm{ML^{-1}T^{-2}}]$ | C | Effective granular stress tensor |
| $\tau$ | $[\mathrm{T}]$ | 6 | Relaxation timescale over which collisions occur |
| $\tau_{f,xx}, \tau_{f,zz}, \tau_{f,xy}$ | $[\mathrm{ML^{-1}T^{-2}}]$ | C | Deviatoric fluid stress components |
| $\boldsymbol{\tau}_f$ | $[\mathrm{ML^{-1}T^{-2}}]$ | C | Deviatoric fluid stress tensor |
| $\phi$ | [ ] | 2 | Friction angle of the granular phase |
| $\phi_c$ | [ ] | 3, 5, C | Critical solid volume fraction |
| $\phi_v$ | [ ] | 2, 3, 4, 5, 6, C | Phase volume fraction |
| $\omega^0$ | [ ] | 6 | Domain only accounting for the curvature of the acceleration field |
| $\omega^+$ | [ ] | 6 | Full rotational domain with Coriolis accelerations acting in the 'upstream' direction |
| $\omega^-$ | [ ] | 6 | Full rotational domain with Coriolis accelerations acting in the 'downstream' direction |
| $\boldsymbol{\omega}, \omega$ | $[\mathrm{T^{-1}}]$ | 3, 6 | Centrifuge rotational velocity vector and scalar quantities |

Notation

# **Abbreviations**

| Symbol | Chapter | Description |
|:---:|:---:|:---:|
| CFL | 5 | Courant–Friedrichs–Lewy number |
| BGK | 6 | Bhatnagar-Gross-Krook |
| DAQ | A | Data Acquisition |
| DEM | 1, 2, 6 | Discrete Element Method |
| DIC | A | Digital Image Correlation |
| LBM | 1, 2, 6 | Lattice-Boltzmann Method |
| MPM | 2 | Material Point Method |
| PT | 3 | Pressure Transducer |
| SPH | 2 | Smoothed-Particle Hydrodynamics |

# Chapter 1

# Introduction

## 1.1 Motivation

Debris flows, a subset of gravity-driven slope hazards, are a serious concern in mountainous regions across the world (Jakob et al., 2005). These catastrophic events are typically triggered by intense rainfall (e.g. Redshaw et al., 2019; Rodolfo et al., 2016) or permafrost thaw (e.g. Allen et al., 2016; Sati, 2022), leading to the rapid movement of substantial volumes of water, soil, rocks, and organic matter. Like other geophysical flows, the substantial threat they pose to both communities and infrastructure situated in mountainous regions worldwide has prompted intensive scientific investigation of their complex dynamics.

The danger posed by debris flows emanates from their high fluid content, enabling them to achieve remarkable velocities and travel great distances. This particular characteristic complicates the prediction of their course and the implementation of diversion strategies. While debris flows are a global phenomenon, the impact of these landslide-style events exhibits notable disparities, intricately linked to variables like economic development, population growth, and the local interplay of climate and topography (Petley, 2012) (Figure 1.1). Among vulnerable European countries, Italy's geological composition, topographic features, and the surge in population density render it notably susceptible to debris flows. This vulnerability is highlighted by multiple catastrophic events within Italy over the past five decades (e.g. Bandis et al., 1999; Costa, 1991; Crosta and Dal Negro, 2003; Guzzetti, 2000), including a series of rainfall-triggered landslides in Southern Italy's Campania region in May 1998, which claimed 167 lives (Guadagno et al., 2011). This tragic event spurred the establishment of comprehensive landslide inventories at both regional and national levels (Trigila and Iadanza, 2008), as well as the development of an early warning system based on critical rainfall thresholds (Rossi et al., 2012).

In stark contrast, developing countries contend with exacerbated challenges due to extreme precipitation and burgeoning populations in previously uninhabited mountain-
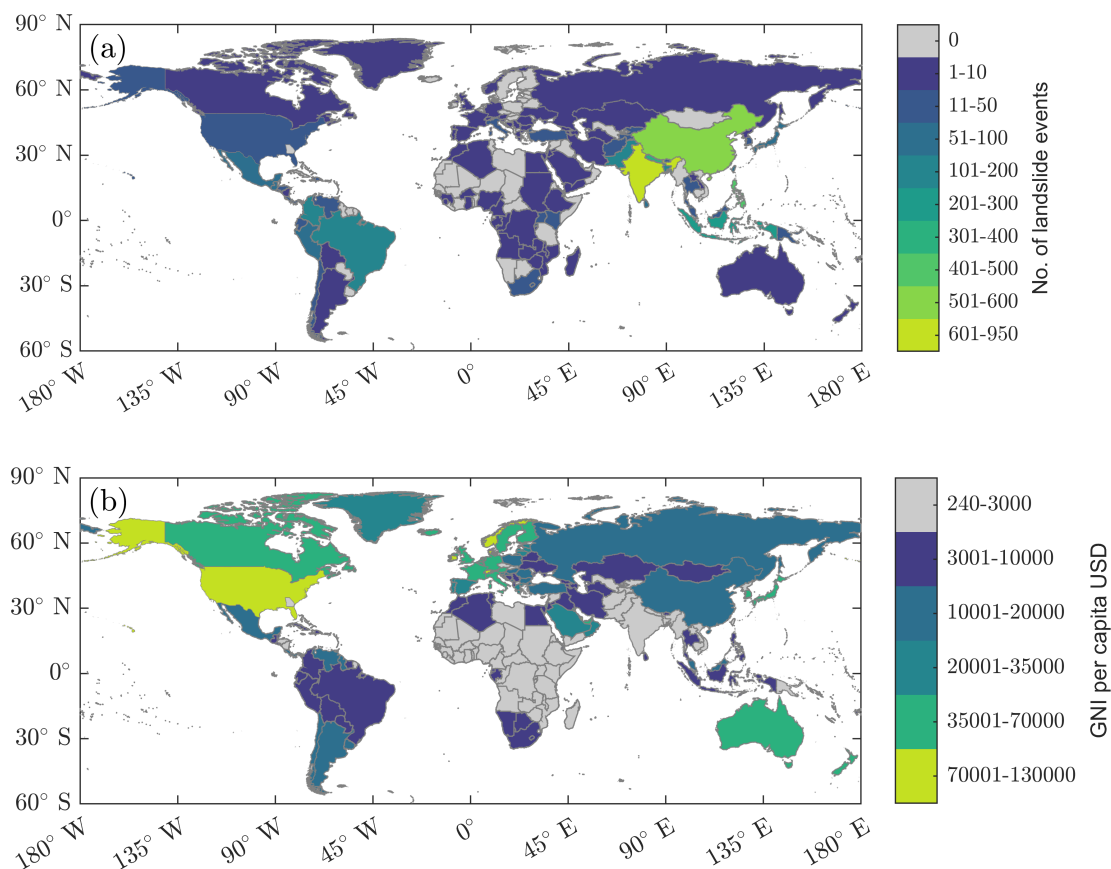
Figure 1.1: **(a)** Number of rainfall-triggered fatal landslide events from 2004 to 2017 by country (data obtained from the Global Fatal Landslide Database (GLFD) (Froude and Petley, 2018)). **(b)** Gross national income per capita (USD) by country (World Bank, 2023).

ous areas. In these regions, effective strategies for landslide mitigation are often lacking. A poignant example occurred in Venezuela in 1999, where a devastating debris flow resulted in tens of thousands of fatalities (García-Martínez and López, 2005). Furthermore, 70% of landslide-related fatalities in 2007 occurred in Asia (Petley, 2008), further highlighting the gravity of the situation. As climate change amplifies the occurrence of severe weather events, the frequency and magnitude of such mass movements are anticipated to surge even further (Gariano and Guzzetti, 2016). Consequently, understanding the intricate behaviour of debris flows and formulating effective mitigation strategies to counter their destructive potential is becoming increasingly important.

Despite persistent efforts, the compositional intricacies of debris flows continue to elude complete understanding. The high fluid volume fraction and elevated relative density of the grains results in the forces developed in both phases significantly contributing

to the dynamics of the mass movement (Iverson, 1997). The granular phase may also comprise a wide range of particle sizes (Kesseler et al., 2018), which, due to the interaction with the fluid phase, leads to complexity at both the grain- and macro-flow scales and the formation of ubiquitous debris flow features such as: a 'dry coarse head and fine watery tail architecture' (Johnson et al., 2012), lateral levees, and finger-like structures.

Laboratory scale experimental models can be employed to replicate particular mechanisms, or rheological conditions, observed in natural debris flow behaviour and study them in isolation. Among the various experimental setups explored, dam break scenarios, particularly column collapse tests, have emerged as an optimal approach for investigating the dynamics of unsteady flow motion.

The underlying concept is that, once these features are comprehensively understood, they can be articulated mathematically and integrated into scalable numerical models capable of predicting natural debris flow behaviour. However, the utility of experimental findings is constrained by scale effects influenced by geometry and force balance dynamics. In natural flows, gravity and inertial forces predominantly govern these processes. Contrastingly, at the laboratory scale, the size of the experiment and the relative impact of other forces, such as viscosity and surface tension due to the incorporation of a fluid phase, can attenuate gravity's role as the prime driver of the flow (Iverson, 2003).

In recent years, Geotechnical centrifuge modelling has emerged as a potential technique to artificially enhance the influence of gravity within these model flows, allowing for the exploration of flow behaviour across an otherwise unattainable parameter space.

## 1.2 Aims and objectives

The primary aim of this project is to investigate the mechanisms governing fluid-grain interactions in experimental debris flows and their scalability with gravity. This outcome can be achieved through the completion of the following objectives:

- To develop a centrifuge model configuration of the classic axisymmetric granular column collapse experiment. This model will allow for an in-depth exploration of the dynamics characterising fluid-grain interactions across a wide parameter space. These parameters include gravitational acceleration, fluid viscosity, and particle size distribution, encompassing both particle size and grading.

- To quantify the variations in fluid-grain interaction dynamics across the parameter space through the analysis of images and fluid pressure signals in order to discern

the dynamic processes that dictate flow outcomes.

- To develop a scalable mathematical framework that captures the observed behaviours.

- To explore the effects of the centrifugal acceleration field on collapse dynamics.

By systematically addressing these objectives, this research aims to advance our fundamental understanding of how experimental debris flow models can be used to explore the mechanics of their natural scale counterparts, ultimately contributing to a broader comprehension of natural processes.

## 1.3   Outline

The material in this thesis will be presented as follows: Chapter 2 provides an overview of the state-of-the-art research on debris flows. The chapter focuses on key aspects, such as debris flow classification, analysis of the flow's heterogeneous structure and complex mechanisms, limitations of common experimental modelling configurations, and a summary of the two most prevalent numerical modelling approaches for natural granular-laden flows.

Chapters 3-6 are self-contained research articles that collectively form the core of this work, focusing on the experimental and numerical modelling of a simplified granular-fluid flow configuration. Chapter 3 delves into the analysis of a series of just-saturated granular column collapse experiments conducted inside a geotechnical centrifuge (https://doi.org/10.1007/s10035-023-01326-x). The primary emphasis lies in studying fluid-grain interaction and characterising the phase front of the collapse.

Building on the concepts of Chapter 3, Chapter 4 investigates the same experimental configuration with a non-Newtonian fluid phase composed of kaolin clay particles suspended in water (https://doi.org/10.1051/e3sconf/202341501030). This chapter explores how the concentration of fines affects phase front behaviour by analysing the same quantities of interest used in characterising the Newtonian collapse case's acceleration phase.

In Chapter 5, the focus shifts from experimental modelling to the development of a two-phase shallow-water model (https://doi.org/10.1007/s10035-023-01391-2). This model is utilised to simulate the physical experiments conducted in Chapter 3, with special attention given to fluid-grain interactions.

Chapter 6 concludes the results chapters, where the DEM-LBM method is employed to examine the influence of centrifugal accelerations and the Coriolis effect on the dynamics of experimental particle-laden flows inside a geotechnical centrifuge (https://doi.org/10.1007/s10035-024-01408-4). The analysis begins by reproducing the Newtonian column collapse experiments discussed in Chapter 3. Subsequently, a parameter space analysis is performed by varying the centrifuge radius and angular velocity.

Chapter 7 provides the research project's comprehensive conclusions and offers insights into potential future research emanating from this study. The concluding remarks highlight the significance of the findings and discuss avenues for further exploration.

Finally, the remaining chapters consist of appendices detailing: the image and signal analysis techniques employed throughout the physical modelling (Appendix A); insight into the complexities of conducting these physical collapses at elevated accelerations (Appendix B); the derivation of the two-phase shallow-water model used in Chapter 5 based on the principles of mixture theory (Appendix C); and the introduction of a planar experimental configuration that was proposed to further understand granular-fluid interactions in debris flows (Appendix D).

Chapter 2

# Debris flows: From natural phenomena to laboratory and numerical representations

## 2.1 Debris flow classification

Due to their inherent complexity, achieving a widely accepted phenomenological description of debris flows has been a more recent advancement compared to other types of natural hazards. Based on the Varnes landslide classification system (Varnes, 1958) and other seminal works (e.g. Hungr et al., 2002; Hutchinson, 1997; Jakob et al., 2005), Hungr et al. (2014) proposed an updated classification encompassing various landslide related phenomena. This classification effectively segregated these mass movements into 32 distinct categories, based on factors such as the movement type, characteristics of the transported materials, water content, and the mass movement's characteristic velocity.

Within the framework of this classification, debris flows are defined as a 'very rapid to extremely rapid surging flow of saturated debris in a steep channel' (Hungr et al., 2014). Here, the term 'flow' denotes that gravitational forces primarily drive the mass movement, while 'saturated' indicates that the voids within the granular matrix are filled with interstitial pore fluid.

While this qualitative delineation is valuable for classification, it fails to encapsulate the diverse array of rheological behaviours observable in debris flows. To address this, adopting a classification approach centred on the mechanical behaviour of the flow through dimensional analysis proves advantageous. This strategy led Iverson (1997) to identify three dimensionless parameters that not only differentiate debris flows from other landslide-like mass movements, but also allow for the sub-classification of debris flows.

The first parameter, termed the Savage number $N_{Sav}$, characterises the relative sig-

nificance of flow resistance resulting from particle collisions as opposed to resistance due to frictional contacts (i.e. Coulomb friction)

$$N_{Sav} = \frac{\dot{\gamma}^2 \rho_p d_p}{n_p(\rho_p - \rho_f)g \tan \phi}, \tag{2.1}$$

where $\dot{\gamma}$ represents the characteristic shear rate of the flow, $\rho_p$ and $\rho_f$ are the densities of the solid and fluid phases, $d_p$ is the diameter of the solid phase grains, $n_p$ is the number of grains, $g$ is gravitational acceleration, and $\phi$ is the friction angle for the granular phase.
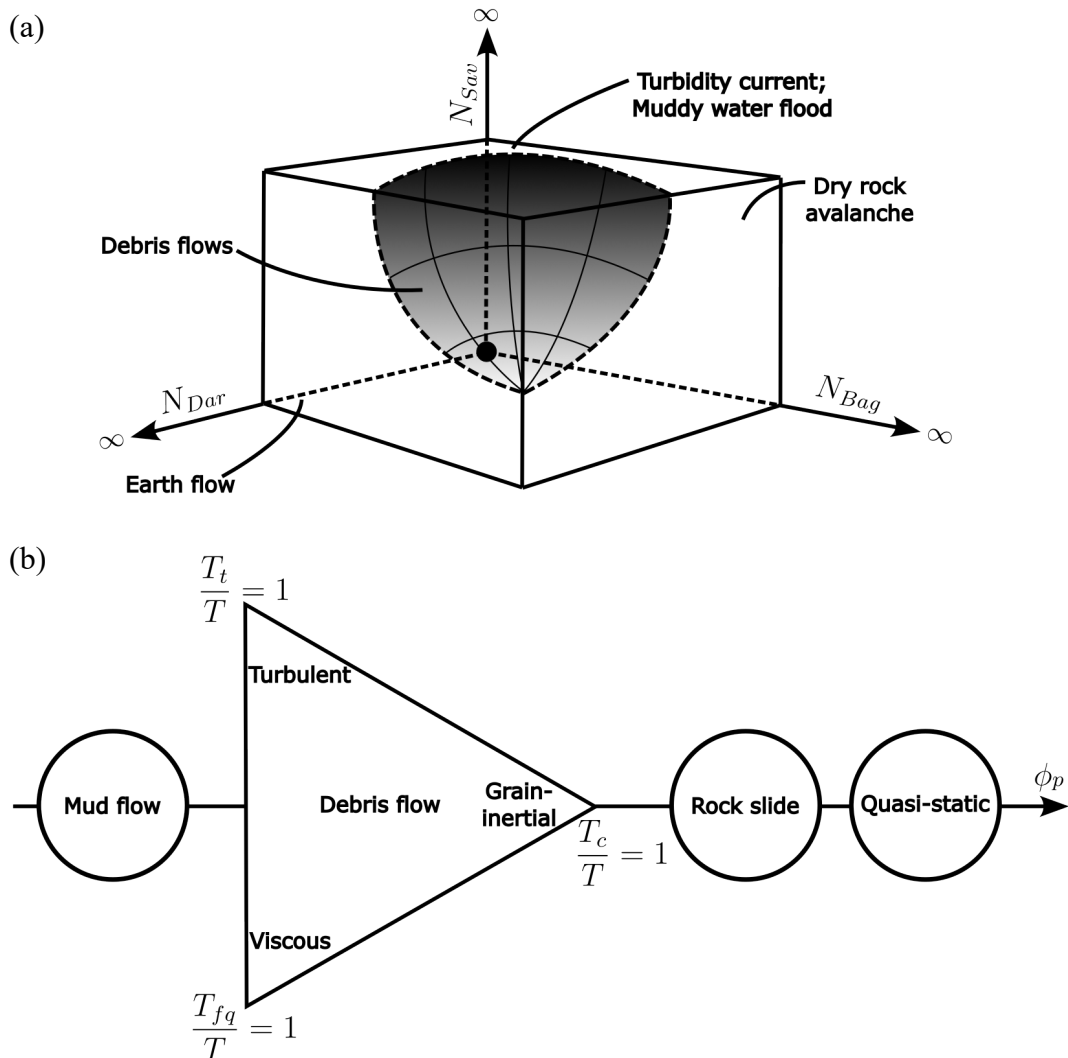


Figure 2.1: (a) Iverson's (1997) classification scheme for debris flows (adapted from Iverson, 1997). (b) Takahashi's (2007) natural particle-fluid flow classification scheme (adapted from Leonardi, 2015).

The second parameter, known as the Bagnold number $N_{Bag}$ (Bagnold, 1954), quantifies the relative impact of inertial grain stresses and viscous shear stresses on the flow's rheology

$$N_{Bag} = \frac{C_B}{1 - C_B} \frac{\rho_p d_p^2 \dot{\gamma}}{\eta_f},$$ (2.2)

where $C_B$ is the bulk sediment concentration and $\eta_f$ is the dynamic viscosity of the fluid. The final parameter, the Darcy number $N_{Dar}$, characterises the extent to which grain interactions are mediated by the pressure of the interstitial pore fluid

$$N_{Dar} = \frac{\eta_f}{C \rho_p \dot{\gamma} k},$$ (2.3)

where $k$ denotes the hydraulic permeability of the granular phase.

Thus, Iverson (1997) proposed that natural debris flow behaviour could be differentiated from other mass movements by the parameter space constraints: $N_{sav} \lesssim 0.1$, $0.2 \lesssim N_{Bag} \lesssim 400$ and $N_{Dar} \gtrsim 5000$, within which $N_{sav}$, $N_{Bag}$ and $N_{Dar}$ could vary (Figure 2.1a). It is worth noting that this restricted parameter space may not be applicable to experimental debris flow configurations (see Section 2.3).

Takahashi (2007) proposed an alternative classification system (Figure 2.1b) that, similar to Iverson's (1997) approach, considered the relative contributions of three stresses namely, particle collision stress $T_c$, viscous shear stress $T_{fq}$ and turbulent mixing stress $T_T$, to flow dynamics. Additionally, Takahashi's (2007) system incorporates the coarse particle concentration, referred to as the solid volume fraction $\phi_p$

$$\phi_p = \frac{V_p}{V_p + V_f},$$ (2.4)

where $V_p$ and $V_f$ denote the volumes of the granular and fluid phases, respectively. The inclusion of $\phi_p$ as a dimension allows for the consideration of the flow water content. Low $\phi_p$ values correspond to mud flows, while sufficiently large $\phi_p$ values indicate negligible fluid content (i.e. a rockslide). Takahashi (2007) proposed that debris flows fall within a $\phi_p$ range of 0.2 to 0.5. The lower limit of this range corresponds to a high $N_{Sav}$ value, as Coulomb friction does not significantly contribute to the total stress $T$. Increasing $\phi_p$ results in greater frictional resistance and $N_{sav} \lesssim 0.1$, which aligns with the debris flow mechanics classification outlined by Iverson (1997). Within this $\phi_p$ range, the ratio of $T_c$, $T_{fq}$ and $T_T$ to $T$ further influences the rheological behaviour of the flow.

While the mechanical classification of debris flows provides valuable insights into their theoretical dynamics, its applicability to debris flow prediction and mitigation is constrained due to its omission of the total mass of flowing material, a crucial parameter when forecasting flow mobility and inundation areas (e.g. Chae et al., 2017; Rickenmann, 1999). This limitation exists alongside the consideration that the composition and, consequently, the rheology of debris flows evolve both spatially and temporally (Iverson, 2003).

## 2.2 Evolution of natural flows

A naturally triggering debris flow unfolds in three principal stages: initiation, transportation, and deposition (Figure 2.2). This section sequentially delves into each phase, elucidating on distinctive aspects of debris flow dynamics that hold paramount significance from a scientific perspective.



Figure 2.2: Aerial photograph of the Daniao tribe debris flow that occurred in Taiwan in 2009 (photograph taken from Tsai et al., 2011). The zones corresponding to each phase of debris flow motion are highlighted.

## 2.2.1 Initiation

Debris flows commonly materialise when a previously stationary mass of unconsolidated granular material, such as soil, attains a critical state, prompting movement down a steep incline (Iverson, 1997). The driver for failure arises from an increasing water content that undermines the material's stability by diminishing the normal effective stress exerted upon it. Typically, the inflow of water stems from abrupt, intense rainfall events (García-Martínez and López, 2005). Additionally, instances occur where water infiltration results from permafrost thawing or glacier melt (e.g. Chiarle et al., 2007; Sattler et al., 2011). These failure mechanisms have undergone comprehensive examination within the framework of slope stability analysis, leveraging methodologies commonly utilised within the discipline of Civil Engineering (Duncan et al., 2014; Fang et al., 2022). Consequently, parameters encompassing the slope's geometric and geomorphological attributes, coupled with the static and temporal loading conditions imposed upon it, have emerged as critical factors when determining its stability. It is important to acknowledge that the mechanisms described above represent general triggers for debris flows on steep slopes; however, it's worth noting that factors such as climate, topography, and lithology can play a substantial role in dictating the precise locations where debris flow initiation occurs (Brayshaw and Hassan, 2009).

## 2.2.2 Transportation

### 2.2.2.1 Surge front architecture

Debris flows, once initiated, exhibit distinctive transport patterns, often involving a series of surges. These surges represent episodic movements, with the initial surge being the most substantial, followed by subsequent smaller ones (Iverson, 1997; McCoy et al., 2010). The transported material spans a wide range of sizes, from fine sediments, such as silts and clays, to larger boulders and organic elements like timber (Turnbull et al., 2015). Although surges can develop in more uniform flows, where the granular phase primarily comprises fine particles, as in Takahashi's (2007) definition of turbulent mud flows, our focus here pertains to the more common scenario of surges transporting granular material with diverse particle sizes.

Surge waves within debris flows typically exhibit a distinct architecture (Figure 2.3). The leading portion, the dense, dry granular 'head', contains the highest concentration of coarse materials and achieves the greatest flow depth (Hungr, 2000). This is followed by
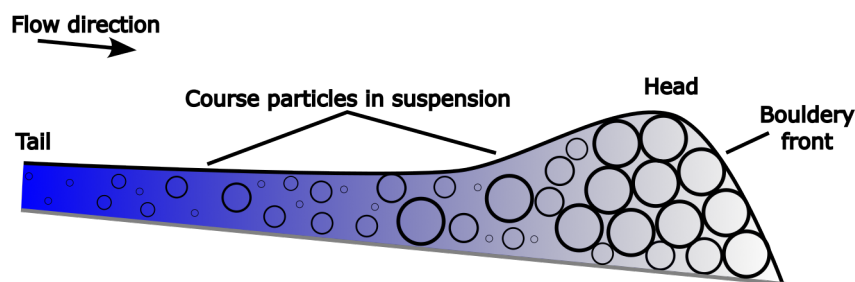
Figure 2.3: Schematic showing the typical distributions of particle size and fluid concentration (blue gradient) within a debris flow surge (inspired by Pierson, 1986).

a progressively more fluidised and shallower 'tail'. While Takahashi (1981) attributed this phenomenon to Bagnold's (1954) theory of dispersive pressure, other studies have reproduced this behaviour through the concepts of kinetic sieving and squeeze expulsion (e.g. Johnson et al., 2012; Savage and Lun, 1988; Vallance et al., 2000). In mixtures of polydispersed grains subjected to shear forces, smaller grains tend to settle into spaces created by the movement of larger grains, leading to a downward migration. This process results in a size-dependent inverse grading throughout the flow depth, as larger particles are pushed towards the flow's surface due to constrictions in the flow-parallel direction. As the flow's velocity at the free surface is larger than the average velocity of the flow, the larger particles are able to migrate to the head of the flow. The presence of larger pore spaces between the boulders at the head of the flow enables easy fluid drainage, causing the head to become dry and its behaviour to be dominated by granular friction (Iverson, 1997).

#### 2.2.2.2 Heterogeneous pore pressure distributions

The architecture of debris flows, as observed through field observations (e.g. Berti et al., 1999) and large-scale experiments (e.g. Major and Iverson, 1999), highlights the spatial and temporal variability in particle concentration. This variability is compounded by the broad spectrum of particle sizes present in field-scale flows, leading to varying porosities within the granular material across both space and time (Iverson et al., 2010b). Consequently, the distribution of pore fluid and, therefore, pore pressure within the flow becomes heterogeneous and strongly coupled to local flow dynamics.

A key mechanism shaping debris flow behaviour involves the generation of excess pore pressure, defined as the deviation of pore pressure from the expected hydrostatic

pressure for a given location and time within the flow (Kaitna et al., 2016). Shear zones within the flow trigger relative movements among particles, leading to either the dilation (increased inter-grain spacing) or contraction (decreased spacing) of the pore space. These shear-induced movements yield local pore pressure gradients, causing interstitial fluid to be expelled or drawn into the spaces opened or closed by the shear motion, thus altering the basal fluid pressure at that specific location (Iverson et al., 2000).

The continuous interplay of dilations and contractions, particularly in the more liquefied regions of debris flows, can sustain positive excess pore pressures over extended periods. Large-scale flume tests (e.g. Major and Iverson, 1999) and field observations (e.g. McArdell et al., 2007) have demonstrated that this time scale can vary from hours to days, spanning from flow initiation to post-depositional consolidation. This prolonged high pore-pressure retention significantly contributes to the enhanced mobility of granular-fluid flows compared to dry granular flows. Elevated basal pore pressures lead to reduced friction between the flow body and its basal boundary by decreasing basal normal stress (Huggel et al., 2005), effectively lubricating the bulk flow's motion.

An in-depth laboratory investigation by Kaitna et al. (2016), involving rotating drum experiments, uncovered a further layer of complexity within the pore-pressure feedback loop. These findings corroborated Iverson's (2015) research and highlighted that the grain size distribution of the solid-phase granular material substantially influences the flow's capacity to maintain elevated pore pressures. The rate at which coarser material from the flow's front is overridden and recirculated into the bulk dictates the speed of pore space contraction within the liquefied flow regions, thus affecting the rate of pore pressure reduction. By increasing the proportion of finer material that remains suspended within the flow, effectively increasing the density of the interstitial fluid, the settling of coarser particles is curtailed, prolonging their suspension within the flow and restraining pore pressure dissipation. The grain size distribution, specifically the inclusion of a high percentage of fine granular material, has also been found to play a significant role in material erosion, entrainment and deposition processes (e.g. de Haas et al., 2015; Roelofs et al., 2022).

### 2.2.3 Deposition

Within the transportation zone, it has been observed that material carried by the flow can be deposited through the development of lateral levees (Iverson, 2014; Johnson et al., 2012). However, the deceleration and cessation of motion of the bulk flow primarily re-

sults from the distinct changes in topography between the transportation and deposition
zones. Specifically, the diminishing slope angle and the topography no longer providing
the necessary lateral confinement essential for the containment of the flow (Delannay
et al., 2017; García-Martínez and López, 2005). Consequently, this lack of confinement
allows the flow to disperse laterally and diminish in height, eventually reaching a critical
threshold that curtails its sustained momentum.

In the context of hazard assessment and risk mitigation, understanding the final
runout distance of the flow and the geometry of the primary deposition area, commonly
known as the alluvial fan, is of utmost importance. To this end, it is common to utilise
geometric, volumetric and material data from previous mass movement events to cal-
ibrate empirical scaling relations that are capable of predicting these significant flow
characteristics (Rickenmann, 1999). However, it is important to recognise the suscepti-
bility of these techniques to uncertainties stemming from the approximation of material
properties (see Section 2.3.1), the volume of flowing material, and the meteorological
conditions during the event.

Analysis of the stages of debris flow motion highlights the complex interplay of spa-
tial and temporal dynamics, revealing the heterogeneous nature of debris flow behaviour.
Local flow characteristics are profoundly influenced by the specific composition of the
flow in a given region. Moreover, this analysis highlights the multi-scale nature of
the mechanisms governing debris flow dynamics, operating across multiple length and
time scales. Hence, while classification schemes based on flow mechanics (discussed
in Section 2.1) offer valuable insights, their limitations become evident in the context of
temporal and spatial variations. Classifications that hold true for certain locations within
the flow at specific moments might not remain applicable to all points throughout the
entire duration of the mass movement event. This intricate variability highlights the
need for a comprehensive understanding of the underlying processes that dictate debris
flow behaviour. Most pertinently, the interaction between the granular and fluid phases.

## 2.3   Field measurements and physical modelling

### 2.3.1   Field measurements and large-scale testing

The most intuitive approach to understand debris flow mechanics is through the observa-
tion of naturally triggered events (McArdell, 2016). Field measurements obtained from
such events play a pivotal role in the validation of research conducted at smaller scales
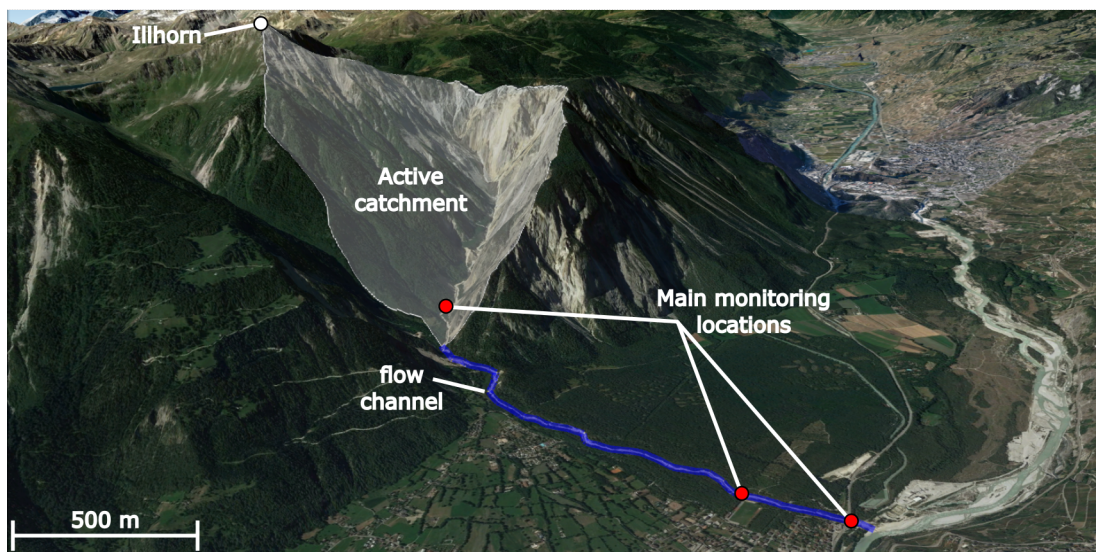
Figure 2.4: Oblique view of the Illgraben catchment as well as the location of the main monitoring locations within the active catchment and along the main flown channel (image taken from Google Earth).

(as elaborated in Section 2.3.3) and provide valuable data for empirical and statistical studies, especially concerning flow runout and volume estimation (Rickenmann, 1999). However, acquiring field measurements from naturally occurring debris flows presents significant challenges. Two primary factors hinder this process:

1. Unpredictable initiation: Debris flows are typically triggered by short, heavy downpours, making the initiation of these events unpredictable.

2. Safety concerns: The inherent danger posed by debris flows limits researchers' ability to approach and gather data during these events.

To address these challenges, researchers often deploy unmanned measurement equipment within catchment areas before an event occurs. Therefore, the choice of catchment is critical, as it should provide recordable mass movement events at a sufficiently high frequency.

One notable catchment that has been extensively studied is the Illgraben catchment in South-west Switzerland (Figure 2.4). Since the opening of the observation station in 2000, this catchment has recorded 75 individual debris flow events (accurate as of 2019) (Hirschberg et al., 2019). In addition to monitoring rainfall within the catchment using a network of rain gauges, various monitoring locations within the active catchment and along the basin's channel are equipped with instruments to measure essential parameters

such as flow depth, flow velocity, basal normal and tangential forces (e.g. McArdell et al., 2007), flow erosion and deposition (Berger et al., 2011; de Haas et al., 2023), and other variations in flow and bed geometry (e.g. Spielmann et al., 2023).

Despite the valuable insights provided by monitored research catchments like Illgraben, they are not without limitations. A significant constraint is that information obtained from naturally occurring debris flows is often constrained by the lack of data on initial and boundary conditions of the mass movement (Iverson et al., 2010b). Furthermore, material parameters derived from the final flow morphology are typically poorly constrained. Thus, interpreting the data recorded from such events is typically a two stage processes, requiring assumptions to be made about the flow's composition before its behaviour can be understood. This is often done by back-calculating the dynamics of an event using a numerical tool where material and boundary input parameters are systematically varied to reproduce the observed flow outcomes (see Section 2.4).



Figure 2.5: Photograph of the USGS debris flow flume during a test (photograph taken from George and Iverson, 2014).

To address the limitations of field measurements, researchers often conduct dynamically similar studies at large-scale flume testing facilities. Such facilities, like those at the US Geological Survey (USGS) in the USA (95 meters long and 2 meters wide) (e.g. Iverson et al., 2010b; Johnson et al., 2012) or the Kadoorie Center in Hong Kong (28 meters long and 2 meters wide) (Lam et al., 2022; Lam and Wong, 2021), offer

the opportunity to study various aspects of debris flow behaviour and their interaction with potential mitigation structures. However, it's important to note that these facilities are limited in number due to the substantial financial backing and space required for their construction. Furthermore, the preparation of a single test in these facilities is time-consuming, making the acquisition of repeatable results for verification relatively uncommon.

### 2.3.2 Laboratory-scale experimental configurations

In contrast to large-scale testing, laboratory experiments offer a distinct advantage in the study of granular-fluid flows. This advantage lies in the ability to exert precise control over all parameters governing the flow and the boundary conditions throughout the duration of the mass movement. This level of control offers the invaluable benefit of generating highly repeatable datasets (Iverson, 2003). Such experiments play a pivotal role not only in the calibration and validation of numerical models used for predicting granular-fluid flow behaviour (e.g. Berzi and Jenkins, 2008; Ceccato et al., 2020; Meng et al., 2022) (see Section 2.4 for further details), but also in advancing our comprehension of intricate flow characteristics.

Laboratory experiments serve as a means to distil specific aspects of natural debris flow behaviour into simplified physical models. This abstraction facilitates parametric studies aimed at understanding the influence of various parameters on the mechanisms under investigation (MiDi, 2004). The ability to isolate and manipulate these parameters enables researchers to gain insight into the nuanced controls governing granular-fluid flows.

Forterre and Pouliquen (2008) categorised most steady-state experimental configurations used to investigate particle-laden flow behaviour into six general configurations (Figure 2.6). While their focus was on dry granular material, these configurations are also applicable to granular flows containing an interstitial fluid. In all six cases, either volume- or pressure-controlled conditions are imposed to simplify the stress-state of the test material.

The first three experimental configurations, the plane shear (Figure 2.6a), the annular shear (Figure 2.6b), and the vertical silo (Figure 2.6c), analyse the response of the granular material to an imposed shear stress (e.g. Contreras and Davies, 2000; Coussot et al., 1998; Iverson et al., 2010a; Major and Pierson, 1992). The plane and annular shear experiments work by shearing the granular material between two surfaces, one static and
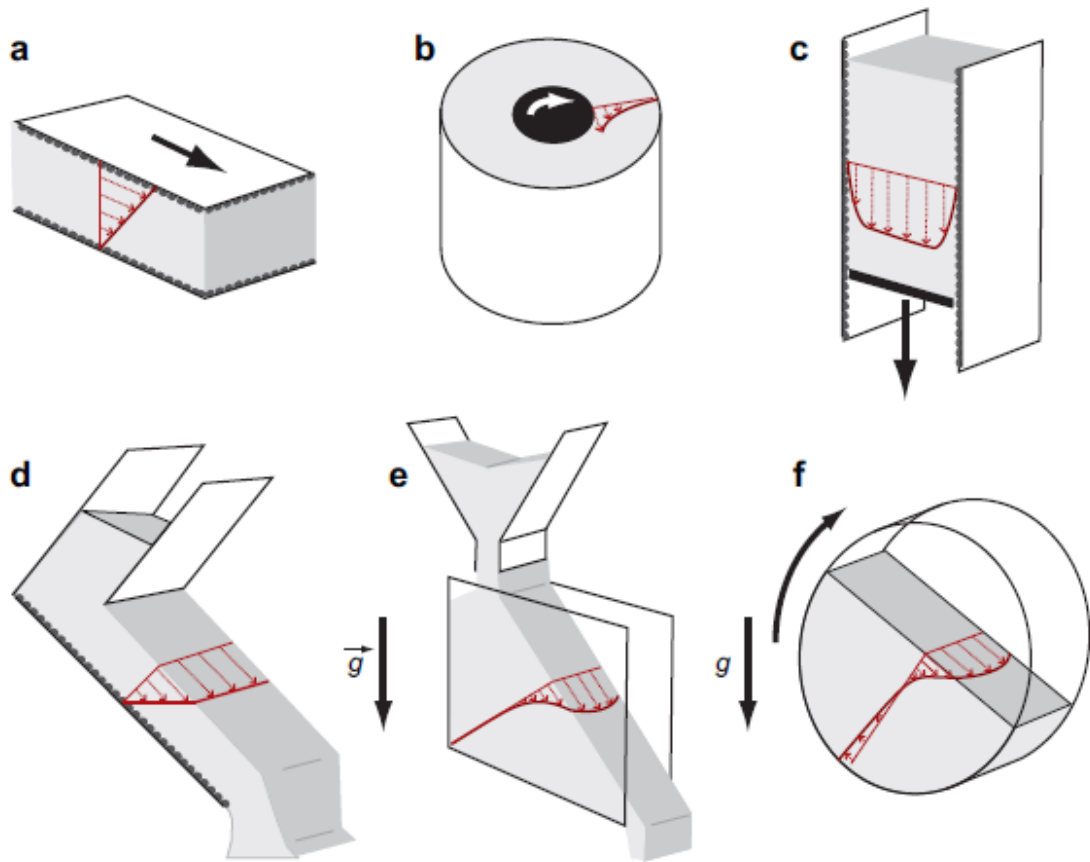
Figure 2.6: Typical experimental configurations for the study of steady dense granular flows (taken from Forterre and Pouliquen, 2008). (**a**) plane shear, (**b**) annular shear, (**c**) vertical silo, (**d**) inclined plane, (**e**) heap flow, and (**f**) rotating drum. Black arrows indicate the forces applied to the system while red arrows highlight the typical shape of the subsequent flow's velocity profile.

one driving the material's deformation, in order to assess variations in the material's behaviour under different loading and shearing conditions. Similar assessments of material properties from in-situ samples are also performed using triaxial shear test configurations (e.g. Gabet and Mudd, 2006; Hu et al., 2016). The vertical silo configuration (Figure 2.6c) is primarily relevant to granular flow in industrial processes, investigating how the dynamics of the collapsing material are controlled by the geometry of the opening through which the material exits and the mass of the material contained within the structure (e.g. Dorbolo et al., 2013; Orpe and Kudrolli, 2007; Pacheco-Martinez et al., 2008).

The remaining three configurations are primarily used to analyse the dynamics of flowing mass movements demonstrating steady flow characteristics. The heap

flow configuration (Figure 2.6e), is used to study the temporal release and evolution of avalanches arising from the accumulation of granular material (Fan et al., 2017; Lemieux and Durian, 2000). The rotating drum configuration (Figure 2.6f) allows researchers to investigate the kinematics of granular flows under steady-state conditions, where the forces driving (predominantly gravity) and retarding (i.e. basal friction) the flow are approximately equal. Such investigations are useful for understanding flow mechanisms that contribute to flow dynamics over prolonged timescales, such as segregation (e.g. Gray, 2001; Kaitna et al., 2016; Turnbull, 2011).

Finally, the inclined plane configuration (Figure 2.6d) is of particular relevance to debris flow research. Much like the large-scale testing facilities discussed in Section 2.3.1, it involves allowing a predetermined quantity of granular material to freely move down an inclined slope where parameters like the roughness of the bed and the lateral confinement of the flow can be adjusted. This configuration can be adapted to investigate unsteady granular motion which, as discussed in Section 2.2, is the behaviour observed over the duration of a natural mass movement. Flow dynamics can then be tracked and analysed throughout the flow's duration. The specific configuration pertinent to the current research, the dam-break over a horizontal plane (e.g. Lajeunesse et al., 2004; Lube et al., 2004; Trepanier and Franklin, 2010; Warnett et al., 2014), will be described in Chapter 3.

### 2.3.3 Scaling

In order to draw meaningful comparisons between laboratory-scale experiments and large-scale events, it is imperative to consider appropriate scaling laws, as emphasized by previous research (e.g. Heller, 2011; Iverson and Denlinger, 2001). As stated by Heller (2011), an experimental model can only achieve complete mechanical similarity to a natural (i.e. prototype) event by meeting the following criteria:

1. Geometric similarity: ensuring that the physical dimensions of the model's geometry are proportional to those of the prototype event. For the analysis of free-surface flows, parameters such as channel width, length, and angle of inclination assume significance.

2. Kinematic similarity: In addition to achieving geometric similarity, kinematic similarity demands that the model faithfully replicates the patterns of motion observed in the prototype flow. This involves maintaining consistent ratios of time,

velocity, acceleration, and discharge (particularly relevant for fluid phenomena) between the model and the prototype (Heller, 2011).

3. Dynamic similarity: In addition to the previous two conditions, dynamic similarity necessitates that the force ratios (see Section 2.1 for examples) in the prototype are identically reproduced in the model.

Failure to meet all three criteria results in experimental flows that exhibit scale effects. Achieving complete mechanical similarity with a laboratory model is typically not possible. As such, experimentalists try to achieve partial similarity but the selected scaling laws are dependent on the processes being investigated. For example, to mitigate the influence of scale effects on flow dynamics, some experimental studies, often conducted using typical flume or chute configurations, employ Froude similarity scaling (e.g. Choi et al., 2015; Kesseler et al., 2018; Scheidl et al., 2013). Froude scaling aims to match the ratio of inertial and gravitational forces within both the model and prototype flows (Heller, 2011). While valuable, Froude scaling has limitations when applied to modelling debris flows, primarily due to the inherent complexity of such flows.

Small-scale models frequently struggle to achieve dynamic similarity with their prototype flows, primarily due to the scale-dependence of certain forces contributing to flow dynamics. Notably, laboratory-scale debris flows tend to overemphasise the contributions of fluid viscosity and particle collisions to bulk shear resistance while underrepresenting the effects of pore pressure diffusion, as compared to their influence on natural flows (Cabrera and Wu, 2017; Iverson, 2015). Furthermore, the simplification of natural flows' often well-graded grain size distribution to a monodispersed mixture in small-scale experiments can overlook vital mechanisms that affect flow behaviour over smaller length and time scales (Sanvitale and Bowman, 2017). Conversely, including smaller particle sizes in small-scale experiments with a fluid phase can lead to an overstatement of surface tension effects relative to gravitational forces at the macro-flow scale (Iverson, 2003; Iverson, 2015).

### 2.3.4 Centrifuge testing

As discussed previously, gravity plays a pivotal role in governing the behaviour of granular flows, serving as the primary driving force. To attain dynamic similarity between an experimental model and a prototype flow, one potential approach is to manipulate the acceleration field applied to the model. This can be accomplished through the utilisation of a geotechnical centrifuge (Taylor, 1995). By rotating a laboratory-scale model

at a given angular velocity at the end of a centrifuge arm, a centripetal acceleration is imposed on the model. When this centripetal acceleration exceeds Earth's gravity by a scaling factor $N$, it augments the self-weight of the material within the model, thereby enabling precise control over the gravitational effects in the model (Cabrera and Wu, 2017). By adopting principles of geometric similarity and constructing an experimental model scaled down by a factor of $N$ compared to the prototype scenario, it is possible to derive valuable scaling laws that establish relationships between parameters in the model and those in the prototype (refer to Table 2.1).

Table 2.1: Centrifuge model scaling relationships most relevant to granular mass flows (Garnier et al., 2007).

| Parameter | Scaling factor (model/prototype) |
|---|:---:|
| Pressure, stress | 1 |
| Strain | 1 |
| Density | 1 |
| Length | $1/N$ |
| Gravity | $N$ |
| Time (inertial) | $1/N$ |
| Force | $1/N^2$ |
| Velocity[a] | 1 |
| Frequency | $N$ |
| Kinetic energy (free-fall) | $N^3$ |
| Acceleration | $N$ |
| Stiffness | $1/N$ |

Centrifuge modelling is a well-established technique in the field of Civil Engineering, widely employed to investigate various geotechnical problems, including the behaviour of soils under different levels of saturation (e.g. Caicedo and Thorel, 2014; Mirshekari and Ghayoomi, 2017), static and dynamic soil-structure interactions (e.g. Marshall et al., 2012; Stewart and McCartney, 2014), and issues related to soil stability and improvement (e.g. Liu et al., 2023; Zhang et al., 2001a). As evidence of its significance, over 100 such facilities have been established worldwide. A selection of these facilities are shown in Figure 2.7, delineating their maximum allowable acceleration and model payload capacities. The centrifuge facility at the University of Nottingham lies in the middle of the distribution, with the capacity to spin a 335 kg payload at a centripetal acceleration equivalent to $150g$.

Recently, centrifuge modelling has found applications in the study of geophysical
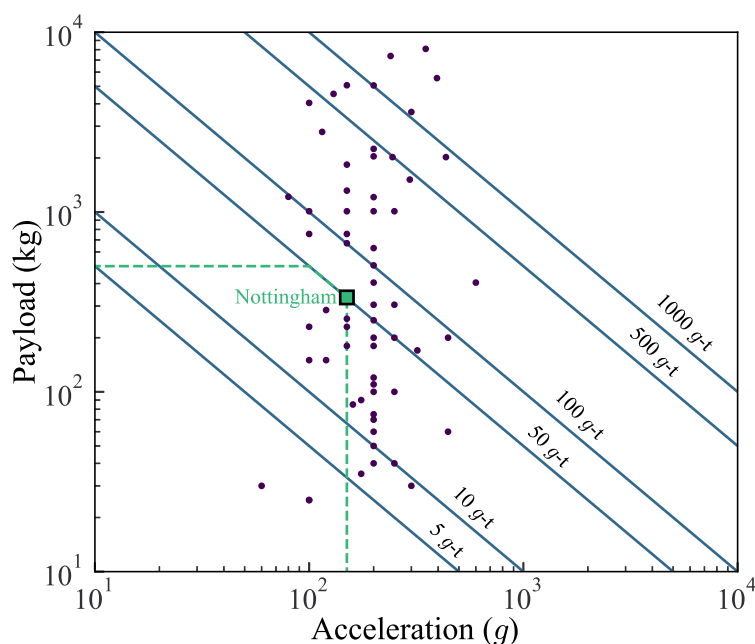
Figure 2.7: Maximum allowable acceleration against the allowable model payload for a selection of centrifuge facilities around the world. The allowable testing range of the University of Nottingham's geotechnical beam centrifuge is confined by the green dashed line (adapted from Idinger, 2016 and Cabrera, 2016).

flow behaviour. This application primarily centres on the exploration of pressure-dependent mechanisms that influence flow behaviour. Initial studies focused on scaling the flow kinematics of simple dry granular flow configurations (e.g. Brucks et al., 2007; Vallejo et al., 2006). More recent fundamental research has delved into specific aspects of geophysical flow behaviour, such as bed erosion and entrainment (Bowman et al., 2010) and particle breakage (Bowman and Take, 2015; Bowman et al., 2012). Additionally, the examination of flow-structure interaction has gained prominence (e.g. Ng et al., 2018; Song et al., 2019), given its direct relevance to disaster mitigation.

While centrifuge modelling has proved invaluable in advancing our understanding of geophysical flows, several areas still require further investigation and improvement. A critical challenge, similar to the one faced by laboratory-scale experiments, pertains to accurately scaling flows to replicate natural observations. While matching the Froude number and elevating the $g$-level can achieve similarity in macro-scale flow characteristics, particle size and size distributions remain influential regulators of flow dynamics (Cui et al., 2018; Jiang et al., 2015). Consequently, some researchers have proposed the need to scale particle size when designing centrifuge experiments (Song, 2016; Turnbull et al., 2015). Moreover, the study of grain-fluid interactions within saturated flows un-

21

der elevated gravitational fields represents a relatively unexplored area (Cabrera et al., 2018; Song et al., 2019). This stems from the complex nature of pore fluid lubrication and drag mechanisms, which operate across a multitude of scales (Huang and Zhang, 2022). The effects of centrifuge configuration on debris flow experiments are discussed in Chapters 3, 5 and 6.

## 2.4 Numerical modelling

In the context of geophysical flow research, laboratory-scale physical experiments serve as invaluable tools for isolating and exploring the fundamental mechanisms governing flow behaviour. However, the insights derived from these experiments remain constrained in their utility unless we can establish meaningful connections to geophysical-scale flows. Consequently, it becomes imperative to express these physical mechanisms in mathematical terms and construct numerical models capable of capturing the dynamic evolution of flow states over time. These numerical models not only serve a pivotal role in predicting geophysical flow behaviour but, once calibrated and validated, extend their utility to the exploration of parameter spaces that are challenging to access through physical experimentation (Cabrera et al., 2020).

Within the domain of granular-laden flow prediction, two main categories of models have gained prominence: the continuum approach and the continuum-discrete approach. The following section provides an overview of these two approaches, highlighting their respective strengths and limitations.

### 2.4.1 The continuum approach using shallow-water equations

#### 2.4.1.1 Dry granular flows

The continuum approach is used throughout the field of fluid mechanics (Batra, 2006). It works on the assumption that local flow properties, such as density, granular temperature, and velocity, change gradually and continuously throughout the flow. Consequently, we can treat the constituents of the flow, such as grains, as part of a continuous medium.

Notably, Savage and Hutter (1989) built upon the pioneering work of Savage (Savage, 1984, 1979), developing what is now regarded as the foundational framework for modelling dry granular flows within this continuum approach. Using differential equations to describe mass and momentum conservation of the system, their model describes

the motion of a finite mass of granular material down an inclined plane, mirroring the classic shallow-water equations but in a granular context (Vreugdenhil, 1994). Like these other models, Savage and Hutter's (1989) formulation assumes a shallow-flow condition, where the flow depth is considerably smaller than the flow's length, and the flow's velocity profile is known and remains uniform throughout the flow (Pudasaini and Hutter, 2007). To account for granular basal frictional resistance, they employ the Mohr-Coulomb friction criterion (Labuz and Zang, 2012), wherein frictional resistance is directly proportional to the applied normal pressure with a constant friction coefficient.

Subsequent models have expanded upon Savage and Hutter's (1989) foundation to accommodate more intricate bed geometries (e.g. Gray et al., 1999; Greve and Hutter, 1993; Hutter and Koch, 1991; Pudasaini and Hutter, 2003) and the lateral spreading of the flow (e.g. Greve et al., 1994; Hutter et al., 1993), thereby capturing a wider range of granular flow dynamics.

### 2.4.1.2 Single phase debris flow models

For continuum models to be utilised in predicting the dynamics of debris flows, it is essential to incorporate a fluid phase into the framework. The simplest approach is to treat the granular material and the fluid as a single, combined phase that exhibits a non-Newtonian constitutive relationship (Delannay et al., 2017). While the specific form of the non-Newtonian rheology may vary, most models introduce rigid flow behaviour at low shear strain rates by including a yield stress term (Iverson, 1997). They also incorporate a rate-dependent component that augments the viscosity of the yielded material typically following either a linear (i.e. a Bingham, 1922 fluid), a shear thickening (i.e. a Bagnold, 1954 fluid) or a shear thinning (i.e. a viscous plastic fluid (Coussot, 2017; Herschel and Bulkley, 1926)) relationship.

Generally, dilatant shear thickening rheology models prove more adept at replicating flows with lower particle concentrations since they can account for particle-particle interactions. Takahashi (1981) proposed a model based on the collisional regime described by Bagnold (1954), which successfully reproduced coarser heads and inversely-graded deposits observed in field-scale debris flows. However, the effectiveness of this modelling approach heavily relies on access to hard-to-obtain calibration data from field-scale flows for accurately representing the non-Newtonian flow rheology (Iverson, 2003).

In an effort to mitigate this, many models (e.g. Frank et al., 2017; Graf and McArdell,

2009; Hussin et al., 2012) have employed the Voellmy fluid rheology, where the Voellmy-Salm friction relation (Salm, 1993) accounts for the basal friction contributions of the two phases as separate terms. This approach makes these models far more amenable to calibration based on previous events. Nevertheless, as previously discussed, many distinct features of debris flow behaviour stem from spatial and temporal variations in the flow's composition, which cannot be fully captured when treating the flow as a single phase.

### 2.4.1.3 Two-phase debris flow models

More recent studies (e.g. Berzi and Jenkins, 2008; Bouchut et al., 2017; Iverson, 1997; Iverson and Denlinger, 2001; Iverson and George, 2014; Kowalski and McElwaine, 2013; Meng et al., 2022; Pitman and Le, 2005) have attempted to improve the efficacy of the continuum approach by treating the grains and the fluid as two separate continuum phases. These methods emanate from the concept of continuum mixture theory (Morland, 1992) and describe the two phases using phase specific mass and momentum equations that are coupled through a phase interaction term, typically expressed as a function of the solid phase volume fraction $\phi_p$ at each location within the flow. A detailed discussion on the evolution and development of two-phase shallow water models is presented in Chapter 5.

Notably, several successful two-phase shallow water models, such as RAMMS (e.g. Cesca and D'Agostino, 2008; Christen et al., 2010; Frank et al., 2017) and LaharFlow (e.g. Bautista et al., 2023; Tierz et al., 2017), have emerged as tools for studying geophysical-scale flow events over complex terrains. These models enable the extraction of critical flow characteristics, including flow paths, bulk velocities, and pressure profiles. Consequently, by systematically varying model parameters and calibrating them against observed natural flows in the region of interest, researchers can utilise these simulations to develop regional-scale hazard assessments (e.g. Frey et al., 2018; Schneider et al., 2014). Performing such studies, however, should be approached with caution due to the complexity of the flow being modelled, juxtaposed with the simplicity of the underlying assumptions in such models. This dynamic can result in numerous combinations of input parameters yielding nearly identical flow outputs.

However, to conduct simulations at the full geophysical scale, certain simplifying assumptions are necessary to manage model complexity. Typically, the granular phase is treated as consisting of a single coarse particle size, with the influence of finer granular material integrated into the dynamics of the fluid phase through the adoption of a non-

Newtonian constitutive law, such as the Voellmy-Salm relation discussed earlier. While these assumptions facilitate modelling, they come with limitations. Specifically, they make it challenging to incorporate the effects of a wide particle size distribution on flow dynamics, particularly issues related to flow segregation and the formation of surge fronts (Hutter et al., 2005). Moreover, the accuracy of these models remains dependent on calibration data derived from past events, resembling the situation encountered in single-phase models.

Nonetheless, these limitations are more manageable when modelling smaller-scale experimental flows, where flow properties can be constrained and accurately determined. In recent years, notable progress has been made in this direction. For instance, Meng et al. (2022) successfully replicated the granular surge front architecture observed in the classic flume experiments conducted by Davies (Davies, 1988, 1990). The real challenge in this type of modelling lies in developing a framework that is applicable both at the geophysical and laboratory scales while minimising the impact of simplifying assumptions, particularly those related to the interaction of different grain sizes and the fluid.

### 2.4.2 The continuum-discrete approach

#### 2.4.2.1 The Discrete Element Method

With the continuing advancement in computer processing power and the growing availability of high-performance computing resources, the discretisation of the granular phase in granular mass movement modelling has gained substantial popularity and feasibility within the academic research community. The Discrete Element Method (DEM) was first used to model contacting granular bodies by Cundall and Strack (1979) where every body is described as a Lagrangian point whose degrees of freedom are regulated by Newton's equation of motion (Leonardi, 2015).

Due to the refinement and extension of the approach over the years since its conception, DEM is now used to study granular mass movement problems encountered at both the geophysical (e.g. Shiu et al., 2023; Zou et al., 2017) and experimental (e.g. Kesseler et al., 2020; Teufelsbauer et al., 2009; Valentino et al., 2008) scales.

#### 2.4.2.2 Coupling DEM with a fluid phase

In the analysis of granular-fluid flows, researchers have developed coupling strategies that enable interaction between the granular DEM phase and a fluid solver capable of

modelling a three-dimensional fluid phase. The choice of fluid solver depends on the required precision of modelling fluid-particle interactions, with higher precision often accompanied by increased computational costs (for more details, see Leonardi, 2015). Instead of analytical modelling (e.g. Herrmann et al., 2007) or using an adaptive fluid mesh (e.g. Zhong et al., 2016), a commonly accepted compromise in this field involves utilising a fluid scheme that also models the fluid as a field of Lagrangian points, simplifying the coupling with the DEM solver.

Among the fluid schemes using Lagrangian descriptions, variations in complexity exist. For example, the Material Point Method (MPM) (Pracht, 1975; Więckowski, 2004) employs a hybrid Lagrangian-Euler description, which, while beneficial for capturing large deformations, can introduce computational costs and reduce accuracy at finer length scales. Smoothed-Particle Hydrodynamics (SPH) offers a relatively simplified Lagrangian approach, modelling the fluid as discrete particles with associated material (density) and kinematic (velocity) properties (Robinson et al., 2014). The Lattice-Boltzmann Method (LBM) stands out as the third and most widely used approach, solving the Boltzmann equation over a lattice or grid composed of fluid points using particle distribution functions (He and Luo, 1997). LBM's popularity in modeling debris flows stems from its ability to handle complex geometries, making it suitable for flows over natural topographies, and its ease of parallelisation for handling large particulate systems. Recent publications have conducted detailed comparisons of these solvers (e.g. Ceccato et al., 2020; Han and Cundall, 2011; Pereira et al., 2012). In this study, a coupled DEM-LBM model, initially developed by Leonardi et al. (2014), will be summarised and applied in Chapter 6.

### 2.4.2.3 Comparing the continuum-discrete approach to other modelling types

In contrast to representing the granular phase as a continuum, the discrete approach offers a distinct advantage by directly accounting for particle-particle interactions. This capability becomes particularly crucial when addressing scenarios involving flows of varying grain sizes and examining flow-structure interaction problems, such as the design of mitigation structures (e.g. Law et al., 2015; Leonardi et al., 2016; Salciarini et al., 2010). However, these interactions models tend to be derived from simplistic linear or Hertzian contact models which are not necessarily well-validated for more complex interaction scenarios, like when a pore fluid is present, which are common in geophysical flows.

Recent research efforts (e.g. Pasqua et al., 2022, 2023) have explored the fusion of

the two modelling strategies, combining the computational efficiency of depth-averaged schemes with the added complexity of a fluid-coupled DEM solver. This approach is especially relevant for modelling large flows over complex topographies with a focus on the flow's interaction with structures at realistic velocities. In this progressive modelling approach, depth-averaged schemes initially track the flow from initiation across the terrain, transitioning into a full three-dimensional representation using DEM-LBM to more accurately depict the interaction between the flow and mitigation structures.

Coupled DEM models offer several advantages over physical experimental modelling, primarily in conducting large parameter space studies for simple experimental configurations efficiently (Zhang et al., 2001b). Researchers have complete control over material parameters for granular and fluid phases, as well as the external force conditions imposed on them. This flexibility is particularly useful for studying the influence of external accelerations on geotechnical centrifuge experimental configurations (Cabrera and Leonardi, 2022), a topic to be discussed further in Chapter 6.

Furthermore, the continuum-discrete modelling approach allows for tracking micro-scale flow parameters, including inter-particle contact forces, individual particle velocities, and the evolution of granular force chains (Zhou et al., 2003), which can be challenging to measure or visualise in physical experiments. This additional information from continuum-discrete numerical modelling provides micro-mechanical insights into complex systems, aiding in the understanding of key flow dynamics.

However, accurate replication of real-world phenomena using the continuum-discrete approach still relies heavily on material parameter calibration. The discrete representation of granular particles introduces additional complexity, making large-scale flow dynamics and model stability highly sensitive to granular material parameters, particularly particle stiffness and restitution coefficients (Zhang et al., 2001b).

Moreover, for computational efficiency, simplifications to the flow description are necessary. This includes assumptions about the size distribution and shape of granular particles, as well as limiting the number of simulated particles. Simulating flows with particles that vary significantly in size or shape can significantly increase runtime and lead to instabilities in the collision laws governing grain interactions (Thornton, 2015). While most simulations assume spherical particle shapes for efficiency, recent studies have explored incorporating particle shape into DEM simulations (e.g. de Bono and McDowell, 2016; Ji et al., 2020; Tolomeo and McDowell, 2023).

Perhaps most pertinently, the interaction between the granular and fluid phases must be explicitly described in the model, typically achieved through a Darcy-style drag

law. However, a consensus on the most appropriate interaction model remains scenario-dependent and has not yet been universally established (as discussed in Chapter 5).

## 2.5 Summary

Debris flows, a subset of geophysical mass movements, exhibit complex behaviours that vary spatially and temporally. Qualitative and quantitative classification systems offer valuable insights into debris flow dynamics, but they capture only a snapshot in time and fail to account for the evolving behaviour seen in natural flows. These disparities are closely linked to local flow composition, specifically the particle size distribution and the solid volume fraction. To gain a comprehensive understanding of macro-scale behaviour, it is imperative to comprehend how local variations in composition influence flow behaviour, particularly the interaction between fluid and granular phases.

While investigating naturally triggered events at a local scale (i.e. specified locations of interest) seems intuitive, challenges related to obtaining suitable research catchments and deriving flow material parameters have led to the development of controlled research environments. Large-scale experimental facilities offer control over flow states but are limited by substantial financial constraints. In contrast, small-scale experimental setups enable cost-effective and precise testing. As such, the dam-break scenario has emerged as a particularly valuable configuration for studying flow dynamics.

Nevertheless, laboratory-scale experiments often struggle to replicate the intricate force balances observed at the geophysical scale. The transition between fluid and granular phase interactions across scales remains poorly understood. Geotechnical centrifuge modelling has recently emerged as a possible technique to approximate geophysical force balances in laboratory models by augmenting the applied gravitational field. It also offers a means to conduct parameter space analyses of granular-fluid flow dynamics as scales shift between the laboratory and geophysical realms.

In recent years, numerical models have emerged as powerful tools for predicting geophysical flow behaviour and exploring localised flow dynamics. Two-phase shallow water models and continuum-discrete approaches have gained prominence, each with complementary strengths and weaknesses. However, both modelling strategies suffer from a lack of consensus regarding the most appropriate method for modelling fluid-granular phase interactions. Achieving such a consensus is crucial for enhancing the effectiveness of these numerical models.

Chapter 3

# Inertial effects in just-saturated axisymmetric column collapses

**Abstract**

*This work introduces a scaling analysis of sub-aerial axisymmetric column collapses of glass beads and Newtonian glycerol-water solutions mimicking some of the behaviours of debris flows. The beads were in a size range where their inertia partly decouples their collapse behaviour from the water column. Experiments explored a range of viscous, surface tension and particle inertia effects through systematic variation of particle size and fluid viscosity. Crucially a geotechnical centrifuge was used to access elevated effective gravitational accelerations driving the collapse, allowing field-scale viscous and surface tension effects to be replicated. Temporal pore pressure and runout front position evolution data was extracted using a pressure transducer and high speed imaging, respectively. A least-squares fitted scale analysis demonstrated that all characteristic dimensionless quantities of the acceleration phase could be described as a function of the column-scale Bond number Bo, the Capillary number Ca, the system size $r^*$, and the grain-fluid density ratio $\rho^*$. This analysis demonstrated that collapses as characterised by pore pressure evolution and front positions were controlled by the ratio of Bo/Ca. This indicates that grain-scale surface tension effects are negligible in such inertial column collapses where they may dominate laboratory-scale granular-fluid flow behaviour where geometric similarity between grain and system size is preserved.

## 3.1 Introduction

Debris flows are a subset of gravity-driven slope hazards comprising a mixture of grains (rocks, soils) and water. The high fluid volume fraction and elevated relative density of the grains results in the forces developed in both phases significantly contributing to the

---

dynamics of the mass movement (Iverson, 1997). The granular phase may also comprise a wide range of particle sizes (Kesseler et al., 2018), leading to complexity at both the grain- and macro-flow scales. With debris flows representing a significant geophysical hazard across the world (Forterre and Pouliquen, 2008), gaining an understanding of the roles of these different components in controlling outcomes may help to effectively model and mitigate their destructive potential.

Information from naturally occurring debris flows is typically limited by the fact that initial and boundary conditions of the mass movement are generally unknown and material parameters obtained from the final flow morphology are poorly constrained (Iverson et al., 2010b). In contrast, laboratory experiments offer a way to control all characteristics of the flow and contacting boundaries for the duration of the mass movement. Hence, data resulting from laboratory-scale flow experiments is repeatable and can be used to understand the influence of individual parameters on the flow's behaviour.

One experimental configuration that has received significant attention, because it replicates the unsteady nature of many geophysical flows, is the collapse of a granular step (Lube et al., 2004). Generally performed on a granular column with an axisymmetric (Lajeunesse et al., 2004; Lube et al., 2004) or quasi-two-dimensional (Lajeunesse et al., 2005) geometry, the column is suddenly released from its initial configuration and collapses until it reaches a stationary final deposit. While dry (Lajeunesse et al., 2004, 2005; Lube et al., 2004; Warnett et al., 2014), fully-submerged (Bougouin and Lacaze, 2018) and wetted (Artoni et al., 2013) granular material have all been used, fewer studies have investigated a situation more reminiscent of debris flows where the column is filled with fluid to a comparable depth to that of the granular material, which we term fully saturated.

The high travel speeds of full scale debris flows mean that even small particles exhibit inertial behaviour where the interaction between grain and fluid can be complex (Kesseler et al., 2018). Dimensional analysis of a simple granular-fluid system suggests that the effects of surface tension are small compared to gravitational forces and fluid viscosity at the macro-scale of geophysical flows (Iverson, 2015). However, it has been found that the flow regime of a collapsing fluid-saturated granular column is primarily determined by the degree of capillary effects between the granular phase and the interstitial fluid due to surface tension (Bougouin et al., 2019).

However, as implied by the laboratory experiments, surface tension undoubtedly contributes to granular-scale flow mechanics, particularly at the flow's surface, and it remains possible that these processes can control mechanisms such as the build-up and

reduction of pore fluid pressure through capillary forces affecting macro-scale flow outcomes (Rondon et al., 2011). Several studies (e.g. Kaitna et al., 2016; McArdell et al., 2007) have shown that the inclusion of high concentrations of fine granular material, like clays and silts, enhance the development of excess pore pressures which reduces the frictional resistance exerted on the bulk flow by the terrain bed. Coupled with the small number of physical studies investigating this phenomenon, the fact that recent numerical models (e.g. Bouchut et al., 2017; Iverson and George, 2014; Kowalski and McElwaine, 2013) have not reached a consensus on the most appropriate way to tractably model the mechanisms driving spatio-temporal variations in the grain size distribution suggests that we do not comprehensively understand the mechanisms at play or how their influence scales. Given the comparative micro-scale over which the interactions between the granular fines and the interstitial fluid occur, provided that a sufficient concentration of granular fines is present in the flow, it seems reasonable to suggest that surface tension may play a role in the development of these excess pore pressures and, hence, influence the macro-scale behaviour of the flow.

One way to try and replicate the stress-dependent processes present in natural scale flows within a laboratory model is to utilise a physical modelling method commonly used in the field of Geotechnical Engineering called centrifuge modelling. By spinning a laboratory-scale model on an arm, the centripetal acceleration from the rotation becomes an effective gravitational acceleration. Thus, the effects of gravity on large 'prototype' structures can be replicated at a small physical scale through enhancing the effective gravitational acceleration (Taylor, 1995). The laboratory model is submitted to the required gravitational acceleration in order to replicate the stress profile within the modelled prototype scenario. The stress-similarity is achieved by attaching the model to the end of a centrifuge beam and submitting it to an elevated gravitational acceleration $G$ which is $N$ times larger than Earth's gravity $g$ (Milne et al., 2012).

In the past two decades, there have been a number of significant works where centrifuge modelling has been used to physically investigate the scaling of the kinematic processes driving granular flows (e.g. Bowman et al., 2012; Brucks et al., 2007; Vallejo et al., 2006). More recently, the focus has shifted to the design of granular flow mitigation structures and the impact forces developed by the flow-structure collision (e.g. Ng et al., 2018; Zhang and Huang, 2022). However, the added complexity of a fluid phase has meant that the use of centrifuge modelling to study debris flows, to date, has been quite limited mainly focusing on debris flow initiation (Milne et al., 2012) and propagation (Bowman et al., 2010).

The current study aims to provide a platform to investigate the role of micro-scale surface tension effects on macro-scale debris flow behaviour by first characterising the collapse response of grain-fluid mixtures with inertial grains by performing axisymmetric fluid-saturated granular column collapse tests using a geotechnical centrifuge. The use of the centrifuge allows a parameter space of particle size, surface tension and fluid viscosity to be explored in regimes where the grains are inertial and surface tension effects should have little influence on macro-scale flow outcomes.

## 3.2   Dimensional analysis

The initial geometry of an axisymmetric, fluid saturated, granular column collapse (Figure 3.1), can be described by two parameters; the initial height of the shared free-surface of the granular-fluid mixture $h_0$, and the radius of the column prior to collapse initiation $r_0$. Assuming that the granular phase is comprised of identical spherical particles situated in a homogeneous packing, the granular phase of the column can be characterised by the particle diameter $d_p$, the particle density $\rho_p$, and the mean solid volume fraction of the column $\phi_p$. Similarly, a Newtonian fluid phase can be characterised by the fluid density $\rho_f$, the fluid dynamic viscosity $\eta_f$, and the fluid surface tension $\sigma_f$. While the initial system is fully saturated, as the collapse progresses, it is possible to obtain flow regions where the depth of the fluid phase is different to that of the granular phase. This can lead to the degree of saturation, the porosity of the granular media, and the surface tension of the fluid phase to significantly influence collapse dynamics.

The current analysis is interested in analysing the evolution of the phase front velocities $u_v$, where subscript $v$ can refer to the fluid $f$ or particle $p$ phases, and the basal
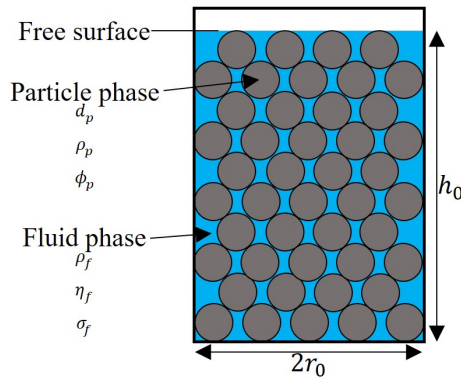


Figure 3.1: Schematic of the initial configuration of a just saturated granular column collapse.

fluid pressure gradient at the centre of the column $\dot{P}$ with time $t$ throughout the duration of the column collapse. A promising place to start to understand this complex system is by utilising Buckingham's $\Pi$ theorem (Buckingham, 1914) to systematically identify dimensionless variables, termed $\Pi$ groups, that provide a homogeneous solution to the physical relationships between key geometric and material parameters, and measured test data. Assuming a constant of gravitational acceleration $G = Ng$, where $N$ is a constant and $g$ is Earth's constant of gravitational acceleration, it is hypothesised that a relationship between $u_v$ and the other defined variables can be postulated as

$$u_v = f_1(h_0, r_0, d_p, \rho_p, \rho_f, t, \dot{P}, \sigma_f, \eta_f, G, \phi_p), \tag{3.1}$$

where $f_1$ is an unknown function. The primary difference between Equation (3.1) and other relationships used in previous analyses to describe simplified debris flow motion (e.g. Iverson, 1997, 2015), is the inclusion of fluid surface tension as a parameter. In contrast to previous analyses, we include fluid surface tension here as a controlling parameter to understand how, in a regime where particle inertia can dilate the granular phase, micro-scale interactions in the pore space may influence macro-scale outcomes.

Temporarily excluding $\phi_p$ as it is a dimensionless quantity, the other 11 variables within Equation (3.1) are derived from combinations of three fundamental physical dimensions: mass, length, and time. Hence, Buckingham's $\Pi$ theorem dictates that the variables can be connected by $11 - 3 = 8$ independent dimensionless $\Pi$ groups. Following a previously described mathematical process (Iverson, 2015), and using $d_p$, $\rho_f$ and $G$ as our initial reference parameters, Equation (3.1) can be rewritten as

$$\frac{u_v}{\sqrt{GL}} =$$
$$f_2\left(\frac{h_0}{r_0}, \frac{r_0}{d_p}, \frac{(\rho_p - \rho_f)N}{\rho_f}, \frac{t}{\sqrt{L/G}}, \frac{\dot{P}}{\rho_f\sqrt{G^3h_0}}, \frac{\rho Gh_0 d_p}{\sigma_f}, \frac{\eta_f\sqrt{Gh_0{}^3}}{\sigma_f d_p}, \phi_p\right), \tag{3.2}$$

where $f_2$ is an unknown function, $L$ is a characteristic length scale and $\rho$ is the effective density of the granular-fluid column calculated as $\rho = \phi_p\rho_p + (1 - \phi_p)\rho_f$. The characteristic length scale $L$ has been intentionally left arbitrary allowing us to explore this dimensionless space over both the column and grain scales (see Section 3.6).

The left-hand side of Equation (3.2) takes the form of a phase Froude number $\mathrm{u}^*_{v,L}$ where again, the subscript $v$ refers to the phase of interest and subscript $L$ refers to the characteristic length scale. $\mathrm{u}^*_{v,L}$ compares the influence of inertial and gravitational

forces at the phase flow front over the length scale of interest. The right-hand side is comprised of eight dimensionless groups that are used to determine $u^*_{v,L}$. The first parameter is the column aspect ratio $a_0$ which has been shown to be the dominant parameter in the scale analysis of dry granular column collapses. The second parameter was defined as the system size (Warnett et al., 2014) $r^*$ and was shown to have some influence on the evolution of the dry collapse case. The third parameter is the relative granular-fluid density ratio accounting for acceleration-scale buoyancy $\rho^*$. When $N = 1$, $\rho^*$ reduces to the simple mass ratio found in traditional fluid-granular flow scale analyses (e.g. Iverson, 1997). Whereas, when $N > 1$, the enhanced gravitational field acts on the difference in densities, normalised as a reference density, as a buoyancy. The fourth parameter, $t^*_L$, is the ratio between $t$ and a characteristic inertial timescale $\sqrt{L/G}$ where, again, $L$ refers to the characteristic length scale of interest. The fifth parameter, $\dot{P}^*$, is the ratio between $\dot{P}$ and the equivalent hydrostatic pressure gradient down the initial height of the column. The sixth parameter is the column Bond number Bo and is defined as the ratio between the inertial forces at the column scale that drive the collapse of the column and the capillary forces at the grain scale induced by deformation of the fluid-air interface. Its influence over the collapse regime of a fluid-saturated granular material under Earth's gravitational acceleration has already been highlighted (Bougouin et al., 2019). The seventh parameter is known as the Capillary number Ca and relates the viscous forces within the fluid at the column scale to surface tension effects at the grain scale. The final parameter is $\phi_p$ which remains unchanged since it is already dimensionless. The inclusion of both Bo and Ca as $\Pi$ groups of interest is crucial for ensuring that macro-scale inertial and viscous forces are scaled appropriately in relation to grain-scale surface tension effects in order to obtain a granular phase whose behaviour is primarily governed by particle inertia. Here, we use centrifuge modelling to extend the accessible model parameter space for a simple axisymmetric, fluid-saturated, column collapse configuration. Hence, we are able to perform a multi-scale analysis of the problem by varying $G$ rather than adapting the physical size of the experimental configuration.

It is important to note that the solution to Equation (3.2) is not unique. The resulting $\Pi$ groups could have been recast into alternative forms. In particular, Ca could be replaced by other previously studied dimensionless quantities like the Stokes St (characteristic particle timescale against characteristic fluid timescale) or Reynolds Re (inertial forces against viscous forces in the fluid) numbers. Ca was determined as the most useful parameter out of this group given that the influence of surface tension has been shown

to vary with scale (Iverson, 2015).

Crucially, four of the dimensionless groups within Equation (3.2) contain $N$ or $G$ suggesting that the behaviour of the analysed system is highly scale dependent. Hence, to sufficiently determine the contributions of these dimensionless groups to collapse behaviour, a multi-scale analysis would be required. Given that the size of an experimental configuration is often limited in a laboratory setting, this type of analysis is unworkable with most laboratory-scale granular-flow test configurations.

## 3.3  Model apparatus

Experiments were conducted using the University of Nottingham's GT50/1.7 geotechnical beam centrifuge. The centrifuge has a platform radius of 2 m and is attached to a swinging platform capable of supporting a payload size of up to 0.9 m high, 0.6 m circumferential and 0.8 m wide (Ellis et al., 2006). The machine is capable of applying a maximum centripetal acceleration of $150g$ to a payload up to 335 kg in mass.

Within a wind-proof strong box, a steel cylinder with an inner radius $r_0 = 54$ mm was positioned in the centre of a 490 mm by 485 mm flat plexiglass sheet (Figure 3.2). A foam o-ring was fixed to the base of the steel cylinder allowing a seal to form between the cylinder and the plexiglass when downward pressure was applied to the cylinder. The cylinder was held in a fixed position by two steel rods that were screwed into the top of the column and tightly pressed against a forked steel plate.

Throughout testing, the cylinder was filled to an initial height $h_0 = 50$ mm of both grains and fluid, creating a just-saturated column with $a_0 = 0.93$. Several previous studies have investigated the effects of varying $a_0$ in both the axisymmetric (Lajeunesse et al., 2004; Lube et al., 2004; Warnett et al., 2014) and quasi-two-dimensional (Lajeunesse et al., 2005; Thompson and Huppert, 2007) collapse. So here, we focus on column configurations where $a_0 \approx 1$, matching a number of reviewed geophysical collapse events (Legros, 2002). A 12 V LED lightsheet was installed beneath the plexiglass sheet, which acted as a diffuser, creating even back-lighting of the test surface.

The fluid-saturated granular column was comprised of spherical soda lime glass beads and an interstitial fluid consisting of a miscible glycerol-water mixture. Table 3.1 details the range of values used for all test parameters of interest. The tested centrifuge rotational speeds were selected such that the tested values of $N$ relative to the centrifuge cradle were 1, 5, 15 and 30. These values were then adjusted so that they were relative to a height of $\frac{2}{3}h_0$ above the horizontal plane to account for variations in centrifugal ac-
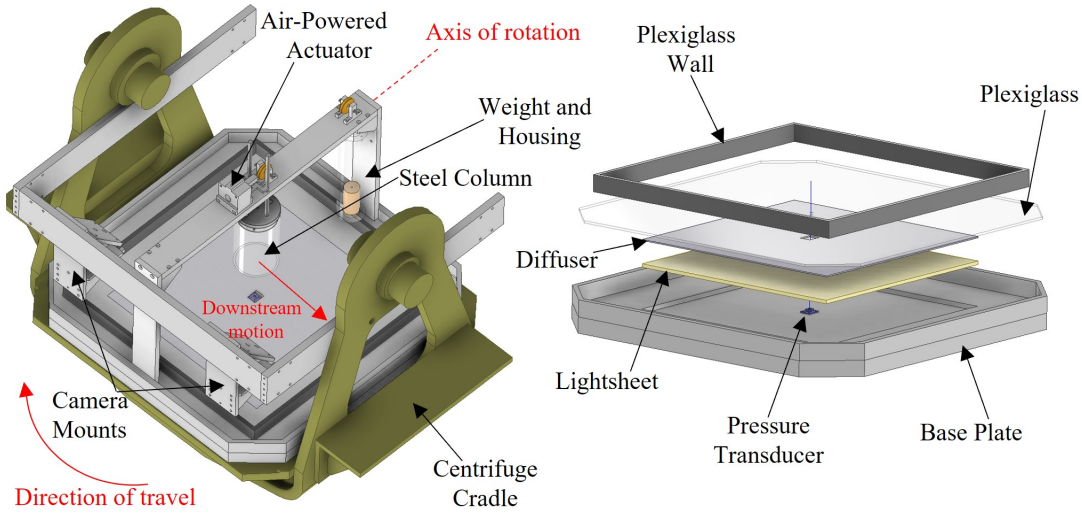
Figure 3.2: Schematic of experimental setup.

celeration across the height of the column. Higher rotational speeds were not explored as the resolution of the recorded videos were limited by the frame rates of the cameras.

Table 3.2 provides a summary of the parameter space obtained across testing for the dimensionless groups from Equation (3.2) calculable from the geometric and material property information given in Table 3.1. Given that the Bond number is always significantly larger than unity while the tested Capillary numbers cover a range of magnitudes smaller and larger than unity, it is evident that the parameter space explored by the current experiments includes flow states that are largely dominated by gravitational forces at the column-scale while the relative influence of surface tension at the grain-scale and viscous forces at the column-scale vary depending on the geometry of the initial column and test material properties.

It should be noted that previous studies (Cabrera and Estrada, 2019; Warnett et al., 2014) have concluded that axisymmetric column collapse experiments conducted over the specified range of $r^*$ are highly susceptible to grain-size effects which can significantly influence the mobility and duration of the collapses. However, by not adhering to the geometric reality of the natural scale, we are able to ensure that the behaviour of the spherical particles is primarily governed by their inertia. As such, the current study complements previous work by focusing on a collapse regime where the influence of particle inertia is promoted instead of grain scale.

Table 3.1: Summary of experimental test parameters.

| Experimental parameters | Symbol | Definition | Range |
|---|---|---|---|
| Initial column height | $h_0$ | | $50\,\mathrm{mm}$ |
| Initial column radius | $r_0$ | | $54\,\mathrm{mm}$ |
| Centrifuge rotational speed | $\omega$ | | $[0, 47, 82, 116]\,\mathrm{rpm}$ |
| Gravitational scale factor[a] | $N$ | | $[1, 4.6, 14, 28.1]$ |
| Temperature of fluid phase | $T$ | | $20 \pm 2\,^\circ\mathrm{C}$ |
| Particle diameter | $d_p$ | | $[2, 4, 6, 8]\,\mathrm{mm}$ |
| Particle density | $\rho_p$ | | $2642 \pm 27.4\,\mathrm{kg\,m^{-3}}$ |
| Mean solid volume fraction[b] | $\phi_p$ | $M_p/(\pi r_0^2 h_0 \rho_p)$ | $0.61 \pm 0.01$ |
| Glycerol mass concentration | $C_g$ | $M_g/(M_g + M_w)$ | $[0, 0.1, 0.52, 0.69, 0.77]$ |
| Water density[b] | $\rho_w$ | | $1000\,\mathrm{kg\,m^{-3}}$ |
| Glycerol density[c] | $\rho_g$ | | $1260\,\mathrm{kg\,m^{-3}}$ |
| Fluid mixture density | $\rho_f$ | $C_g\rho_g + (1 - C_g)\rho_w$ | $1000\text{-}1201\,\mathrm{kg\,m^{-3}}$ |
| Fluid mixture viscosity[d] | $\eta_f$ | $\eta_0\left[\frac{1 - C_g/C}{1 - (k_0 C - 1)C_g/C}\right]^{(-2.5C)/(2 - k_0 C)}$ | $1\text{-}52.1\,\mathrm{cP}$ |
| Water surface tension[c] | $\sigma_w$ | | $72.5\,\mathrm{mN\,m^{-1}}$ |
| Glycerol surface tension[c] | $\sigma_g$ | | $63.4\,\mathrm{mN\,m^{-1}}$ |
| Fluid mixture surface tension | $\sigma_f$ | $C_g\sigma_g + (1 - C_g)\sigma_w$ | $65.5\text{-}72.5\,\mathrm{mN\,m^{-1}}$ |

[a] Calculated using an effective radius of $1.87\,\mathrm{m}$ between the centrifuge's axis of rotation and $\frac{2}{3}h_0$ from the base of the column to account for variations in centrifugal acceleration across the height of the column

[b] Formula used by Warnett et al. (2014)

[c] Obtained from Lide (2004) for a temperature of $20\,^\circ\mathrm{C}$

[d] Equation (11) from Takamura et al. (2012) where $\eta_0 = 1\,\mathrm{cP}$ (i.e. the viscosity of water at $20\,^\circ\mathrm{C}$), constant $C = 1.2$ and $k_0 = -0.012(T + 273.15) + 4.74$

Table 3.2: Summary of the dimensionless parameter space calculable from the geometric and material property information in Table 3.1.

| Dimensionless variables | Range |
|---|---|
| $a_0$ | 0.93 |
| $r^*$ | $6.75 - 27.0$ |
| $\rho^*$ | $1.63 - 35.0$ |
| Bo | $26.6 - 3480$ |
| Ca | $0.06 - 45.2$ |

### 3.3.1 Test procedure

The fully-saturated granular column was prepared after the model was loaded onto the centrifuge. A predefined mass of granular material $M_p$ was poured into the tube which had been previously filled by a predefined volume of interstitial fluid $V_f$ where the respective mass of water $M_w$ and glycerol $M_g$ used was defined by the glycerol mass concentration required for that test. The column was compacted from the top using a steel rod until the desired initial column height $h_0 = 50\,\mathrm{mm}$ was achieved, and the surface of the fluid was level with the top of the grains. The repeatability of this preparation method is demonstrated by the small range of $\phi_p$ values achieved across all tests as stated in Table 3.2. While the achieved packing fractions suggest that the column packing configuration can be described as a poured random packing (Dullien, 2012), we follow the logic of previous authors (e.g. Iverson and George, 2014; Rondon et al., 2011) by assuming that the granular column is initially in a dense configuration as $\phi_p$ is greater than the critical solid volume fraction $\phi_c = 0.6$ which is generally used as a criteria to assess whether a granular flow is going to contract or dilate.

Prior to initiating collapse, the centrifuge with the experiment mounted on it was spun up to a speed submitting the model to an enhanced gravitational acceleration $G = Ng$ where $g = 9.81\,\mathrm{m\,s^{-2}}$. Once spun up, a weighted pulley system was triggered by an air-powered actuator to lift the cylinder and initiate the collapse of the fully-saturated granular column over the horizontal test plane. From analysis of the raw basal pressure data and the high-speed camera footage, the time scale for the cylinder to be lifted up to a height of $h_0$, $t_{col}$, can be approximately calculated as $t_{col} \approx 2.5\sqrt{h_0/(Ng)}$. This equates to a mean release velocity that obeys Sarlin et al.'s (2021) criterion for a release process that has no influence on the dynamics of a quasi-two-dimensional collapse consisting of dry spherical glass beads. Li et al. (2022) suggested that a lower release velocity may be satisfactory to achieve this effect for wetted granular material given the potential

build-up of cohesive forces between adjacent grains. Further investigation is required to confirm this theory and extend it to the fully saturated regime, as well as considering other collapse geometries like the axisymmetric case. However, we deem the dry criterion to be sufficient for the current study.

### 3.3.2 Front measurement

*Lifting the steel cylinder initiated the collapse of the fluid-saturated granular column. The temporal evolution of the collapse was recorded by two Go-Pro cameras at a resolution of 1080×1920 pixels and an acquisition rate of 240 frames per second. The images were first treated for fisheye distortion effects (Scaramuzza and Siegwart, 2007). The experimental spatial domain within the images is then calibrated using black markers positioned around the edge of the lightsheet. The markers are used within the digital image correlation (DIC) scheme developed by Blaber et al. (2015) to produce an orthonormal image plane. Radial distance values could be taken from the post-processed images at a spatial resolution of 0.5 mm. The upstream and downstream directions, which refers to whether the flow is propagating with (upstream) or against (downstream) the relative motion of the centrifuge, of the collapse are recorded on separate cameras to improve image resolution. This also allows for the contributions of Coriolis acceleration and the Eötvös effect[††] to be considered (Taylor, 1995) with respect to the upstream and downstream directions of motion as shown in Figure 3.2.

Figure 3.3 shows the collapse evolution of two test cases, both with $d_p = 8$ mm, at $N = 1$ [(**a**)-(**e**)] and $N = 14$ [(**f**)-(**j**)] from the downstream direction. A multi-threshold image analysis scheme was developed to create masks of the individual fluid and particle phases for each image frame. These calibrated masks were then used to obtain the averaged instantaneous front positions, $r_f$ and $r_p$, and the final front positions, $r_{f,F}$ and $r_{p,F}$, of the fluid and particle phases, respectively. Tracking the phase fronts separately was necessary in order to evaluate how variations in the chosen parameter space affected phase front interactions.

For tests that remained within the measurement domain [(**a**)-(**e**)], $r_{f,F}$ and $r_{p,F}$ are defined as the position of the phase fronts when the collapsing material ceases to move, which is formalised as an average fluid front velocity less than $2.4 \times 10^{-3}$ m s$^{-1}$ (0.01 mm per frame). However, for tests at elevated $G$, $N > 1$, [(**f**)-(**j**)] the propagation

---

*See Appendix A.1.3 for further details on test image processing

[††]See Chapter 6 for the definitions and a detailed analysis of the influence of Coriolis accelerations and the Eötvös effect on collapse dynamics
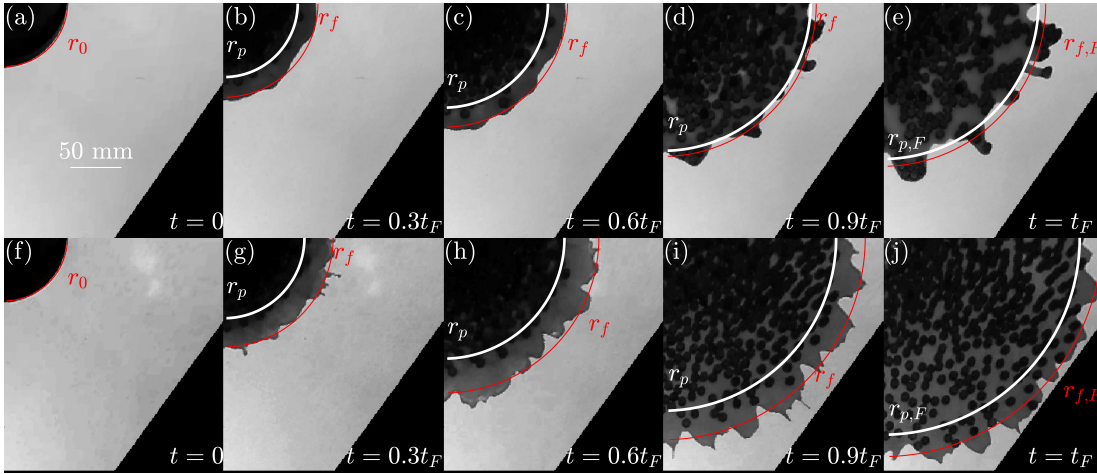
Figure 3.3: Snapshots of the collapse sequence downstream of centrifuge motion for two columns, both with $d_p = 8\,\text{mm}$, with gravitational acceleration coefficient $N = 1$ [(**a**)-(**e**)] and $N = 14$ [(**f**)-(**j**)]. The averaged radial position of the fluid (red) and particle (white) phase fronts, where the top left of each image is the point of origin, are shown.

of the two phases extended beyond the measurement area. In these cases, $r_f$ and $r_p$ were taken as the average radial distance of the respective phase fronts from the final image frame, where the entirety of both phase fronts remained inside the measurement area.

### 3.3.3  Pore pressure measurement

**The evolution of basal fluid pressure under the centre of the granular column was measured with a miniature pressure transducer (PT) which was covered by a sheet of filter paper. The sensor had a pressure range of 200 kPa and recorded data at a frequency of 125 kHz. Measurement accuracy was found to be $\pm\,0.1\,\text{kPa}$ by calculating the average reading error when supplying a known pressure to the transducer. Figure 3.4 provides an example of the filtering strategies implemented to clean the signal for a collapse test where $d_p = 2\,\text{mm}$, $N = 4.6$ and $C_g = 0$. From the data, a number of different effects can be seen. In particular, the large spike in pressure located around $0.16 - 0.17\,\text{s}$ after collapse initiation is a result of the vibrations across the runout surface emanating from the weight used to lift the steel column colliding with the actuator located at the bottom of its housing. Given that signal noise comprised a number of identifiable elements such as this vibration, Fourier transformations of the signal were used to define a cutoff frequency $f_c$ for a low-pass filtering scheme.

---

**See Appendix A.2.2 for further details on pressure sensor calibration
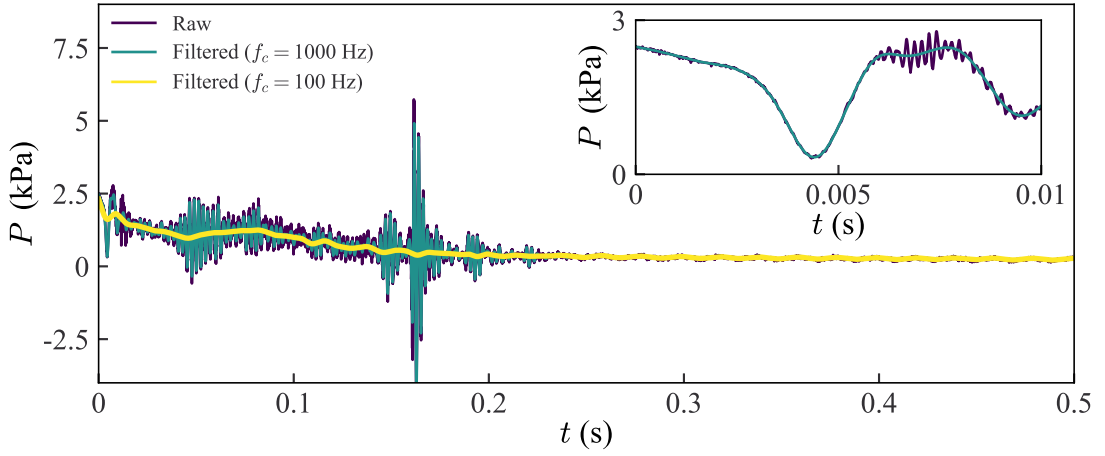
Figure 3.4: Time evolution of basal fluid pressure at the centre of the column, $P$, for $d_p = 2\,\mathrm{mm}$, $N = 4.61$, and $C_g = 0$. The column collapse was initiated at time $t = 0$. The raw signal, the reconstructed signals filtered with $f_c = 1000\,\mathrm{Hz}$, and $f_c = 100\,\mathrm{Hz}$ are all shown. The inset shows the magnified initial pressure evolution of the test demonstrating how well the reconstructed signal with $f_c = 1000\,\mathrm{Hz}$ captures the early pressure drop and recovery.

The overall trend of the signal, highlighted in yellow in Figure 3.4, from collapse initiation through to runout completion, was approximated using a fourth-order low-pass digital Butterworth filter with $f_c = 100\,\mathrm{Hz}$ within the Matlab (2020) signal processing toolbox. Pressure changes relating to column dilation occurring over the first few milliseconds of the collapse were also of interest and were captured using a higher cutoff frequency equal to $f_c = 1000\,\mathrm{Hz}$. The inset of Figure 3.4 demonstrates the filtering schemes ability to capture the significant pressure drop and recovery at the onset of collapse. Pore pressure measurements were only considered for tests where $N > 1$ to ensure that the noise of the signal was less significant than the total drop in pressure. Pressure measurements were also not recorded for tests undertaken at $N = 28.1$.

## 3.4  Column mobility

The influence of particle size $d$ and gravitational acceleration $N$ on the temporal evolution of the collapse front was investigated by examining the temporal evolution of $r_f$ from time $t = 0$ until the time where $r_{f,F}$ is achieved $t_F$. Figure 3.5 presents the evolution of the difference between the instantaneous fluid phase front position and the initial fluid phase front position $r_{f,0}$ normalised by the initial fluid phase front position, known as the normalised fluid runout length, $(r_f - r_{f,0})/r_{f,0}$ for particle diameters $d_p = 2\,\mathrm{mm}$,
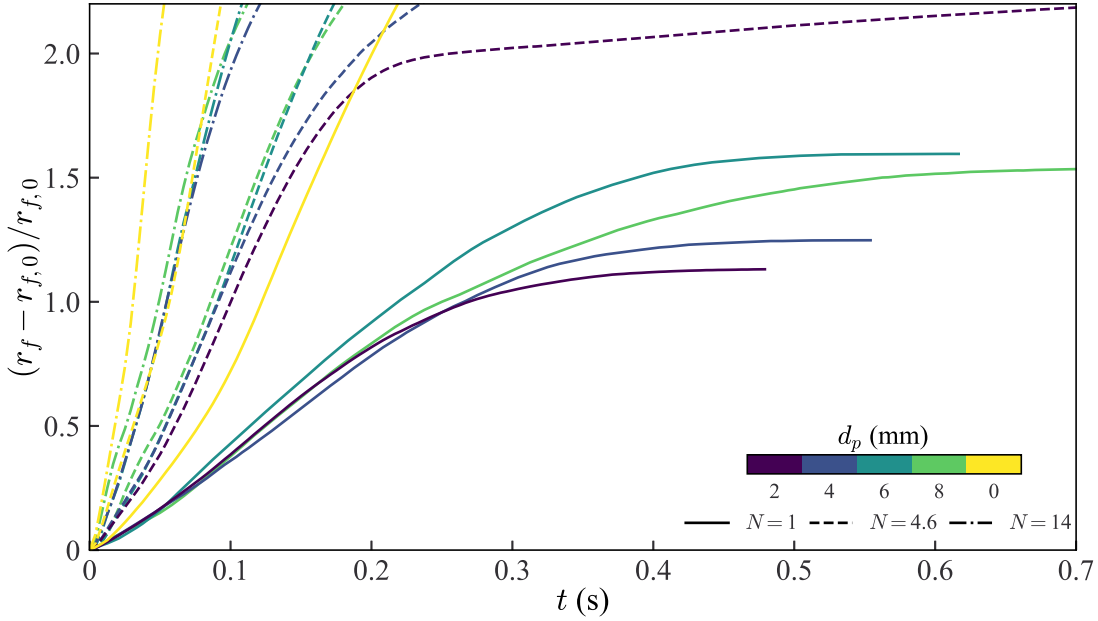
Figure 3.5: Temporal evolution of the normalised fluid runout length $(r_f - r_{f,0})/r_{f,0}$ in time $t$ for varying particle sizes $d_p$ and values of $N$ downstream of centrifuge motion. Collapses of a grain-free fluid phase $d_p = 0$ at all values of $N$ are also shown.

$d_p = 4\,\mathrm{mm}$, $d_p = 6\,\mathrm{mm}$, and $d_p = 8\,\mathrm{mm}$, at $N = 1$, $N = 4.61$ and $N = 14$, downstream of centrifuge motion. Figure 3.5 also includes data from a set of experiments where the column had no grains, just the fluid phase, illustrating the limiting case (i.e. $d_p = 0\,\mathrm{mm}$) for each $N$. The selected tests have a constant $\eta_f$ at each value of $N$ with $\eta_f/\eta_w = [\,1,\,6.7,\,21.5\,]$ for $N = 1$, $N = 4.61$ and $N = 14$.

Tests at $N = 1$ appear to follow the three distinct collapse stages described by previous authors (Lajeunesse et al., 2004; Lube et al., 2004; Warnett et al., 2014). On initiation, the flow front initially accelerates to reach a state of quasi-steady flow. In the runout phase, the flow retards until movement ceases and the final deposit is formed where $r = r_{f,F}$. The time at which $r = r_{f,F}$, $t_F$, for these test cases increases with grain size $d_p$, similar to the relationship found by Bougouin et al. (2019). That study reasoned that the capillary forces between grains, whose magnitude is controlled by the level of surface tension between the interstitial fluid and the ambient air, was the key contributor to this phenomena. Larger capillary forces are present within granular mixtures with smaller pore spaces, an allegory of particle size, which restricts the mobility of grains and results in a lower $t_F$ value. Even though the particle sizes used in the current study are at the top end of the particle sizes used by Bougouin et al. (2019), suggesting that the current regime is primarily controlled by inertial forces, the influence of surface ten-
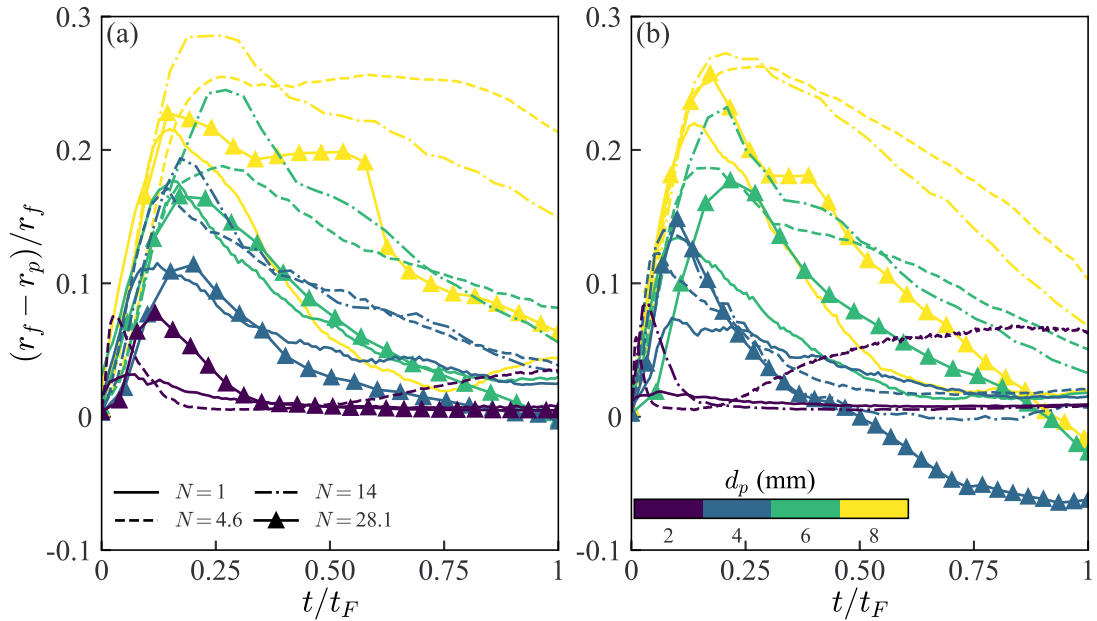
Figure 3.6: Temporal evolution of the normalised distance between the phase fronts $(r_f - r_p)/r_f$ against normalised time $t/t_F$ for all particle sizes $d_p$ at varying $N$ upstream (**a**) and downstream (**b**) of centrifuge motion.

sion is still identifiable in this runout stage. This may result from a number of factors including; fluid seepage scaling more strongly with $N$ than grain scale inertia (Cabrera and Leonardi, 2022; Cabrera et al., 2016), the high free surface energy of plexiglass which increases its wettability and aids the propagation of a fluid film across its surface (Blajan et al., 2013) and, particle clustering that can lead to localised capillary effects which reduces the speed of the granular phase.

In contrast, for $N > 1$, $t_F$ primarily decreases with increasing pore space. This trend tends towards the edge case of the collapse of the singular fluid phase. Similarly to the case of $N = 1$, the retardation present in the temporal evolution of the tests containing a granular phase is due to surface tension giving rise to capillary forces which reduces flow mobility. Crucially, by comparing to the edge case, it is evident that the level of retardation reduces with increasing $N$, suggesting that the influence of capillary forces on the temporal evolution of the collapse reduces with increased scale. This result is reassuring as the macro-scale behaviour of geophysical-scale debris flows are predominantly controlled by gravitational and viscous forces (Iverson, 2015).

Given that the interaction between the granular and fluid phases has been shown to significantly affect flow mobility, it is logical to consider the temporal evolution of both constitutive phases through their relative positions to one another. Figure 3.6 shows

the evolution of the normalised distance between the fluid and granular phase fronts $(r_f - r_p)/r_f$ with normalised time $t/t_F$ for particle diameters $d_p = 2\,\text{mm}$, $d_p = 4\,\text{mm}$, $d_p = 6\,\text{mm}$, and $d_p = 8\,\text{mm}$, at $N = 1$, $N = 4.61$, $N = 14$ and $N = 28.1$ for the upstream and downstream propagation directions. Similarly to Figure 3.5, tests have been selected so all tests conducted at the same $N$ use interstitial fluids with the same viscosity. $\eta_f/\eta_w = 44.8$ for the tests conducted at $N = 28.1$.

Initially, all collapses exhibited a drainage phase where the fluid front accelerates away from the granular material. For a given value of $N$, the maximum distance between the two phase fronts increases with pore space as the space for the fluid to exit the granular structure increases while the influence of capillary effects reduce. For a given value of $d_p$, the maximum relative distance increases with $N$ until $N = 14$. Increasing $N$ to 28.1 sees a reduction in the maximum relative distance possibly resulting from the reduced impact of solid-fluid interactions as the flow becomes dominated by inertia.

Figure 3.6 also shows how the granular front's ability to catch up to the fluid front varies with $d_p$ and $N$. The two fronts were considered to be approximately aligned when the normalised relative distance was less than 0.05. For all tests conducted with $N = 1$, the granular front was able to completely catch up to the fluid front by the end of the runout phase. The granular front did not overtake the fluid fronts over the duration of these tests which is likely due to the significant impact that surface tension has on laboratory-scale granular-fluid flows.

For a given $d_p > 2\,\text{mm}$ and $N > 1$, the final separation between the two phase fronts reduced with increasing $N$. For collapses propagating in the downstream direction, the granular front was even able to overtake the fluid front for $N = 28.1$. It is clear that the enhanced gravitational acceleration field is supplying more kinetic energy to the granular phase which allows it to catch up to the fluid front. Hence, the separation between the two phase fronts reduces when a larger acceleration field ($N$) is applied.

Figure 3.6 also shows the influence of the Coriolis acceleration[††] on the mobility of the flow. During the initial stages of the post-collapse propagation, the maximum separation between the two phase fronts for each test was generally greater for the collapsing section propagating in the downstream direction. This was somewhat expected as the Coriolis acceleration[††] will promote the drainage and subsequent propagation of the fluid away from the centre of the test area in the downstream direction while impeding it in the upstream direction. Similarly, during the latter stages of recorded motion,

---

[††]See Chapter 6 for the definitions and a detailed analysis of the influence of Coriolis accelerations and the Eötvös effect on collapse dynamics

the ability of the granular front to catch up to the fluid front, resulting in a lower final separation, also increased when aided by the Coriolis acceleration[††]. Similar effects have been noted in recent numerical works (Cabrera et al., 2020; Leonardi et al., 2021) where the density of the flow is highly dependent on the flow propagation direction relative to centrifuge motion. Naturally, the magnitude of these effects increased with $N$, as the magnitude of the Coriolis acceleration[††] also increases with $N$.

While the influence of the Coriolis acceleration[††] does vary with particle size, it only appears to have a significant affect on flow dynamics when the collapses containing smaller particle sizes (i.e. $d_p = 2\,\mathrm{mm}$) enter a 'creep-like' flow regime where, in the downstream direction, the fluid front is again able to accelerate away from the granular front. Whereas, for the larger particle sizes, the Coriolis acceleration[††] only further propagates the reduction of $(r_f - r_p)/r_f$ with normalised time. Similarly, the influence of the Eötvös effect[††] appeared to be negligible on flow dynamics prior to the creep phase which is likely due to the fact that natural scale particle inertia has been preserved. Given that the current study focuses on debris flow mechanics, which are best replicated within the experiment prior to the flow entering a monolayer (i.e. the initial acceleration phase), we have deemed the asymmetry induced by the Coriolis acceleration and the Eötvös effect[††] to be negligible for the particular collapse period of interest (see Section 3.6).

## 3.5 Fluid pressure evolution

As well as having a dominant effect on the possible separation between the two phase fronts, the drainage phase of the collapse is key to the reduction of pore pressure from the initially static column configuration. Figure 3.7 details the evolution of the normalised basal fluid pressure at the centre of the column $P$ with time $t$ for particle diameters, $d_p = 2\,\mathrm{mm}$, $d_p = 4\,\mathrm{mm}$, $d_p = 6\,\mathrm{mm}$, and $d_p = 8\,\mathrm{mm}$, at **(a)** $N = 4.61$, and **(b)** $N = 14$, respectively. Again, tests have been selected that have a shared $\eta_f$ value for every value of $N$. In this case, the time-frame shown has been restricted to the first $0.5\,\mathrm{s}$ of each collapse at which point the residual normalised pressure is referred to as $P_F^*$.

At the beginning of each test conducted at both $N = 4.61$ and $N = 14$, $P \approx \rho_f G h_0$ which illustrates that pressures within the column are hydrostatic prior to the collapse. Upon release, the height of fluid above the pressure sensor reduces throughout the collapse as the granular-fluid mixture propagates out away from the column centre. This

---

[††]See Chapter 6 for the definitions and a detailed analysis of the influence of Coriolis accelerations and the Eötvös effect on collapse dynamics
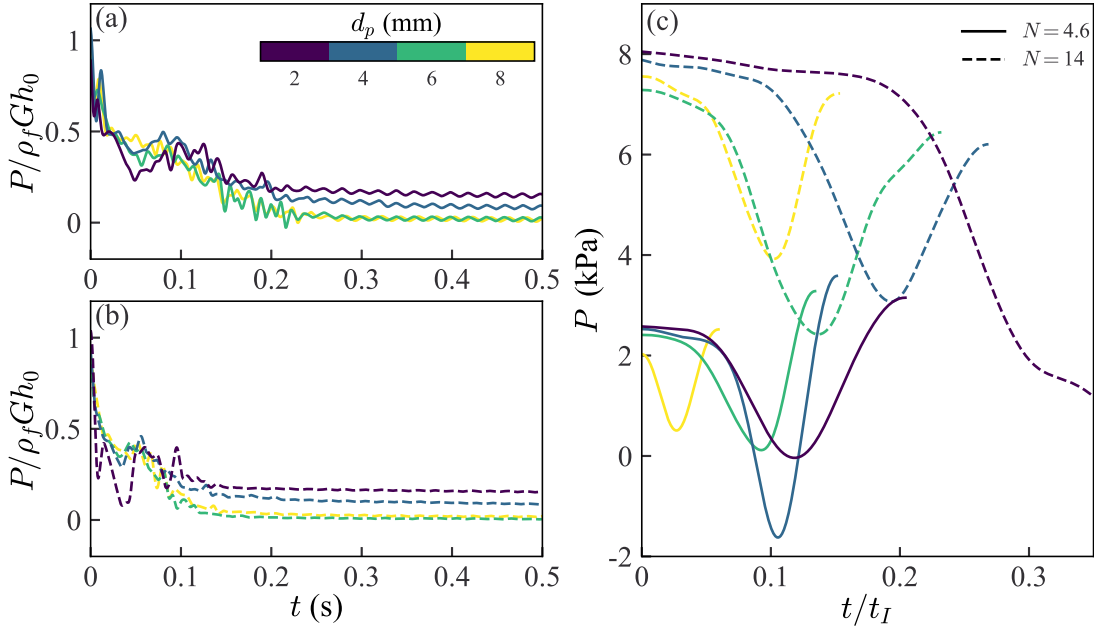
Figure 3.7: Temporal evolution of the dimensionless basal fluid pressure at the centre of the column $P/\rho_f G h_0$, filtered using $f_c = 100\,\text{Hz}$ with time $t$ for all particle sizes $d_p$ at (**a**) $N = 4.61$ and (**b**) $N = 14$. (**c**) Basal fluid pressure at the centre of the column $P$, filtered at $f_c = 1000\,\text{Hz}$, against $t/t_I$ immediately after the release of the column.

results in a progressive reduction of $P$ until $P = P_F$.

The influence of $d_p$ on the temporal evolution of $P$ can be illustrated through its influence of $P_F^*$. For a given $N$, $P_F^*$ increases with decreasing $d_p$ and $P_F^*$ for particle sizes $d_p = 6\,\text{mm}$ and $d_p = 8\,\text{mm}$ is approximately equal to $0\,\text{kPa}$ where no fluid remains above the PT. This demonstrates the reduced influence of the granular phase on $P_F^*$ as $d_p$ increases. It can be reasoned that the increased pore space improves the fluid's ability to displace from the centre of the measurement domain over the test duration. Conversely, a smaller pore space limits the fluid's ability to exit the granular material which itself has reduced mobility due to capillary effects. A similar particle size dependency has been observed in the case of post-depositional seepage in natural scale debris flows (e.g. Major and Iverson, 1999). The influence of $d$ also appears to slightly increase with $N$.

Figure 3.7c focuses on another characteristic feature of the evolution of $P$, which is the reduction and recovery of basal pore pressure observed over the inertial column timescale $t_I = \sqrt{h_0/G}$ immediately after collapse initiation. While the magnitude of this initial pressure reduction increases with $N$, the more interesting variation is largely controlled by $d_p$ with the magnitude of the pressure drop generally increasing as $d_p$ de-

46

creases for a given $N$. This effect is more pronounced when $N = 14$. The recovery of this initial pressure reduction also appears to reduce as $N$ increases. As this variation in pressure reduction occurs immediately after the release of the column, it is likely to be the result of initial particle rearrangement. It has been found previously that the critical solid volume fraction for spherical grains $\phi_c \approx 0.57$ (Rondon et al., 2011). This suggests that all tests in the current study were conducted with dense granular packings which means that, upon the onset of the collapse, the granular structure must initiate its displacement by first dilating. This allows the interstitial pore fluid to move into the additional pore space created by the dilation which, based on the pore pressure feedback loop described by Iverson et al. (2000), causes a reduction in basal fluid pressure. Rondon et al. (2011) demonstrated the presence of the pore pressure feedback loop for a quasi-two-dimensional fully-submerged granular column collapse configuration exposed to the acceleration field of Earth's gravity. The study was carried out using only a singular particle size ten times smaller than the smallest particle used in the current work. A submerged collapse would not experience any influence from surface tension so any differences in behaviour based on particle size would emanate from viscous interactions between the fluid and the grains. In the current configuration, capillary forces arising from the presence of surface tension will cause a further reduction in $P$.

## 3.6   Scale analysis

As collapse dynamics clearly depend on $N$, dimensionless parameters used previously in the literature, $a_0$ and $\phi_p$, are not enough to characterise the phenomena governing the behaviour of the fluid-saturated granular column collapse in the current test configuration. The observed interplay between the fluid and particle fronts also suggests that the viscous nature of the interstitial fluid must also be recognised to explain these flow states.

To characterise the acceleration phase of each collapse, the maximum velocities of the two phase fronts $u_{f,m}$ and $u_{p,m}$, and the time after collapse initiation that these maximum velocities were achieved $t_{f,m}$ and $t_{p,m}$, were evaluated. A linear approximation of the pressure gradient over the first significant pressure drop at the centre of the column, $\dot{P}_m$, was recorded as indicative of the pore pressure response in the early collapse stages. Using these terms, Equation (3.2) can be rewritten into the following form
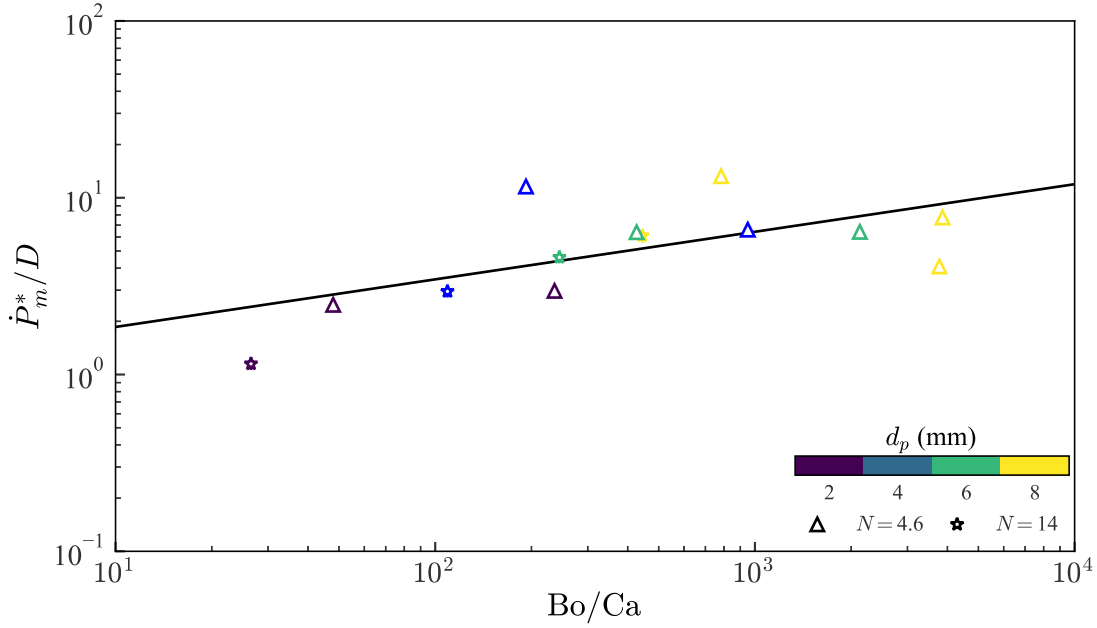
Figure 3.8: $\dot{P}_m^*$ normalised by $D = (\rho^*)^\beta (r^*)^\gamma$ against Bo/Ca for all particle sizes $d_p$ at $N = 4.61$ (triangle) and $N = 14$ (star). The black line indicates the power law fit provided in Equation (3.4) using the exponents found in Table 3.3.
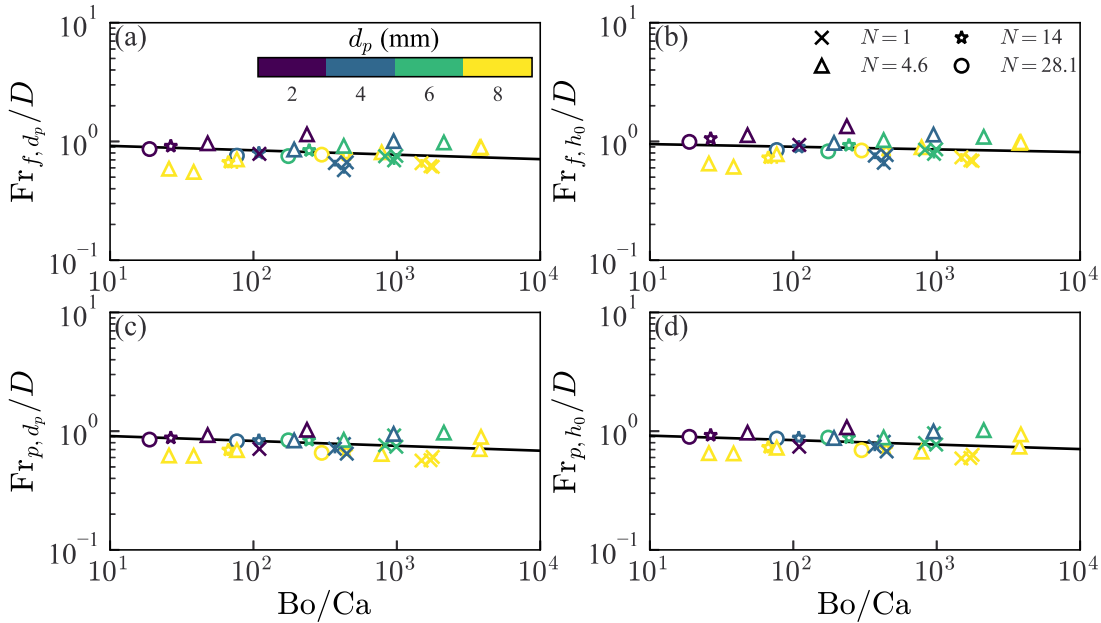


Figure 3.9: $\mathrm{Fr}_{v,L}$ normalised by $D = (\rho^*)^\beta (r^*)^\gamma$ against Bo/Ca for all particle sizes $d_p$ at all $N$. (a) $v = f$ and $L = d_p$, (b) $v = f$ and $L = h_0$, (c) $v = p$, and $L = d_p$ and (d) $v = p$ and $L = h_0$. The black line indicates the power law fit provided in Equation (3.4) using the exponents found in Table 3.3. Error bars signify the absolute measurement error of the independent variable. In this case, these bars are very small.
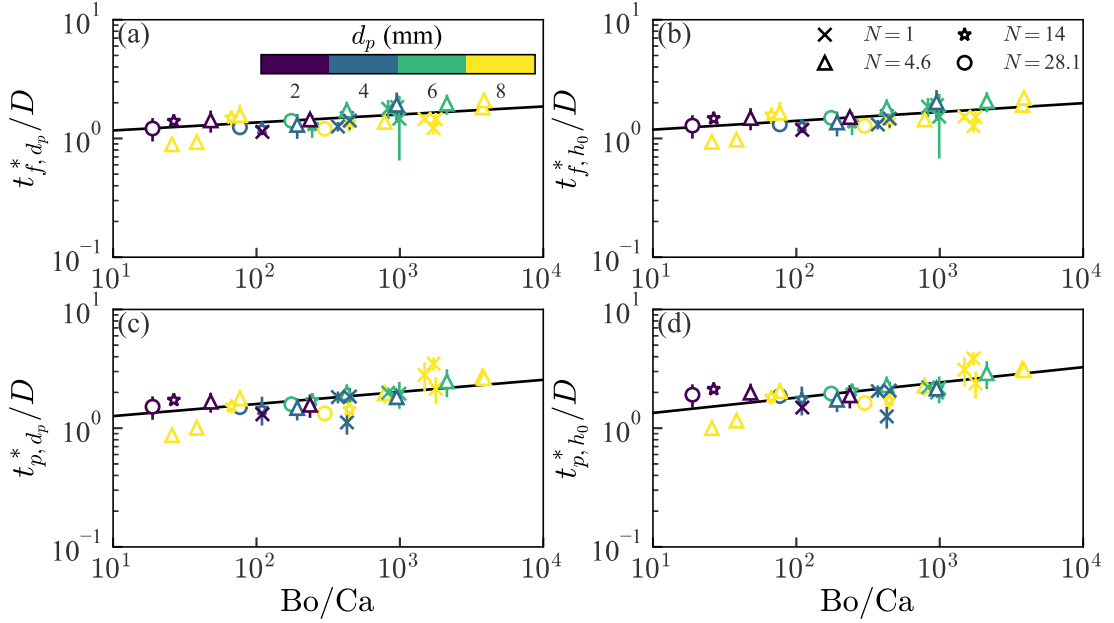
Figure 3.10: $t_{v,L}^*$ normalised by $D = (\rho^*)^\beta (r^*)^\gamma$ against Bo/Ca for all particle sizes $d_p$ at all $N$. **(a)** $v = f$ and $L = d_p$, **(b)** $v = f$ and $L = h_0$, **(c)** $v = p$, and $L = d_p$ and **(d)** $v = p$ and $L = h_0$. The black line indicates the power law fit provided in Equation (3.4) using the exponents found in Table 3.3. Error bars signify the absolute measurement error of the independent variable.

$$\frac{u_{v,m}}{\sqrt{GL}} = f_3 \left( \frac{h_0}{r_0}, \frac{r_0}{d_p}, \frac{(\rho_p - \rho_f)N}{\rho_f}, \frac{t_{v,m}}{\sqrt{L/G}}, \frac{\dot{P}_m}{\rho_f \sqrt{G^3 h_0}}, \frac{\rho G h_0 d_p}{\sigma_f}, \frac{\eta_f \sqrt{G h_0}^3}{\sigma_f d_p} \right),$$

(3.3)

where $f_3$ is an unknown function and, again, the subscript $v$ refers to the phase of interest. Noting that $\phi_p$ remained approximately constant throughout the experiments, this parameter was disregarded from all further analyses. Thus eight dimensionless groups are defined: $Fr_{v,L}$, $a_0$, $r^*$, $\rho^*$, $t_{v,L}^*$, $\dot{P}_m^*$, Bo and Ca, where subscript $L$ is equal to $d_p$ or $h_0$ depending on the characteristic length scale of interest.

Values of $Fr_{v,L}$ and $t_{v,L}^*$ were obtained for each test by averaging the upstream and downstream values of $u_{v,m}$ and $t_{v,m}$, respectively. This had the added benefit of limiting the contributions of Coriolis acceleration and the Eötvös effect[††] on the scale analysis. The significance of each parameter in Equation (3.3) was tested through the implementation of a non-linear regression scheme with a weighting that favoured power-law fits

---

[††]See Chapter 6 for the definitions and a detailed analysis of the influence of Coriolis accelerations and the Eötvös effect on collapse dynamics

Table 3.3: Summary of exponents used to fit Equation (3.4) for all characteristic dimensionless quantities of interest. The normalised root mean squared error $\mathrm{RMSE}_N$ of each fit is also detailed.

| $Q$ | $\alpha$ | $\beta$ | $\gamma$ | $\mathrm{RMSE}_N$ |
|---|---|---|---|---|
| $\mathrm{Fr}_{f,d_p}$ | -0.04 | 0.07 | 0.30 | 0.15 |
| $\mathrm{Fr}_{f,h_0}$ | -0.02 | 0.08 | -0.25 | 0.27 |
| $\mathrm{Fr}_{p,d_p}$ | -0.04 | 0.04 | 0.34 | 0.13 |
| $\mathrm{Fr}_{p,h_0}$ | -0.04 | 0.04 | -0.16 | 0.31 |
| $t_{f,d_p}{}^*$ | 0.07 | 0.18 | 0.54 | 0.09 |
| $t_{f,h_0}{}^*$ | 0.07 | 0.18 | 0.04 | 0.16 |
| $t_{p,d_p}{}^*$ | 0.10 | 0.16 | 0.50 | 0.13 |
| $t_{p,h_0}{}^*$ | 0.13 | 0.13 | -0.03 | 0.17 |
| $\dot{P}^*$ | 0.27 | -0.46 | 0.80 | 0.26 |

that minimised the degrees of freedom to reasonably portray the data set. Given that we do not have an a priori understanding of the combined and relative influence of each $\Pi$ group within the dimensionless parameter space, a generalised power-law fit provides a reasonable starting point for this process. The outcome is that all measured quantities, meaning $\dot{P}_m^*$, $\mathrm{Fr}_{v,L}$ and $t_{v,L}^*$, appear to be independent of each other for all phases and scales. Figures 3.8, 3.9 and 3.10 show the finalised fits for $\dot{P}^*$, $\mathrm{Fr}_{v,L}$ and $t_{v,L}{}^*$ against Bo/Ca, respectively. The low measurement error for the majority of points in Figs 3.8 and 3.9 further highlights the minimal influence that the Coriolis acceleration[††] had over the collapse period of interest. In the case of $\dot{P}_m^*$, the absolute measurement error for each data point lies within each respective marker. It is important to note that this error differs from the fluctuations in pressure gradient throughout the signal which is significantly larger. The variation of all measured quantities of interest $Q$ can be described by the following relation

$$Q = \left(\frac{\mathrm{Bo}}{\mathrm{Ca}}\right)^\alpha (\rho^*)^\beta (r^*)^\gamma, \tag{3.4}$$

where $\alpha$, $\beta$ and $\gamma$ are constants that are summarised in Table 3.3. Equation (3.4) demonstrates that the selected characteristic quantities associated with the initial acceleration phases of the granular and fluid flow fronts and the initial post-collapse pressure gradient can be reasonably well predicted by a simplistic power law model consisting of three dimensionless parameters.

---

[††]See Chapter 6 for the definitions and a detailed analysis of the influence of Coriolis accelerations and the Eötvös effect on collapse dynamics
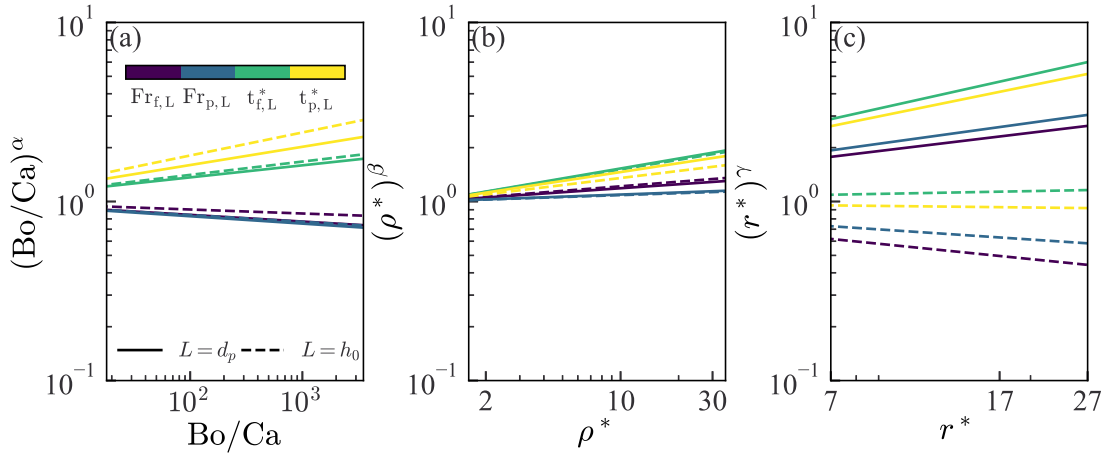
Figure 3.11: **(a)** $(\mathrm{Bo/Ca})^\alpha$ against Bo/Ca. **(b)** $\rho^{*\beta}$ against $\rho^*$. **(c)** $r^{*\gamma}$ against $r^*$. Fits for $\mathrm{Fr}_{f,d_p}$, $\mathrm{Fr}_{f,h_0}$, $\mathrm{Fr}_{p,d_p}$, $\mathrm{Fr}_{p,h_0}$, $t^*_{f,d_p}$, $t^*_{f,h_0}$, $t_{p,d}{}^*$, and $t^*_{p,h_0}$ are shown.

### 3.6.1 Quantification of scaling parameter influence

Equation (3.4) provides significant insight into the factors governing the behaviour of these characteristic flow states. The relative influence of each parameter on the right-hand side of Equation (3.4) on the mobility of the granular and fluid phases is investigated further in Figure 3.11 where each parameter to the power of its exponent is plotted against itself for all variations of $\mathrm{Fr}_{v,L}$ and $t^*_{v,L}$.

Considering Bo/Ca as a single parameter within Equation (3.4) means that the fits of $Q$ are decoupled from the influence of surface tension at the grain-scale. Instead, it is the balance of column-scale gravitational and viscous forces that influence flow behaviour. While the influence of surface tension at varying levels of $N$ was discussed previously, the relatively large particle sizes used has allowed all cases of $Q$ to be surface tension independent at all scales. Figure 3.11a shows that $(\mathrm{Bo/Ca})^\alpha$ decreases as Bo/Ca increases for all cases of $\mathrm{Fr}_{v,L}$. Given that column collapses are gravity-driven processes, the rate at which gravitational forces increase will dominate the rate at which inertial forces increase for all phases and scales. This means that column mobility, and therefore $t^*_{v,L}$, increases as gravitational force contributions increase with respect to viscous effects.

Figure 3.11b demonstrates that $(\rho^*)^\beta$ increases with $\rho^*$ in all cases. According to Bougouin and Lacaze (2018), the range of $\rho_p/\rho_f$ values used categorises the observed flow states into the inertial regime where inertial fluid forces have a significant impact on flow behaviour. However, the influence of particle inertia still dominates, which causes $\beta$ to vary depending on the phase of the flow. Generally, the magnitude of $\beta$ is greater

for the particle phase for both quantities of interest at both the column- and granular-scales. It would be interesting to achieve higher values of $\rho^*$ by either reducing $\rho_f$ or increasing $\rho_p$ and see how flow states where fluid inertial effects are no longer important (i.e. the free-fall regime) scale with Equation (3.4).

Warnett et al. (2014) found that increasing $r^*$ increased the mobility of the collapse in the dry case. In the current study, Figure 3.11c shows that the influence of $r^*$ is predominantly dependent on the scale of interest. Generally, increasing $r^*$ reduced the mobility of the column at the column-scale while increasing it at the grain-scale with respect to velocity and collapse duration. This outcome is logical as $r^*$ is a ratio between the column- and grain-scales. Previously, this effect was found to saturate when $r^* \approx$ 107, a value that is significantly higher than what is covered by the parameter space of the current study. As $r^*$ was varied by changing the particle size, we are unable to determine whether $r_0$, and other parameters defining the column geometry, have a significant impact on the evolution of the flow as $N$ increases.

## 3.7 Discussion

The wide particle size distribution in debris flows coupled with comparatively high fluid volume fraction leads to macro-scale flow features that can originate from micro-scale processes. This makes similitude between laboratory experiments and geophysical-scale movement events particularly difficult. For example, surface tension can not be important in the geophysical flow when considering overall flow scale, but becomes important in a laboratory prototype with reduced geometric scale. This means that the true role of surface tension through fines in the geophysical flow may actually be masked by these scaling artefacts in the laboratory. This research attempts to evaluate laboratory flows where the particles are inertial, in an attempt to isolate the response of those grains as differentiated from fine grains in a debris flow.

To mimic debris flows, we used a just-saturated granular column collapse configuration, consisting of glass grains in a size range where their inertia was significant, facilitated by using a geotechnical centrifuge. Grain size, gravitational acceleration and fluid viscosity were systematically varied to analyse their influence on the front evolution of grain and fluid phases alongside the basal pore pressure.

The drainage phase, where the fluid front accelerates away from the granular front, was found to be accentuated by both increasing the granular pore space and, increasing the level of gravitational acceleration up until $N = 14$. Larger tested values of $N$

resulted in collapse dynamics becoming less dependent on grain-fluid interactions and particle inertia dominating the dynamics of the granular phase. Without enhanced gravitational acceleration, just-saturated granular columns evolved in a similar way to previous experiments (dry, underwater, saturated); comprising acceleration, quasi-steady and retardation phases. The duration of these runout events primarily decreased with particle size as larger capillary forces, which limit grain mobility, developed within the granular materials with smaller pore spaces. In contrast, the collapse duration of tests exposed to elevated levels of gravitational acceleration decreased with both increasing pore space and increasing $N$ for a given particle size. The latter showing that the influence of capillary forces on the evolution of the collapse reduces with increased scale.

Analysis of the temporal evolution of the basal pore pressure at the centre of the column also highlighted the major influence of pore space as $N$ increases, particularly during the initial drainage phase post-collapse initiation. The magnitude of the initial pressure drop increases with decreasing particle size at a given level of elevated gravitational acceleration. Similarly to the conclusions of previous authors (Iverson et al., 2000; Rondon et al., 2011), this pore size dependent pressure drop is surmised to emanate from the pore-pressure feedback loop for a dense granular configuration. The presence of capillary forces within the just-saturated column configuration caused the pore pressure to drop further when the particle size was smaller.

Buckingham's $\Pi$ theorem was used to postulate a relationship between 11 fundamental test variables that characterise the acceleration phase of each column collapse using 8 independent dimensionless $\Pi$ groups. A non-linear regression scheme was used to evaluate the influence of each parameter and found that all measured quantities of interest, specifically, $\dot{P}_m^*$, $\mathrm{Fr}_{v,L}$ and $t_{v,L}^*$, are independent of each other at all scales and are well described by $Q = (\mathrm{Bo/Ca})^\alpha (\rho^*)^\beta (r^*)^\gamma$ where $\alpha$, $\beta$ and $\gamma$ are dependent on $Q$. Crucially, the inclusion of both Bo and Ca within a single parameter means that all quantities of interest are decoupled from grain-scale surface tension effects and it is the balance of column-scale gravitational and viscous forces that govern acceleration phase collapse behaviour as seen in natural-scale debris flows with a granular phase including inertial particles.

The current study has been effective in highlighting the collapse response of grain-fluid mixtures with inertial grains. This provides a start point for exploring separately the role of fines, where their effect may be negligible on the inertial/flow scale, but which may nevertheless control processes within the much smaller pore spaces. This work is timely given the findings of Kaitna et al. (2016) highlighting the importance of fine

granular material to the maintenance of excess pore pressures in steady-state granular-fluid flows. Developing a large dataset of unsteady granular-fluid flow experiments, where the impact of including fine granular material can be quantified, will be crucial to the development of a more mechanically precise pore pressure evolution model.

## 3.8   Supplementary content

The raw video files for all completed tests are available at `https://doi.org/10.17639/nott.7277`.

Chapter 4

# Fines-controlled drainage in just-saturated, inertial column collapses

**Abstract**

*The wide particle size distributions, over several orders of magnitude, observed in debris flows leads to a diverse range of rheological behaviours controlling flow outcomes. This study explores the influence of different scale grains by conducting subaerial, fully saturated granular column collapse experiments with extreme, bimodal particle size distributions. The primary particles were of a size where their behaviour was controlled by their inertia while a suspension of kaolin clay particles within the fluid phase acts at spatial scales smaller than the pore space between the primary particles. The use of a geotechnical centrifuge allowed for the systematic variation of gravitational acceleration, inertial particle size and the degree of kaolin fines. Characteristic velocity- and time-scales of the acceleration phase of the collapse were quantified using high-speed cameras. Comparing tests containing fines to equivalent collapses with a glycerol solution mimicking the enhanced viscosity but not the particle behaviour of the fines, it was found that all characteristic dynamic quantities were dependent on the degree of fines, the system size, the grain fluid-density ratio and the column– and grain-scale Bond and Capillary numbers. We introduce a fine-scale Capillary number showing that, although surface tension effects at the column scale are negligible, fines do control the movement of fluid through the pore spaces.

55

## 4.1   Introduction

The influence of a wide particle size distribution on the dynamics and outcomes of naturally occurring debris flows is still disputed. Field studies (e.g. McArdell et al., 2007) and large-scale testing (e.g. Johnson et al., 2012) have shown that events containing high quantities of fine granular material, like clays and silts, often achieve increased mobility through the development of significant excess pore pressures which reduce the frictional energy losses between the bulk flow and the terrain bed.

Recent two-phase shallow water models (Bouchut et al., 2017; Iverson and George, 2014; Kowalski and McElwaine, 2013) have attempted to capture the temporal and spatial variation of the grain size distribution by modelling aspects of unsteady debris flow behaviour. However, there is still no consensus on the most appropriate, computationally efficient way to implement this complexity. This suggests that a more refined understanding of the mechanisms controlling grain-scale flow dynamics is required to allow conclusions to be made on what physical processes are most influential on global flow outcomes. Given the small length and time scales associated with these effects, it seems pertinent to analyse them further by conducting laboratory-scale experiments where it is possible to fully control the initial and boundary conditions of the flow (Iverson et al., 2010b). A notable study (Kaitna et al., 2016) utilised a drum centrifuge configuration to evaluate the influence of the particle size distribution on steady-state flow dynamics. They found that mixtures that contained higher percentages of fine granular material exhibited more significant and prolonged excess pore pressures which reduced bulk flow resistance. While this is encouraging, further parametric investigations are required to quantitatively evaluate the influence of the inclusion of fines on flow dynamics and understand the mechanisms at play.

A recent study (Webb et al., 2023b)[†] attempted to isolate the influence of inertial grains on flow dynamics over a wide parameter space by conducting $g$-elevated, fluid-saturated granular column collapse experiments where water-glycerol mixtures were used as a pseudo-fluid. The current study attempts to build on this work and introduce an extreme bimodal grain size distribution by using a fluid phase comprised of kaolin clay particles and water. As such, by varying gravitational acceleration, the coarse grain diameter and the percentage of fines, the influence of the fine length- and time-scales on acceleration phase collapse dynamics is evaluated and compared within the previously established parameter space.

---
[†]Webb et al. (2023b) is shown in Chapter 3

## 4.2 Methodology

### 4.2.1 Experimental setup

The experiment (see Figure 4.1) consists of rapidly releasing a granular-fluid mixture, which is initially accommodated within a partially filled steel cylinder, over a horizontal plane where it is allowed to spread under the influence of a prescribed gravitational acceleration $G$. By spinning the apparatus at the end of a geotechnical beam centrifuge, the collapse can occur at an elevated gravitational acceleration $G = Ng$ where $N$ is dependent on the effective radius and rotational speed of the model, and $g = 9.81\,\mathrm{m}$ $\mathrm{s}^{-2}$.

The current study focused on the collapse of fluid saturated granular columns with an initial height $h_0 = 50\,\mathrm{mm}$ and a column radius $r_0 = 54\,\mathrm{mm}$. The granular phase was comprised of soda lime glass spheres with a density $\rho_p = 2642\pm27.4\,\mathrm{kg\,m}^{-3}$ and a mean packing fraction $\phi_p = 0.61\pm0.01$. The fluid phase consisted of kaolin clay particles suspended in water. Tests were conducted over a wide parameter space by varying $G = [9.81, 45.22, 137.64, 275.45]\,\mathrm{m\,s}^{-2}$, the coarse grain diameter $d_p = [4, 8]\,\mathrm{mm}$, and the degree of fines suspended within the fluid by mass $C_k = [0.1, 0.2]$. Assuming a characteristic collapse strain rate $\dot{\gamma} = \sqrt{G/h_0}$, the density, viscosity and surface tension of the fluid phase was varied between $\rho_f = [1165, 1330]\,\mathrm{kg\,m}^{-3}$, $\eta_f = [7.65, 108.30]\,\mathrm{cP}$, and $\sigma_f = [92.59, 98.96]\,\mathrm{mN\,m}^{-1}$, respectively. The evolution of the collapsing mixture was recorded by two Go-Pro cameras and the temporal evolution of the collapse front was obtained through the image analysis procedure detailed in Webb et al. (2023b)[†].

### 4.2.2 Dimensional analysis

Buckingham's $\Pi$ theorem (Buckingham, 1914) can be used to examine how different test parameters may impact the propagation of the collapse. As such, a relationship between the flow front velocity $u$ at time $t$ with the collapse test parameters can be hypothesised as

$$u = f_1\left(h_0, r_0, d_p, \rho_p, \phi_p, C_k, d_k, \rho_f, \eta_f, \sigma_f, t, G\right), \tag{4.1}$$

where $f_1$ is an unknown function and $d_k$ is a reference length scale for the kaolin clay particles taken as $5\,\mu\mathrm{m}$. The theorem then states that the 11 dimensional quantities in

---

[†]Webb et al. (2023b) is shown in Chapter 3
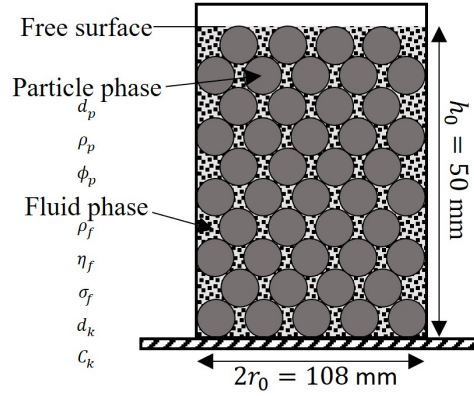
Figure 4.1: Schematic of the initial column configuration prior to collapse initiation.

Equation (4.1), which are functions of mass, length and time scales, can be interrelated by 8 dimensionless $\Pi$-groups. Following the methodology described in Iverson (2015), Equation (4.1) can be transformed into the following form

$$\frac{u}{\sqrt{GL}} = f_2 \left( \phi_p, C_k, \frac{r_0}{d_p}, \frac{t}{\sqrt{LG^{-1}}}, \frac{(\rho_p - \rho_f)\,N}{\rho_f}, \frac{\rho G d_p h_0}{\sigma_f}, \frac{\rho G d_p d_k}{\sigma_f}, \right.$$
$$\left. \frac{\eta_f \sqrt{G h_0^3}}{\sigma_f d_p}, \frac{\eta_f \sqrt{G d_p^3}}{\sigma_f d_k} \right), \quad (4.2)$$

where $f_2$ is an unknown function, $L$ is the characteristic length scale of interest and $\rho$ is the granular-fluid mixture effective density $\rho = \phi_p \rho_p + (1 - \phi_p)\,\rho_f$. The parameter on the left-hand side of Equation (4.2) is the flow front Froude number $u_L^*$ which is the ratio of inertial and gravitational forces over a characteristic length scale $L$. The first two parameters on the right-hand side of Equation (4.2) are the dimensionless parameters $\phi_p$ and $C_k$ which remain unchanged from Equation (4.1). The third parameter, $r^*$ is the ratio between $r_0$ and $d_p$. The fourth parameter, $t_L^*$, compares $t$ against the length scale dependent characteristic inertial timescale $\sqrt{LG^{-1}}$. The fifth parameter is the relative granular-fluid density ratio accounting for acceleration-scale buoyancy effects $\rho^*$. The sixth and seventh parameters are referred to as the column- and grain-scale Bond numbers, Bo and Bo$_k$, respectively. The first parameter quantifies the relative influence of inertial forces at the column scale against capillary forces at the grain scale while the latter is an analogous quantity relating grain scale inertial forces to kaolin scale capillary effects. The final two parameters are scale-relative Capillary numbers. The first relates column scale viscous forces to grain scale capillary effects Ca while

58

the second compares grain scale viscous forces to kaolin scale capillary effects $Ca_k$. As stated in Iverson (2015), given that $\Pi$ groups can be recast through multiplication, the dimensionless parameter set in Equation (4.2) is not a unique solution to Equation (4.1). This set was deemed suitable as it has significant overlap with the dimensionless set used in the previous scale analysis study (Webb et al., 2023b)[†]. The included force ratio terms also allow for comparison across all three length scales of interest ($h_0$, $d_p$ and $d_k$) which is critical in interpreting the contribution of the fine particulate to flow dynamics throughout the acceleration phase.

## 4.3 Results and discussion

The acceleration phase of each collapse was characterised by the maximum velocity of the flow front $u_m$, and the time elapsed between collapse initiation and the instance where $u_m$ was achieved $t_m$. The two camera angles allowed averaged values of the two quantities to be taken which reduces the impact of external forces resulting from centrifuge modelling like the Coriolis force[††].

Given that $\phi_p$ remains approximately constant across all tests, Equation (4.2) can be simplified as follows

$$\mathrm{Fr}_{m,L} = f_3 \left( C_k, r^*, t^*_{m,L}, \rho^*, \mathrm{Bo}, \mathrm{Bo_k}, \mathrm{Ca}, \mathrm{Ca_k} \right), \tag{4.3}$$

where $\mathrm{Fr}_{m,L}$ and $t^*_{m,L}$ are equivalent to $\mathrm{Fr}_L$ and $t^*_L$ evaluated at $u_m$ and $t_m$, respectively. The characteristic length scales of interest $L$ are $d_p$ and $h_0$ meaning that there are four quantities of interest $Q$ related to the acceleration phase of the collapse; $\mathrm{Fr}_{m,d_p}$, $\mathrm{Fr}_{m,h_0}$, $t^*_{m,d_p}$, and $t^*_{m,h_0}$.

To evaluate the effect of the inclusion of fines on the acceleration phase, a single dataset containing the quantities collected from the current study and the same quantities published in Webb et al. (2023b)[†] for the Newtonian fluid test cases, where $C_k = 0$, and $\mathrm{Bo}_k$ and $\mathrm{Ca}_k$ values are not considered, was developed. The influence of every parameter in Equation (4.3) was then evaluated using a non-linear regression scheme and, as was found for the Newtonian fluid dataset, the measured quantities of interest can be described by empirical power law fits that are independent of the other quantities

---

[†]Webb et al. (2023b) is shown in Chapter 3

[††]See Chapter 6 for the definitions and a detailed analysis of the influence of Coriolis accelerations and the Eötvös effect on collapse dynamics

Chapter 4: Fines-controlled drainage in just-saturated, inertial column collapses

Table 4.1: Summary of exponents for Equation (4.4) for all $Q$ along with the normalised root mean squared error $\mathrm{RMSE}_N$ of each fit.

|  | $\mathrm{Fr}_{\mathrm{m,d_p}}$ | $\mathrm{Fr}_{\mathrm{m,h_0}}$ | $t^*_{m,d_p}$ | $t^*_{m,h_0}$ |
|---|---|---|---|---|
| $k_1$ | -0.04 | -0.04 | 0.09 | 0.11 |
| $k_2$ | 0.07 | 0.15 | -0.48 | -0.63 |
| $k_3$ | 0.18 | 0.27 | -0.40 | -0.55 |
| $k_4$ | 0.10 | 0.11 | 0.22 | 0.23 |
| $k_5$ | 0.30 | -0.19 | -0.48 | -0.07 |
| $\mathrm{RMSE}_N$ | 0.14 | 0.19 | 0.11 | 0.10 |

of interest. For the current combined dataset, this relationship is defined as

$$Q = \left(\frac{\mathrm{Bo}}{\mathrm{Ca}}\right)^{k_1} \left(\frac{\mathrm{Bo_k}}{\mathrm{Ca_k}}\right)^{k_2 C_k} (\mathrm{Ca_k})^{k_3 C_k} (\rho^*)^{k_4} (r^*)^{k_5}, \tag{4.4}$$

where $k_1$–$k_5$ are constants summarised in Table 4.1. Figure 4.2 details the finalised fits for each $Q$. The structure of Equation (4.4) allows Newtonian- and non-Newtonian-fluid tests to be fitted to the same power law as terms that include parameters associated with the kaolin-scale can be neglected as $C_k = 0$.

Equation (4.4) is very similar in structure to the empirical fit found for $Q$ in the case of the purely Newtonian fluid dataset

$$Q = \left(\frac{\mathrm{Bo}}{\mathrm{Ca}}\right)^{\alpha} (\rho^*)^{\beta} (r^*)^{\gamma}, \tag{4.5}$$

where $\alpha$, $\beta$, and $\gamma$ are constants. It is reassuring to see that the general trend and, the coefficients of the terms that are independent of kaolin-scale phenomena (i.e. $k_1$, $k_4$ and $k_5$), are largely comparable in both magnitude and sign for Equation (4.4) and Equation (4.5) for all $Q$. The normalised root mean squared error $\mathrm{RMSE}_N$ has also reduced for every $Q$.

The most significant outcome from this study is the appearance of the $\mathrm{Ca}_k$ term in Equation (4.4). This suggests that the inclusion of fine granular material results in all acceleration phase quantities of interest being dependent on surface-tension effects emanating from the kaolin-scale. In contrast, as demonstrated by Equation (4.5), surface tension effects were not pertinent to the behaviour of the Newtonian fluid test case.

The relative importance of each force ratio term in Equation (4.4) associated with the grain- and kaolin-length scales can be quantified by comparing their magnitude and sign to the magnitude and sign of $(\mathrm{Bo/Ca})^{k_1}$. Figure 4.3 shows the plots of
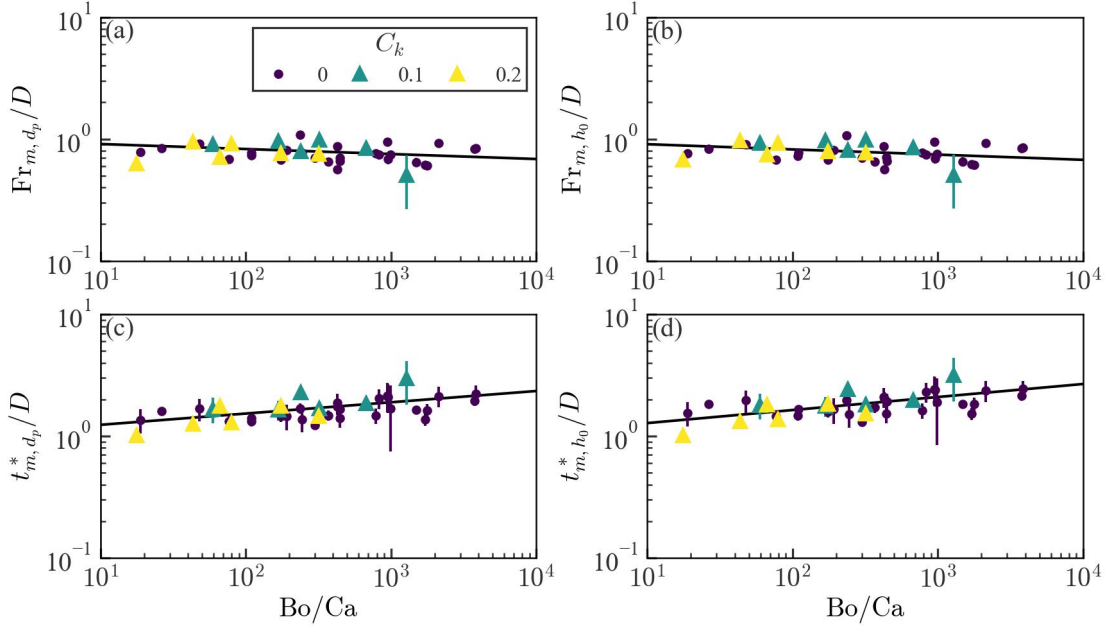
Figure 4.2: **(a)** $\mathrm{Fr}_{\mathrm{m,d_p}}$, **(b)** $\mathrm{Fr}_{\mathrm{m,h_0}}$, **(c)** $t^*_{m,d_p}$, and **(d)** $t^*_{m,h_0}$ normalised by $D = \left(\frac{\mathrm{Bo}_k}{\mathrm{Ca}_k}\right)^{k_2 C_k} (\mathrm{Ca}_k)^{k_3 C_k} (\rho^*)^{k_4} (r^*)^{k_5}$ against Bo/Ca for all values of $C_k$. The black line defines the power law fit described by Equation (4.4) using the exponents provided in Table 4.1. Error bars define the absolute error of the independent variable.
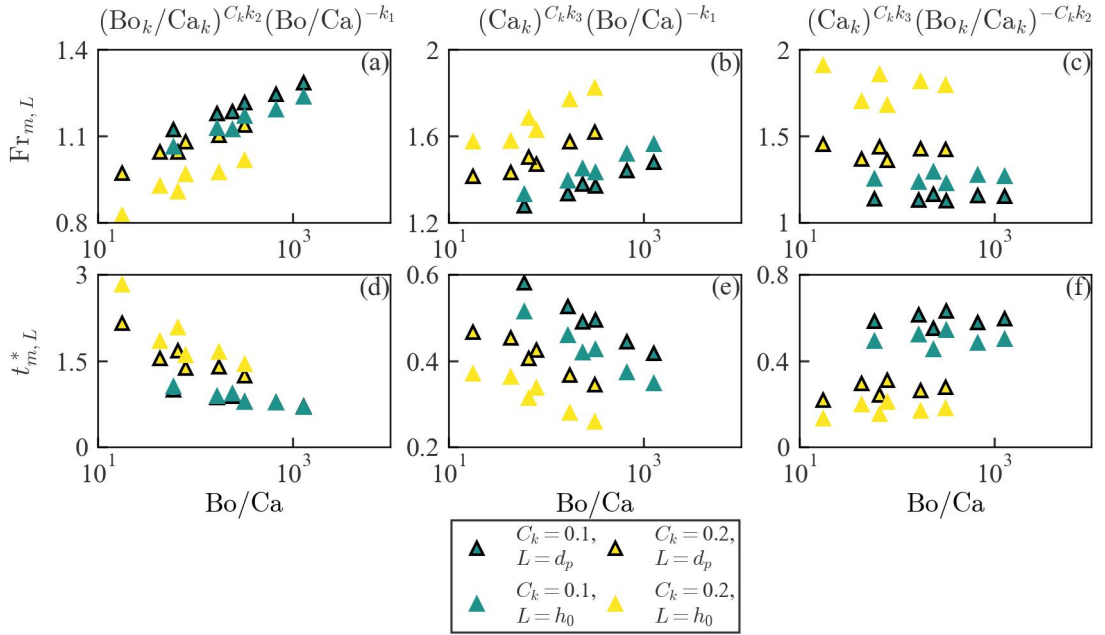


Figure 4.3: Comparison of the force ratio influence for $\mathrm{Fr}_{\mathrm{m,L}}$ and $t^*_{m,L}$ for all values of $C_k$ and $L$.

$(\mathrm{Bo}_k/\mathrm{Ca}_k)^{C_k k_2} (\mathrm{Bo}/\mathrm{Ca})^{-k_1}$, $(\mathrm{Ca}_k)^{C_k k_3} (\mathrm{Bo}/\mathrm{Ca})^{-k_1}$ and $(\mathrm{Bo}_k/\mathrm{Ca}_k)^{C_k k_3} (\mathrm{Bo}_k/\mathrm{Ca}_k)^{-C_k k_2}$ against $\mathrm{Bo}/\mathrm{Ca}$ for $\mathrm{Fr}_{m,L}$ and $t^*_{m,L}$. The figure shows that for $\mathrm{Fr}_{m,L}$ and $t^*_{m,L}$, the trend for both characteristic length scales is similar for all values of $C_k$.

The relative influence of grain- and kaolin-scale phenomena increases with $\mathrm{Bo}/\mathrm{Ca}$ for $\mathrm{Fr}_{m,L}$ while the influence of both scales reduces with $\mathrm{Bo}/\mathrm{Ca}$ for $t^*_{m,L}$. More significantly, Figure 4.3b suggests that kaolin-scale surface tension effects are more influential to $\mathrm{Fr}_{m,d}$ and $\mathrm{Fr}_{m,h_0}$ than the driving forces at the column scale. Furthermore, Figure 4.3c shows that for $\mathrm{Fr}_{m,L}$, kaolin-scale phenomena are more influential than grain-scale phenomena while Figure 4.3f shows that for $t^*_{m,L}$, grain-scale phenomena are more influential than kaolin-scale phenomena. Logically, these effects are exaggerated by increasing $C_k$.

## 4.4    Conclusions and further work

A series of fully saturated, axisymmetric granular column collapse experiments using a fluid phase comprised of kaolin particles suspended in water were conducted to investigate the effects of a bimodal grain size distribution on acceleration phase drainage behaviour. The use of a geotechnical centrifuge allowed for a wide test parameter space where gravitational acceleration, inertial grain diameter, and the percentage of fines within the fluid phase could be varied during testing. A dimensionless parameter space consisting of 8 parameters, obtained using Buckingham's $\Pi$ theorem, was postulated to characterise acceleration phase collapse dynamics. The data gathered from the current series of tests was combined with the Newtonian fluid tests from a previous study and a non-linear, least squares fitting analysis was undertaken to investigate the influence of each dimensionless parameter on the four measured quantities of interest $Q$: $\mathrm{Fr}_{m,d}$, $\mathrm{Fr}_{m,h_0}$, $t^*_{m,d}$, and $t^*_{m,h_0}$. As was found for the Newtonian fluid test cases, all values of $Q$ scaled independently of each other and scaled with $Q = \left(\frac{\mathrm{Bo}}{\mathrm{Ca}}\right)^{k_1} \left(\frac{\mathrm{Bo}_k}{\mathrm{Ca}_k}\right)^{k_2 C_k} (\mathrm{Ca}_k)^{k_3 C_k} (\rho^*)^{k_4} (r^*)^{k_5}$ where $k_1$–$k_5$ are constants dependent on $Q$. Unlike the Newtonian fluid test case, the inclusion of kaolin particles appears to couple all $Q$ with kaolin-scale surface tension effects which, for the range of the $\mathrm{Bo}/\mathrm{Ca}$ values tested, was more influential to $\mathrm{Fr}_{m,d}$ and $\mathrm{Fr}_{m,h_0}$ than column-scale inertial and viscous forces. Future work involves considering the influence of a bimodal grain size distribution on the maintenance of excess pore pressures by conducting similar analyses for the reduction of fluid pressure at the base of the column over the duration of the collapse.

Chapter 5

# Continuum modelling of a just-saturated inertial column collapse: Capturing fluid-particle interaction

**Abstract**

*This work presents a simple two-phase flow model to analyse a series of axisymmetric granular column collapse tests conducted under elevated gravitational accelerations. These columns were prepared with a just-saturated condition, where the granular pores were filled with a Newtonian fluid up to the column's free surface. In this configuration, unlike the fully submerged case, air-water-grain contact angles may be important to flow dynamics. The interaction between a Newtonian fluid phase and a monodispersed inertial particle phase was captured by an inter-phase interaction term that considers the drag between the two phases as a function of the particle phase porosity. While this experimental setup has broad applications in understanding various industrial processes and natural phenomena, the focus of this study is on its relevance to predicting the motion of debris flows. Debris flows are challenging to model due to their temporally evolving composition, which can lead to the development of complex numerical models that become intractable. The developed numerical scheme in this study reasonably reproduces the particle-size and gravitational acceleration dependencies observed within the experimental runout and basal fluid pressure reduction data. However, discrepancies between the model and physical experiments primarily arise from the assumption of modelling the granular phase as a continuum, which becomes less appropriate as particle size increases.

---

Chapter 5: Continuum modelling of a just-saturated inertial column collapse:
Capturing fluid-particle interaction

# 5.1 Introduction

Granular-fluid flows have emerged as a prominent area of scientific inquiry, owing to their extensive prevalence in both industrial and natural contexts (Warnett et al., 2014). In this current study, our research focuses on a subset of natural granular mass movements that fall under the classification of gravity-driven landslides (Jakob et al., 2005). Notably, we direct our attention towards one specific type known as debris flows, which pose significant threats to communities and infrastructure situated in mountainous regions worldwide (Delannay et al., 2017). Particularly in developing countries, population exposure to such hazards is on the rise (Nadim et al., 2006). Despite past scientific attention, the increasing frequency and intensity of flow triggering events, such as periods of high rainfall intensity (e.g. Redshaw et al., 2019; Rodolfo et al., 2016), melting of glaciers and permafrost (e.g. Allen et al., 2016; Sati, 2022) and, production of wildfires (e.g. Grimsley et al., 2016; Oakley et al., 2018), occurring near urban areas, make it imperative to gain a deeper understanding of the underlying mechanics governing debris flow behaviour.

Numerical modelling plays a vital role in the prediction and formulation of effective mitigation strategies for debris flows. The complex nature of debris flows, with comparatively high fluid volume fractions (Pierson, 2005) and wide particle size distributions (Turnbull et al., 2015), presents challenges not present in other gravity-driven mass movements. As a result, both the fluid and solid phases, as well as their inter-phase interaction, significantly influence macro-scale flow behaviour (Iverson, 1997). To develop models that can approximate field-scale flow conditions, it is necessary to adopt an idealised flow rheology. This simplification enables the formulation of tractable models that can yield valuable insights into debris flow dynamics.

Debris flows have most commonly been modelled as a single, homogeneous granular-fluid (e.g. Takahashi, 1981; Takebayashi and Fujita, 2020). Another approach is to treat the fluid and granular material as separate continuum phases coupled by a phase interaction term (e.g. Berzi and Jenkins, 2008; Iverson, 1997; Iverson and Denlinger, 2001). To simplify computations, depth averaged equations are commonly used to describe the conservation relations of the phases and the bulk flow. These equations were originally derived under the assumption of a homogeneous density profile (Savage and Hutter, 1989). However, this approach overlooks the fact that the solid volume fraction varies spatially and temporally, which contributes to the diverse range of rheological behaviours observed in mass movement events, including the development of excess

pore pressures (Iverson, 2003). Field observations (e.g. McArdell et al., 2007; McCoy et al., 2010) and large-scale testing (e.g. Johnson et al., 2012) have well-documented this fact.

More recent models have sought to increase the complexity in which the two phases can be modelled separately. Some models (e.g. Iverson and George, 2014; Pitman and Le, 2005) describe how the interactions between the granular and fluid phases alter flow dynamics. Iverson and George (2014) do this through the generation and dissipation of excess pore pressures, while maintaining a heterogeneous flow profile by not allowing the two phases to separate. Kowalski and McElwaine (2013) described each phase using separate mass equations but a single momentum equation. Gray and Kokelaar (2010) achieved separation between two phases in a similar way but focussed on particle size segregation by considering two granular phases of differing particle size instead. Further phase separation has been achieved in other models (e.g. Bouchut et al., 2017; Meng et al., 2022) by describing each phase with its own mass and momentum equation.

While these recent models represent a significant improvement over earlier efforts, the diversity of modelling strategies discussed demonstrates that there is no consensus on the most appropriate way to efficiently model these two-phase flows, and that different approaches can inform us about different aspects of a flow. Additionally, these models only account for debris flows with uniform particle sizes. However, as stated by Iverson (1997), and more recently demonstrated experimentally, many aspects of macro-scale flow behaviour, such as flow mobility (de Haas et al., 2015), bed erosion (Roelofs et al., 2022), and the accumulation and dissipation of excess pore pressures (Kaitna et al., 2016), are highly dependent on the grain size distribution of the flow, particularly the amount of fine, silt, and clay material present. Consequently, current numerical methods do not allow the micro-scale effects from the inclusion of fine granular material to influence macro-scale flow behaviour.

One possible approach to incorporate micro-scale effects is to include them in the interphase interaction term so that they can impact the pore-scale. In this study, we aim to explore the potential of this method by examining the extent to which micro-scale effects can be accurately reproduced in the macro-scale flow behaviour of a simplified experimental flow.

In particular, the unsteady collapse of a granular column has been a widely utilised test configuration in the last two decades to examine how the column's initial geometry and composition influence its dynamics (e.g. Bougouin and Lacaze, 2018; Cabrera and Estrada, 2019; Lajeunesse et al., 2004; Lube et al., 2004; Thompson and Huppert, 2007).

For the case of a dry granular collapse, where many controlling parameters exhibit scale-invariance, scaling relationships from laboratory-scale experiments have been linked to geophysical granular flows (Delannay et al., 2017). However, the inclusion of a fluid phase within the granular mixture introduces a stress-dependent grain-fluid interaction (Iverson, 2015), causing the force ratios in laboratory-scale experiments to deviate from those in large-scale geophysical flows (Heller, 2011). Achieving dynamic similarity in the crucial pore pressure control processes of the flow can be attained by artificially increasing the effective gravitational acceleration through centrifugation, as demonstrated by Webb et al. (2023b)[†] in their study of axisymmetric fluid-saturated granular column collapses.

## 5.2    Experimental configuration

Webb et al. (2023b)[†] performed experiments using the experimental setup illustrated in Figure 5.1, which was attached to the arm of a geotechnical beam centrifuge. The experiments involved the rapid release of a granular-fluid mixture consisting of monodispersed spherical glass beads and a Newtonian water-glycerol mixture that was initially confined within a partially filled steel cylinder. It is worth noting that, while a polydispersed granular composition would have more accurately represented the composition of geophysical flows, the chosen simplification offers advantages in terms of analysing and comparing the experimental data. Furthermore, this simplification substantially reduces the complexity of the numerical model employed in attempts to replicate the collapse behaviour.

The mixture was just-saturated and allowed to spread on a horizontal plane under the influence of a prescribed gravitational acceleration $G$ governed by the rotation rate of the centrifuge. The radius of the steel cylinder $r_0$ and the initial height of both the granular and fluid phases $h_{v,0}$, where $v = p, f$ corresponds to the particle and fluid phases, respectively, were equal and held constant (i.e. $h_{p,0} = h_{f,0} = h_0$). This resulted in a column aspect ratio $a_0 = h_0/r_0 \approx 0.93$ while the particle size $d_p$, gravitational acceleration $G$, and fluid viscosity $\eta_f$ were varied systematically to explore a wide parameter space. $\eta_f$ was held constant for each test conducted at a given $G$, making the study primarily focused on the influence of $d_p$ and $g$ on collapse dynamics.

The study conducted by Webb et al. (2023b)[†] recorded the entire evolution of each collapse within the measurement area using two high-speed cameras. Snapshots at dif-

---

[†]Webb et al. (2023b) is shown in Chapter 3
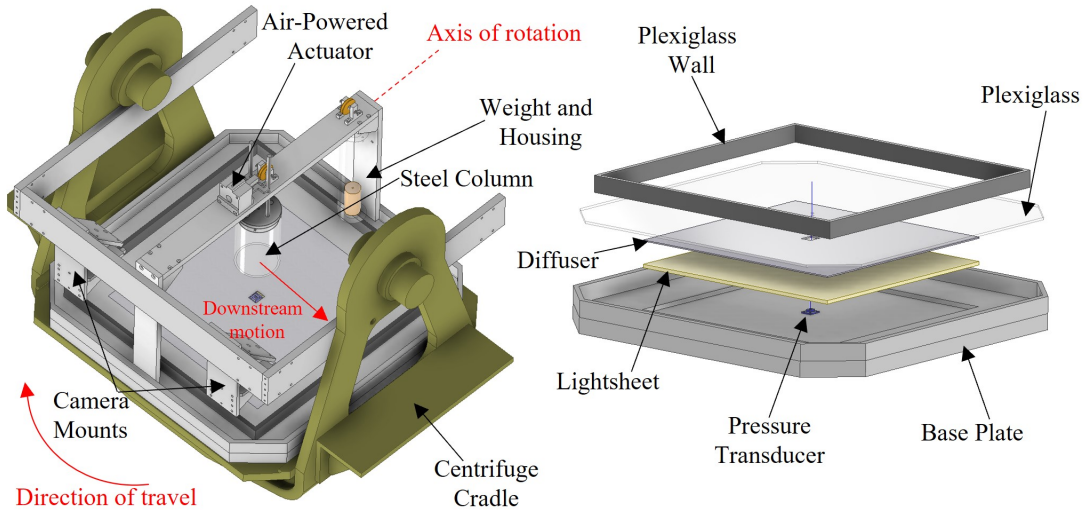
Figure 5.1: The axisymmetric collapse apparatus used by Webb et al. (2023b)[†].
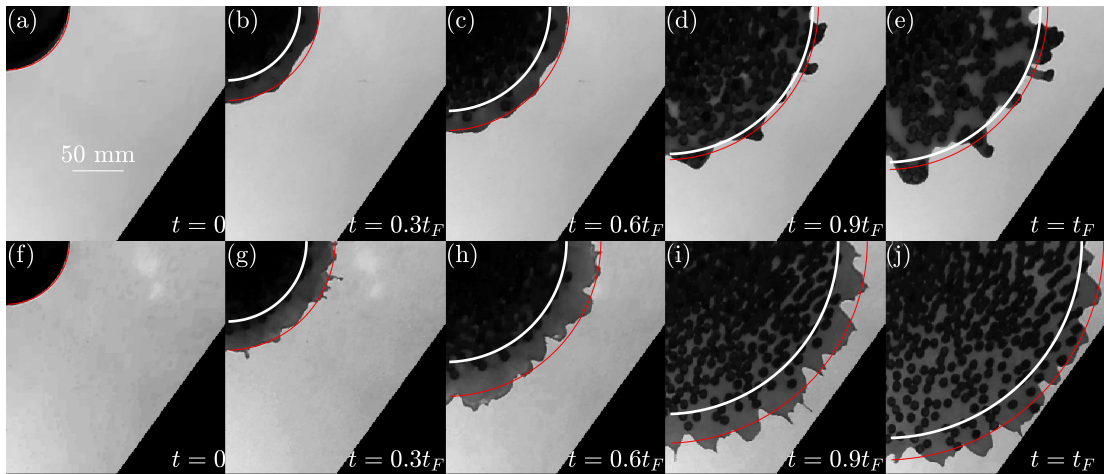


Figure 5.2: Snapshots of the collapse sequence downstream of centrifuge motion for two columns, both with $d_p = 8\,\text{mm}$, with **(a)-(e)** $G = 9.81\,\text{m}\,\text{s}^{-2}$ and **(f)-(j)** $G = 137.64\,\text{m}\,\text{s}^{-2}$ from Webb et al. (2023b)[†]. The averaged radial position of the fluid (red) and particle (white) phase fronts are shown.

ferent times $t$ from two recorded collapses are depicted in Figure 5.2, where the end of the recorded collapse period is denoted as $t_F$ (see Webb et al., 2023b[†] for details). A multi-threshold image analysis scheme was employed to track the average radial position of both the fluid and granular fronts throughout each collapse. Furthermore, a pressure transducer placed at the centre of the steel cylinder below the column allowed the authors to record the evolution of the basal fluid pressure at this location.

The objective of this study is to develop a numerical model that can reproduce the $d_p$- and $G$-dependent behaviour observed in these granular-fluid mixture collapses. The model's accuracy will be evaluated by comparing predicted time series of runout, velocity, and basal fluid pressure with the experimental data. To simplify the analysis, all radial experimental quantities discussed will be presented as the average of upstream and downstream values. This approach is adopted due to the minimal variation observed in the collapse behaviour between the two directions, attributable to the Coriolis accelerations and the Eötvös effect[††] commonly encountered in centrifuge modelling (Taylor, 1995).

## 5.3   Modelling

### 5.3.1   Depth averaged equations

[*]A schematic representation of the numerical model used to replicate the flow dynamics observed in the experiments is illustrated in Figure 5.3. The model depicts the motion of distinct granular and fluid continuum phases with specific densities $\rho_v$, where, again, $v = p, f$ corresponds to the particle and fluid phases, respectively, spreading across a horizontal plane. The model takes into account the separate influences of gravitational and basal drag forces on the behaviour of the two phases, while their motion is tightly coupled through a phase interaction term.

Like many previous studies on gravity-driven multiphase flows (e.g. Bouchut et al., 2017; Kowalski and McElwaine, 2013; Meng et al., 2022), the current work will simplify the system of equations by depth averaging the flow to improve computational efficiency. This assumption is based on the following premises: (i) for the particle sizes considered, surface tension effects of the fluid can be disregarded (Webb et al.,

---

[†]Webb et al. (2023b) is shown in Chapter 3

[††]See Chapter 6 for the definitions and a detailed analysis of the influence of Coriolis accelerations and the Eötvös effect on collapse dynamics

[*]See Appendix C for a derivation of the model from continuum mixture theory
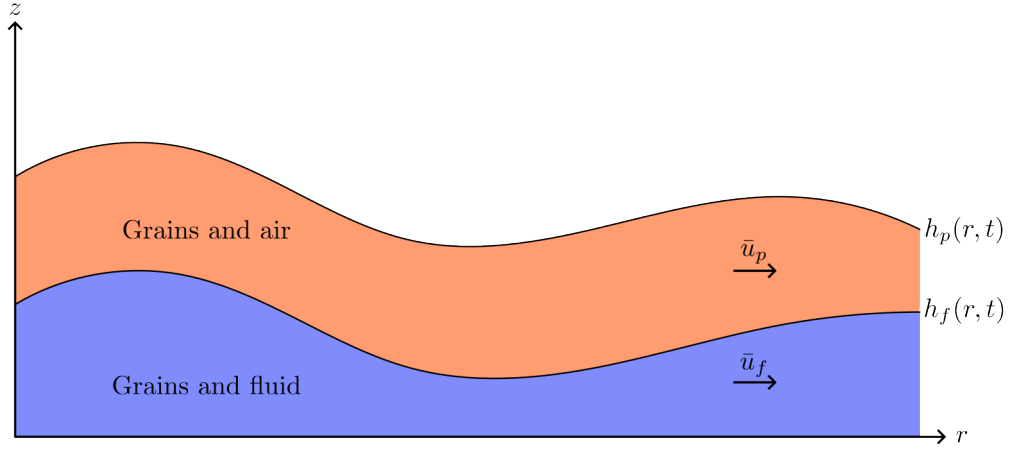
Figure 5.3: Sketch of a 2-D slice of an undersaturated granular collapse modelled as two coupled continuum phases.

2023b)[†]; (ii) the generation of excess pore pressures is eliminated through the exclusion of fine materials from the granular phase (Kaitna et al., 2016) and the small scale of the modelled flow (Iverson, 2015); and (iii) the shallow depth of the flow results in negligible accelerations perpendicular to the main direction of motion. The validity of the last assumption will be discussed in Section 5.3.4, given the initial configuration of the granular-fluid mixture before the collapse.

Given the simplicity of the experimental flow, and in the interest of computational efficiency, it was deemed reasonable to model the motion of the flow in an axisymmetric coordinates system by only considering one lateral spatial dimension $r$ and the vertical spatial dimension $z$. The nature of the experiment being modelled, and the range of particle sizes used, allows for the further assumption of an always exactly saturated or undersaturated granular phase (i.e. $h_f \leq h_p$). By employing the conversion process outlined in Appendix C, the original unified system of equations proposed by Meng et al. (2022) is transformed into a revised set of equations. These constitute a system of depth-averaged mass and momentum conservation equations describing the evolution of the phase thickness $h_v(r, t)$ and the depth-averaged phase velocity $\bar{u}_v(r, t)$ in an undersaturated granular flow

$$\partial_t h_p + \partial_r(h_p \bar{u}_p) = -\frac{h_p \bar{u}_p}{r}, \tag{5.1}$$

$$\partial_t h_f + \partial_r(h_f \bar{u}_f) = -\frac{h_f \bar{u}_f}{r}, \tag{5.2}$$

---

[†]Webb et al. (2023b) is shown in Chapter 3

Chapter 5: Continuum modelling of a just-saturated inertial column collapse: Capturing fluid-particle interaction

$$\partial_t(h_p\bar{u}_p) + \partial_r\left(h_p\bar{u}_p^2 + \frac{1}{2}Gh_p^2\right) =$$
$$-\frac{h_p\bar{u}_p^2}{r} - \mu_b\frac{\bar{u}_p}{|\bar{u}_p|}Gh_p\left(1 - \gamma^*\frac{h_f}{h_p}\right) + \frac{\eta_f\phi_f^2}{\rho_p\phi_p k}\min(h_f, h_p)(\bar{u}_f - \bar{u}_p), \quad (5.3)$$

$$\partial_t(h_f\bar{u}_f) + \partial_r\left(h_f\bar{u}_f^2 + \frac{1}{2}Gh_f^2\right) = -\frac{h_f\bar{u}_f^2}{r} + \frac{\eta_f\phi_f}{\rho_f k}\min(h_f, h_p)(\bar{u}_p - \bar{u}_f), \quad (5.4)$$

for the particle and fluid phases, respectively, where $\phi_v$ is the phase volume fraction which is assumed to be constant for both phases and obey the relation $\phi_f = 1 - \phi_p$. $G$ is the gravitational acceleration acting parallel to the $z$-direction, $\mu_b$ is the basal friction coefficient, $\gamma^*$ is the density ratio between the two phases such that $\gamma^* = \rho_f/\rho_p$, and $k$ is the permeability of the granular phase where $k = (\phi_f^3 d_p^2)/(180\phi_p^2)$ as defined by Carman's equation (Pailha and Pouliquen, 2009) which has been shown to agree well with studies investigating the dynamics of sediments and bed-load transport (Goharzadeh et al., 2005; Ouriemi et al., 2009). The influence of particle size on the dynamics is incorporated within the permeability term.

Consistent with previous studies (e.g. Bouchut et al., 2017; Meng et al., 2022), we assume that $\phi_p$ corresponds to a critical solid volume fraction $\phi_c$, which we take to be the average solid volume fraction of the granular material before collapse. Accordingly, we set $\phi_p = \phi_c = 0.61$ and $\phi_f = (1 - \phi_c) = 0.39$. While acknowledging that the assumption of a constant $\phi_v$ is not valid during the later stages of the collapse (as depicted in Figure 5.2), it serves as a reasonable simplification for the initial acceleration phase when the column is predominantly undergoing free-fall. To further improve computational efficiency, we approximate the $\bar{u}_p/|\bar{u}_p|$ term in Equation (5.3) with $\tanh(\bar{u}_p/u^*)$, where $u^* = 10^{-3}\,\mathrm{m\,s^{-1}}$ is a velocity scale below which the granular friction is approximated as viscous. Finally, we set $\mu_b$ to 0.8 where we discuss the rationale for this value in Section 5.3.4.

## 5.3.2 Behaviour of the model in limiting cases

The model can be reduced to the familiar case of a singular granular phase by taking $h_f = 0$. On the other hand, if the limit $h_p = 0$ is applied, we obtain a similar solution describing the motion of a singular fluid phase. However, since $\phi_f = 1 - \phi_p$ and $\phi_p$ is a constant, the volume of fluid per unit azimuthal angle predicted by the model would be inexact. Hence, for flow cases where both phases are present, regions of the flow that are comprised of only the fluid phase will be volumetrically incorrect. We can avoid this

issue for the case of a purely fluid column collapse by setting $\phi_f = 1$ as in Section 5.3.4.

In the case of a two-phase system, given that the interaction force between the phases remains finite, as $k \to 0$, $\bar{u}_p \to \bar{u}_f$ for all $t$. This implies that for the initial configuration of the physical experiments conducted by Webb et al. (2023b)[†], which corresponds to a granular material that is just saturated, it is possible to say that $h_p = h_f = h(r,t)$. Therefore, by multiplying the mass and momentum continuity equations of each phase by their respective densities, $\rho_v$, and then summing the results, the model reduces to the equations of motion for a single phase.

Another interesting limiting case is when we consider the drainage of the fluid phase out of a low permeability static granular phase by setting $\bar{u}_p = 0$ and assuming $k$ is small. The resulting model describes the motion of a slow fluid whose momentum depends only on the fluid pressure gradient and the phase interaction force. This system can be written as follows

$$\partial_t(h_f) + \partial_r(h_f \bar{u}_f) = 0, \tag{5.5}$$

$$\partial_r\left(\frac{1}{2}Gh_f^2\right) = \frac{\eta_f \phi_f}{\rho_f k}h_f(-\bar{u}_f). \tag{5.6}$$

Rearranging Equation (5.6) for $\bar{u}_f$ and substituting the result into Equation (5.5), we reassuringly recover the vector form of the Dupuit-Boussinesq aquifer flow relation (e.g. Guérin et al., 2014)

$$\phi_f \partial_t(h_f) = \frac{1}{2}G\frac{\rho_f k}{\eta_f}\nabla^2(h_f^2) = \frac{K}{2}\nabla^2(h_f^2), \tag{5.7}$$

where $K = (G\rho_f k)/\eta_f$ is the hydraulic conductivity of the granular phase.

### 5.3.3 Numerical method

The spatial discretisation of Equations (5.1)–(5.4) was carried out using the second-order central-upwind scheme developed by Kurganov and Petrova (2007) for solving the Saint-Venant system of equations. A $0.5\,\mathrm{m}$ test domain was discretised into 1000 cells, resulting in a cell width $\Delta r = 5 \times 10^{-4}\,\mathrm{m}$. Given that the column expands into regions where no grains are initially present, it was important to ensure that the model was positivity preserving, i.e., capable of handling the transition between cases where $h_v \neq 0$ and $h_v = 0$ (Bouchut et al., 2017). To achieve this, the more sophisticated cell boundary depth correction algorithm of Chertock et al. (2015) was employed. An

---

[†]Webb et al. (2023b) is shown in Chapter 3

explicit second-order Runge-Kutta method was implemented to discretise the system in time. To ensure the stability of the scheme, a CFL number of 0.2 was used. The system's phase data was stored at time intervals $\Delta t = 1 \times 10^{-3}$ s.

### 5.3.4 Regularisation of vertical velocity components

To begin to assess the validity of the model, we start by conducting a comparison with the experimental findings for a single fluid phase only collapse (i.e. $\phi_f = 1$ and $\phi_p = 0$). For the numerical model, we define the instantaneous phase front position $r_v(t)$ as the largest radial distance where $h_v(r, t) > 0.1$ mm while the definition for the experimental case remains the same as in Webb et al. (2023b)[†]. Similarly, we introduce the normalised phase runout length $r_v^*$, defined as the normalised difference between the instantaneous position of the phase front and the initial column radius $(r_v - r_0)/r_0$.

A comparison of the numerical and experimental temporal evolution of $r_f^*$ for purely fluid columns across all tested values of $G$ is visualised in Figure 5.4. In the experimental case, the visibility of the collapsing column is initially obstructed by the steel cylinder used to construct it, causing a delay between the release of the column and the captured motion of the phase fronts in the camera footage. To address this issue, the numerical evolution of $r_f^*$ has been shifted to align with the experimental signal by setting the $r_f^*$ at $t = 0$ for the numerical signal to the $r_f^*$ for the experimental signal at $t = 0$ for each respective collapse test. This alignment approach was compared against the manual determination of the cylinder's release time by analysing the collapse images. The comparison indicated that both methods yielded similar results in terms of the magnitude of the temporal offset. However, unlike the fitting approach, manually identifying the release time of the column was prone to human error, which could introduce significant variations in the magnitude of the temporal offset. This was more of an issue for the higher $G$ tests where the duration of the collapses are relatively short compared to the frequency of image capture, which remained constant and, therefore, independent of the applied gravitational force.

It is evident from Figure 5.4 that the velocity of the fluid phase front in the numerical model is significantly higher than that observed in the corresponding experimental data at all values of $G$. This is to be expected since the initial configuration of the fluid columns does not meet the shallow depth assumption crucial to the model's derivation, namely $a_0 \ll 1$ does not hold, and Equations (5.3) and (5.4) do not incorporate terms

---

[†]Webb et al. (2023b) is shown in Chapter 3
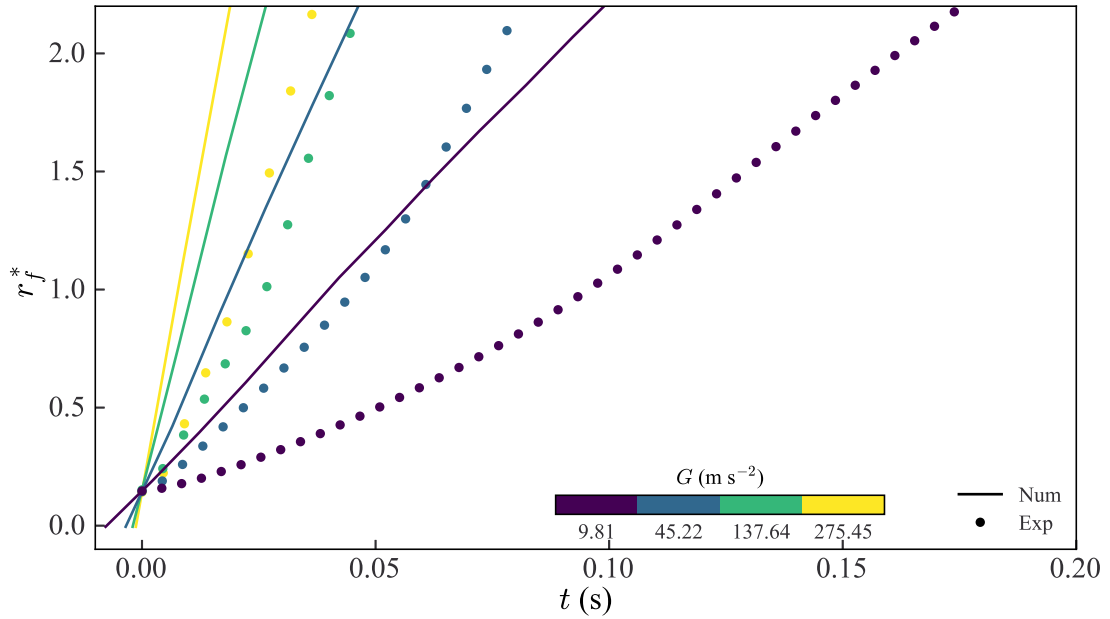
Figure 5.4: Comparison of the numerical and experimental temporal evolution of the normalised average fluid runout length $r_f^*$ with time $t$ for purely fluid column collapses for all values of $G$.

accounting for the vertical acceleration of the two phases or their subsequent dissipation upon impact with the horizontal plane (Larrieu et al., 2006). We note that, if a Chézy style basal drag term were added for the fluid phase, it would decelerate the simulated fluid phase front, whereas the experimental fluid fronts accelerate over the spreading distances considered.

In order to address this issue, we implemented the mass 'raining' scheme as described in Larrieu et al. (2006). Originally designed for a singular granular phase, the scheme divides the flow into two distinct components. The first component consists of a shallow layer of material that spreads horizontally, with a height smaller than that of the experimental column being simulated. The second component, known as the 'rain', is gradually introduced to the flow over a specific duration equivalent to the free-fall of the column. By incrementally adding mass, the injected potential energy into the modelled system is significantly reduced compared to the potential energy of the complete column. Consequently, the effects of energy dissipation during the collapse can be mimicked in the model.

In our study, we extend the application of this scheme to both the granular and fluid phases. The adjusted initial configuration of each phase, denoted as $v = p, f$, can be characterised by its initial radius $r_0$, and initial height $h_{v,1} = C_r r_0$. Thus, the progressive

Chapter 5: Continuum modelling of a just-saturated inertial column collapse:
Capturing fluid-particle interaction

supply of mass to the flowing material in each phase is quantified using a phase-specific volume flux per unit area

$$q_v(r,t) = \begin{cases} Gt & \text{for } 0 \leq r \leq r_0, \\ 0 & \text{for } r > r_0, \end{cases} \tag{5.8}$$

up to a time related to the free-fall of the specific column phase $t_{v,ff} = \sqrt{2(h_{v,0} - h_{v,1})/G}$. Accordingly, the mass conservation Equations (5.1) and (5.2) become

$$\partial_t h_p + \partial_r(h_p \bar{u}_p) = -\frac{h_p \bar{u}_p}{r} + q_p, \tag{5.9}$$

$$\partial_t h_f + \partial_r(h_f \bar{u}_f) = -\frac{h_f \bar{u}_f}{r} + q_f. \tag{5.10}$$

for the fluid and particle phases, respectively. Following Larrieu et al. (2006), no source term was added to the momentum equations, as it is assumed that the mass is added with no horizontal momentum (i.e. in a state of free-fall).

A comparison between the temporal evolution of $r_f^*$ for purely fluid columns at all tested values of $G$ for both numerical models and the experimental data is shown in Figure 5.5. For the numerical model utilising Larrieu et al.'s (2006) mass rainfall scheme (i.e. mass conservation Equations 5.9 and 5.10), the value of $C_r$ has been varied.

As in Figure 5.4, the numerical evolution of $r_f^*$ has been offset from the experimental signal to ensure that $r_f^*$ at $t = 0$ for both signals is equal for each respective collapse test. Firstly, The temporal evolution of $r_f^*$ by the numerical model employing the mass rainfall scheme matches the results of the original scheme when $C_r = 0.93$ (see Figure 5.5). This is because, when $C_r = a_0$, $h_{v,0} = h_{v,1}$ resulting in no mass being added to the initial system as $t_{v,ff} = 0$. It is also shown that adjusting the phase mass conservation equations significantly improves the agreement between the model and experiments regardless of the value of $C_r$. To ensure consistency, a $C_r$ value of 0.05 is used from this point on as it provides the best compromise for simulating tests at all $G$ levels. Larrieu et al. (2006) found that using $C_r \leq a_0$ had no effect on the long-term spreading dynamics of the collapse. Therefore, the range of $C_r$ values considered here only affects short-term spreading dynamics.

Finally, we adopt the assumption that $\mu_b = 0.8$ based on the coefficient determined by Larrieu et al. (2006) who used it to reproduce the runout scaling laws proposed in previous works (Lube et al., 2005, 2004) for a dry axisymmetric granular column col-
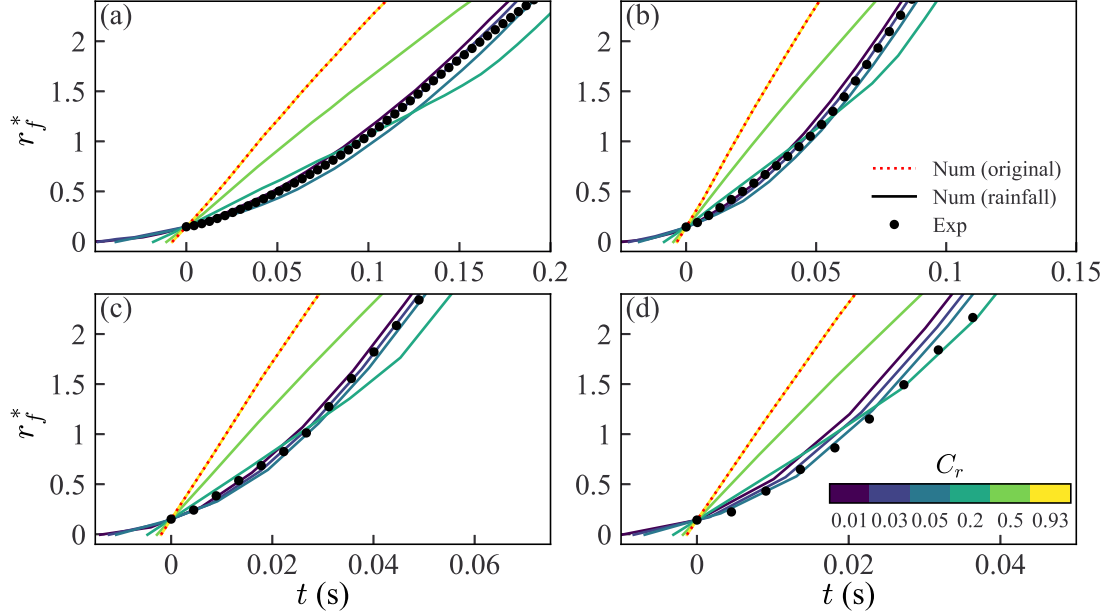
Figure 5.5: Comparison of the two numerical schemes, the original and the one now utilising the mass introduction scheme of Larrieu et al. (2006), and experimental temporal evolution of the normalised average fluid runout length $r_f^*$ with time $t$ for purely fluid column collapses with varying values of $C_r$ for **(a)** $G = 9.81\,\mathrm{m\,s^{-2}}$, **(b)** $G = 45.22\,\mathrm{m\,s^{-2}}$, **(c)** $G = 137.64\,\mathrm{m\,s^{-2}}$ and **(d)** $G = 275.45\,\mathrm{m\,s^{-2}}$.

lapse (where $\phi_f = 0$ and $\phi_p = 1$). This coefficient is notably high and may be attributed to the lack of consideration of interior flow dissipation mechanisms in shallow water models.

## 5.4 Calibration assessment

### 5.4.1 Runout

After tuning the model parameters using purely fluid collapse test data, we proceed to evaluate the model's ability to describe the collapse of granular-fluid mixtures by comparing the temporal evolution of $r_f^*$ and $r_p^*$ with experimental results for all values of $d_p$ and $G$.

By considering the pre-collapsed column configuration, we can characterise the modelled system using both dimensionless parameters, $\gamma^*$ and $a_0$, and three dimensional parameters, $G$, $h_0$ and $\eta_f/(\rho d_p^2)$, where $\rho$ represents the effective column density $\rho =$

$\phi_p\rho_p + \phi_f\rho_f$ (Webb et al., 2023b)[†]. These dimensional parameters can be combined to yield another dimensionless group, denoted as $B = (Gd_p^4\rho^2)/(h_0\eta_f^2)$, which is analogous to the square of the ratio of the column Bond Bo and Capillary Ca numbers $(\text{Bo}/\text{Ca})^2$. Webb et al. (2023b)[†] found Bo/Ca to be a key parameter in the prediction of the maximum phase front velocity.

Considering that $a_0$ remains constant and $\gamma^*$ exhibits only minor variations of approximately 8% across the parameter space under investigation, we plot the runout evolution of the numerical simulations in dimensionless $r_v^* - t_{h_0}^*$ space. Here, $t_{h_0}^*$ represents the ratio between $t$ and the characteristic column inertial timescale $\sqrt{h_0/G}$. This approach yields a family of curves primarily determined by the value of $B$ (Figure 5.6). Specifically, when $B \ll 1$, it corresponds to tightly coupled grains and fluid, wherein the collapse is governed by drag forces. On the other hand, when $B \gg 1$ it indicates nearly independent behaviour between the grains and fluid phases.

To ensure consistency, we have, again, offset the numerical time signal from the experimental time signal. Both the fluid and particle phases have been offset by the same time period, such that their $r_f^*$ values are equal at $t_{h_0}^* = 0$. This strategy enables the numerical fluid and particle runout time series to remain in phase.

The overall evolution of a collapsing mixture, previously reported by Webb et al. (2023b)[†] and many other authors (e.g. Leonardi et al., 2021; Ng et al., 2018), is successfully replicated in the model (Figure 5.6). The collapse consists of acceleration, quasi-steady, and retardation stages, with the duration of each stage primarily controlled by $G$, with each stage duration decreasing as $G$ increases. The simulations also partially reproduce the particle-size-dependent (i.e. pore space dependent) behaviour observed in the experiments. Specifically, the model incorporates a permeability-dependent interaction term in Equations (5.3) and (5.4) to exhibit the effects of granular capillarity, resulting in the fluid phase front of a collapse containing a coarser particle phase (i.e. larger $d_p$) achieving higher peak velocities and separating itself further from the particle phase front (Webb et al., 2023b)[†].

The runout distances predicted by the model for both phases overestimate those measured experimentally for every test case. However, it is evident that, for a given $G$, the performance of the model improves as $d_p$ decreases. Given that the volume of the granular phase is constant across all of the experiments, this is likely due to the collapses with a granular phase consisting of smaller particles, containing more particles. Hence, it is more appropriate to model the granular phase as a continuum. Moreover, the model's

---

[†]Webb et al. (2023b) is shown in Chapter 3
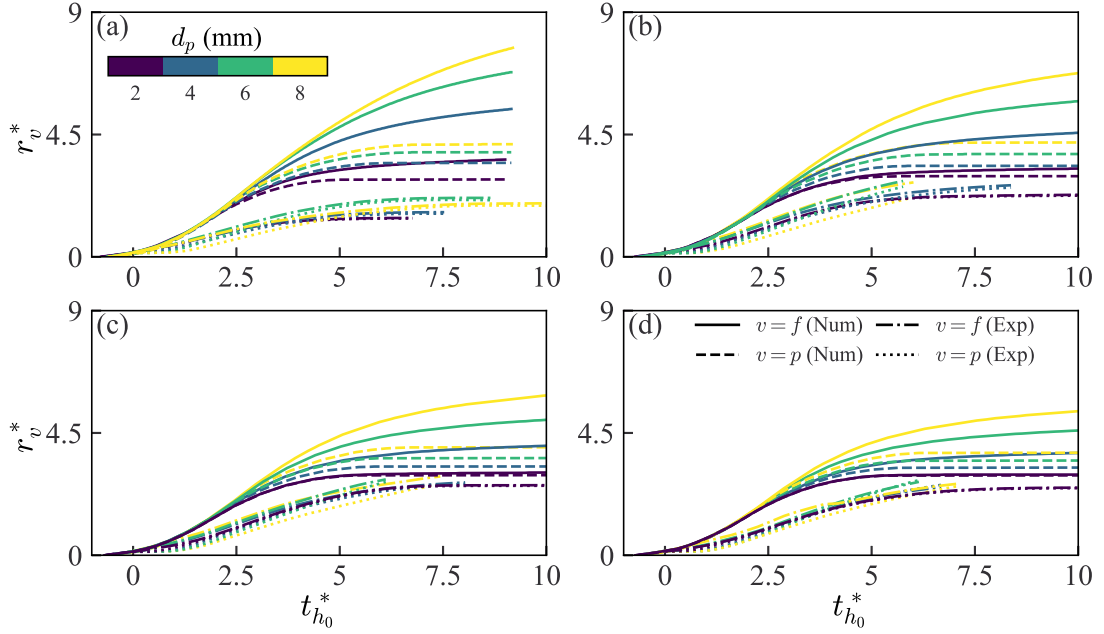
Figure 5.6: Comparison of the numerical and experimental temporal evolution of the normalised phase runout length $r_v^*$ with normalised time $t_{h_0}^*$ for collapses containing a particle phase at (a) $G = 9.81\,\mathrm{m\,s^{-2}}$, (b) $G = 45.22\,\mathrm{m\,s^{-2}}$, (c) $G = 137.64\,\mathrm{m\,s^{-2}}$ and (d) $G = 275.45\,\mathrm{m\,s^{-2}}$.

prediction of the final runout and the temporal evolution of the particle phase improves as $G$ increases. This is because capillary interaction between particles becomes less significant as the particle inertia increases with $G$ (Iverson, 2015). We do not model capillary interactions, hence model and experiment become more closely matched at higher $G$.

The omission of capillary forces likely contributes to the significant overestimation of the separation between the phase fronts during the collapse. To address this effect, it would be worthwhile to explore the incorporation of the Capillary number Ca into the phase interaction term, as a means to consider the influence of grain-scale surface tension effects (Webb et al., 2023b)[†]. However, investigating this aspect is beyond the scope of the present study.

Additionally, the assumption of a constant fluid velocity profile with flow depth (i.e. plug flow), and the omission of a fluid drag term, does not consider the increased viscous stress imposed on the fluid by the horizontal plane as the fluid depth reduces, resulting in a more turbulent flow (Batchelor, 2000), which is the case during a significant portion of the collapse spreading stage. Nevertheless, the reduction in the separation

---
[†]Webb et al. (2023b) is shown in Chapter 3

between the two phases as $G$ increases is encouraging, suggesting that particle inertial (i.e. $d_p$) effects become less dominant with increased scale, given that the macro-scale dynamics of geophysical-scale debris flow behaviour are primarily driven by gravitational and viscous forces (Iverson, 1997).

### 5.4.2 Velocity

In this section, we compare the temporal evolution of the phase front velocity $u_v$ for both the experimental and numerical test cases. The normalised phase front velocity $u_{v,h_0}^* = u_v/\sqrt{h_0 g}$ is presented against $t_{h_0}^*$ for all collapses containing a particle phase and all values of $g$ in Figure 5.7 where, again, the numerical simulation for each test has been offset from the experimental data in the time domain. As discussed in Section 5.4.1, Figure 5.7 demonstrates that the experimental evolution of both phases throughout the collapses, for all values of $d_p$ and $G$, comprises three distinct stages of motion, including a steady state. In contrast, the simulated collapse fronts never appear to reach a steady state of motion. Similar to the temporal evolution of $r_v^*$, the peak velocities of the phase fronts observed in the experiments were lower than those predicted by the simulations for all test cases. Although the simulations reasonably modelled the time after collapse initiation when these peak velocities occur, they tended to be faster than those observed in the experiments. We attribute the discrepancies between the simulation and experimental results for the temporal evolution of $u_{v,h_0}^*$ primarily to the continuum modelling assumption and the resulting transfer and dissipation of granular momentum, particularly for larger particle sizes.

Analysing the collapses in $u_{v,h_0}^* - t_{h_0}^*$ space further highlights the interference of the steel column on the acceleration stage of the experimental collapses. A particle size-dependent lag, where the granular phase front begins to move, was observed for all values of $G$, and the magnitude of the lag increased with $d_p$. This result is due to the larger particle sizes being trapped by the rising column for longer since the speed at which the column is lifted is proportional to $G$. The lifting speed of the column was designed to comply with Sarlin et al.'s (2021) criterion, which defines a threshold lift velocity that prevents the release mechanism from influencing the dynamics of a collapsing dry granular phase. Contrary to the suggestion of Li et al. (2022), we found that this criterion cannot be lowered for a granular material in the initially just-saturated condition. Although increasing the mass of the counterweight used to lift the column could have achieved greater column lifting speeds, it would likely have an adverse effect
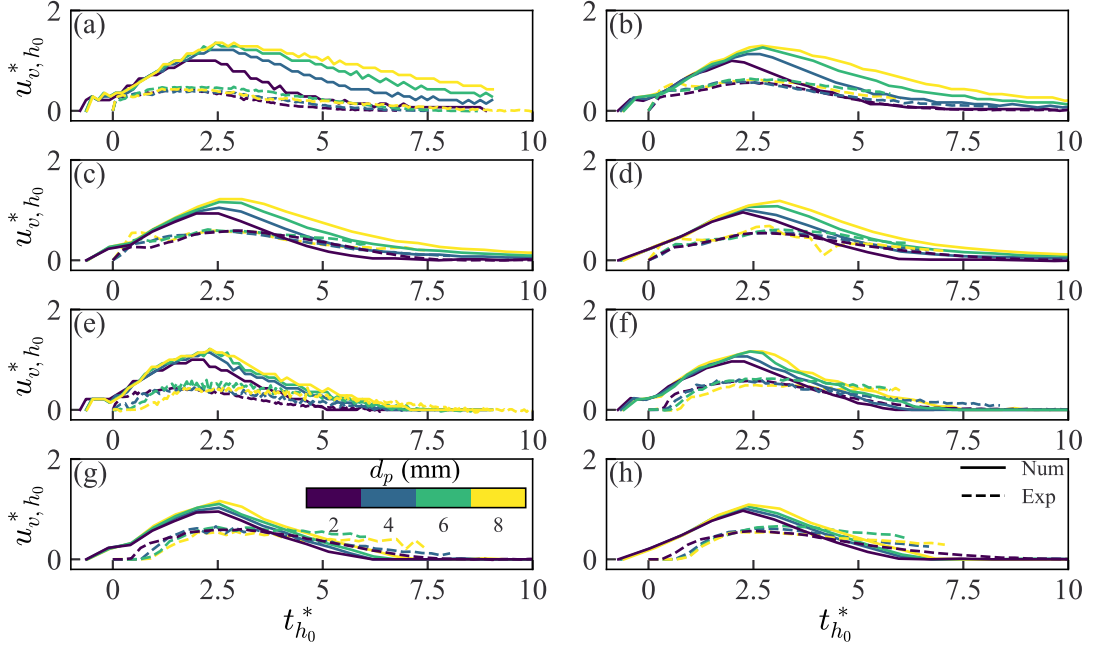
Figure 5.7: Comparison of the numerical and experimental evolution of the normalised phase front velocity $u^*_{v,h_0}$ with normalised time $t^*_{h_0}$ where (**a**)-(**d**) $v = f$ and (**e**)-(**h**) $v = p$ for collapses containing a particle phase at $G = 9.81\,\mathrm{m\,s^{-2}}$ [(**a**), (**e**)], $G = 45.22\,\mathrm{m\,s^{-2}}$ [(**b**), (**f**)], $G = 137.64\,\mathrm{m\,s^{-2}}$ [(**c**), (**g**)] and $G = 275.45\,\mathrm{m\,s^{-2}}$ [(**d**), (**h**)].

on the release of the granular material due to the increased viscous stresses induced between the inner walls of the cylinder and the saturated granular mixture. This effect is discussed in detail in Section 5.5.1.

Since the particle phase is initially held stationary by the rising column, the initial discharge of the fluid phase is highly dependent on the capillarity of the granular phase (i.e. $d_p$). Hence, the peak value of $u^*_{f,h_0}$ during the acceleration stage increases with $d_p$ at all values of $G$. As found by Webb et al. (2023b)[†], the dependency on $d_p$ is not as prominent at $G = 9.81\,\mathrm{m\,s^{-2}}$ as surface tension effects have a large influence on the initial fluid front velocity at low $G$. The influence of $d_p$ increases as $G$ increases to $45.22\,\mathrm{m\,s^{-2}}$ and begins to reduce for subsequent increases in $G$ as gravitational and viscous forces begin to dominate flow dynamics.

---

[†]Webb et al. (2023b) is shown in Chapter 3

## 5.5 Fluid pressure

With the model parameters calibrated to best match the experimental runout data, we will use these settings to predict the evolution of basal fluid pressure at the column's centre and compare it to the corresponding observations from the physical experiments.

### 5.5.1 Experimental pressure signal reduction

Upon collapse initiation, the significant acceleration of the steel cylinder relative to the initial motion of the collapsing mixture induces viscous shear stresses between the two surfaces that are capable of partially lifting the collapse material. This causes the fluid pressure being applied to the pressure sensor at the base of the column $P$ to drop and subsequently rise when the weight of the collapsing material overcomes the viscous shear stresses impeding its downward motion. This experimental discrepancy appears to have no influence on the pressure variation observed during the initial dilation of collapsing material containing a granular phase, which was investigated previously (Webb et al., 2023b)[†], as it occurs after the pressure spike associated with the dilative motion of the collapsing mixture and over a much longer timescale. The duration of this effect is largely dependent on the column composition. For purely fluid collapses, the column's influence dissipates $t \approx \sqrt{h_0/G}$ after collapse initiation. However, for collapses containing a granular phase, the effect is prolonged, and increases with decreasing $d_p$, due to the capillary action introduced by the presence of a granular matrix.

As these complexities are not indicative of an initially unconstrained collapse, and would not be replicated within the numerical model, the pressure time series for each test was reduced to remove these effects by only considering pressure data after which the collapsing mixture had lost contact with the steel column. This also limits the contribution of the flow's vertical acceleration on the pressure measurement. As was the case in Webb et al. (2023b)[†], only pressure data from the collapses undertaken at $G = 45.22 \, \mathrm{m\,s^{-2}}$ and $G = 137.64 \, \mathrm{m\,s^{-2}}$ were considered, as pressure measurements were not recorded for tests undertaken at $G = 275.45 \, \mathrm{m\,s^{-2}}$ and the pressure signals for tests where $G = 9.81 \, \mathrm{m\,s^{-2}}$ had significant signal-to-noise ratios. Unfortunately, the sensor was damaged during the test with $d_p = 2 \, \mathrm{mm}$ and $G = 137.64 \, \mathrm{m\,s^{-2}}$, and therefore had to be removed from the dataset.

In line with the previous work, a fourth-order low-pass Butterworth filter with a cut-

---

[†]Webb et al. (2023b) is shown in Chapter 3

off frequency $f_c = 100\,\mathrm{Hz}$ was employed to filter the pressure signal for each test. To determine the time at which the mixture no longer made contact with the steel column, multiple steps were taken. First, the pressure time series was normalised with respect to the hydrostatic pressure of the column before collapse $\mathcal{P} = \rho_f G h_{f,0}$ to obtain $P^* = P/\mathcal{P}$. Next, a surrogate signal was constructed that only included the data points corresponding to the last time when the signal was roughly equal to a constant $A_p$, where $A_p$ ranged from 0.001 to 0.99 in increments of 0.001. Consequently, the surrogate signal decreased between each data point and did not increase with time. By using a lower threshold value of $A_p = 0.3$, the largest difference in time between consecutive points in the surrogate signal was identified as the time during which the column lifting effects were significant. As a result, the start of the reduced signal was set as the first data point after this prolonged time difference. Finally, the endpoint of the reduced signal was identified as the start of the longest concurrent subsequence during which the dimensionless pressure gradient $P^*/t_{h_0}^*$, remained below the selected threshold gradient $B_p = 0.1$.

The normalised reduced pressure data was fitted to a three-parameter exponential curve

$$P^* = a_p \exp\left(-b_p t_{h_0}^*\right) + c_p, \tag{5.11}$$

where $a_p$, $b_p$, and $c_p$ are constants. This fitting procedure enables a trend to be extrapolated, which is useful for directly comparing the pressure time series of different collapse tests (see Figure 5.8). As the reduced signal began at an average normalised pressure of $P_r^* = 0.45 \pm 0.03$, we consider pressure trends up to $P^* = 0.5$. Given the satisfactory representation of the experimental data by the exponential fit, we henceforth refer to the fitted trend as the experimental data.

## 5.5.2 Numerical pressure signal reduction

Since the numerical model assumes shallow-water conditions, the basal fluid pressure at the centre of the column during the simulated collapse tests is determined by the equation $P = \rho_f G h_{f|r=r_0/2}$. The utilisation of Larrieu et al.'s (2006) mass 'raining' scheme results in the basal fluid pressure prior to collapse initiation $P_0 = C_r \mathcal{P}$. During the collapse tests, the injection of fluid phase mass into the system causes $P$ to increase gradually until it reaches a value of approximately $0.8\mathcal{P}$ at $t = t_{f,ff}$ before dissipating as expected for an unconstrained collapse. To enable a direct comparison between the model predictions and experimental findings, we only analysed the basal fluid pressure

Figure 5.8: The raw and fitted experimental temporal evolution of the reduced dimensionless basal fluid pressure at the centre of the column $P^*$ with time $t$ at (a) $G = 45.22\,\mathrm{m\,s^{-2}}$ and (b) $G = 137.64\,\mathrm{m\,s^{-2}}$.

data from each simulation starting from the time when $P = 0.5\mathcal{P}$ for the final time.

### 5.5.3 Definition of pressure reduction

Before comparing the numerical and experimental pressure time series, it is crucial to understand the constraints imposed by the data collection process on our analysis. Typically, the dissipation of fluid pressure is considered from a Lagrangian reference frame, where the time series records the evolution of pressure for a fixed 'packet' of the flow during collapse (Batchelor, 2000). This approach allows you to analyse how internal flow deformations, such as particle suspension and no suspension within the fluid phase, promote the generation or dissipation of non-hydrostatic pore pressures (Iverson, 2005).

However, in practical scenarios, recording pressure data from a Lagrangian reference frame is often unfeasible. Previous studies have addressed such challenges in natural flows by measuring the fluid pressure at a fixed location in the flow (Eulerian reference frame) and the height of the flow's free surface passing over that point $H$ (e.g. McArdell et al., 2007). By comparing the recorded pressure with the theoretical pressures of complete granular phase suspension ($\rho G H$) and sedimentation ($\rho_f G H$), an estimation of the amount of suspended granular material within the flow can be made.

In our study, the evolution of flow height cannot be determined from the test images, which prevents the consideration of excess pore pressures at the measurement location. However, we can assess the influence of excess pore pressures within the reduced pressure signal by calculating the timescale of slope-normal diffusion of excess pore-fluid pressure $(\eta_f H^2)/(kE)$, where $E$ is the elastic bulk modulus of the solid-fluid mixture, which is approximated as $E = 10^7$ Pa (Iverson, 2015). For our tests, the timescale values range from $10^{-5} - 10^{-3}$ s, which is at least two orders of magnitude smaller than the time at which the reduced pressure signal begins (approximately 0.08 s and 0.05 s after collapse initiation for tests at gravitational accelerations of $45.22 \, \mathrm{m\,s^{-2}}$ and $137.64 \, \mathrm{m\,s^{-2}}$, respectively). Therefore, it is reasonable to assume that all excess pore pressures have dissipated before the reduced pressure signal is captured. Consequently, the remaining fluid pressure component within the reduced signal can be assumed to be hydrostatic and dependent only on the height of fluid above the sensor location.

Based on these assumptions, and as described by the numerical model, the temporal evolution of the reduced pressure signal corresponds to the spreading of fluid away from the centre of the column. Thus, when referring to pressure reduction, we mean the reduction in hydrostatic pressure in the Eulerian reference frame due to the spreading of the fluid phase away from the pressure sensor.

### 5.5.4 Comparison of pressure reduction

The temporal evolution of the reduced normalised basal fluid pressure at the centre of the column $P^*$, obtained from the physical experiments, is shown in Figure 5.9. The figure indicates that, in general, for a given $G$, the rate of pressure reduction increases with increasing pore space (i.e. increasing $d_p$). Collapse tests that involve only a fluid phase, corresponding to an infinite pore space (or $d_p = 0$ mm), act as an upper bound for the experiments that contain a granular phase.

The collapses involving 8 mm particles may experience a lower rate of pressure reduction due to the column release mechanism. As shown in Figure 5.7, a substantial amount of fluid drained out of the granular skeleton while it was restrained by the column. This would lead to a higher initial pressure drop, resulting in a slower rate of reduction over the duration of the pressure signal under consideration.

In contrast, the residual value of $P^*$ at $t = 0.25$ s also exhibits a dependence on $d_p$ but, increases as $d_p$ decreases. This trend is likely attributable to the smaller pore spaces and increased capillary forces, which make it more difficult for the fluid to escape from
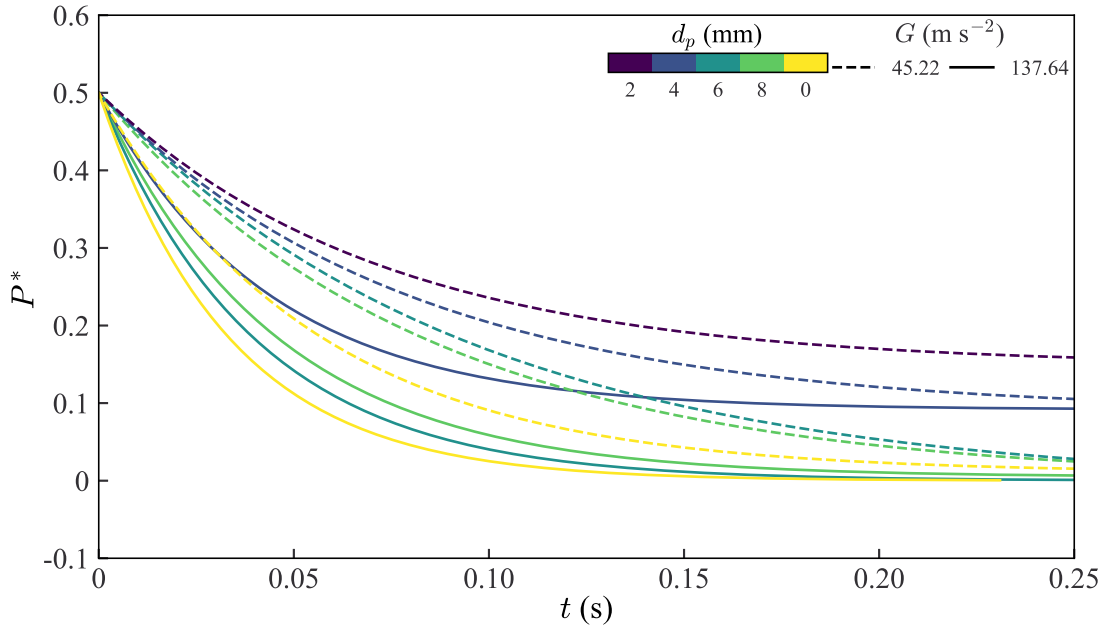
Figure 5.9: Experimental temporal evolution of the reduced dimensionless basal fluid pressure at the centre of the column $P^*$ with time $t$ for varying $d_p$ and $G$.

the granular phase, resulting in higher residual fluid pressures at the collapse centre. Conversely, for tests involving larger particle sizes (i.e. 6 and 8 mm), the residual pressure at the centre of the column approached 0, which was also the case for the pure fluid collapses.

Encouragingly, the patterns observed in the evolution of $P^*$ with $t$, as depicted in Figure 5.10, through the numerical model, display similar correlations with $G$ and $d_p$. The incorporation of a $d_p$-dependent interaction term leads to an increase in the rate of pressure reduction with increasing $d_p$, for a given $G$. Although the model forecasts residual pressures at $t = 0.25$ s that grow with decreasing $d_p$, they do not approach 0 for larger particle sizes. Additionally, in all scenarios, the residual pressure is overestimated by the model, likely due to the assumption of a continuous granular phase, which results in an overestimation of the magnitude of the interaction term and the selection of a high $\mu_b$ value, which was necessary to reduce the phase front velocities.

Comparison of the numerical simulations to the experimental results by constraining $G$, as shown in Figure 5.11, demonstrates that in all cases, similar to the temporal evolution of $u^*_{v,h_0}$, the predicted rate of pressure reduction by the model is higher than that observed in the experiments. It is probable that this inconsistency is mainly due to the assumption of a hydrostatic pressure distribution and neglecting the vertical accelera-
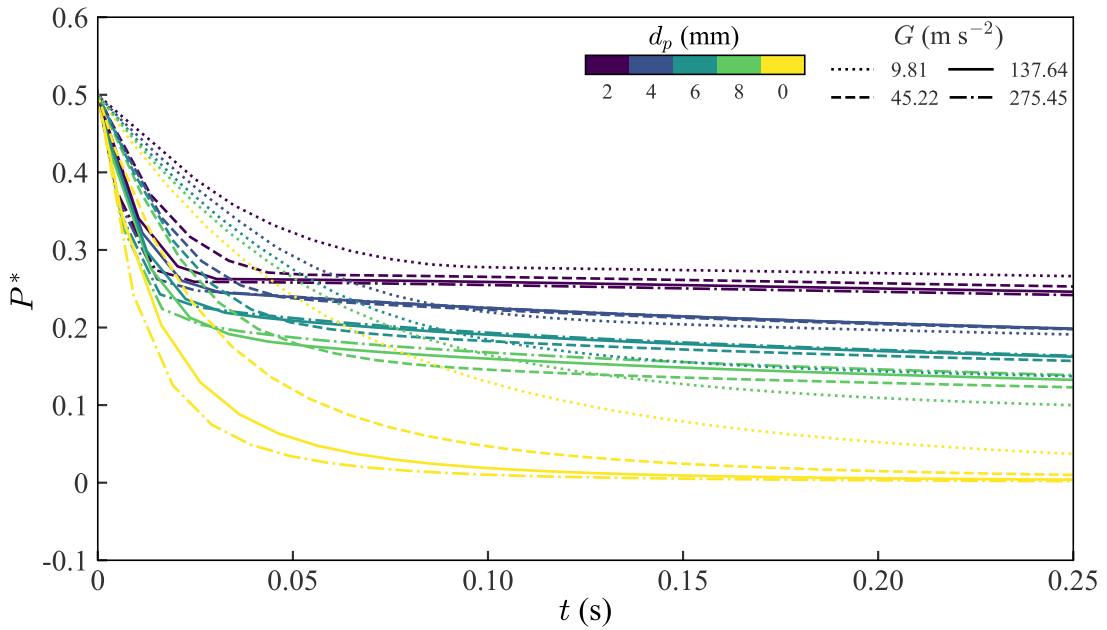
Figure 5.10: Simulated temporal evolution of the reduced dimensionless basal fluid pressure at the centre of the column $P^*$ with time $t$ for varying $d_p$ and $G$.

tions experienced by both constituent phases during the initial collapse of the column, which would increase the force and subsequently the pressure, applied to the horizontal plane located at the basal surface.

In order to evaluate the pressure scaling relations predicted by the model, it is essential to compare the experimental and numerical results in $P^* - t^*_{h_0}$ space, as illustrated in Figure 5.12. As the only source of momentum transfer for the fluid phase is via its interaction with the granular phase, it is reassuring to observe that the experimental and numerical curves for the purely fluid collapses (i.e. $d_p = 0\,\text{mm}$) conducted at different $G$ levels approximately collapse onto single curves, respectively. This reaffirms that, within the tested parameter range, the reduction of basal fluid pressure during fluid column collapses is predominantly determined by the magnitude of $G$, while particle size effects play a secondary role.

Additionally, analysing the data in $P^* - t^*_{h_0}$ space shows that for a specific particle size, the pressure reduction curve's gradient for the experimental data increases with increasing $G$, which is the opposite of the trend predicted by the numerical model. This opposing scaling in $P^* - t^*_{h_0}$ space implies that the interaction term utilised in the model does not reflect the observed scaling behaviour for basal fluid pressure reduction, emphasising the need for further investigation of the underlying mechanisms at play.
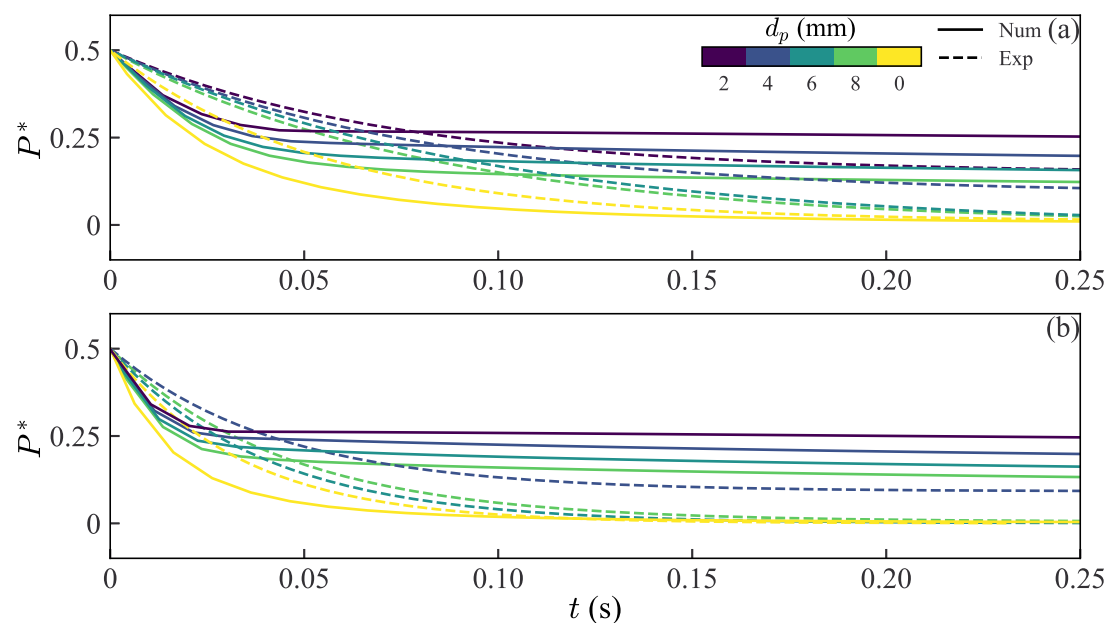
Figure 5.11: Numerical and experimental temporal evolution of the reduced dimensionless basal fluid pressure at the centre of the column $P^*$ with time $t$ for varying $d_p$ at (**a**) $G = 45.22\,\mathrm{m\,s^{-2}}$ and (**b**) $G = 137.64\,\mathrm{m\,s^{-2}}$.



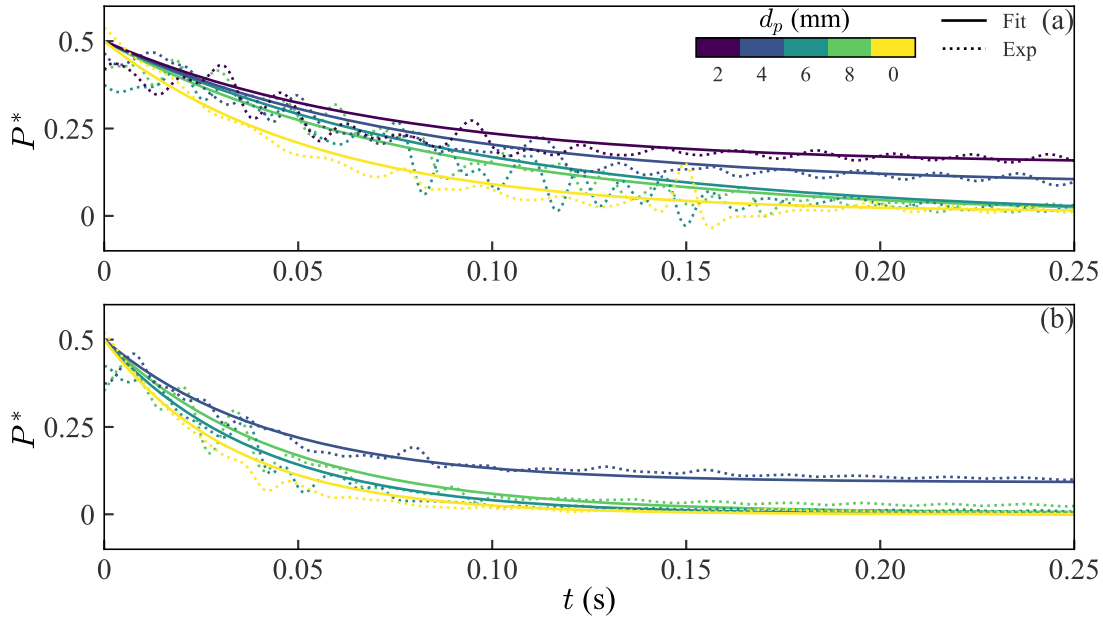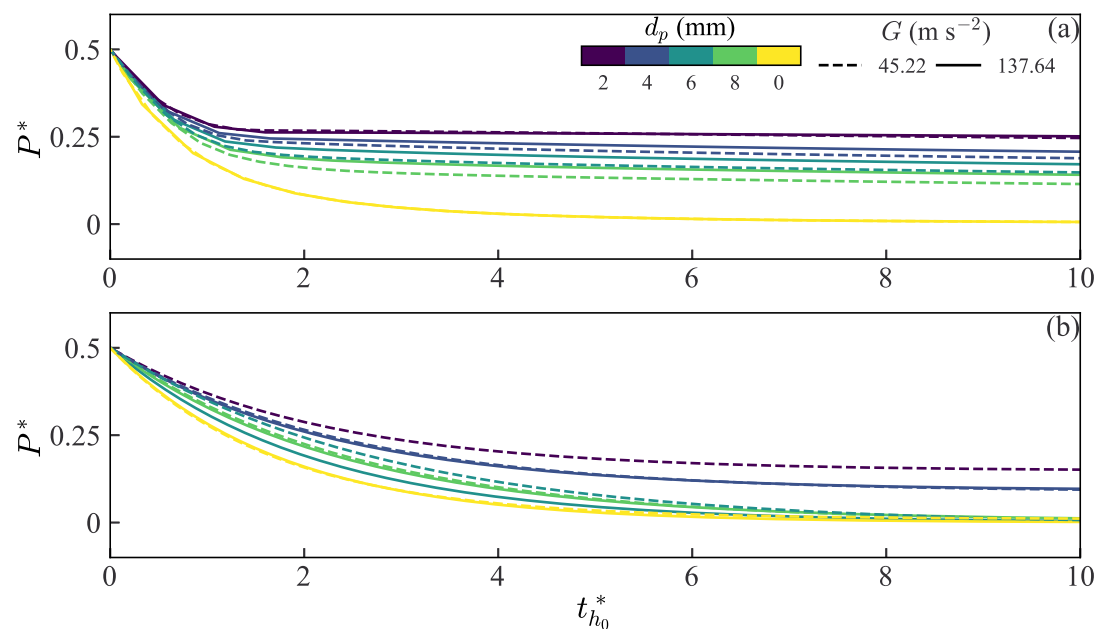Figure 5.12: (**a**) Numerical and (**b**) experimental temporal evolution of the reduced dimensionless basal fluid pressure at the centre of the column $P^*$ with normalised time $t_{h_0}^*$ for varying $d_p$ and $G = 45.22\,\mathrm{m\,s^{-2}}$ and $137.64\,\mathrm{m\,s^{-2}}$.

## 5.6 Discussion

The dynamic complexity of debris flows, in part, arising from their spatially and temporally evolving composition, results in significant challenges when modelling these phenomena. As such, numerical models that attempt to capture the diversity of flow behaviours observed in field-scale flows can become intractable (Turnbull et al., 2015) and, therefore, unsuitable for the development of effective hazard mitigation strategies. Hence, obtaining a greater understanding of the interaction between the fluid and granular phases constituting the flow is crucial to developing appropriate modelling assumptions that lead to cost-effective predictive methodologies.

In the present study, a two-phase depth averaged model was proposed to capture the essential grain-fluid interaction processes observed during the fluid-saturated granular column collapse experiments conducted by Webb et al. (2023b)[†] using elevated $G$-levels to reflect the grain inertia in large-scale events. The grain-fluid interaction force consists of a Darcy-drag style relation where the drag between the two phases is a function of the granular phase permeability as described by Carman's equation. The axisymmetric geometry of the experimental setup was taken advantage of by developing a system of equations that could be expressed in a conservative form using a polar coordinates system. The individual system of equations for both the fluid and granular phases can be recovered as limit cases of the two-phase system.

Numerical simulations of the experiments were undertaken with the model where its spatial and temporal discretisation were carried out using a second-order central-upwind scheme (Kurganov and Petrova, 2007) and an explicit second-order Runge-Kutta method, respectively.

From initially comparing the numerical and experimental runout results of collapses consisting of a singular fluid phase, it was evident that the numerical model was significantly overestimating the initial acceleration of the fluid front. This was due to the initial configuration of the columns not adhering to the depth averaged assumption that was critical to the model's derivation. This was counteracted by employing the mass 'raining' scheme of Larrieu et al. (2006) to incrementally introduce phase mass into the system, thus, eliminating the overestimation of vertical accelerations.

The ability of the tuned model was then tested by assessing how well it replicated the temporal evolution of both the granular and fluid phase fronts for a series of just-saturated granular column collapse tests where both $d_p$ and $G$ were varied. While the

---

[†]Webb et al. (2023b) is shown in Chapter 3

model could successfully replicate the acceleration, quasi-steady and retardation stages of motion expected for an unsteady mass movement, the runout out distances predicted by the model overestimate those measured experimentally for every test case. The model's performance improved with decreasing $d_p$ which is a key indication that this discrepancy largely emanates from the modelling assumption of a continuum granular phase. Moreover, it is important to acknowledge that this continuum approximation issue may extend to field-scale scenarios as well, as debris flows often transport boulders with diameters comparable to the flow depth. However, the model does predict a reduction in phase separation for a given $d_p$ as $G$ increases, illustrating that particle inertial effects become less dominant with increased scale.

Similarly, when comparing numerical and experimental temporal evolutions of the phase front velocity, it was hypothesised that the continuum assumption was responsible for the model overestimating the peak phase velocities. Analysing the collapse in $u_{v,h_0}^* - t_{h_0}^*$ space also highlighted a particle-size dependent lag in the experimental data that was the result of interference from the steel column. Crucially, the initial discharge of the fluid phase was found to be heavily dependent on the permeability of the granular phase. While the influence of $d_p$ on this effect increases to $G = 45.22\,\mathrm{m\,s^{-2}}$, it reduces thereafter as macro-scale gravitational and viscous forces become dominant.

In order to directly compare the experimental and numerical basal fluid pressure time series, both had to undergo a reduction process to eliminate the influence of the steel column being lifted and the implementation of the mass 'raining' scheme, respectively. Comparing the datasets in $P^* - t$ space clearly showed that the model was able to replicate the strong $d_p$ and $G$ dependencies exhibited within the experimental hydrostatic pressure reduction curves. Specifically, for a given $G$, the rate of pressure reduction increases with $d_p$, while, for a given $d_p$, the rate of pressure reduction increases with $G$.

Discrepancies in the magnitude of the pressure reduction rate and the residual basal fluid pressures between the model and the experimental findings can again be reasoned to emanate from the assumption of a continuum granular phase and interference from the steel column. Additionally, analysing the trends in $P^* - t_{h_0}^*$ space revealed that the numerical dimensionless pressure reduction curves decreased with increasing $G$, which opposes the trend observed in the experimental data. Thus, it can be determined that, while the chosen inter-phase interaction term allows the model to replicate the mechanisms governing the phase interaction at the grain-scale, it does not quite obtain the scaling behaviour observed experimentally.

Future extensions of the model would be focussed on incorporating the effects of

polydispersed granular phases, meaning inertial and sub-inertial granular material, on macro-scale flow behaviour by altering the inter-phase interaction term. Webb et al. (2023a)[‡] explored the influence of different grain scales by conducting the same column collapse experiments as Webb et al. (2023b)[†], but with a particle phase consisting primarily of inertial grains while kaolin clay particles were suspended within the fluid phase. A scale analysis of the collapse runouts found that the quantities used to characterise the phase runout were highly dependent on the degree of fines, as well as dimensionless quantities that characterised the column- and inertial grain-scales. Further testing is required to obtain basal fluid pressure evolution collapse data before the model can be extended.

## 5.7   Supplementary content

The raw video files for all completed tests are available at `https://doi.org/10.17639/nott.7277`.

---

[‡]Webb et al. (2023a) is shown in Chapter 4
[†]Webb et al. (2023b) is shown in Chapter 3

Chapter 6

# Performance and limits of a geotechnical centrifuge: DEM-LBM simulations of saturated granular column collapse

**Abstract**

*This study investigates the dynamics of granular flows in geotechnical centrifuge models, focusing on the effects of centrifugal and Coriolis accelerations. While conventional laboratory-scale investigations often rely on Froude scaling, geotechnical centrifuge modelling offers a unique advantage in incorporating stress-dependent processes that fundamentally shape flow rheology and dynamics. Using the Discrete Element Method (DEM) and the Lattice-Boltzmann Method (LBM), we simulate the collapse of a just-saturated granular column within a rotating reference frame. The model's accuracy is validated against expected trends and physical experiments, demonstrating its strong performance in replicating idealised collapse behaviour. Acceleration effects on both macro- and grain-scale dynamics are examined through phase front and coordination number analysis, providing insight on how centrifugal and Coriolis accelerations influence flow structure and mobility. This work enhances our understanding of granular flow dynamics in geotechnical centrifuge models by introducing an interstitial pore fluid and considering multiple factors that influence flow behaviour over a wide parameter space.

---

Chapter 6: Performance and limits of a geotechnical centrifuge: DEM-LBM
simulations of saturated granular column collapse

# 6.1 Introduction

Centrifuge modelling is a well-established technique in the field of civil engineering,
widely employed to investigate common soil stability and soil-structure interaction
problems (Schofield, 1980). By rotating a laboratory-scale model at a given angular
velocity at the end of a centrifuge arm (Figure 6.1), a centripetal acceleration is imposed
on the model. When this centripetal acceleration exceeds Earth's gravity by a scaling
factor $N$, it augments the self-weight of the material within the model, thereby enabling
precise control over the gravitational effects in the model (Cabrera and Wu, 2017).
Recently, the technique has been used to simulate the conditions prevalent in geophysi-
cal granular mass movements such as landslides and debris flows (e.g. Bowman et al.,
2010; Cabrera and Wu, 2017; Vallejo et al., 2006).

In contrast to traditional laboratory-scale studies of large granular mass movements,
which usually rely on Froude scaling to determine the velocity scale (e.g. Delannay et
al., 2017; Kesseler et al., 2018; Turnbull et al., 2015), geotechnical centrifuge modelling
offers a unique advantage. This advantage lies in its ability to incorporate stress-related
processes that play a critical role in determining the flow's behaviour and, consequently,
the overall dynamics in real-world scenarios (Brucks et al., 2007; Iverson, 2015). This
becomes especially important when examining how the flow interacts with potential
mitigation structures (e.g. Huang and Zhang, 2022; Ng et al., 2018; Song et al., 2018;
Zhang and Huang, 2022). Stress-dependent mechanisms also significantly affect the
dynamics of partially or fully saturated granular flows. For instance, phenomena such
as surface tension effects caused by capillary bridges between adjacent grains (Bougouin
et al., 2019), or at the surface of the flow itself, can have a significant impact on flow
behaviour in laboratory experiments, even though they are relatively minor compared
to gravitational forces in natural mass movements (Webb et al., 2023b)[†]. Moreover, in
addition to the flow's particle size distribution, the magnitude of the confining stress at
a specific point within the flow greatly influences the buildup and dissipation of excess
pore pressures. As previously observed, these pressures can significantly affect flow
mobility and dynamics (Kaitna et al., 2016; McArdell et al., 2007; Rondon et al., 2011).

Consider a simplified scenario of a centrifuge test as depicted in Figure 6.2, where
there are three particles in contact with a horizontal surface (i.e. the base of a centrifuge
model) of length $L_c$ that is being spun at a rotational velocity $\omega$ and at distance of $R_c$

---

[†]Webb et al. (2023b) is shown in Chapter 3
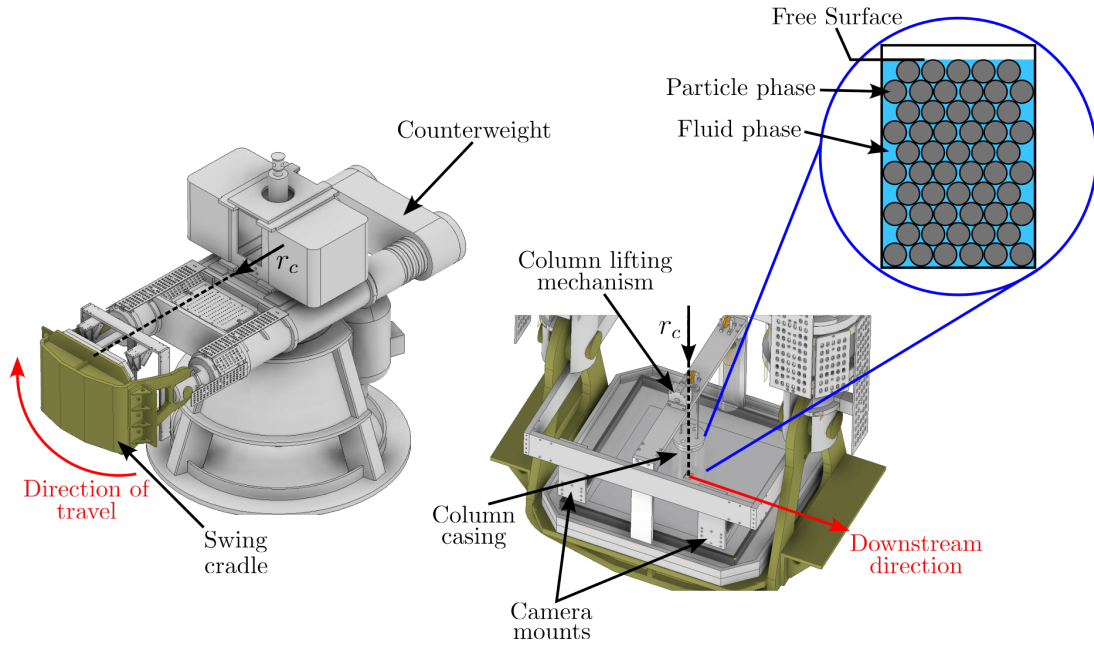
Figure 6.1: Schematic of the column collapse experimental configuration loaded on to
the geotechnical centrifuge.

from the centre of the centrifuge. The Cartesian reference frame $xz$ remains aligned with
the horizontal surface and, therefore, spins together with the model. While the central
particle remains stationary, the two outer particles move away from the centreline of
the model at velocity $\boldsymbol{u}$. The particle acceleration field can be expressed as the sum of
centrifugal acceleration $\boldsymbol{a}_{cf}$ and the Coriolis acceleration $\boldsymbol{a}_{co}$

$$\boldsymbol{a} = \boldsymbol{a}_{cf} + \boldsymbol{a}_{co} = -\boldsymbol{\omega} \times (\boldsymbol{\omega} \times \boldsymbol{r}_c) - 2\boldsymbol{\omega} \times \boldsymbol{u}, \tag{6.1}$$

where $\boldsymbol{r}_c$ is the coordinate direction aligned with the gravity vector. The direction and
magnitude of $\boldsymbol{r}_c$ depend on the position of the objects, in this case, the particles, relative
to the centrifuge's axis of rotation. It is important to note that, for completeness, we
should consider the external acceleration vector, gravity $\boldsymbol{g}$, in Equation (6.1). However,
if $\boldsymbol{\omega}$ is sufficiently large, its effects are often considered negligible (Cabrera et al., 2020).
As described in Equation (6.1), $\boldsymbol{a}_{cf}$ consistently acts away from the centre of rotation
and parallel to $\boldsymbol{r}_c$, while the direction of $\boldsymbol{a}_{co}$ depends on both the direction of $\boldsymbol{u}$ and $\boldsymbol{\omega}$.
To simplify matters, $\boldsymbol{a}$ is often approximated as an equivalent increased gravity (Taylor,
1995)

$$a \equiv \omega^2 R_c \equiv Ng, \tag{6.2}$$
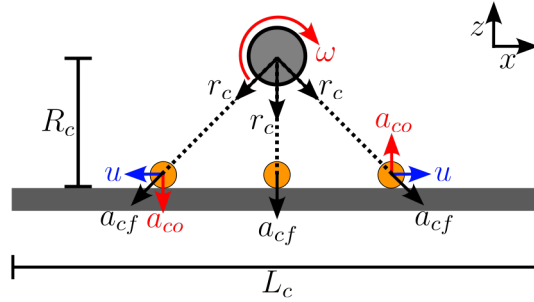
Figure 6.2: Schematic of the acceleration forces acting upon particles in the rotating
frame of reference of a geotechnical centrifuge experiment.

where $g$ is Earth's gravitational acceleration and $N$ serves as a scale factor. Both $\boldsymbol{a}_{cf}$
and $\boldsymbol{a}_{co}$ can impose non-vertical accelerations on the particles, thereby influencing their
horizontal velocity. In the case of $\boldsymbol{a}_{cf}$, this is know as the Eötvös effect. In smaller
geotechnical centrifuges, where $R_c \approx 2\,\text{m}$ and $L_c \approx 0.8\,\text{m}$, the magnitude of the hor-
izontal component of $\boldsymbol{a}_{cf}$ can equate to 20 % of the presumed increased gravitational
acceleration calculated from Equation (6.2). While this may have a negligible effect
when modelling typical civil engineering applications, it complicates the translation of
experimental observations from centrifuge models of granular mass movements, which
are inherently more dynamic processes, to natural flows.

To conduct a comprehensive experimental study investigating the impact of centrifu-
gal and Coriolis accelerations on granular flow dynamics, one would need to use mul-
tiple centrifuges of varying sizes, considering the dependency on $R_c$. Therefore, such a
study is well-suited for numerical modelling which offers the potential to significantly
expand the parameter space of physical experiments. Furthermore, such simulations can
serve as effective tools for scaling up our insights from laboratory-scale experiments to
these larger geophysical phenomena.

Recent investigations have utilised the Discrete Element Method (DEM) to explore
the effects of centrifugal and Coriolis accelerations on both steady (Cabrera et al., 2020;
Leonardi et al., 2021) and unsteady (Zhang and Huang, 2022; Zhang et al., 2023) dry
granular flow configurations. Numerical modelling not only facilitates the study of $\boldsymbol{a}_{cf}$
when varying $R_c$ but also allows for the independent examination of the effects of $\boldsymbol{a}_{cf}$
and $\boldsymbol{a}_{co}$. While these studies represent significant progress in understanding the mech-
anisms and scaling of centrifuge modelling effects, additional complexities, such as the
presence of an interstitial pore fluid, need to be considered.

The study aims to enhance our understanding by employing numerical modelling to

examine a just-saturated granular column collapse configuration within a geotechnical centrifuge. Two recent experimental studies (Webb et al., 2023a,b)[‡†] have provided valuable insights into the system, with a strong focus on grain-fluid interaction and its influence on macro-scale flow features. By utilising the Lattice-Boltzmann Method (LBM) to model the fluid phase and coupling it with DEM, this study initially seeks to replicate the flow states observed in these physical experiments. Subsequently, the study investigates the influences of centrifugal and Coriolis accelerations on both grain-scale and macro-scale flow dynamics.

## 6.2 Fluid-saturated granular column collapse

The current research aims to explore the impact of centrifuge modelling on granular-fluid flows by focusing on the dynamics of a simple axisymmetric, just-saturated granular column collapse (see Figure 6.1). Although this configuration has been extensively studied under normal laboratory conditions (i.e. $g = 9.81\,\mathrm{m\,s^{-2}}$) (e.g. Lai et al., 2017; Lajeunesse et al., 2004; Li et al., 2022; Lube et al., 2004; Trepanier and Franklin, 2010), recent investigations (Webb et al., 2023a,b)[‡†] have also examined its dynamics within a geotechnical centrifuge. However, these studies primarily focused on grain-fluid interaction and did not thoroughly investigate the contributions of varying centrifugal and Coriolis accelerations to the collapse dynamics.

To bridge this knowledge gap, we conducted experiments using the same collapse configuration system as in the aforementioned studies, in order to provide empirical data to compare against the numerical model presented in this work (see Sections 6.3 and 6.4). The collapse of the granular column was initiated using a modified classical weighted-pulley system, designed for hands-free operation within the University of Nottingham's GT50/1.7 geotechnical beam centrifuge (Ellis et al., 2006 for details). The evolution of the collapses were recorded using two high speed cameras and image processing was used to extract the location of both phase fronts throughout the duration of the experiment (see Figure 6.3). A full description of the physical system and image analysis can be found in Webb et al. (2023b)[†].

Given, that the flow spreads axisymmetrically, specifically, sections of the flow travel 'upstream' and 'downstream' of centrifuge motion (Webb et al., 2023b)[†], this experimental configuration provides an ideal test case for comprehending the role of cen-

---

[‡]Webb et al. (2023a) is shown in Chapter 4
[†]Webb et al. (2023b) is shown in Chapter 3
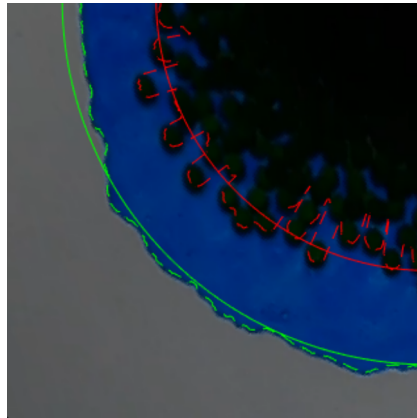
Figure 6.3: Example of the phase front extraction technique used during the experimental image analysis (available at http://doi.org/10.17639/nott.7277). The raw (dashed) and averaged (line) radial positions of the fluid (green) and granular (red) phase fronts are shown.

trifugal and Coriolis accelerations in influencing the behaviour of dynamic flows. By using experimental comparison to assess the numerical model, we aim to gain valuable insights into the mechanics of granular-fluid flows in a geotechnical centrifuge setting that would be unachievable from experimental testing alone.

## 6.3   The LBM-DEM framework

The numerical tool chosen for the current work was used previously by Cabrera et al. (2020) and Leonardi et al. (2021) to investigate the behaviour and modelling effects of a granular flow down a rough incline within a geotechnical centrifuge. The code is an extension of the original work by Leonardi et al. (2014) which has been modified and extensively used for the study of laboratory- and large-scale fluid-granular flow mechanisms (e.g. Leonardi et al., 2019; Leonardi et al., 2015; Marchelli et al., 2020), and even saturated granular column collapses (Ceccato et al., 2020). The code employs a compound approach to modelling complex granular-fluid systems known as the DEM-LBM method. This method has gained popularity in the last two decades, and can be now considered a standard approach for the simulation of particle-driven flow (Feng and Michaelides, 2004; Han et al., 2007; Han and Cundall, 2013; Xiong et al., 2014). The behaviour of the granular and fluid phases are simulated using independent numerical schemes but are coupled together by imposing phase interaction forces. Further additional forces, accounting for the external forces imposed on an object within a rotating

domain, are also accounted for.

The code solves the collisions of particle pairs within the flow using a standard Discrete Element Method (DEM) approach. A linear spring-dashpot model is used to determine the surface-normal $F_n$ and tangential $F_t$ contact forces through their respective contact stiffness, $k_n$ and $k_t$, and damping, $\alpha_n$ and $\alpha_t$, coefficients. $F_n$ is defined as a function of the overlap $\xi$ between the two colliding bodies

$$F_n = k_n\xi + 2\alpha_n\sqrt{k_n m}\frac{d\xi}{dt}, \tag{6.3}$$

while the magnitude of $F_t$ is regulated by a Coulomb friction relation

$$F_t = \max\left(\mu_s F_n, k_t\zeta + 2\alpha_t\sqrt{k_t m_p}\frac{d\zeta}{dt}\right), \tag{6.4}$$

where $m_p$ is the grain mass, $\mu_s$ is the static friction coefficient of the particles, and $\zeta$ is the elongation of a tangential spring that represents elastic tangential deformations. There are analogous relations for particle-wall interactions where $\mu_s$ is substituted for the particle-wall friction coefficient $\mu_{s,w}$.

To ensure that it was possible for the completely spherical particles to form into the stable heaps on the flat surface that were observed in previous experiments (see Ceccato et al., 2020; Marchelli et al., 2020), an additional torque which opposes the rotational motion of the particles $M_r$ was also implemented

$$M_r = \mu_r F_n\frac{d_p}{2}, \tag{6.5}$$

where $\mu_r$ is the rolling friction coefficient of the particles and $d_p$ is the particle diameter. It should be noted that, for collisions between particles that differ in size, $m_p$ and $d_p$ should be exchanged for effective values that are representative of the collision (see Marchelli et al., 2020).

The dynamics of the fluid phase are described using the Lattice Boltzmann method (LBM) which is formulated from kinetic theory at the mesoscopic scale (Leonardi et al., 2014). Fluid advection is expressed using a density function $f(\boldsymbol{x}, \boldsymbol{c}, t)$, that describes the probability of finding fluid molecules at a location $\boldsymbol{x}$, with microscopic velocity $\boldsymbol{c}$ at time $t$. $f$ is discretised in space by considering a finite number of advection directions $i$ across a regularly spaced lattice, such that $f_i(\boldsymbol{x}, t) = f(\boldsymbol{x}, \boldsymbol{c_i}, t)$ where $\boldsymbol{c_i}$ is the direction dependent weighted lattice velocity for a given fluid cell. The current work uses the D3Q19 lattice configuration, which delineates the lattice into 19 advection di-

rections across 3 dimensions. Also due to the lattice symmetry, it is possible to recover the incompressible Navier-Stokes equations and, hence, obtain the macroscopic fluid density $\rho_f$, velocity $\boldsymbol{u}_f$, and pressure $p_f$ at each location $x$ and for all values of $t$ as follows

$$\rho_f = \sum_i f_i, \quad \boldsymbol{u}_f = \sum_i f_i \boldsymbol{c}_i / \rho, \quad p_f = c_s^2 \cdot \rho_f, \tag{6.6}$$

where $c_s^2 = 1/3$. The streaming and collisional behaviour of the fluid particles is captured using the Bhatnagar-Gross-Krook (BGK) (Wolf-Gladrow, 1995) approach for modelling a kinetic gas

$$(\delta_t + \boldsymbol{u}_f \cdot \nabla)f = -\frac{f - f^{\text{eq}}}{\tau}, \tag{6.7}$$

where $\tau$ is the relaxation timescale over which collisions occur and $f^{\text{eq}}$ is the value of the probability density function at equilibrium for a given macroscopic velocity (for more details, see Leonardi et al., 2014). This recovery links the macroscopic viscosity of the fluid $\eta_f$ to the mesoscopic collision operator as follows

$$\eta_f = \frac{\tau - 1/2}{3}. \tag{6.8}$$

Thus, viscosity can be set by the user by altering the timescale by which the distribution function is relaxed towards thermodynamic equilibrium (Succi, 2001). Following the work of Leonardi et al. (2014), the evolution of the fluid free surface is updated using Janßen and Krafczyk's (Janßen and Krafczyk, 2011) volume-of-fluid method, with a full-slip boundary condition, to improve computational efficiency.

The two phases are coupled through the exchange of a drag force $f_d$, which is calculated as the integral of all the drag contributions between individual fluid points interacting with each granular particle, using the immersed-boundary method (Švec et al., 2012). As such, the fluid mesh size $\Delta_f$ must be smaller than the characteristic DEM particle diameter $D$. It should be noted that this stipulation on the lattice spacing also implies that the fluid pressure is effectively resolved at the pore scale (Ceccato et al., 2020), down to the precision offered by the lattice spacing itself.

The work of Leonardi et al. (2021) has been extended so that both the fluid and granular phases can be submitted to an elevated gravitational acceleration field as would be imposed to a model while being spun on a geotechnical centrifuge. This is achieved by imposing both $\boldsymbol{a}_{cf}$ and $\boldsymbol{a}_{co}$ on each phase as external forces. Within the LBM framework, the acceleration applied to the fluid phase, which is a function of space, is computed based on the centroid of every lattice node. $\boldsymbol{a}_{cf}$ and $\boldsymbol{a}_{co}$ can be imposed independently

so that it is possible to investigate the influence of each on collapse dynamics separately.

In order to model the contacts of colliding grains, the time-step required by the DEM is generally smaller than the time step required for the LBM. Hence, the schemes are staggered so that multiple DEM time steps are run for every LBM time steps. While a complete explanation of the DEM-LBM scheme is out of the scope of the current work, where we have only detailed its most significant components, a comprehensive explanation of the method can be found in Leonardi et al. (2015).

## 6.4 Simulation methodology

### 6.4.1 Simulation parameter space

Similar to the approach taken by Webb et al. (2023b)[†] in their image analysis, our simulations utilise the axisymmetric nature of the experiment. By modelling only a quarter of the column (see Figure 6.4), we significantly reduce computational time for each simulation.

The initial configuration of the granular-fluid column is characterised by two parameters: the initial column height $h_0$ and radius $r_0$. As was the case for the two previous studies (Webb et al., 2023a,b)[‡†], we set $h_0 = 50$ mm and $r_0 = 54$ mm for each phase, resulting in a column aspect ratio of $a_0 = h_0/r_0 = 0.93$. The granular phase comprises monodispersed particles with a mean diameter $D = 8 \times 10^{-3}$ m ($\pm 10\%$ to prevent crystallisation within the initial configuration (Leonardi et al., 2021)) and a particle density $\rho_p = 2650$ kg m$^{-3}$. This is the largest size used in the two previous studies and was selected as it minimises surface tension effects when in contact with a thin film of fluid (Webb et al., 2023b)[†] (see Section 6.5.2 for further discussion). Moreover, the number of particles $n_p$ that have to be modelled ensures computational efficiency, with $n_p = 261$, corresponding to an initial mean solid volume fraction $\phi_p = 0.61$. The parameters for modelling the particles using the DEM scheme are summarised in Table 6.1. Using the real stiffness of the grains would result in unreasonably long simulation times. Since the collapse dynamics of interest are not influenced by particle deformability (Roux and Combe, 2002), the linear contact stiffness $k_n$ has been instead calibrated so that the particles are sufficiently rigid to make elastic deformations negligible.

The three Newtonian fluids used in this study are miscible glycerol-water mixtures,

---

[†]Webb et al. (2023b) is shown in Chapter 3
[‡]Webb et al. (2023a) is shown in Chapter 4
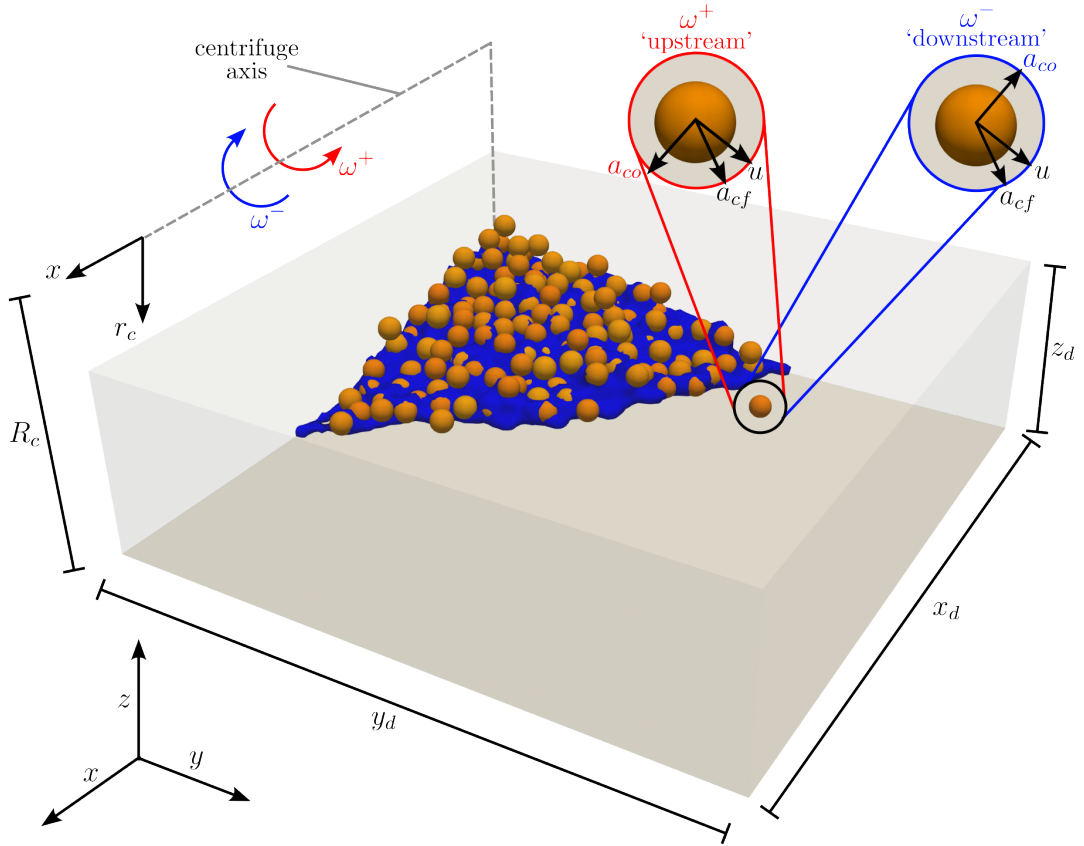
Figure 6.4: Schematic of the simulation domain during a column collapse containing 261 particles. The frictional boundaries are shown as grey planes and the insets highlight the direction of the centrifugal and Coriolis accelerations acting on a particle for the defined rotational reference frame.

characterised by two parameters: the ratio between the fluid mixture viscosity $\eta_f$ and the viscosity of water $\eta_w$ denoted by $\eta_f^* = [50, 100, 150]$, and the density of the fluid mixture $\rho_f = [1203.8, 1219.7, 1227.5]\,\mathrm{kg\,m^{-3}}$, respectively. The viscosity of the fluids were required to be significantly higher than those used previously by Webb et al. (2023b)[†] as $\eta_f$ is directly related to the relaxation time, and, therefore, the stability of the fluid in the LBM scheme (Leonardi et al., 2014). Further details about the preparation of the physical experiments can be found in Webb et al. (2023b)[†].

The final model considerations are those dictating the relative contribution of centrifugal and Coriolis accelerations to collapse dynamics. Following Cabrera et al.'s (2020) approach, we consider the following three external forcing cases

(i) A constant acceleration field $\boldsymbol{a} = N\boldsymbol{g}$ where the far field condition $R_c \gg h_0$ is

---

[†]Webb et al. (2023b) is shown in Chapter 3

Table 6.1: Summary of DEM simulation parameters.

| Model parameter | Range |
|---|---|
| $n_p$ | 261 |
| $D$ (m) | 0.008 |
| $\rho_p$ (kg m$^{-3}$) | 2650 |
| $k_n$ (N m$^{-1}$) | $10^6$ |
| $k_t$ (N m$^{-1}$) | $\frac{2}{7}k_n$ |
| $\mu_{rest}$ | $0.77^a$ |
| $\alpha_n$ | $0.08^b$ |
| $\alpha_t$ | 0.5 |
| $\mu_s$ | $0.5^c$ |
| $\mu_{s,w}$ | $0.079^d$ |
| $\mu_r$ | $\mu_{s,w}$ |

[a] See Yang and Hunt (2006).
[b] See Equation (3) from Hu et al. (2010).
[c] Obtained using the fixed cone test (Henein, 1980).
[d] Obtained using the tilting table test for singular grains (Henein, 1980).

assumed, notated as $Ng$.

(ii) A rotating domain that only accounts for the curvature of the acceleration field arising from the centrifugal acceleration (i.e. $\boldsymbol{a} = \boldsymbol{a}_{cf}$), notated as $\omega^0$.

(iii) A complete acceleration field for a rotational domain (i.e. $\boldsymbol{a} = \boldsymbol{a}_{cf} + \boldsymbol{a}_{co}$) where contributions of the Coriolis effect in the downstream and upstream direction, notated as $\omega^-$ and $\omega^+$, respectively, will be considered independently.

To understand how $\boldsymbol{a}_{cf}$ and $\boldsymbol{a}_{co}$ can influence collapse dynamics, we explore the parameter space for $N = [5, 8, 10, 12, 15]$ and $\log(R_c/h_0) = [2, 3, 3.7, 4, 5, 6, 7]$, where $\log(R_c/h_0) = 3.7$ corresponds to the dimensions of the previously conducted physical collapses (Webb et al., 2023b)[†].

## 6.4.2 Simulation geometry

The simulation domain is depicted as a rectangular box (Figure 6.4) bounded by static frictional walls in the $x$, $y$, and $z$ planes. It is characterised by three length parameters $[x_d, y_d, z_d] = [0.2, 0.2, 0.07]$ m while the lattice spacing for the fluid phase $\Delta_f = 2 \times 10^{-3}$ m. Notably, during the column construction process, some adjustments are made to the domain, which will be discussed in Section 6.4.3.

---

[†]Webb et al. (2023b) is shown in Chapter 3

The modelled centrifuge is positioned above the column, with its rotation axis located outside the simulation domain. For simplicity, we define the radius of the centrifuge $R_c$ as the distance between the axis of rotation and the horizontal plane over which the collapsing material will spread. For the simulations considering the forcing case of the full rotational domain (i.e. $\boldsymbol{a} = \boldsymbol{a}_{cf} + \boldsymbol{a}_{co}$), the collapse will be simulated twice so that the flow can be considered in both the $\omega^+$ and $\omega^-$ directions.

### 6.4.3 Column construction

The dynamics of granular column collapses in both dry and wet conditions are significantly affected by the initial configuration of the column (e.g. Rondon et al., 2011). Therefore, it is crucial to closely replicate the physical procedure used in the experiments for the numerical simulations. In this study, we employ a two-step procedure to mimic the experimental conditions.

First, particles are poured into a quarter-cylinder container with a radius of $r_0$, under a constant natural gravitational field ($a = g$) and allowed to settle. To ensure free-fall settling, $z_d$ was increased to 6 m during the settling simulations.

The column is then consolidated under the acceleration field that will be prescribed for the collapse simulation and allowed to consolidate. It was found that initially pouring the particles into the container under the influence of an elevated acceleration field resulted in a much looser column. Additionally, when the prescribed acceleration field considers a rotating domain (external forcing cases (ii) or (iii)), particles near the top of the column, being less constrained, tended to favour the container edge toward which the fictitious forces pushed them, resulting in an uneven free surface. Hence, this two-stage settling procedure was implemented to limit these effects.

### 6.4.4 Front and signal processing

An assessment of the model's validity was performed by analysing the evolution of the averaged phase front positions $r_v$ where subscript $v = p, f$ for the particle and fluid phases, respectively. For the numerical simulations, $r_v$ was obtained using a two-step procedure. At each saved time-step, the Cartesian domain was divided into $n$ concentric sectors originating from the collapse centre (Figure 6.5f). Here, $n = 50$ sectors were utilised for the fluid phase, and $n = 16$ for the particle phase. The value of $n$ was required to be significantly lower for the granular phase due to it being comprised of far less particles than the fluid phase. The furthest fluid and granular point in each sector
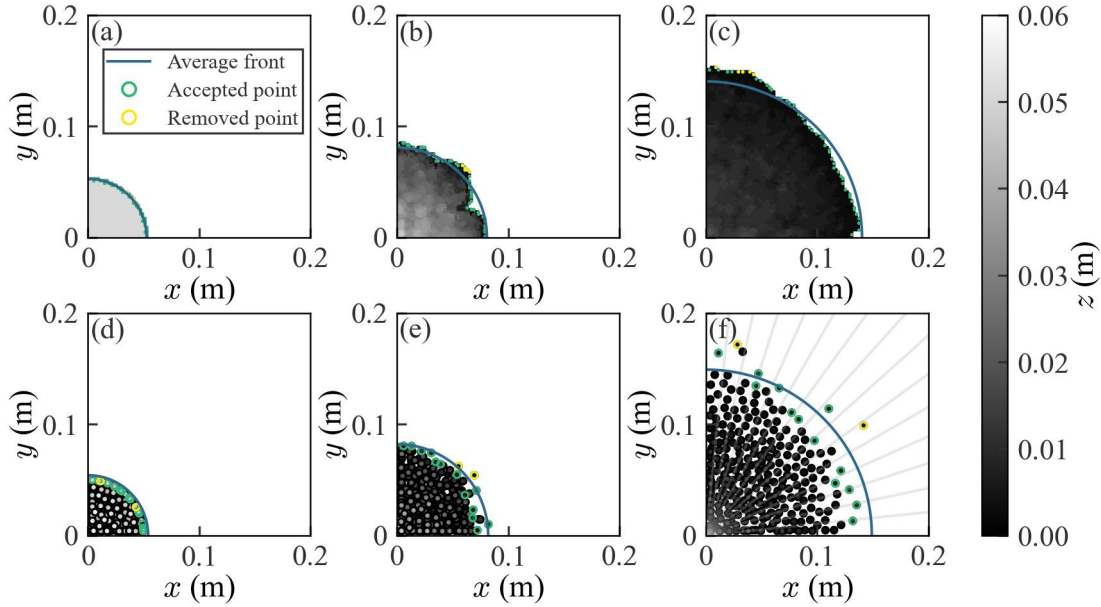
Figure 6.5: Extraction of the fluid [(**a**)-(**c**)] and particle [(**d**)-(**f**)] phase fronts for a simulated collapse moving downstream of centrifuge motion where $a = a_{cf} + a_{co}$, $R_c = 2$ m, $N = 5$, and $\eta_f^* = 150$ at $t = 0$ [(**a**),(**d**)], 0.1 [(**b**),(**e**)] and 0.35 s [(**c**),(**f**)]. $r_v$ (blue), the particle and fluid points making up the phase front (green edge) and the particle and fluid points removed from the phase front (yellow edge) are all shown. An example of the concentric sectors (grey) splitting up the domain is displayed in (**f**).
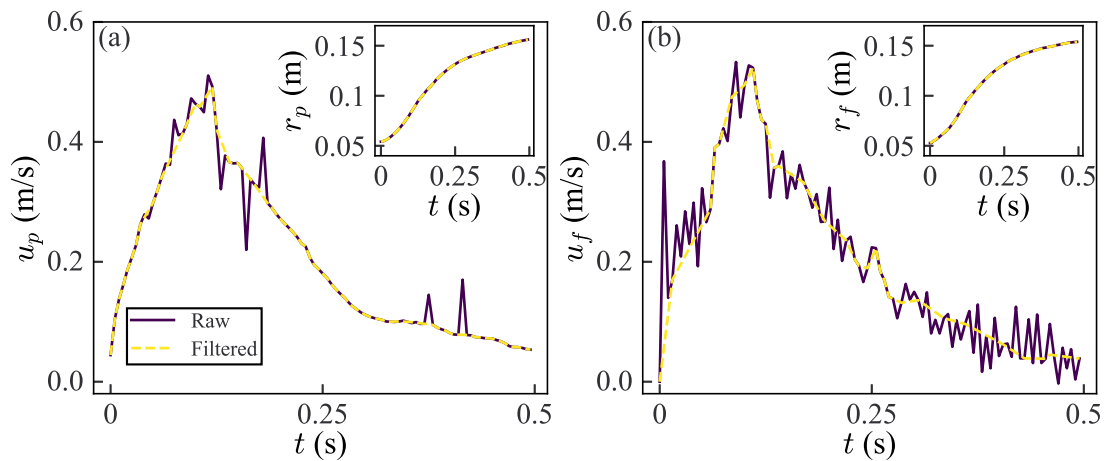


Figure 6.6: Comparison of the raw and filtered phase velocity $u_v$ and radial position $r_v$ (insets), where (**a**) $v = p$ and (**b**) $v = f$ for a simulated collapse moving upstream of centrifuge motion where $a = a_{cf} + a_{co}$, $R_c = 2.7$ m, $N = 5$, and $\eta_f^* = 100$.

were then identified as part of the phase front. Before averaging the radial distance of these points to obtain $r_v$, points with a radial distance from the origin larger than the 90th percentile of the chosen points were excluded, thereby eliminating points that had escaped from the phase front. While this makes no substantial difference for the fluid phase, removing these points in the case of the granular phase is crucial. For the particle phase, the radius of the particle is also considered when calculating the position of the front. An example of this procedure is shown in Figure 6.5.

The resulting averaged phase front signal underwent a noise reduction process. Firstly, it was assumed that $r_v$ monotonically increases with time, allowing the removal of signal sections where $r_v$ decreased. Secondly, analysis of the phase front velocity, $u_v = \Delta r_v / \Delta t$, against time (Figure 6.6) revealed distinct spikes caused by significant fluctuations in phase front position. These spikes were removed by identifying all peaks in the signal and discarding those with a prominence exceeding 0.001. Notably, filtering was carried out in dimensionless space (see Section 6.5 for further details), facilitating the use of the same prominence value for all simulations, regardless of $N$. While this processing strategy is not without limitations, unlike methods based on moving average signal reduction, it preserves the magnitude and relative temporal evolution of the signal, resulting in minimal changes to $r_v$ (see insets of Figure 6.6).

## 6.5 Model verification

### 6.5.1 Family of curves

We begin to evaluate the model's performance by investigating its ability to reproduce expected behavioural trends under variations in $N$ and $\eta_f$. The interaction between the two phases will be discussed in Section 6.5.2.

The evolution of $r_v$ for a set of simulations conducted using the forcing case $\boldsymbol{a} = N\boldsymbol{g}$ at a constant $\log(R_c/h_0) = 3.7$ and varying $N$ and $\eta_f^*$ are presented in Figure 6.7a. Reassuringly, all simulations demonstrate the three sequential stages of motion that are characteristic of an unsteady collapse: acceleration, quasi-steady motion and retardation.

The model also demonstrates consistent adherence to the expected trends as we independently vary $N$ and $\eta_f^*$. Specifically, we observe that $r_v$ propagates faster as $N$ increases while its speed of propagation decreases with increasing $\eta_f^*$. Furthermore, with increasing $N$, the separation between simulations for a given $N$ reduces, particularly
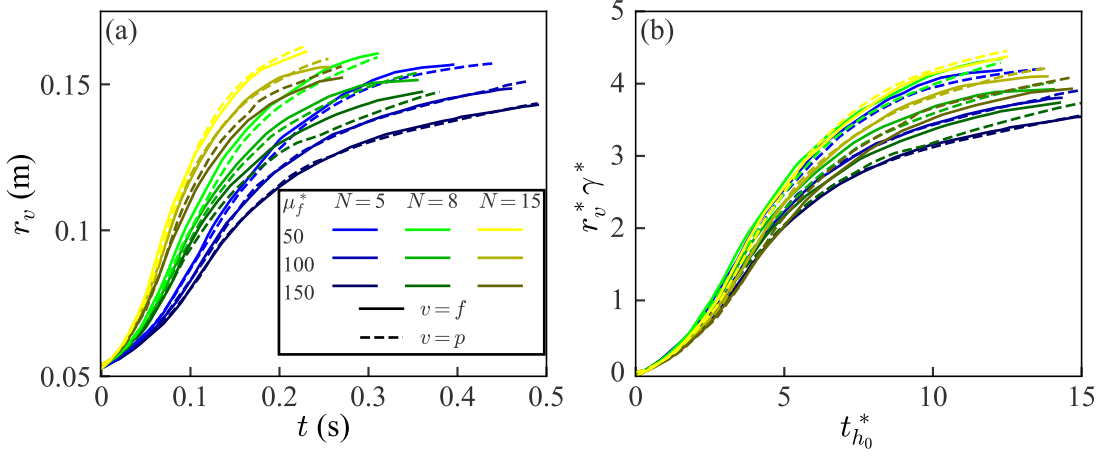
Figure 6.7: Temporal evolution of the fluid and granular phase fronts in (a) dimensional and (b) $\gamma^*$-weighted dimensionless space for a series of simulation conducted with $\log(R_c/h_0) = 3.7$ and $\boldsymbol{a} = N\boldsymbol{g}$.

during the acceleration and quasi-steady stages of motion. This observation implies that the influence of flow inertia increases with $N$ which is consistent with previous findings reported by Webb et al. (2023b)[†] and fundamental scaling principles (e.g. Iverson, 1997).

Following the approach of Webb et al. (2024a)[‖], the anticipated behaviour of the numerically modelled just-saturated column configuration can be characterised using three dimensionless parameters: $a_0$, the fluid-grain density ratio $\gamma^* = \rho_f/\rho_p$ and $B = (NgD^4\rho^2)/(h_0\eta_f^2)$. Here $\rho$ represents the effective column density, defined as $\rho = \phi_p\rho_p + (1 - \phi_p)\rho_f$.

The parameter $B$, analogous to the square of the ratio of the column Bond and Capillary numbers $(\text{Bo}/\text{Ca})^2$ (Webb et al., 2024a)[‖], quantifies the relative influence of column-scale inertial and viscous forces on collapse dynamics (Webb et al., 2023b)[†]. Since $a_0$ is held constant, we plot the evolution of the phase radial position in dimensionless density-weighted $\gamma^*r_v^*$-$t_{h_0}^*$ space (Figure 6.7b), where $r_v^* = (r_v - r_0)/r_0$ and $t_{h_0}^* = t/\sqrt{h_0/(Ng)}$. This transformation results in, approximately, a family of curves dependent on $B$, with increasing $B$ indicating a higher relative influence of column-scale inertia, leading to the faster propagation of $r_v^*\gamma^*$. Encouragingly, a similar result was obtained previously when modelling the collapses using a two-phase shallow water model (Webb et al., 2024a)[‖].

---

[†]Webb et al. (2023b) is shown in Chapter 3
[‖]Webb et al. (2024a) is shown in Chapter 5

Table 6.2: Summary of experimental test parameters.

| Test No. | $\log(R_c/h_0)$ | $N$ | $\eta_f^*$ |
|----------|-----------------|-----|------------|
| 1 | 3.7 | 5 | 50 |
| 2 | 3.7 | 5 | 100 |
| 3 | 3.7 | 5 | 150 |
| 4 | 3.7 | 15 | 100 |

## 6.5.2 Comparison with physical experiments

In this section, we further evaluate the performance of the numerical model in replicating
the expected dynamics of fluid-saturated granular column collapses. We compare the
simulation results with data obtained from four physical experiments (see Table 6.2). As
such, the simulations are conducted with $\log(R_c/h_0) = 3.7$, and they are subjected to
a complete rotational domain forcing case ($\boldsymbol{a} = \boldsymbol{a}_{cf} + \boldsymbol{a}_{co}$). For each test, we perform
two simulations to consider both the $\omega^-$ and $\omega^+$ forcing cases. The analysis is carried
out in $r_v^*$-$t_{h_0}^*$ (Figure 6.8) and $u_{v,h_0}^*$-$t_{h_0}^*$ (Figure 6.9) space, where $u_{v,h_0}^*$ represents the
dimensionless phase front velocity $u_{v,h_0}^* = u_v/\sqrt{h_0 N g}$ where $\sqrt{h_0 N g}$ is akin to a scaled
characteristic flow velocity equivalent to the local wave speed of the flow (Gray and
Edwards, 2014). Hence, $u_{v,h_0}^*$ is equivalent to a temporally evolving, phase specific
Froude number (Gray et al., 2003).

Overall, the model captures many of the experimental observations effectively. In
particular, it predicts well the time after release of the phase peak velocity, and achieves
runout distances comparable to the physical experiments. However, there are two main
sources of discrepancies between the simulations and the physical experiments, as discussed in detail by Webb et al. (2024a)[I] and summarised below.

### 6.5.2.1 Experimental-model discrepancies

The first source of discrepancy, referred to as 'experimental-model discrepancies', originates from the process of lifting the cylindrical steel casing to initiate the granular-fluid
column collapse. The presence of the casing causes a delay between collapse initiation
and a noticeable change in $r_v^*$ (Figure 6.8) because the camera's view of the collapsing
column is initially obstructed. Additionally, the initial value of $r_v^*$ is larger than $r_0$ due
to the casing's thickness. The release mechanism also leads to a lag between the initial
runout of the granular and fluid phases. The relatively large particle size of the granu-

---

[I] Webb et al. (2024a) is shown in Chapter 5
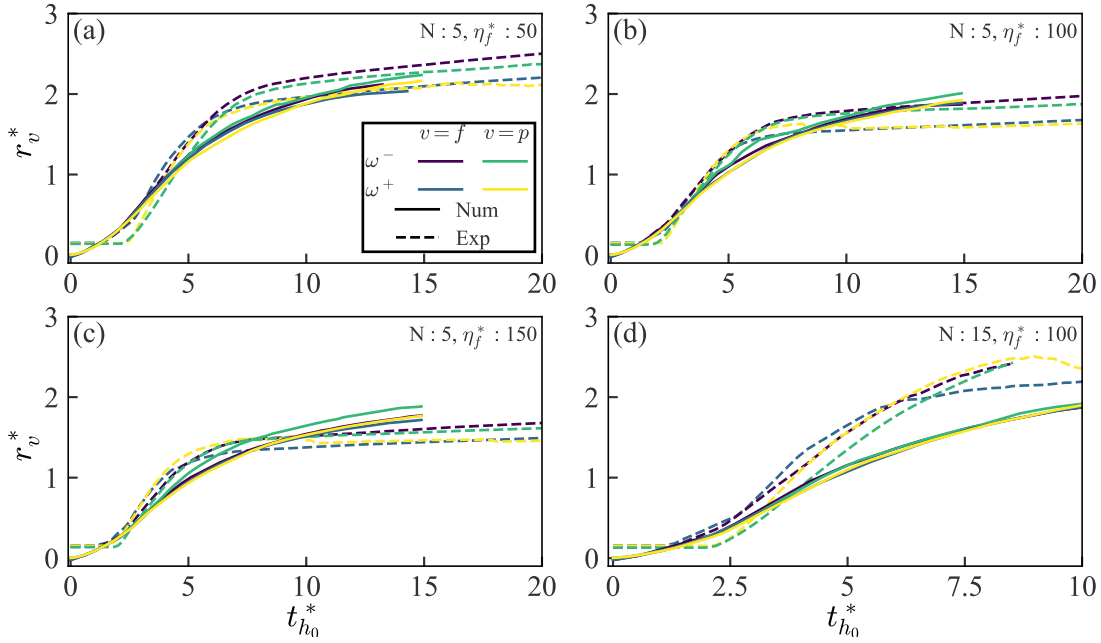
Figure 6.8: Comparison of the numerical and experimental evolution of the dimensionless phase front position $r_v^*$ with dimensionless time $t_{h_0}^*$ of four column collapses where (**a**) $N = 5$ and $\eta_f^* = 50$, (**b**) $N = 5$ and $\eta_f^* = 100$, (**c**) $N = 5$ and $\eta_f^* = 150$, and (**d**) $N = 15$ and $\eta_f^* = 100$.
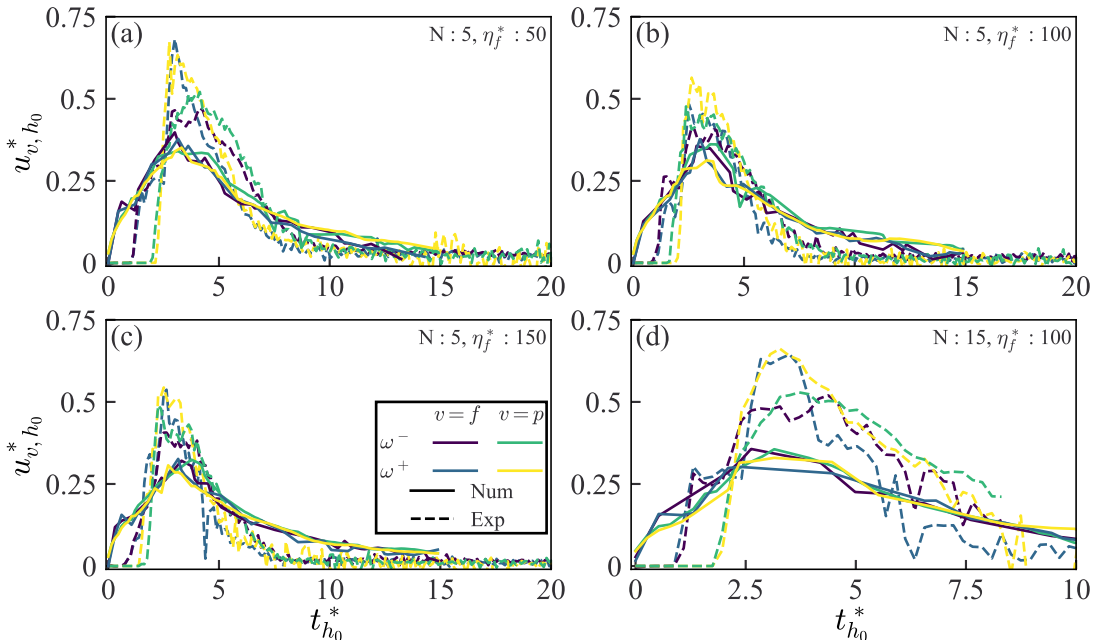


Figure 6.9: Comparison of the numerical and experimental evolution of the dimensionless phase front velocity $u_{v,h_0}^*$ with dimensionless time $t_{h_0}^*$ of four column collapses where (**a**) $N = 5$ and $\eta_f^* = 50$, (**b**) $N = 5$ and $\eta_f^* = 100$, (**c**) $N = 5$ and $\eta_f^* = 150$, and (**d**) $N = 15$ and $\eta_f^* = 100$.

lar phase causes particles to be trapped until the casing displaces far enough to release them, while the fluid can seep out from under the casing. This inter-phase lag increases with decreasing $\eta_f^*$ due to easier fluid permeation through the granular skeleton and increases with increasing $N$ due to the growing pressure gradient. Moreover, during the lifting process, the acceleration applied to the casing, relative to the collapsing mixture, induces viscous shear stresses, partially lifting the granular-fluid column with the casing. As a result, the initial gravitational potential energy, and, therefore, the peak phase velocity $u_{v,m}$, $\text{Fr}_{v,h_0}$ in dimensionless space (Figure 6.9), of the physical collapses are larger than the model's predictions. This discrepancy also increases with increasing $N$. Furthermore, the delayed collapse of the granular phase may result in it behaving more like a dry material, leading to increased mobility and a larger $\text{Fr}_{v,h_0}$.

### 6.5.2.2   Model simplification discrepancies

The second source of discrepancy, termed 'model simplification discrepancies', arises from the simplifications made in the model. Firstly, the model does not consider fluid turbulence, which becomes significant when the fluid height during the horizontal spreading phase reduces to less than a particle diameter. At such small flow heights, fluid turbulence increases due to the increased shear rate imposed on the fluid by the horizontal surface over which it flows (Batchelor, 2000). Consequently, the model underestimates the reduction in phase front velocity after $\text{Fr}_{v,h_0}$ is achieved, resulting in a more gradual retardation compared to the physical experiments (Figure 6.9). This effect is more pronounced for tests using higher viscosity fluids, potentially contributing to the overestimation of residual flow runout in simulations conducted at $N = 5$. Although Smagorinsky's turbulence model has been implemented in LBM schemes to account for fine-scale turbulence contributions to macro-scale flow dynamics (e.g. Ceccato et al., 2020; Feng et al., 2010), its omission in our study was deemed appropriate given our focus on the acceleration phase and peak flow behaviour, simplifying the model and avoiding calibration of additional parameters. Furthermore, the complexity of potential boundary layer effects and the energy cascade assumption made by the turbulence model raise uncertainties regarding its suitability.

Secondly, the model employs a Darcy-drag style phase interaction term, simplifying the actual interaction occurring in the physical experiments. Notably, the model neglects surface tension, a potentially significant force contribution, which plays a vital role in the macro-scale flow dynamics of laboratory-scale and low N centrifuge tests (e.g. Bougouin et al., 2019; Iverson, 2015; Rondon et al., 2011; Webb et al., 2023b)[†].

Surface tension effects can alter flow dynamics in two primary ways. Firstly, during the horizontal spreading phase, capillary bridges can form between contacting or closely situated particles, limiting the granular phase's ability to surpass the fluid phase front (Webb et al., 2023b)[†] (Figure 6.8). In contrast, in numerical simulations, particles can accelerate freely away from the fluid front if their inertia overcomes the inter-phase drag and, for the forcing case $\omega^+$, the fictitious retardation due to the rotating reference frame. Secondly, surface tension effects may contribute to the larger separation between downstream and upstream flow fronts observed in the physical experiments during the retardation phase (Figure 6.8). The extent of surface tension's influence on decelerating the flow would be greater for the $\omega^+$ forcing case, where $\boldsymbol{a}_{cf}$ already slows down the flow, and more particles are likely to be in contact due to the higher flow density (Leonardi et al., 2021) (see Section 6.6.1).

In conclusion, the numerical model reasonably demonstrates the idealised behaviour of a fluid-saturated granular column collapse within a centrifuge, particularly during the acceleration phase. Although certain discrepancies arise from experimental conditions and model simplifications, we have provided a qualitative understanding of these sources and their effects. The model's capability in replicating fundamental dynamics and yielding reasonable results underlines its applicability in studying these complex collapse phenomena.

## 6.6 Implications of centrifuge modelling

With the validation of the model complete, the current section investigates the influence of centrifuge modelling on flow dynamics.

### 6.6.1 Coordination number

Before looking at how the acceleration field affects macro-scale flow dynamics, it is important to understand its contribution to dynamics at the grain-scale. Thus, we begin by looking at the temporal evolution of the granular matrix. Specifically, we look at how the distribution of the particle coordination number $n_c$ (i.e. the number of particles in contact with a particle) evolves as a function of the percentage of grains $P_p$, where $P_p$ is the ratio between the number of particles with the same $n_c$ value and $n_p$. Figure 6.10 shows the distribution of $n_c$ at varying values of $t_{h_0}^*$ throughout the collapse, with a

---

[†]Webb et al. (2023b) is shown in Chapter 3
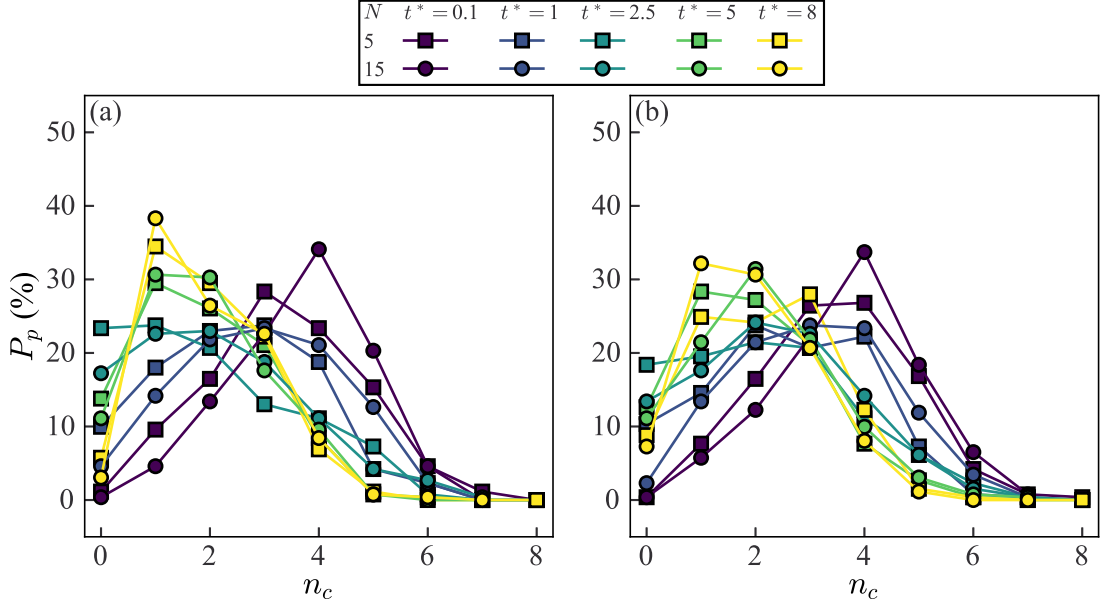
Figure 6.10: Evolution of the coordination number $n_c$ as a function of the percentage of grains $P_p$ for a series of collapse simulations with $\boldsymbol{a} = N\boldsymbol{g}$ where $N = [5,15]$, $\log(R_c/h_0) = 3.7$, and (a) $\eta_f^* = 50$ and (b) $\eta_f^* = 150$.

particular focus on the acceleration stage (i.e. $t_{h_0}^* < 3$), for a series of collapses where $N = [5, 15]$, $\log(R_c/h_0) = 3.7$ and $\eta_f^* = [50, 150]$ exposed to an acceleration field $\boldsymbol{a} = N\boldsymbol{g}$. Reassuringly, the mean value of $n_c$ is initially relatively high for all simulations and decreases as the collapsing material accelerates. $n_c = 3$ acts as a pivotal point where the $P_p$ value remains relatively constant throughout the collapse, especially when $\eta_f^* = 150$. Independently increasing both $N$ and $\eta_f^*$ appears to reduce phase separation. This insight is particularly highlighted by the lower $P_p$ values at $n_c = [0,1]$ at each value of $t_{h_0}^*$. In the case of $N$, this behaviour is partially attributed to the column construction process (see Section 6.4.3), which results in denser initial column configurations as $N$ increases, as indicated by the peak $n_c$ values at $t_{h_0}^* = 0.1$.

Our primary focus is on phase front dynamics. Therefore, the temporal variation in $P_p$ values for lower $n_c$ values is of particular interest, as these particles are likely to contribute to or interact with the granular phase front. As such, it seems worthwhile to analyse how the three different forcing cases contribute to the number of particles with low $n_c$ values. We capture these variations by plotting the cumulative $P_p$ value of particles where $n_c = [0,1]$, defined as $P_p^{[0,1]}$, against $t_{h_0}^*$ for the three forcing cases (Figure 6.11), where the full rotational domain case considers Coriolis accelerations in both the upstream ($\omega^+$) and downstream ($\omega^-$) directions, for $N = [5, 15]$, $\log(R_c/h_0) =$
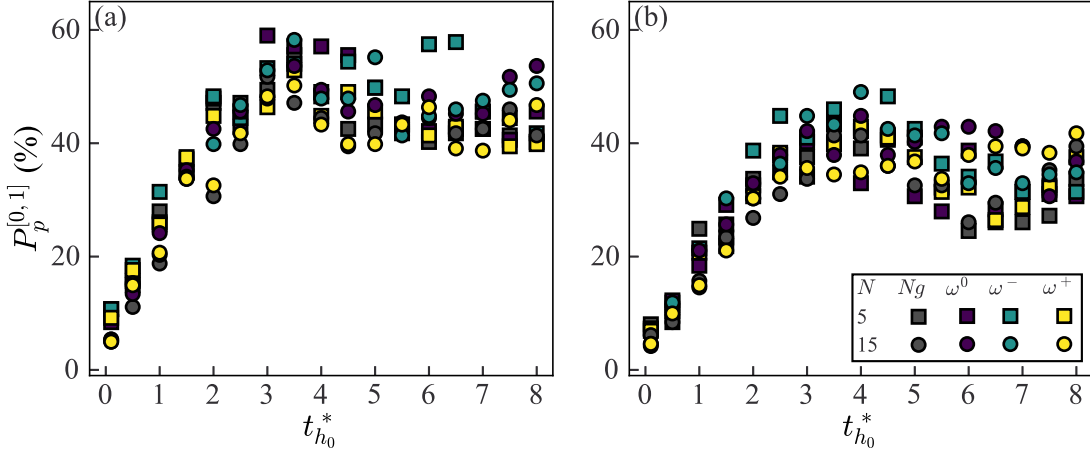
Figure 6.11: Temporal evolution of the cumulative particle percentage $P_p$ of particles where the particle coordination number $n_c = [0,1]$, defined as $P_p^{[0,1]}$. The parameter space considered includes simulations where $N = [5,15]$, $\log(R_c/h_0) = 3.7$, and when the dimensionless fluid viscosity $\eta_f^*$ is equal to (a) 50 or (b) 150.

3.7 and $\eta_f^* = [50, 150]$.

Despite the highly unsteady nature of granular matrix compactness, discernible trends emerge within the data. As observed in Figure 6.11, generally, $P_p^{[0,1]}$ increases throughout the acceleration stage until reaching a peak value at $t_{h_0}^* \approx 3.5$ aligning well with the time at which $u_v = u_{v,m}$ for the collapses discussed in Section 6.5.2. Subsequently, $P_p^{[0,1]}$ stabilises at a residual value as the collapse decelerates. The peak and residual $P_p^{[0,1]}$ magnitudes are sensitive to the fluid viscosity, decreasing with increasing $\eta_f^*$. This outcome is fairly logical as the fluid phase interacts with the granular phase through drag meaning that a more viscous fluid would have more control over the behaviour of the granular phase and less particles would 'escape' from the bulk. Within the physical experiments, the formation of capillary bridges due to the presence of surface tension would further maintain granular phase connectivity.

Figure 6.11 also shows the influence of the forcing case on the evolving structure of the granular matrix. While $P_p^{[0,1]}$ values for the differing cases are initially close, they begin to spread during the acceleration stage. Among simulations with the same $N$ and $\eta_f^*$, the simulations conducted with the forcing cases $\omega^0$ and $\omega^-$ typically achieved larger $P_p^{[0,1]}$ values than the simulations conducted with the forcing cases $\boldsymbol{a} = N\boldsymbol{g}$ and $\omega^+$. This is reassuring given that when $\boldsymbol{a} = N\boldsymbol{g}$ there is no horizontal acceleration component driving the collapse and while there is a horizontal acceleration component driving the collapse for $\omega^+$, $\boldsymbol{a}_{co}$ is acting in a direction such that it promotes flow densification (Leonardi et al., 2021). Opposing statements can be made for the former two

forcing cases. This finding is in agreement with the work of Zhang et al. (2023) who
stated that the variation in particle coordination number was the main mechanism that
allowed Coriolis accelerations to contribute to flow dynamics. For simulations where
$\eta_f^* = 50$, this trend continues to be the case during the collapse retardation stage while
the trend becomes less clear when $\eta_f^* = 150$. Independently varying $N$ does not appear
to make a significant difference to the behaviour described previously in this section.

## 6.6.2 $N$ scaling

In this section, we explore how macro-scale flow behaviour scales with $N$. We do this
by using the maximum phase front velocity $u_{v,m}$ as a simplistic indicator of acceleration
stage phase front characteristics (Webb et al., 2023b)[†]. We examine the $u_{v,m}$-$N$ rela-
tionship through a series of simulations, wherein we systematically vary the parameters
$\eta_f^*$, $\log(R_c/h_0)$, and the applied forcing case. The resulting $u_{v,m}$-$N$ space is illustrated
in Figure 6.12.

A noteworthy observation from Figure 6.12 is evident when considering the forcing
case where $\boldsymbol{a} = N\boldsymbol{g}$. The relationship between $u_{v,m}$ and $N$ can be expressed by the
equation

$$u_{v,m} = \alpha_v \sqrt{h_0 N g}, \tag{6.9}$$

where $\alpha_v$ is a constant influenced by $\eta_f^*$ and the phase of interest (i.e. whether $v = p$
or $v = f$). This constant characterises the proportion of the column's free-fall velocity
that is attained by the phase front of interest. Thus, a lower $\alpha_v$ value suggests that the
$v$ phase is experiencing significant confinement from the other phase and the external
forcing conditions. In contrast, an $\alpha_v$ value closer to 1 suggests that the phase is trav-
elling close to its free-fall velocity. The extension of this scaling to the other forcing
cases is discussed in Section 6.6.3. Given that $h_0$ and $g$ are constants within our ex-
perimental configuration, Equation (6.9) simplifies to reveal that $u_{v,m}$ scales with $\sqrt{N}$.
This outcome aligns with the theoretical velocity scaling relation for a centrifuge model
exposed to a constant gravitational field. The adequacy of these scaling fits, and those
later shown in Section 6.6.3, is also corroborated by their low values of normalised root
mean square error $\text{RMSE}_{\text{N}}$.

Furthermore, analysing the $\alpha_v$ values, as deduced from granular-scale dynamics (as
discussed in Section 6.6.1), demonstrates that higher fluid viscosities generally lead to
decreased mobility of both granular and fluid phases, resulting in lower values of $\text{Fr}_{\text{v,h}_0}$.

---

[†]Webb et al. (2023b) is shown in Chapter 3
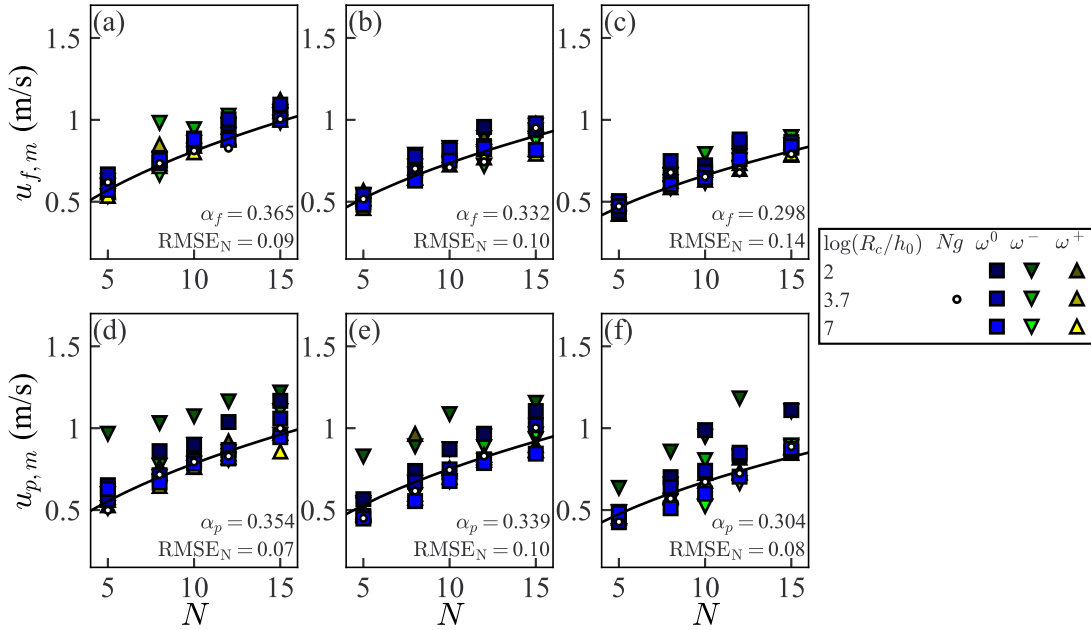
Figure 6.12: Maximum [(a)-(c)] fluid and [(d)-(e)] particle phase front velocities, $u_{f,m}$ and $u_{p,m}$, respectively, against $N$ for [(a), (d)] $\eta_f^* = 50$, [(b), (e)] $\eta_f^* = 100$, and [(c), (e)] $\eta_f^* = 150$. The fitted trend line (black) corresponding to $u_{v,m} = \alpha_v \sqrt{h_0 N g}$ is also shown for the forcing case $\boldsymbol{a} = N\boldsymbol{g}$ in each subplot.

Interestingly, for cases with $\eta_f^* = [100, 150]$, we observe $u_{p,m} > u_{f,m}$, indicating that the granular phase advances ahead of the fluid phase. However, as discussed in Section 6.5.2, the influence of surface tension makes this behaviour improbable for physical collapses at the laboratory scale.

While the impact of the forcing case and $\log(R_c/h_0)$ will be elucidated in Section 6.6.3, it is important to highlight that within the $u_{v,m}$-$N$ space, forcing cases involving horizontal accelerations ($\omega^0$, $\omega^-$ and $\omega^+$) manifest a shift in $\alpha_v$. The magnitude and direction of this shift are contingent on the specific forcing case and the value of $\log(R_c/h_0)$. Logically, $u_{v,m}$ values associated with simulations subjected to partially or fully rotational domain forcing cases approach the values observed for $\boldsymbol{a} = N\boldsymbol{g}$ as $\log(R_c/h_0)$ increases and the relative magnitude of the horizontal acceleration component diminishes. Additionally, it is observed that this shift is comparatively smaller for the fluid phase compared to the granular phase because the fluid is not frictional and, hence, there is no feedback effect between velocity and pressure (see Section 6.6.3 for further discussion).

### 6.6.3 Influence of centrifuge radius

In this section, we delve into an investigation of the influence exerted by the centrifuge's size, relative to the model's dimensions, on the dynamics of collapse. Our focus remains on the characteristic quantity of interest $u_{v,m}$ while introducing the variable $\log(R_c/h_0)$ as a pertinent factor. However, rather than examining this relationship within the $u_{v,m}$-$\log(R_c/h_0)$ space, where two independent parameters ($N$ and $\eta_f^*$) remain, we opt for a more streamlined approach. We introduce $\alpha_v$-$\log(R_c/h_0)$ as our new parameter space, where $\alpha_v$ is computed using the same methodology outlined in Section 6.6.2 but encompasses all simulated scenarios (refer to Figure 6.13). Consequently, the parameter $\alpha_v$ renders the analysis independent of the parameter $N$.

Our decision to employ the $\alpha_v$-$\log(R_c/h_0)$ space as the basis for data exploration is fortified by the statistical properties of our findings. Specifically, the mean and standard deviation of the $\text{RMSE}_\text{N}$ values, characterising the fits to Equation (6.9), are determined to be 0.1 and 0.05, respectively, suggesting that the parameter reduction method is reliable. It is crucial to emphasise that the adoption of $\alpha_v$ as a surrogate for $u_{v,m}$ only facilitates a clearer visualisation of the data. Hence, the trends discussed subsequently throughout this section persist when the data is examined within the $u_{v,m}$-$\log(R_c/h_0)$ space for each distinct value of $N$.

Reiterating the outcomes derived from the preceding sections, Figure 6.13 demonstrates the increase in collapse mobility, where $\alpha_v$ serves as an analogous measure, with decreasing $\eta_f^*$ for a given forcing case and $\log(R_c/h_0)$ value. More notably, the examination of data within the $\alpha_v$-$\log(R_c/h_0)$ space highlights the influence of the horizontal acceleration component on phase mobility. Firstly, for given values of $\eta_f^*$ and $\log(R_c/h_0)$, $\alpha_v$ generally decreases with the relative magnitude of the horizontal acceleration component which is defined by the forcing case. Thus, the forcing, $\omega^-$ (associated with Coriolis-induced flow expansion), $\omega^0$ (lacking Coriolis acceleration contribution), and $\omega^+$ (promoting flow densification), achieve descending $\alpha_v$ values. A reduction in $\log(R_c/h_0)$ not only enlarges the separation between $\alpha_v$ values corresponding to distinct forcing cases but also shifts the average $\alpha_v$ value of these three forcing cases away from the $\alpha_v$ value obtained when $\boldsymbol{a} = N\boldsymbol{g}$, a case where centrifuge-induced horizontal accelerations are absent. This result aligns with expectations, as reducing $\log(R_c/h_0)$ also increases the relative magnitude of the horizontal acceleration component. Additionally, Figure 6.13 suggests that the contribution of horizontal accelerations becomes nearly negligible when $\log(R_c/h_0) > 4$, making it suitable to assume $\boldsymbol{a} = N\boldsymbol{g}$. This
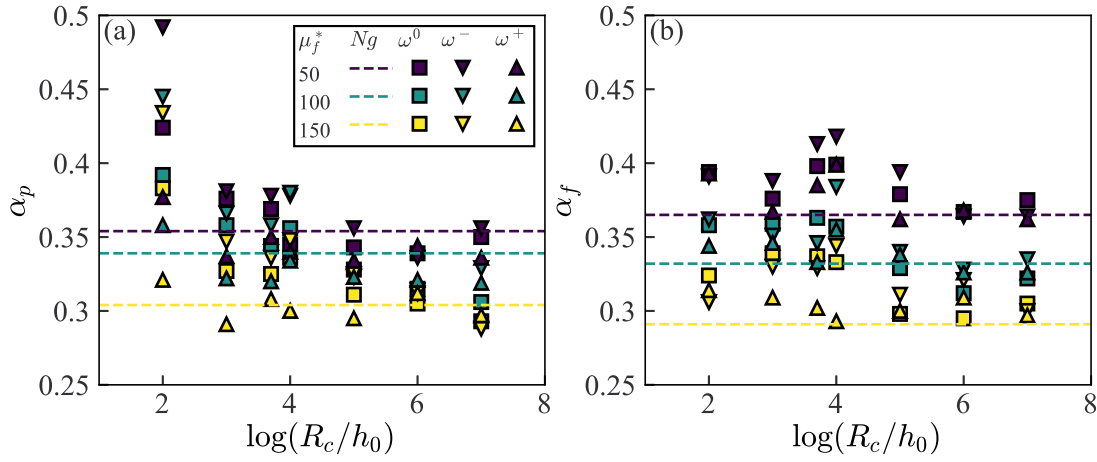
Figure 6.13: **(a)** $\alpha_p$ and **(b)** $\alpha_f$ against $\log(R_c/h_0)$ for all conducted collapse simulations. The mean and standard deviation of the $\text{RMSE}_\text{N}$ values characterising the fits to Equation (6.9) for the combined dataset are 0.1 and 0.05, respectively.

finding is consistent with the observations of Cabrera et al. (2020), who established the validity of this assumption when $\log(R_c/h_0) > 3.9$ for a dry flow travelling down a rough inclined surface.

The less intuitive aspect is the reduced sensitivity of the fluid phase to a decrease in $\log(R_c/h_0)$. While $\alpha_f$ generally increases for the forcing cases $\omega^0$, $\omega^-$ and $\omega^+$ as $\log(R_c/h_0)$ decreases, the rate of increase is notably less pronounced than that of $\alpha_p$. We posit that this disparity arises from the fact that the fluid is not frictional. Thus, the influence of the Coriolis force on fluid dynamics is weaker in comparison to the granular phase when the confining pressure (*a*) is varied. This discrepancy may also partially result from the specific conditions prevailing at the juncture of maximum flow velocity, where $\alpha_v$ is defined. At this critical stage of collapse, it is likely that the particles comprising the particle phase front are predominantly positioned ahead of or in direct contact with the fluid phase front. Consequently, the interplay and consequent drag between the particle phase front and the fluid phase become minimal. In contrast, the fluid phase front continues to engage with numerous particles behind the particle phase front. Consequently, at lower values of $\log(R_c/h_0)$, $\alpha_p$ assumes significantly larger values than $\alpha_f$, primarily attributable to the reduced interaction between the phases along the granular phase front. Further numerical and experimental work would need to be undertaken to truly understand the mechanisms at play. It seems particularly pertinent to assess the influence of the Coriolis acceleration on completely dry and fluid only collapses to remove the additional complexity of the interplay between the phases.

## 6.7    Conclusions and further work

In this study, we utilised the DEM-LBM numerical framework to simulate the collapse
behaviour of a just-saturated granular column. The model working volume was defined
within a rotating frame of reference to replicate the experimental conditions found in a
geotechnical centrifuge. By focusing on just-saturated collapses, our research aimed to
understand how centrifuge conditions impact granules and pore fluid differently. The
primary advantage of a numerical approach is its ability to explore a parameter space that
would be impractical in physical experiments. Specifically, we examined the effects of
both centrifugal and Coriolis accelerations on flow dynamics by separately considering
their contributions and varying the centrifuge radius $R_c$. We also systematically varied
the fluid viscosity $\eta_f$ and the gravitational scaling factor $N$, which are more typical test
variables.

The validation of the numerical model consisted of a two-stage approach. Firstly,
by ensuring that the predicted temporal evolution of key parameters, including phase
front runout $r_v$ and velocity $u_v$, conformed to expected trends dictated by variations
in $N$ and $\eta_f$. Secondly, by comparing the numerical predictions to physical collapse
experiments. The model exhibited a high degree of accuracy in capturing the complex
behaviours observed during the granular column collapse. Discrepancies between the
model's predictions and experimental data could be attributed to specific experimental
conditions, such as the lifting of the cylindrical casing during column release, as well
as the simplifications inherent in the model's treatment of fluid-grain and fluid-surface
interactions. Despite these limitations, the model reasonably reproduced the idealised
behaviour of a fluid-saturated granular column collapse within a centrifuge, particularly
during the acceleration phase.

The remainder of the study aimed to understand how acceleration field conditions
contribute to collapse dynamics. Its effects on the flow grain-scale behaviour were ex-
amined by analysing the temporal evolution of the coordination number $n_c$. Specifically,
the evolution of the number of particles with $n_c \leq 1$, which are those more likely to in-
teract with the granular phase front. While increasing the fluid viscosity was found to
reduce flow dilation, as found in previous studies (Leonardi et al., 2021; Zhang et al.,
2023), both the centrifugal acceleration and the Coriolis acceleration significantly in-
fluenced the evolution of the granular matrix.

At the macro-scale, the maximum phase front velocity $u_{v,m}$ was used to characterise
acceleration stage phase front dynamics. Under constant acceleration conditions, ne-

glecting centrifugal and Coriolis accelerations, $u_{v,m}$ scaled with $\sqrt{N}$ and $\alpha_v$ which is a phase-specific constant dependent on fluid viscosity. This relationship matches the theoretical velocity scaling relation for a centrifuge model exposed to a constant gravitational field.

Based on the assumption that this relationship holds for all forcing cases, the contributions of $R_c$ were investigated by utilising the $\alpha_v$-$\log(R_c/h_0)$ parameter space, making it independent of $N$. It was found that both the centrifugal and Coriolis accelerations had a significant impact on flow mobility, with centrifugal acceleration's influence increasing as $R_c$ decreased, resulting in a more pronounced curvature effect. Depending on its direction, Coriolis acceleration either expanded or densified the flow. Moreover, it was found that when $\log(R_c/h_0) > 4$, the contribution of horizontal accelerations become almost negligible which is consistent with the findings of Cabrera et al. (2020). Hence, at $\log(R_c/h_0)$ values greater than 4, it is suitable to assume a constant acceleration field (i.e. $a = Ng$). As such, with regards to the design of centrifuge experiments, this could be considered a safe value for considering the Coriolis acceleration to be negligible.

To enhance our comprehension of this subject, forthcoming research should prioritise the investigation of the Coriolis acceleration's influence on both dry and fluid-only collapses in order to better appreciate the dynamics of the fluid-saturated case, particularly with regards to particle settlement and consolidation. Furthermore, it would be beneficial to explore the influence of a rotating domain on granular flows that contain non-Newtonian interstitial fluids. Additionally, the study of surface tension effects within the phase coupling term holds potential for a deeper understanding of granular flow behaviour in more intricate scenarios.

Chapter 7

# Conclusions

## 7.1 Conclusions

The work described in this thesis aimed to explore the underlying mechanisms governing interactions between fluids and granular materials in experimental granular-fluid flows. Special attention was given to assessing the applicability of these findings to larger scale geophysical flows, such as debris flows. Considering the substantial hazards associated with debris flows, the project not only conducted physical experiments to deepen our comprehension of grain-fluid dynamics but also integrated these new insights into scalable mathematical models. These models, if incorporated into more complex schemes, have the potential to serve the dual purpose of enhancing our ability to predict debris flow behaviour and developing strategies to mitigate their impact.

In an effort to examine grain-fluid interactions in isolation from the intricate dynamics of debris flows, a simplified laboratory-scale experiment involving the collapse of an axisymmetric granular column was conducted. To explore how the dynamics of the phase interaction varied with scale, a geotechnical centrifuge was employed to artificially elevate the gravitational acceleration acting on the model. Variations in gravitational acceleration, particle size, and fluid viscosity were introduced to investigate collapse dynamics within a parameter space where the inertia of the model grains (glass beads) was significant. Throughout the experiments, the initial column saturation level was maintained at a just-saturated level, and the initial mean packing fraction was held at 0.61 (i.e. a close-packed column). The evolution of the collapse fronts were recorded using two high-speed cameras, while the basal fluid pressure at the centre of the column was monitored using a pressure sensor. A repository containing all collected runout data associated with the experiments conducted as part of this project is available at https://doi.org/10.5281/zenodo.10912850.

The initial part of the experimental investigation concentrated on the behaviour of column mixtures composed of uniform-sized inertial particles and Newtonian fluids of varying viscosity. Analysis of the collected image and pressure data revealed that

two main factors significantly influenced the interaction between the granular and fluid phases, as well as macro-scale flow dynamics. These key factors were the size of the granular pore spaces (an analogue for particle size) and the strength of the gravitational acceleration applied to the model. The size of the granular pore spaces emerged as the primary determinant of flow mobility at a given gravitational acceleration. This was due to the size of the porous network within the granular structure, in conjunction with fluid viscosity, predominantly governing the fluid's ability to permeate through the granular medium. Conversely, an increase in gravitational acceleration caused a shift in the dynamics, reducing the influence of grain-fluid interactions and instead emphasising the role of particle inertia. This shift resulted from a reduction in the impact of capillary forces between wet grains, which typically dominate flow dynamics at lower levels of gravitational acceleration such as those found in traditional laboratory experiments.

The application of Buckingham's (1914) Π theorem and a non-linear regression scheme revealed a simple power-law connection between three dimensionless parameters that characterise the initial state of the fluid-granular column which can predict several measured quantities of interest that characterise the acceleration phase of the collapsing mixtures. The main finding of this analysis is that, within the examined parameter space, all quantities of interest can be predicted independently from grain-scale surface tension effects. Instead, it is the balance of column-scale gravitational and viscous forces that govern acceleration phase collapse behaviour as seen in natural-scale debris flows with a granular phase including inertial particles.

The second stage of experimental testing involved conducting similar column collapse experiments with a non-Newtonian fluid, consisting of fine kaolin clay particles suspended in water. The concentration of these fines varied between 10 % and 20 % by mass. The purpose of introducing fine granular particles into the mixture was to extend the findings from the previous experiments with Newtonian fluids and explore how an extreme bimodal grain size distribution influenced the interaction between grains and the non-Newtonian fluid within an analogous parameter space. In this set of experiments, due to potential damage to the fluid pressure sensor caused by the fines, the analysis relied solely on image data.

By combining the data from both Newtonian and non-Newtonian fluid experiments and applying Buckingham's (1914) Π theorem, along with a least-squares fitting analysis, a power law relationship between the measured quantities of interest and five dimensionless parameters representing the initial column configuration was established. These additional dimensionless parameters were introduced to account for the presence

of the fine grains in the fluid phase, incorporating a fine grain length-scale and the fines concentration. This analysis revealed that, within the tested parameter range, the inclusion of kaolin clay particles in the fluid led to the measured variables of interest becoming coupled with micro-scale surface tension effects, a phenomenon that could be disregarded when dealing with a Newtonian fluid.

Having gained valuable insights from the physical experiments on the mechanisms governing grain-fluid interactions and macro-scale flow dynamics, the next step was to translate these findings into mathematical descriptions. To achieve this, a two-phase depth-averaged continuum model was developed, building upon the work of Meng et al. (2022), and implemented within Matlab (2020), in an effort to replicate the behaviour observed in Newtonian fluid experiments and gain a deeper understanding of collapse dynamics.

Drawing inspiration from the insights presented in previous chapters, the interaction between the grain and fluid phases was characterised using a Darcy-drag style relationship, heavily dependent on the permeability of the granular phase (i.e. the pore space size). Notably, the model diverged from other two-phase models by incorporating Larrieu et al.'s (2006) mass 'raining' scheme, which allows for phase mass to be gradually introduced into the system. This approach was necessary as the initial configuration of the granular columns did not conform to the depth-averaged assumption, a fundamental requirement for the model's derivation, resulting in a significant overestimation of vertical accelerations.

Once calibrated, the model effectively reproduced the overall dynamics of an unsteady collapse. However, treating the granular phase as a continuous medium led to an overestimation of flow runout distances and peak velocities, especially when considering larger particle sizes where the applicability of the continuum assumption is limited. Further analysis of the experimental data also revealed that interference from the column lifting mechanism contributed to some of the temporal disparities between the experimental and numerical runout and pressure signals.

Overall, the model successfully captured the relationship between macro-scale flow outcomes and variations in granular matrix pore space (i.e. particle size), especially regarding the temporal evolution of the basal fluid pressure. It also replicated the reduction in the influence of phase interaction on runout dynamics as the gravitational acceleration increased. However, the model did not fully reproduce the observed scaling behaviour in the case of the basal fluid pressure reduction. Therefore, further work is required to refine and improve our understanding of these phenomena.

Chapter 7: Conclusions

With an improved understanding of the scaling behaviour of fluid-grain interactions, the latter part of this research project delves into exploring the impact of geotechnical centrifuge modelling on collapse dynamics. This exploration is particularly relevant as geotechnical centrifuge modelling remains relatively underutilised in the field of granular flow research. To undertake this investigation, we employed a numerical framework known as DEM-LBM, which combines discrete and continuum modelling approaches. This framework was used to simulate the collapse of a just-saturated granular column within the rotating reference frame of a geotechnical centrifuge.

This modelling approach extends the work originally presented by Leonardi et al. (2021), enabling the simulation of both the fluid and granular phases subjected to an elevated gravitational field, akin to the conditions found within a geotechnical centrifuge. Utilising numerical simulations provided the advantage of exploring a parameter space that would be impractical to investigate through physical experiments. Specifically, we systematically varied factors such as the gravitational scaling factor, fluid viscosity, and the radius of the modelled centrifuge. The last of which, could only be physically tested by conducting experiments with multiple centrifuges. Additionally, this approach allowed for the independent examination of the influence of centrifugal and Coriolis accelerations on collapse dynamics.

Initially, the model was validated against experimental data, accounting for discrepancies arising from specific experimental conditions and simplifications in the model's representation of fluid-grain interactions. It was found that the model reasonably reproduced the idealised behaviour of a collapsing fluid-saturated granular column within a centrifuge, particularly during the acceleration phase.

Subsequently, the study shifted its focus to the contribution of centrifugal and Coriolis accelerations to the dynamics of collapse. This was investigated at the grain-scale primarily through the temporal evolution of the average particle contacts, known as the coordination number. A significant discovery was made in that increasing fluid viscosity reduced the overall dilation of the granular phase. Moreover, both the centrifugal acceleration and the direction of Coriolis acceleration significantly influenced the structure of the granular matrix.

At the larger flow-scale, the model was able to capture the expected centrifuge scaling relationship of the flow front velocity. This relationship demonstrates that the maximum phase front velocity is proportional to the column's free-fall velocity when centrifugal and Coriolis accelerations are not considered. Assuming that this scaling holds for all forcing cases, the study concluded by investigating the centrifuge's impact on the dy-

namics of the collapse front as a function of its radius. Key takeaways include the significant influence of both centrifugal and Coriolis accelerations on flow mobility and the growing prominence of the centrifugal acceleration at smaller centrifuge radii due to increased effective curvature. Furthermore, in alignment with Cabrera et al. (2020), the model identified a limiting centrifuge radius ratio, $\log(R_c/h_0) > 4$, beyond which the horizontal effects of centrifugal and Coriolis accelerations become negligible. Consequently, conducting centrifuge experiments with a radius surpassing this limiting value allows for the assumption that the centrifuge model is subjected to a constant gravitational field, a concept pivotal for more effective model design.

## 7.2 Future work

From this research project, a combination of physical and numerical modelling forms a robust foundation for delving into the influence of grain-fluid interactions on the macroscale behaviour of fluidised granular flows. This was achieved by employing simplified laboratory-scale experiments that were designed to mimic specific aspects of geophysical flow behaviour, particularly the stress-dependent nature of grain-fluid interactions. The following section explores potential avenues for further research, aiming to enhance the existing study and broaden its applicability to a wider contexts.

In the context of the experimental modelling carried out in this research, several important parameters affecting collapse dynamics were examined. However, it is important to note that the range of parameters tested was relatively limited, primarily focusing on a granular column that was just saturated, had an aspect ratio close to one, consisted mainly of inertial particles, and utilised a fluid where the variation in its rheological properties was limited. Expanding the scope of these parameters would significantly enhance our comprehension of grain-fluid interactions in granular-fluid flows. Some specific conditions worth exploring include:

1. The degree of granular material saturation and its impact on particle collisions.

2. The behaviour of granular materials with non-inertial particle sizes (e.g. sand), especially how their dynamics scale within the stress-elevated environment of a geotechnical centrifuge.

3. Granular-fluid mixtures containing a higher concentration of fine granular material (e.g. kaolin concentrations exceeding 50%) with a specific focus on the concentration dependent variations in pore fluid pressure reduction behaviour.

In terms of the collapse analysis process, image data was primarily utilised to examine configuration-dependent changes in macro-scale collapse dynamics by analysing the evolution of the individual phase fronts over time. Additionally, analysing the collapse evolution at the grain-scale, focusing on the motion of individual particles throughout the collapse using techniques such as Particle Image Velocimetry (PIV) (e.g. Capart and Young, 1998; Dalziel et al., 2007; White et al., 2003) or Voronoï based imaging (e.g. Capart et al., 2002), would be highly beneficial. However, such imaging techniques may suffer from the high speed nature of the experiments given that, in the current experimental configuration, image capture is limited to 240 frames per second. As such, it may be difficult to track individual particles between frames given the significant distance that they can travel at higher $g$-levels. Utilising a camera with an increased frame rate would be extremely beneficial if this extension to the project was to be considered.

Furthermore, to continue the development of the two numerical models used in the project, creating a new experimental setup that allows for the examination of a similar parameter and problem space without the influence of the lifting mechanism affecting flow behaviour could be considered. Thus, a proposed development of a new inclined planar collapse configuration is discussed in Appendix D.

Enhancements to the two-phase shallow water model could significantly improve its ability in modelling the granular phase and its interactions with the fluid phase. Currently, the model assumes a constant solid volume fraction $\phi_p$ for the granular phase in both space and time. While this assumption simplifies computational processes, it deviates from the true nature of granular flows. To address this, it is recommended to introduce an additional differential equation that accounts for the spatial and temporal variations in $\phi_p$. Iverson and George (2014) achieved this by considering how the dilation and contraction of the pore space emanates from the divergence of granular velocity through the flow depth.

Another aspect to consider is the inclusion of a secondary fine granular phase suspended within the fluid, similar to the scenario discussed in Chapter 4. This could be accomplished by adjusting the inter-phase interaction term in the model. However, to calibrate such a model, additional experimental data would be necessary. Given that the interaction term requires further investigation due to its incomplete scaling description of experimental results for the Newtonian fluid test case, dedicating time and effort to this endeavour would be worthwhile.

Similarly, enhancing the DEM-LBM scheme's efficacy involves refining its modelling assumptions to better align with the behaviour real-world experimental flows. A

crucial enhancement would entail incorporating surface tension effects into the phase coupling term, offering insight into granular-fluid flow behaviour in more intricate scenarios, such as polydispersed granular mixtures where particle size can be a significant factor. Notably, Leonardi's (2015) scheme already accommodates non-Newtonian fluid rheologies, complementing further experimental research exploring the impact of fluid rheology on collapse dynamics.

In the context of analysis, the DEM-LBM model, initially used solely for runout data analysis, could provide further benefit through the extraction of basal fluid pressure data. This has the potential to shed light on how the investigated parameter space influences the mechanisms governing pressure reduction within the flow.

The model could also be utilised in trying to further understand the effects of conducting granular-fluid flow experiments using a geotechnical centrifuge. A focused examination of friction's role in a material's behaviour, particularly the distinct behaviour of granular and fluid phases under Coriolis accelerations at small centrifuge radii, is recommended. In order to better appreciate the dynamics of the fluid saturated case, it would be pertinent to conduct an investigation that concentrated on collapsing columns comprised of a single granular or fluid phase.

Finally, considering the limitations of physical laboratory experiments in capturing the dynamics of granular-fluid flows across a multitude of scales, it is challenging to directly obtain pore-scale data. Given the significant impact that excess fluid pressures can have on macro-scale flow dynamics, the DEM-LBM model emerges as an ideal numerical scheme for investigating grain collision dynamics at the pore-scale. This exploration holds the potential to solidify our understanding of the mechanisms leading to excess pore pressure generation which are still an area of great debate in the field of geophysical flow research.

# Experimental image, pressure and non-Newtonian fluid data processing

This Appendix details the image and pressure data processing techniques used for the physical column collapse experiments undertaken in this work. The experimental procedures followed to acquire the fluid parameters of the non-Newtonian fluid mixtures used in Chapter 4 will also be briefly discussed. The goal of this Appendix is to provide further insight and lessons learnt into the data extraction processes that were used during the project that is potentially missing from the papers presented in previous chapters.

## A.1 Image data processing

### A.1.1 Image capture

The temporal evolution of the collapses was recorded by two GoPro Hero 8 Black cameras at a resolution of $1080 \times 1920$ pixels and at an acquisition rate of 240 frames per second. The cameras were mounted approximately 0.4 m above the plexiglass to a camera rig that was separately fixed to the centrifuge cradle to increase camera stability. The cameras were controlled by a computer, connected over Wi-Fi, through the Camera Controller application developed by Meyer ([2021]). All apparatus components that were located within the view of the two cameras were coated in a matte black paint to limit lens glare emanating from reflected light emitted from the lightsheet.

### A.1.2 Distortion removal

The GoPro Hero 8 is equipped with a wide angle fish-eye lens which introduces extreme lens distortion into each test image. The Matlab ([2020]) Computer Vision Toolbox camera calibration application, which employs the fish-eye camera model calibration algorithm presented by Scaramuzza and Siegwart ([2007]), was used to undistort the lines
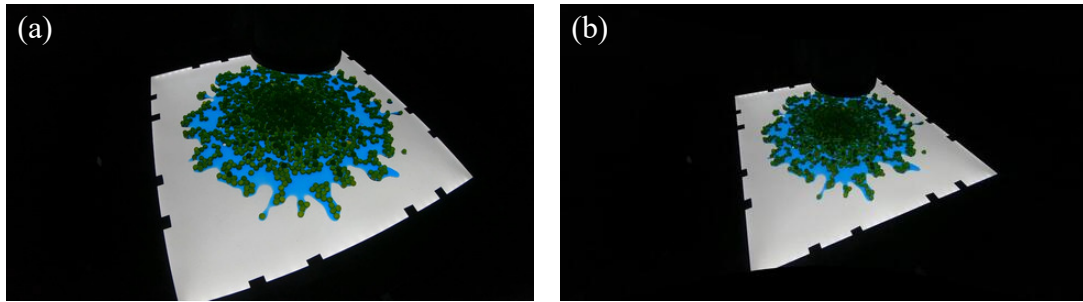
Figure A.1: (**a**) Distorted test image. (**b**) Undistorted test image where the omnidirectional fish-eye camera model calibration algorithm described by Scaramuzza and Siegwart (2007) has been applied through the use of the Matlab (2020) Computer Vision Toolbox camera calibration application. The black markers which were used as control points to transform the image can be seen at the edge of both images.

of perspective in every test image. Briefly, the onmidirectional camera calibration algorithm initially calculates the intrinsic camera parameters, comprised of mapping coefficients, the location of the distortion centre and a $2 \times 2$ stretch matrix, from a set of calibration images of a target object, a planar checkerboard pattern in this case, where the location and orientation of the target object is altered from image to image. Along with the camera extrinsic parameters that relate a world coordinate system to a camera-relative coordinate system through a $3 \times 1$ rotation matrix and a $3 \times 1$ translation matrix, the intrinsic parameters are used to convert the distorted image to an undistorted image where lines of perspective now appear straight. A typical result from the distortion removal process is shown in Figure A.1. While the images remain $1080 \times 1920$ pixels in size, the distortion removal process has resulted in the production of black, or 'dead', pixels arching above and below the test area.

### A.1.3   Image transformation

While obtaining the fixed point coordinates for the control points is straightforward (see Figure A.1), background vibrations from the movement of the centrifuge and the release of the steel tube, which initiates the granular column collapse, causes the cameras to shake. This leads to the moving point coordinates of the control points, which are the pixel coordinates of the control points within the test image, to differ from frame to frame. Hence, the moving point coordinates must be obtained for every image captured throughout the duration of the test. The initial moving point coordinates of the control points are selected by the user from the first test image. The movement of the selected coordinates within the remaining test images are then tracked by an open source 2D
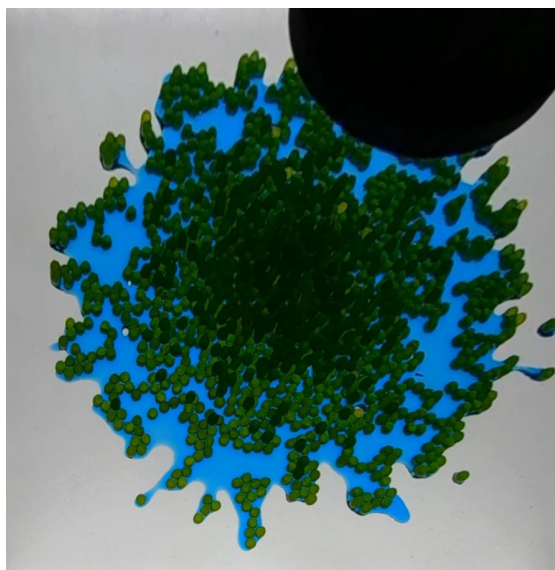
Figure A.2: Typical transformed test image where 1 pixel within the image is equivalent to 0.5 mm in the object plane.

Digital Image Correlation (DIC) software Ncorr (Blaber et al., 2015). The DIC algorithm uses image processing techniques to calculate displacements within interrogation windows, which are small regions of interest, between successive test images. In this case, the software has been modified to track the evolution of $n_w$ interrogation windows which are $32 \times 32$ pixels in size and centred on the $n_w$ visible control point locations initially selected by the user within the test image. The relative displacements of these control points are tracked across each test frame which allows the pixel coordinate location of each corner to be calculated for all test images. The sub-pixel accuracy of Ncorr has been shown to compare favourably to other commercially available DIC softwares and Finite Element Models (e.g. Harilal and Ramji, 2014) which provides great confidence in the validity of the image transformation as both the moving point coordinates and the fixed point coordinates can be measured to a high level of accuracy.

From preliminary testing, the relative displacement of a moving control point is generally less than 5 pixels in the vertical and horizontal coordinate directions relative to an image's pixel coordinate system. This suggests that the size of the interrogation window selected to track the lightsheet corners is sufficient.

The relative vertical and horizontal displacements for a given test image are then added to the original moving point coordinates to obtain the moving point coordinates for that test image. During the transformation, a scale factor of 2 is applied meaning that 1 pixel within the transformed image is equivalent to 0.5 mm in the object plane

which is equivalent to the approximate spatial resolution of the original distorted test image. This allows morphological flow information to be extracted directly from the transformed images, an example of which is shown in Figure A.2, at any stage throughout the evolution of the collapse.

### A.1.4 Image masking

Even though the camera shutter speed and aperture settings were set to minimise variations in the background light intensity provided by the lightsheet, variations near the source of the light and along the evolving flow front could still be observed. To limit the effects of this noise during image analysis, while maintaining the structure of the flow, the test images were masked, where all background pixels were set to a grey scale pixel intensity of 0 (black), following a common segmentation approach based on intensity thresholding. Whilst other segmentation techniques, based on texture (e.g. Ilea and Whelan, 2011) or clustering (e.g. Yuheng and Hao, 2017) methods exist, threshold by intensity segmentation was used due to the significant colour contrast between the background lightsheet and the foreground flow.
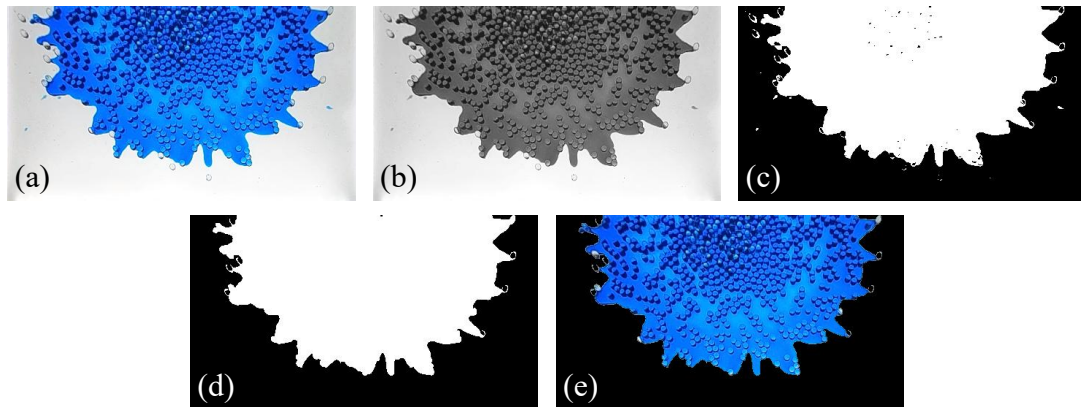


Figure A.3: Visual representation of the image masking process. (**a**) Original cropped test image. (**b**) Grey scale cropped test image (pixel intensities within the grey scale integer range of 0 and 255). (**c**) Binary test image (pixel intensities within the binary integer range of 0 and 1). (**d**) Mask of test image. (**e**) Original test image with the mask applied.

To simplify later image analyses, the steel test tube was completely removed from the majority of test frames by initially cropping the transformed test images and removing the image pixels found in the upper 45% of pixel rows (Figure A.3a). The in-built Matlab (2020) function 'rgb2gray' was used to set the image colour map to grey scale

where all pixels within the image were assigned a grey scale intensity value ranging from 0 (black) to 255 (white) (Figure A.3b). Matlab's Image Processing Toolbox was then used to design a threshold segmentation scheme, consisting of image binarisation, hole filling and region removal stages.

The image binarisation stage was carried out using a grey scale threshold where grey scale image pixels with an intensity lower than this value are included within the binary image foreground (pixel intensity of 1), and those with a greater intensity value are included within the binary image background (pixel intensity of 0) (Figure A.3c). Through the evaluation of test image histograms, it was deemed that image contrast enhancement, typically achieved using the adaptive histogram equalisation technique CLAHE (Zuiderveld, 1994), was not required prior to thresholding due to the extreme levels of contrast already present between the fluid, the particles and the lightsheet in the original grey scale images. Otsu's method (Otsu, 1979), which can be used to obtain the appropriate grey scale threshold of an image, was also disregarded as it was deemed more appropriate to binarise all images using a singular threshold value given the consistent lighting conditions produced by the diffused light system.

The resulting binary test images often showed, as seen by the small regions of black within the white mass in Figure A.3c, that the threshold segmentation incorrectly characterised parts of the image foreground as being a part of the image background. Small regions of white pixels within the black background of the binary image could also occur due to small droplets of interstitial fluid resulting from spray during the release of the steel column. This was corrected by setting pixel regions smaller than the area of the particle size being tested that were initially characterised as foreground to background regions. This version of the binary image, displayed in Figure A.3d, was then used to mask the original RGB test image (Figure A.3e). The entire masking process has been visually summarised in Figure A.3. For the case of the official experiments, where matte beads that were either red or yellow in colour were used, an analogous process was followed to obtain a mask of the image that only considered the granular phase front. In this case, instead of using rgb2gray to create the grey scale image, the blue colour channel of the original image was used instead. Since the fluid phase was dyed blue, this created extreme contrast between the two phases within the grey scale image.

## A.1.5 Data extraction

With the shape of the two phase fronts captured by independent masks, the final task is to obtain an average distance measurement between the edge of the two phases (i.e. the edge of the two masks) and the central position of the original column which has been referred to in the previous chapters as $r_v$. This was achieved by taking the masks of the two phases for each test image and converting them to a polar coordinates system with respect to the radius from the column centre $r$ and the angle $\theta$, where the $x$ and $y$ directions of the Cartesian image reference frame can be defined in a polar reference frame as follows

$$x = r\cos\theta, \tag{A.1}$$

$$y = r\sin\theta. \tag{A.2}$$

Dividing the $\theta$ domain into 1000 subdomains, the phase front edge could then be acquired from the image masks by extracting the material point that was furthest from the column centre for each value of $\theta$ (Figure A.4b). Hence, the value of $r_v$ for the test image was then defined as the average distance from the column centre of phase $v$ across the $\theta$ domain (Figure A.4c). The phase front extraction process has been described visually in Figure A.4.
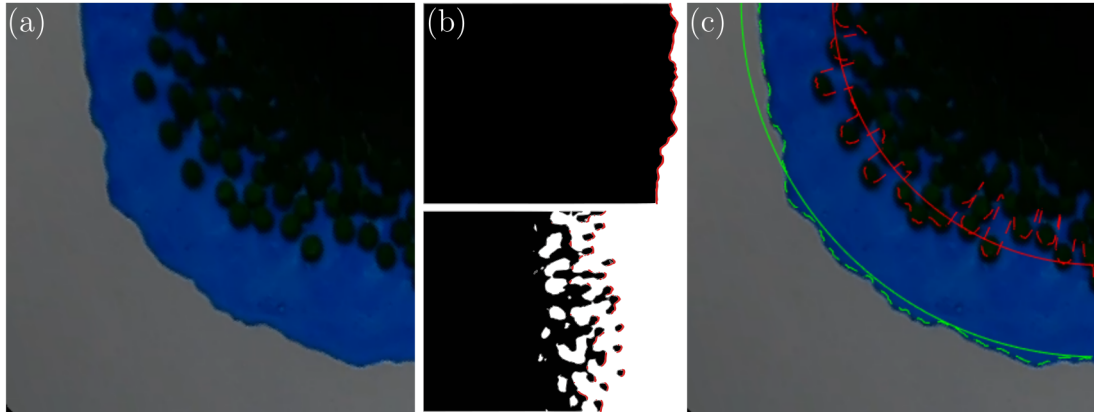


Figure A.4: Visual representation of the data extraction process used to obtain the average phase front radius of each test image. (**a**) Original transformed and cropped test image. (**b**) Masks of the fluid (top) and granular (bottom) phases transformed to the polar reference frame where the red markers represent the extracted phase front position for each $\theta$ subdomain. (**c**) Example of the final phase front extracted from the test image (available at http://doi.org/10.17639/nott.7277). The raw (dashed) and averaged (line) radial positions of the fluid (green) and granular (red) phase fronts are shown.

## A.2    Fluid pressure data processing

### A.2.1    Pressure measurement acquisition

The evolution of basal fluid pressure beneath the centre of the granular column was monitored using a Honeywell miniature pressure sensor (Model 24PCDFA6G), positioned approximately 1 mm into the plexiglass surface (refer to Figure A.5). This sensor had a pressure range of 200 kPa, and its measurement accuracy, determined by calculating the average reading error when applying a known pressure to the sensor, was within $\pm\,0.1$ kPa. The sensor was directly linked to a junction box, which transmitted data to an NI 9205 Data Acquisition (DAQ) module at a sampling rate of 125 kHz. Subsequently, the data was relayed to the CompactRIO system situated near the centrifuge's axis of rotation, which then transferred it to an external computer for subsequent analysis.

The sensor operates by converting the deformation of a flexible diaphragm into an electrical voltage output, which can be calibrated to obtain the applied pressure (as detailed in Section A.2.2). It's important to note that the diaphragms' dynamic behaviour can be highly sensitive to chemical changes, highlighting the need to maintain their cleanliness. When Newtonian fluids were used, a simple post-test rinse with water sufficed to uphold the sensor's integrity.

However, in the experiments conducted in Chapter 4, where fine kaolin clay particles were suspended within the fluid phase, additional protective measures were necessary to prevent the kaolin clay from adhering to the diaphragm and altering its deformation characteristics. Various strategies were explored, employing filter paper as a semi-permeable barrier to cover the sensor opening, while still allowing accurate pressure readings. While this approach succeeded at lower gravitational levels, higher fluid pressures and faster particle velocities frequently led to the filter paper tearing around the sensor opening, enabling clay particles to enter the sensor. Several sensors were rendered inoperable as a consequence, leading to the decision, as discussed in Chapter 4, not to collect fluid pressure data for the non-Newtonian fluid experiments. Consequently, for future projects aiming to measure fluid pressure in fluids containing a suspension of fine particles, it is recommended to employ pressure sensors that can accommodate porous stones inserted into them. These stones can act as a barrier to prevent fine particles from infiltrating the sensor. Numerous manufacturers offer these stones in varying porosity grades, allowing the system to be configured based on the size of the fine particles present.
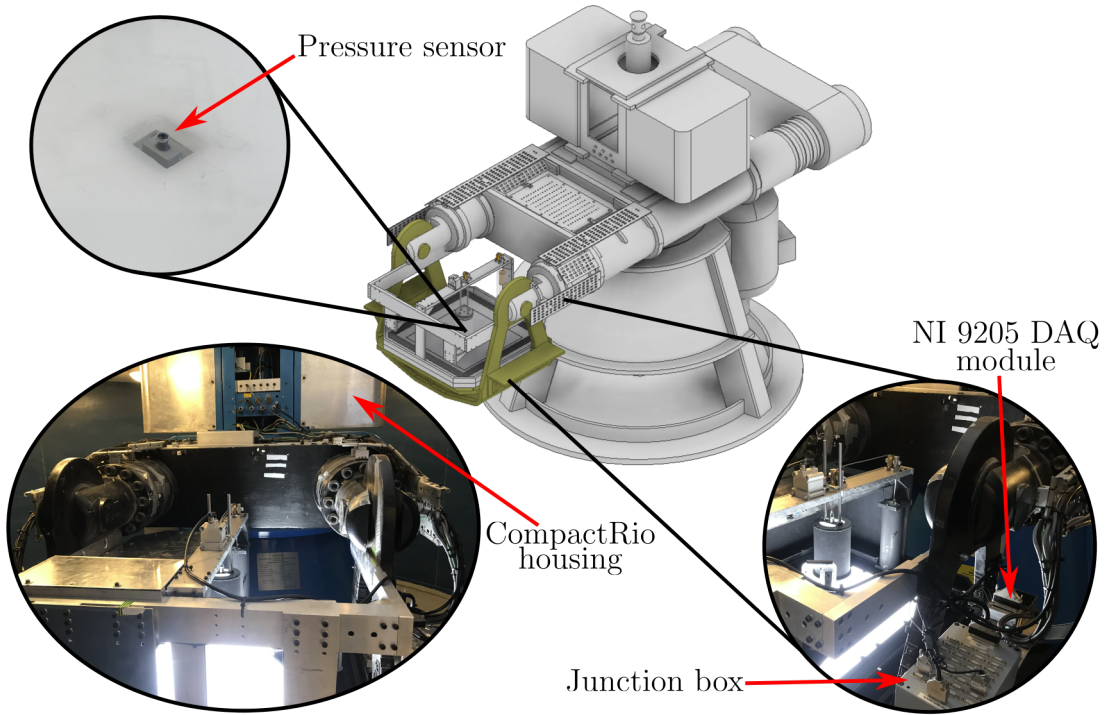
Figure A.5: Schematic detailing the key components of the pressure acquisition system.

## A.2.2 Instrument calibration

This section outlines the general procedure employed to calibrate the pressure sensors utilised in the experiments. Given that calibration occurred on multiple occasions during the project, such as when a sensor required replacement due to damage or to verify that its calibration parameters had not drifted over time, I am going to refrain from presenting specific calibration data.

The calibration of the pressure sensor involved a two-step process. Initially, the aim was to transform the voltage output $V$ from the sensor into a pressure value $P$ equivalent to the hydrostatic pressure exerted by the fluid column directly above the sensor. This phase of the calibration took place under Earth's gravity using a simple standpipe arrangement (refer to Figure A.6). This setup enabled systematic variation of the fluid level $h_w$ up to a height of 3 m, equivalent to a hydrostatic pressure $P = \rho_w g h_w$ of 30 kPa, considerably higher than the fluid pressure encountered during centrifuge testing. Utilising this data, you could establish a linear relationship between the pressure sensor's voltage output $V$ and the externally supplied hydrostatic pressure $P$, described by the following expression

$$V = V_0 + a_V P, \tag{A.3}$$

where $V_0$ represents the $y$-intercept, and $a_V$ signifies the linear gradient.
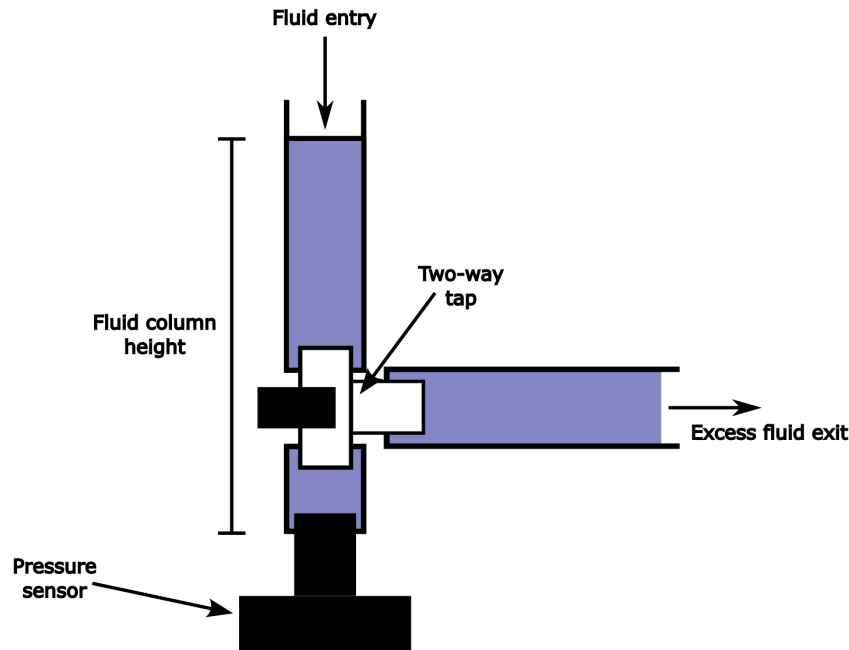


Figure A.6: Experimental standpipe configuration for pressure sensor calibration in Earth's Gravity. A two-way valve is employed to regulate the fluid level above the pressure sensor, enabling conversion into equivalent hydrostatic pressure. To ensure complete air bubble removal from the standpipe prior to calibration, both the sensor and the short section of tubing below the two-way valve are saturated with water before increasing the fluid level.

The second stage of calibration accounted for the pressure sensor's behaviour within the elevated acceleration field of the centrifuge. Exposure to the heightened acceleration field alone, considering that the diaphragm's axis of deformation is perpendicular to the centrifugal acceleration's line of action (see Figure 3.2), was adequate to deform the sensor's diaphragm and record a change in voltage output. Consequently, calibration flights were conducted, with the sensor positioned in the experimental apparatus, mimicking its placement during official tests and subjected to various, systematic $G$ levels. This process aimed to determine the voltage output associated with the natural deformation of the diaphragm at test-specific $G$ levels. These flights were executed without constructing a fluid column on top of the sensor, but the sensor's opening was filled with water to maintain the diaphragm's saturation, as it would be under standard test conditions. Subsequently, the voltage output corresponding to the natural diaphragm deformation under elevated acceleration could be subtracted from the signal output of the column collapse experiments. This ensured that a pressure reading of 0 kPa in the

signal aligned with the scenario where no fluid column extended above the sensor's opening. For a comprehensive description of this pressure sensor calibration method, the reader is referred to Cabrera (2016).

# A.3 Obtaining non-Newtonian fluid material parameters

This section provides an overview of the techniques employed to determine the material parameters of the non-Newtonian fluids used in the experimental testing discussed in Chapter 4. The focus is on fluids comprising kaolin clay particles suspended in water. The key parameters of interest are fluid density $\rho_f$, viscosity $\eta_f$, and surface tension $\sigma_f$.

## A.3.1 Density

The calculation of $\rho_f$ is straightforward and akin to determining the average column density $\rho$ as discussed in previous chapters. $\rho_f$ is obtained as a weighted average of the mass densities of the water and kaolin clay phases defined as

$$\rho_f = C_k \rho_k + (1 - C_k)\rho_w, \tag{A.4}$$

where $C_k$ is the mass concentration of kaolin clay suspended in water, and $\rho_k$ and $\rho_w$ are the densities of kaolin clay and water, respectively.

## A.3.2 Viscosity

As the kaolin-water suspension is non-Newtonian, with shear-rate dependent viscosity, a representative value for viscosity $\eta_f$ was required for the scaling analysis. A characteristic shear rate $\dot{\gamma}$ was defined relative to the expected free-fall velocity of the column

$$\dot{\gamma} = \sqrt{G/h_0}. \tag{A.5}$$

A Brookfield viscometer was used to measure the viscosity at various shear rates ranging between $0.46\,\mathrm{s}^{-1}$ and $92.6\,\mathrm{s}^{-1}$ which are typical shear rates in the drainage and runout phases of the collapses. Power law functions relating $\eta_f$ and $\dot{\gamma}$ were then fitted for each test fluid, providing representative viscosity values corresponding to the gravitational acceleration used in each test. Figure A.7 shows the data collected from the Brookfield

viscometer tests, and the subsequent power law fits, for the two non-Newtonian fluids used in Chapter 4 where $C_k = [0.1, 0.2]$.
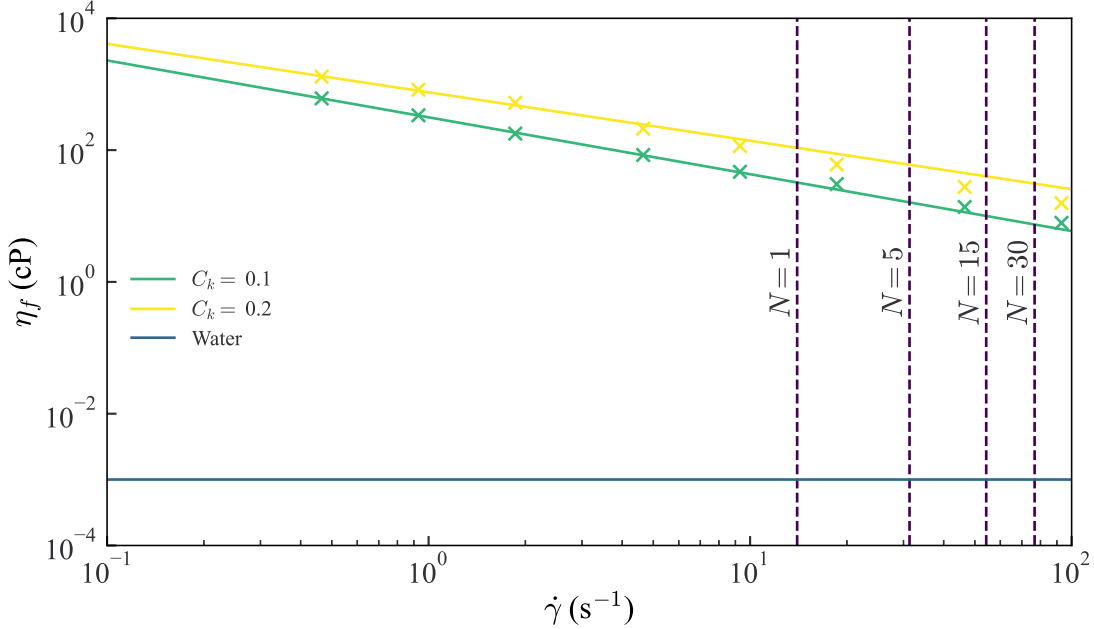


Figure A.7: Data from the Brookfield viscometer tests for the two non-Newtonian fluid suspension used in Chapter 4 showing fluid viscosity $\eta_f$ against shear rate $\dot{\gamma}$. The power law lines of best fit for each kaolin concentration are also shown.

### A.3.3 Surface tension

The surface tension of the non-Newtonian fluids were determined using the classic capillary rise method, based on the equilibrium of forces acting on a capillary tube liquid column (Dole, 1951; Richards and Carver, 1921). A Tensiometer from Duran Wheaton Kimble was employed for this purpose. The surface tension of the fluid was calculated using the height difference between the capillary rise and depression $h_c$, introduced by applying negative and positive pressures within the apparatus

$$\sigma_f = \frac{1}{2} h_c r_c \rho_f g, \tag{A.6}$$

where $r_c$ is the radius of the capillary. Calibrations to $g$ based on latitude, longitude, and altitude coordinates of the test location were also conducted. Calculation of the surface tension for each non-Newtonian fluid used throughout Chapter 4 was repeated five times to ensure a sufficient level of accuracy for the scaling analysis.

# Collapse complexities

The following Appendix details a set of experiments aimed at investigating peculiar trends observed in the initial stages of pressure signals, as mentioned in Chapters 5 and 6. The pressure complexity will first be highlighted before discussing the methodology followed to investigate its cause. The methodology as to how this complexity was dealt with when analysing the pressure signals was summarised previously in Section 5.5.1. The Appendix then goes on to investigate how these newfound insights might impact the conclusions drawn in Chapter 3. Specifically, those concerning the evolution of phase front separation and the scaling relation described by Equation (3.4).

## B.1 Understanding the mechanisms controlling the delay in column release

Figure B.1 displays the unfiltered pressure signal $P$ against $t^*_{h_0}$ for the collapse of a column filled with only water at $G = 45.22\,\mathrm{m\,s^{-2}}$. In theory, the collapse of an unconfined fluid column should yield a hyperbolic pressure dissipation curve, corresponding to the gradual loss of hydrostatic pressure over time. However, in our experiments, prior to the anticipated smooth dissipation curve, there is an initial drop in pressure, followed by a subsequent increase, ending at $t^*_{h_0} \approx 1$. This phenomenon has been consistently observed in terms of magnitude and timescale, suggesting that the experimental setup exerts external forces on the collapsing mixture.

This behaviour was first investigated by analysing the force balance of the column lifting mechanism under an elevated gravitational acceleration (as illustrated in Figure B.2). Assuming a frictionless pulley system and that the mass of the steel cylinder $M_c$ is always less than the mass of the steel mass used to lift the column $M_m$, the resultant force of the system $F_r$ is given by

$$F_r = F_m - F_c, \tag{B.1}$$
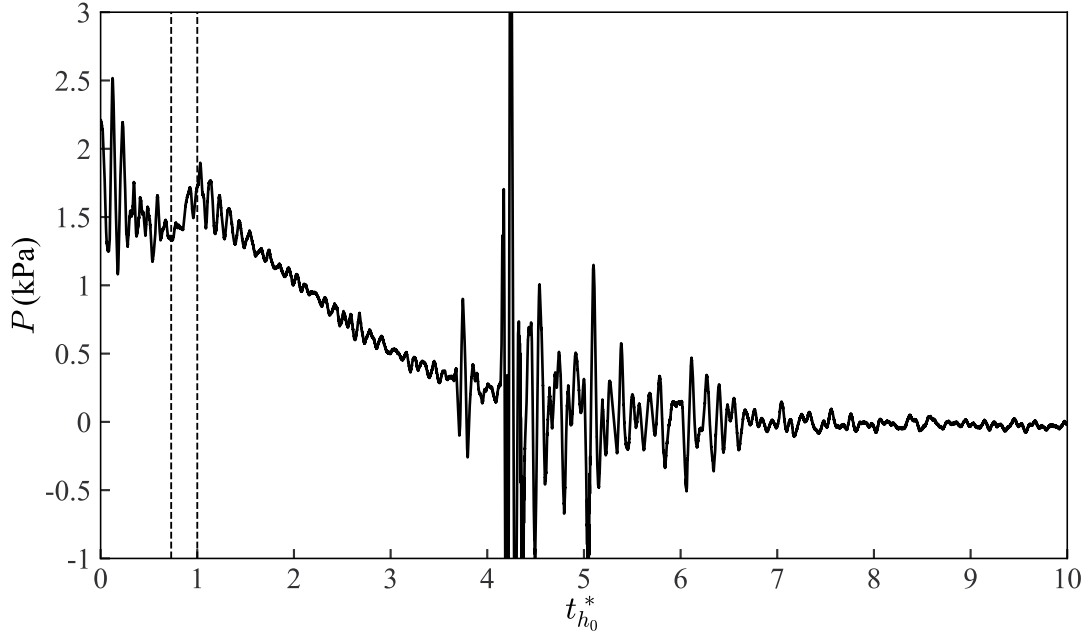
Figure B.1: Evolution of the raw basal fluid pressure signal with $t_{h_0}^*$ for a water only collapse at $G = 45.22\,\mathrm{m\,s^{-2}}$. The dotted lines align with the times at which the minimum and maximum pressure of the pressure dip occur.

where $F_m = GM_m$ and $F_c = GM_c$ are the weights of the steel mass and the steel cylinder, respectively. Consequently, the resultant acceleration of the system $a_r$ can be calculated as

$$a_r = \frac{F_r}{M_m + M_c}. \tag{B.2}$$

Considering that the free surface of the collapsing mixture accelerates towards the horizontal plane with an acceleration of $G$, the time at which point the free surface of the collapsing mixture is in line with the bottom of the steel cylinder $t_{\mathrm{meet}}$ can be determined as

$$t_{\mathrm{meet}} = \sqrt{\frac{h_0}{G + a_r}}. \tag{B.3}$$

For the collapse scenario shown in Figure B.1, where $h_0 = 50\,\mathrm{mm}$, $M_m = 3.6\,\mathrm{kg}$ and $M_c = 0.92\,\mathrm{kg}$, $t_{\mathrm{meet}} = 0.0263\,\mathrm{s}$. Nondimensionalising $t_{\mathrm{meet}}$ by $t_I$ yields $t_{\mathrm{meet}}^* = 0.79$. This theoretical value of the instance where the collapsing mixture is no longer in contact with the steel cylinder, is a good approximation of when the dip in pressure in the experiment reaches its minimum at $t_{h_0}^* \approx 0.73$. The maximum of the subsequent rise in pressure occurs just after $t_{h_0}^* = 1$ which is when the free surface of an unconfined column would be expected to collide with the horizontal plane.

Based on a detailed analysis of collapse images and pressure data, we formulated a qualitative hypothesis for this mechanism. Upon collapse initiation, the significant acceleration of the steel cylinder relative to the initial motion of the collapsing column induces viscous shear stresses between the two surfaces that are capable of partially lifting the collapse material. This results in a reduction in pressure applied to the pressure sensor, reaching a minimum at $t_{h_0}^* \approx t_{\text{meet}}^*$ when the column is theoretically no longer in contact with the cylinder. The subsequent rise in pressure is attributed to the dynamic pressure generated by the lifted material impacting the horizontal plane, ceasing at $t_{h_0}^* \approx 1$ when the free surface of the collapsing material collides with the horizontal plane.
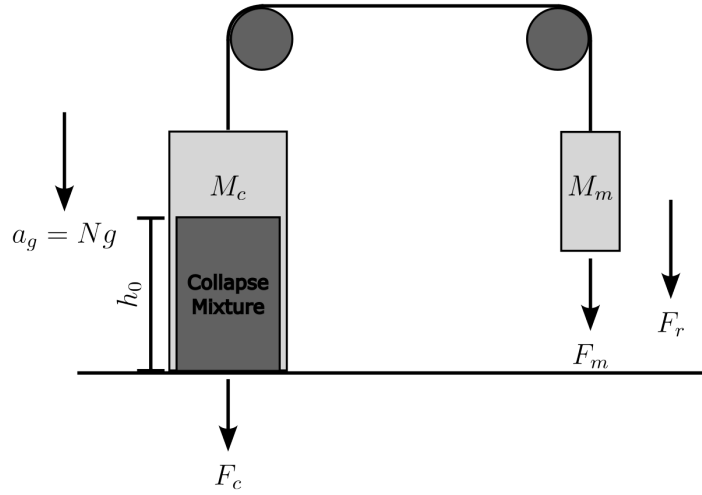


Figure B.2: Schematic of the force balance during the column lifting process.

To validate this hypothesised mechanism and gain a deeper understanding of this effect, a series of purely fluid column collapse experiments were conducted where $\eta_f$, $h_0$, $M_m$, $G$, the roughness of the cylinder and, the ability for air to enter the top of the cylinder were all varied. Table B.1 summarises these experiments, while the unfiltered pressure signals from these tests are presented in Figure B.3 in $t_{h_0}^*$-$P$ space where test w05005H has been used as a reference case in each subplot.

Figure B.3a demonstrates that both the roughness of the internal cylinder wall and the fluid viscosity have little influence on the magnitude and timescale of the dip and rise effect. Even in the case of Test g05005H, which uses the most viscous fluid used throughout all centrifuge testing, the timing of the peak of the rise is only offset by approximately $0.25t_I$ from the w05005H which uses a fluid phase of water. Hence, for the range of viscosities studied, the shear stress between the fluid and the steel cylinder appears significant enough to lift a proportion of the collapsing column as the steel

Chapter B: Collapse complexities

Table B.1: Summary of the experiments performed to better understand the influence of the column lifting mechanism.

| Test ID | $h_0$ (mm) | $\eta_f$ (cP) | $G$ (m s$^{-2}$) | $M_m$ (kg) | Notes |
|---|---|---|---|---|---|
| w05005H | 50 | 1.0 | 45.2 | 3.6 | |
| g05005H | 50 | 156.8 | 45.2 | 3.6 | |
| w05005L | 50 | 1.0 | 45.2 | 2.6 | |
| w10005L | 100 | 1.0 | 45.2 | 2.6 | |
| w05005H1 | 50 | 1.0 | 45.2 | 3.6 | Air inflow reduced by half. |
| w05005H2 | 50 | 1.0 | 45.2 | 3.6 | No air inflow. |
| w05005HSP | 50 | 1.0 | 45.2 | 3.6 | Cylinder interior lined with 240 grit sandpaper. |
| g05014H | 50 | 15.7 | 137.4 | 3.6 | |

cylinder accelerates away from the horizontal plane.

Figure B.3b illustrates the impact that varying $G$ has on this behaviour. Increasing $G$ by a factor of three results in a proportional increase in pressure difference between the maximum and minimum pressures of the dip. The duration of the dip appears to scale with $t_I$.

Figure B.3c presents a subset of experiments aimed at investigating whether the phenomenon is due to suctions induced by insufficient air volume displacing the collapsing material as the cylinder is lifted. The results indicate that covering one of the holes at the top of the cylinder leads to no change in behaviour, implying that the effect persists even when air flow into the top of the cylinder is reduced by half. Completely sealing the top of the cylinder induced significant suctions between the cylinder wall and the collapse material, causing the entire column to be lifted and negative pressures to be induced. Therefore, it was concluded that the level of air flow into the top of the tube was not the primary source of the lifting behaviour.

Figure B.3d explores the influence of cylinder lifting speed and the initial height of the column. Reducing the lifting speed of the column by decreasing the mass of the steel mass results in a pressure dip of similar magnitude to the reference test w05005H, with $t^*_{\text{meet}}$ shifted by approximately 0.41. This is likely due to the fact that, at collapse initiation, the gap between the bottom edge of the rising column and the horizontal plane over which the collapse spreads widens more slowly. Consequently, the rate of fluid discharge from the centre of the column is reduced because the rising column can interfere with the motion of the fluid for a longer duration.
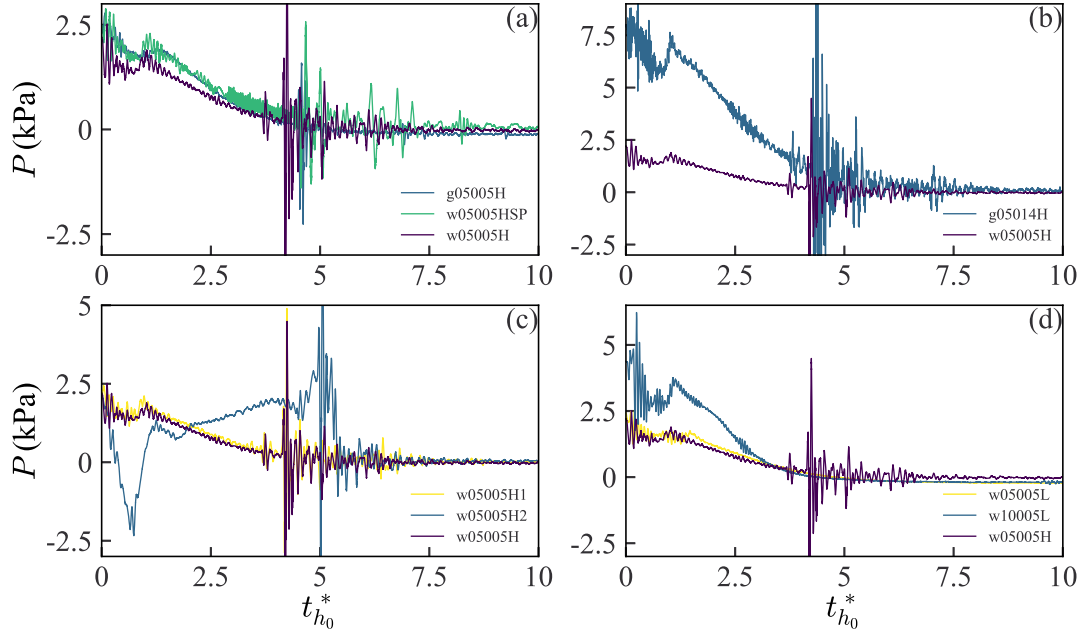
Figure B.3: Evolution of the raw basal fluid pressure $P$ signals with $t^*_{h_0}$ for the different experiments performed to investigate the influence of the column lifting mechanism. The effects of (**a**) column roughness and viscosity, (**b**) gravitational acceleration, (**c**) the entry of air into the column, and (**d**) the mass of the steel mass used to lift the column were all considered.

Conversely, increasing the initial height of the column, along with a lighter steel mass, results in an increase in pressure variation proportional to the increase in surface area and a shift in $t^*_{\text{meet}}$ by approximately 0.07. In this case, the reduced discharge rate due to the slower column release speed is mostly compensated for by the increased pressure head of the taller column, leading to a reduction in the offset. The increased contact area results in greater viscous effects between the collapse material and the column wall, causing more fluid to be lifted along with the column and a larger reduction in pressure during the early stages.

# B.2 Quantifying the delay of the granular column release

The issues concerning the column lifting mechanism emerged later in the project, particularly during the numerical modelling phases outlined in Chapters 5 and 6. Consequently, it becomes essential to evaluate its implications on the findings drawn from the

Table B.2: Summary of $t_{\mathrm{gap}}$ values across the examined $G$-$d_p$ parameter space. $t_{\mathrm{gap}}^*$ values for each inertial particle size are also shown.

| $G$ (m s$^{-2}$) | $t_{\mathrm{gap}}$ (s) | | | |
| --- | --- | --- | --- | --- |
| | $d_p = 2\,\mathrm{mm}$ | $d_p = 4\,\mathrm{mm}$ | $d_p = 6\,\mathrm{mm}$ | $d_p = 8\,\mathrm{mm}$ |
| 9.81 | 0.026 | 0.037 | 0.045 | 0.052 |
| 45.22 | 0.012 | 0.017 | 0.021 | 0.024 |
| 137.64 | 0.007 | 0.010 | 0.012 | 0.014 |
| 275.45 | 0.005 | 0.007 | 0.009 | 0.010 |
| $t_{\mathrm{gap}}^*$ | 0.367 | 0.519 | 0.636 | 0.735 |

physical experiments detailed in Chapters 3 and 4. One crucial aspect to consider is the time delay between the initiation of collapse, where the fluid phase begins to flow from the column, and the onset of lateral motion in the granular material. Calculating the time required for the gap between the column and the horizontal plane to equal the inertial grain diameter, denoted as $t_{\mathrm{gap}}$, proves to be a logical step.

Utilising Equation (B.2), with given parameters $M_m = 3.6\,\mathrm{kg}$, $M_c = 0.92\,\mathrm{kg}$, and $a_r = 0.593G$, and considering the initial rest state of the cylinder, we can express the time taken for the column to raise by a distance $S$ as follows:

$$S = \frac{1}{2} a_r t^2. \tag{B.4}$$

By rearranging Equation (B.4) for $t$ and substituting the inertial particle height $d_p$ for $S$, $t_{\mathrm{gap}}$ can be determined. A summary of relevant $t_{\mathrm{gap}}$ values across the examined parameter space is presented in Table B.2. Intuitively, $t_{\mathrm{gap}}$ is a function of both $G$ and $d_p$, increasing linearly with the square root of both variables. Hence, defining a dimensionless version of $t_{\mathrm{gap}}$, denoted as $t_{\mathrm{gap}}^*$, by normalising it by the inertial timescale of the collapse $\sqrt{h_0/G}$ proves useful. As shown in Table B.2, $t_{\mathrm{gap}}^*$ is solely dependent on $d_p$ and, again, increases linearly with the square root of the variable.

## B.3 Influence of the column release mechanism on phase front separation

Given that the release mechanism results in a delay in the release of the granular phase, it is imperative to reassess prior conclusions concerning phase separation evolution. As discussed in Section 3.4, Figure 3.6 depicted the variation in the temporal evolution of phase front separation due to variations in $d_p$ and $G$. A modified version of this
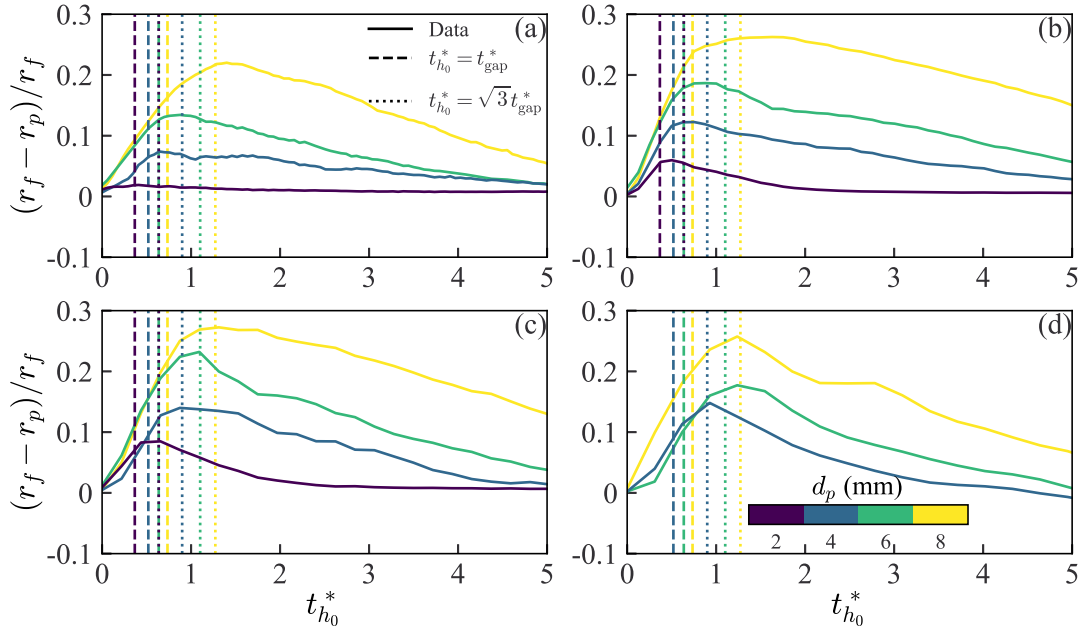
Figure B.4: Temporal evolution of the normalised distance between the phase fronts $(r_f - r_p)/r_f$ against normalised time $t^*_{h_0}$ for all particle sizes $d_p$ at (a) $G = 9.81\,\mathrm{m\,s^{-2}}$, (b) $G = 45.22\,\mathrm{m\,s^{-2}}$, (c) $G = 137.64\,\mathrm{m\,s^{-2}}$, and (d) $G = 275.45\,\mathrm{m\,s^{-2}}$ upstream of centrifuge motion.

figure, represented as Figure B.4, presents $(r_f - r_p)/r_f$ plotted against $t^*_{h_0}$, allowing for the identification of reference times corresponding to the points where the column has ascended by one and three particle diameters, denoted as $t^*_{h_0} = t^*_{\mathrm{gap}}$ and $t^*_{h_0} = \sqrt{3}t^*_{\mathrm{gap}}$, respectively.

Figure B.4 reveals that in all collapse tests, a significant portion of phase separation occurs prior to time $t^*_{h_0} = t^*_{\mathrm{gap}}$, while the maximum phase separation is attained closer to time $t^*_{h_0} = \sqrt{3}t^*_{\mathrm{gap}}$. Thus, the initial increase in phase separation can be attributed to the granular phase being restrained by the rising column during the initial collapse stages. Consequently, this initial phase separation is influenced by the column lifting mechanisms and accounts for the observed variations dependent on $G$ and $d_p$. It is noteworthy that with a maximum value of 1.3 for $\sqrt{3}t^*_{\mathrm{gap}}$ within the tested parameter range, the confinement of the granular phase spans only a small fraction of the total collapse duration (approximately 15% in the most extreme cases).

Therefore, the assertions made in Chapter 3 concerning the dependence on $G$ and $d_p$ during the stage of collapse where the granular phase begins to converge with the fluid phase remain pertinent. Future investigations should prioritise exploring the impact of column release velocity on phase separation dynamics. Specifically, emphasis should

be placed on understanding its influence on the time of maximum phase separation attainment, which in the present scenario occurs at approximately $t_{h_0}^* = \sqrt{3} t_{\mathrm{gap}}^*$.

## B.4 Influence of the column release mechanism on runout scalings
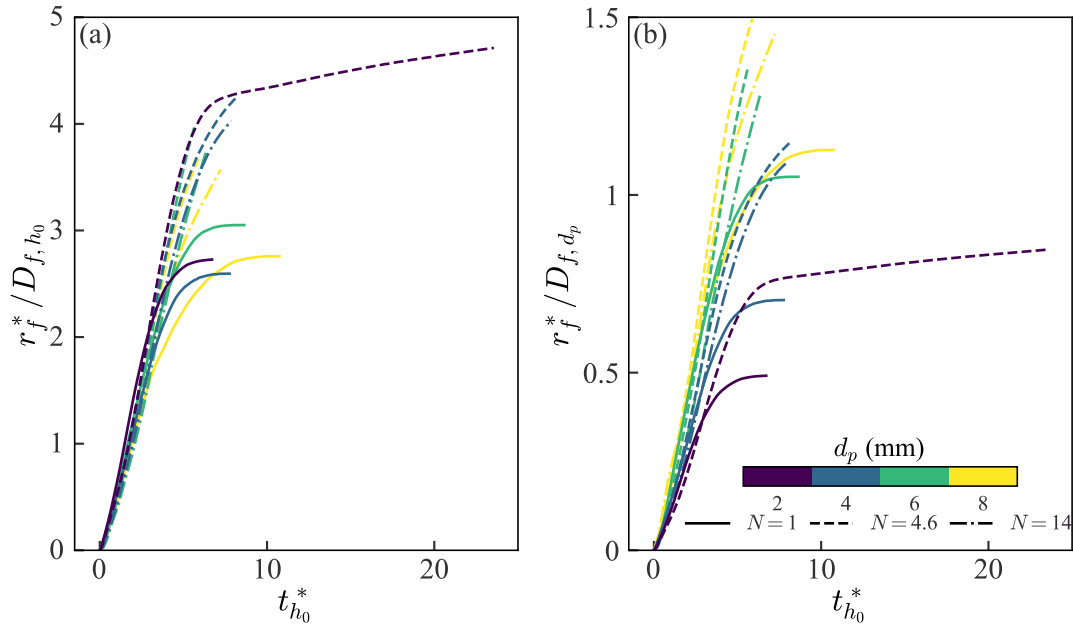


Figure B.5: Temporal evolution of the normalised fluid runout length $r_f^*$, scaled by $D_{f,L}$, where **(a)** $L = h_0$, and **(b)** $L = d_p$, with timescale $t_{h_0}^*$, for varying particle sizes $d_p$ and values of $N$ downstream of centrifuge motion.

To validate the scaling relations found through the dimensional analysis and parameter space reduction outlined in Chapter 3 (specifically represented by Equation 3.4), it is important to reinterpret the evolution of the phase front runout in a dimensionless framework, as implied by these scaling relations. The evolving parameter of interest for this assessment is the normalised phase front runout $r_v^*$ divided by the scaling factor $D_{v,L} = (\mathrm{Bo}/\mathrm{Ca})^\alpha (\rho^*)^\beta (r^*)^\gamma$, where the exponents $\alpha$, $\beta$, and $\gamma$ correspond to those stated in Table 3.3 for the pertinent quantity of interest, $\mathrm{Fr}_{v,L}$. For instance, in the case where $v = f$ and $L = h_0$, the exponents $[\alpha, \beta, \gamma] = [$ -0.02, 0.08, -0.25$]$.

To achieve a dimensionless representation, the temporal domain is once again normalised by employing $t_{h_0}^*$. Consequently, Figures B.5 and B.6 depict the temporal progression of the scaled phase front runout in $r_v^* D_{v,L}$-$t_{h_0}^*$ space for the fluid ($v = f$) and
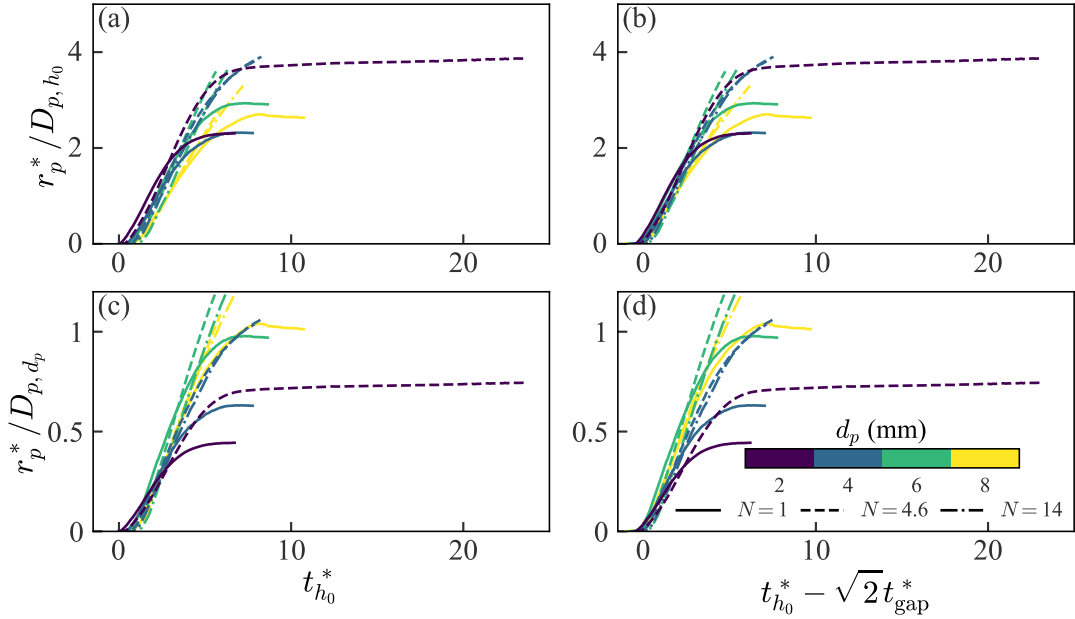
Figure B.6: Temporal evolution of the normalised particle runout length $r_p^*$, scaled by $D_{p,L}$, where [(a), (b)] $L = h_0$, and [(c), (d)] $L = d_p$, with timescales $t_{h_0}^*$ [(a), (c)], and $t_{h_0}^* - \sqrt{2}t_{gap}^*$ [(b), (d)], for varying particle sizes $d_p$ and values of $N$ downstream of centrifuge motion.

granular ($v = p$) phases, respectively. For the evolution of the fluid phase fronts , scaling the system by $D_{f,h_0}$ (Figure B.5a) results in a reasonably good collapse of the test curves during the early stages of the collapse. This is somewhat expected as the scaling is derived from the peak velocity of the phase front. However, deviations become apparent during the deceleration phases of the collapse, where capillary effects become more significant, as discussed in Chapter 3.

Figure B.5b, where the system is scaled by $D_{f,d_p}$, exhibits a more pronounced spread at the early stages of the collapse, but the general trends observed in Figure B.5a persist. Notably, tests conducted with a granular phase comprised of $2\,\text{mm}$ particles show the greatest deviation during the early collapse stages. Consequently, the scaling relation, predicated on the assumption of negligible surface tension effects, begins to falter for these smaller particle sizes.

Similar conclusions can be made from the scaled runout behaviour of the granular phase front (Figures B.6a and B.6c), where the collapse is generally satisfactory during the acceleration phase but demonstrates increasing deviation as the flows decelerate. However, unlike the scaled fluid phase fronts, a significant temporal lag is present between the experiments, largely dependent on particle size. This lag likely stems from

the release delay of the granular material due to the column lifting mechanism.

To address this, Figures B.6b and B.6c apply a temporal shift to the collapses equivalent to $\sqrt{2}t_{\text{gap}}^*$, representing the time taken for a gap equivalent to two particle diameters to open up between the horizontal runout plane and the base of the column. The shift, especially evident in Figure B.6, results in a better collapse of the test curves, suggesting that the scaling relations do not adequately account for the release delay of the granular material, which is an effect arising from the experimental configuration.

Overall, the scaling relations demonstrate a significant degree of data collapse during the initial stages of the flow, which is promising given that the scaling was derived from the peak velocity of the phase front. However, as the flows decelerate and the influence of capillary effects between the granular and fluid phases becomes more pronounced, the scaling relations begin to break down. Although the scaling relations overlook the release delay of the granular phase, it appears that this can be rectified by adjusting the collapse by a timescale of $\sqrt{2}t_{\text{gap}}^*$. Further investigations are warranted to optimise this temporal shift and understand its variation with column lifting speed.

# Shallow water model derivation

The following Appendix outlines the derivation of the two-phase shallow water model employed in Chapter 5 to replicate the experiments on fluid-saturated column collapses outlined in Chapter 3. Beginning with the basics of continuum mixture theory, it explains the steps taken to formulate a mathematical representation of an undersaturated two-phase granular mixture, moving within a axisymmetric coordinate framework. This derivation leads renders a system of equations, which are refined in Chapter 5 to effectively simulate high-$g$ collapse scenarios.

## C.1   Governing equations

In order to replicate the flow dynamics observed in the experiments detailed in Chapter 3, the theoretical model will describe the grains and the fluid as two continuum phases with constant specific densities $\rho_v$, where $v = p, f$ for the granular and fluid phases, respectively.

Continuum mixture theory (Morland, 1992) will provide the framework to describe the equations governing the behaviour of each phase. The theory is based on the idea that both phases occupy each spatial point within the flow concurrently, where the volumetric proportion of each phase is described by its volume fraction $\phi_v$. Hence, under the assumption of a fully saturated granular phase,

$$\phi_p + \phi_f = 1. \tag{C.1}$$

As such, the mass continuity equations for the granular and fluid phases are

$$\partial_t(\rho_p \phi_p) + \nabla \cdot (\rho_p \phi_p \boldsymbol{u}_p) = 0, \tag{C.2}$$

$$\partial_t(\rho_f \phi_f) + \nabla \cdot (\rho_f \phi_f \boldsymbol{u}_f) = 0, \tag{C.3}$$

145

Chapter C: Shallow water model derivation

and the respective momentum continuity equations are

$$\rho_p \phi_p [\partial_t(\boldsymbol{u}_p) + (\boldsymbol{u}_p \cdot \nabla)\boldsymbol{u}_p] = -\nabla \cdot \boldsymbol{\sigma}_p + \rho_p \phi_p \boldsymbol{g} + \boldsymbol{\beta}_p, \qquad (C.4)$$

$$\rho_f \phi_f [\partial_t(\boldsymbol{u}_f) + (\boldsymbol{u}_f \cdot \nabla)\boldsymbol{u}_f] = -\nabla \cdot \boldsymbol{\sigma}_f + \rho_f \phi_f \boldsymbol{g} + \boldsymbol{\beta}_f, \qquad (C.5)$$

where $\boldsymbol{u}_v$ and $\boldsymbol{\sigma}_v$ are the velocities and the symmetric stress tensors for each phase. Gravitational acceleration vector is denoted as $\boldsymbol{g}$ while $\boldsymbol{\beta}_v$ is the interaction force exerted on the $v$ phase by the other. Newton's third law implies that $\boldsymbol{\beta}_p + \boldsymbol{\beta}_f = 0$ resulting in no mass being transferred between the two phases.

Following the work of de Boer and Ehlers (1990) and Meng et al. (2022), the granular stress tensor is defined as

$$\boldsymbol{\sigma}_p = \phi_p p_f \boldsymbol{I} + \boldsymbol{\sigma}'_p, \qquad (C.6)$$

where $\boldsymbol{I}$ is the unit tensor, $p_f$ is the fluid pressure within the mixture and $\boldsymbol{\sigma}'_p$ is the effective granular stress which only considers the contribution of inter-particle contact forces (Terzaghi, 1943). The fluid stress tensor can also be decomposed into two components

$$\boldsymbol{\sigma}_f = \phi_f p_f \boldsymbol{I} - \boldsymbol{\tau}_f, \qquad (C.7)$$

where $\boldsymbol{\tau}_f$ is the deviatoric stress tensor for the fluid. Given the rheological behaviour of the fluids used within the experiments, it is assumed that $\boldsymbol{\tau}_f$ can be described by a Newtonian fluid rheology.

$$\boldsymbol{\tau}_f = \phi_f \eta_f [\nabla \boldsymbol{u}_f + (\nabla \boldsymbol{u}_f)^T], \qquad (C.8)$$

where $\eta_f$ is the constant dynamic viscosity of the fluid phase and $T$ is the transpose.

Typically, as in Bouchut et al. (2015), the interaction terms, $\boldsymbol{\beta}_f$ and $\boldsymbol{\beta}_p$, can be deconstructed into two components

$$\boldsymbol{\beta}_f = -\boldsymbol{\beta}_p = \boldsymbol{f}_B + \boldsymbol{f} = -\phi_f \nabla p_f + \boldsymbol{f}, \qquad (C.9)$$

where $\boldsymbol{f}_B$ is the contribution of the buoyancy force $-\phi_f \nabla p_f$ and $\boldsymbol{f}$ is the remaining interphase body force consisting of the contributions from the drag force, virtual mass force and lift force (Phan et al., 2022). Following the derivation of Meng et al. (2022), the $-\phi_f \nabla p_f$ term will be amalgamated with the partial fluid pressure gradient term $-\nabla(\phi_f p_f)$ term which arises when Equation (C.7) is substituted into Equation (C.5) confirming that the dynamics of the fluid is governed by the pore water pressure gradient

$-\phi_f \nabla p_f$ which is in accordance with Darcy's law (Morland, 1992).

As was done by Bouchut et al. (2016), it is assumed that $\boldsymbol{f}$ can be well approximated as an interphase Darcy drag force resulting from the relative motion of the two phases

$$\boldsymbol{f} = C_{dd}(\boldsymbol{u}_p - \boldsymbol{u}_f), \tag{C.10}$$

with the drag coefficient $C_{dd}$ taking the form of that described by Pailha and Pouliquen (2009) and Iverson and George (2014)

$$C_{dd} = \eta_f \frac{\phi_f^2}{k}, \tag{C.11}$$

where the permeability of the granular phase $k$ is described using Carman's formula for a packing of monodispersed spheres with diameter $d_p$

$$k = \frac{\phi_f^3 d_p^2}{180 \phi_p^2}. \tag{C.12}$$

Substituting Equations (C.6), (C.7) and (C.9) into Equations (C.4) and (C.5), the momentum conservation equations for both phases can be rewritten as

$$\rho_p \phi_p [\partial_t(\boldsymbol{u}_p) + (\boldsymbol{u}_p \cdot \nabla)\boldsymbol{u}_p] = -\nabla \cdot \boldsymbol{\sigma}_p' - \phi_p \nabla p_f + \rho_p \phi_p \boldsymbol{g} + C_{dd}(\boldsymbol{u}_f - \boldsymbol{u}_p), \tag{C.13}$$

$$\rho_f \phi_f [\partial_t(\boldsymbol{u}_f) + (\boldsymbol{u}_f \cdot \nabla)\boldsymbol{u}_f] = \nabla \cdot \boldsymbol{\tau}_f - \phi_f \nabla p_f + \rho_f \phi_f \boldsymbol{g} + C_{dd}(\boldsymbol{u}_p - \boldsymbol{u}_f), \tag{C.14}$$

for a fully saturated mixture. Equation (C.14) reduces to the Navier-Stokes equation for a pure Newtonian fluid when $\phi_f = 1$ and assuming that the interaction force between the two phases is 0. Similarly, Equation (C.13) can take the form of a momentum continuity equation for a dry granular material by setting $\phi_f = 0$ and assuming that both the buoyancy force and the interaction force are 0.

## C.2   Boundary conditions

For the purposes of generality, consider that the two-phase flow being modelled advances down a slope with an angle of inclination $\zeta_s$ (see Figure C.1). We also define a two-dimensional Cartesian coordinates system, $Oxz$, where the $x$-axis is directed down the slope and the $z$-axis is directed upwards. It is straightforward to describe this model

Chapter C: Shallow water model derivation
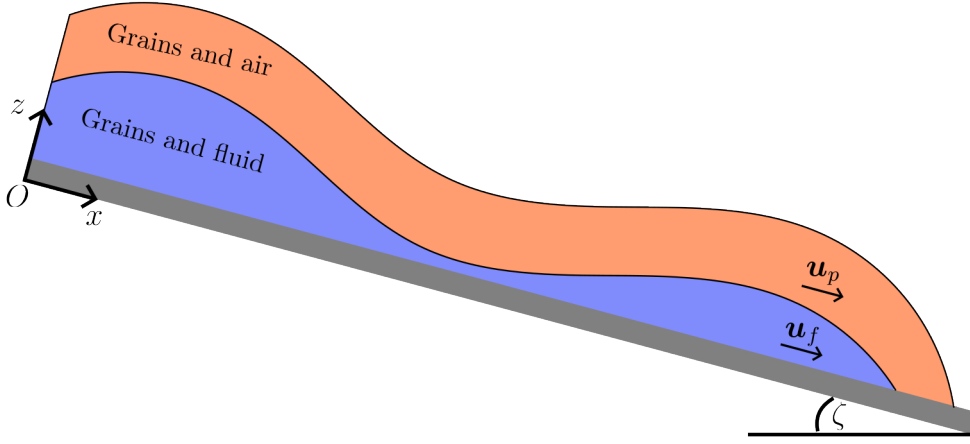


Figure C.1: Sketch of a 2-D slice of an undersaturated granular flow travelling down an incline modelled as two coupled continuum phases.

in three dimensions by adding another coordinate directed across the slope $y$, but for simplicity, the current model will only consider the two former dimensions. Hence, the phase velocity $\boldsymbol{u}_v$ can be broken down into components pointing down the slope and perpendicular to the slope such that $\boldsymbol{u}_v = [u_v, w_v]$. Similarly, $\boldsymbol{\sigma}'_p$, $\boldsymbol{\tau}_f$ and $\boldsymbol{g}$ can also be deconstructed into components relative to the defined Cartesian axis such that $\boldsymbol{\sigma}'_p = [\sigma'_{p,xx}, \sigma'_{p,zz}, \sigma'_{p,xz}]$, $\boldsymbol{\tau}_f = [\tau_{f,xx}, \tau_{f,zz}, \tau_{f,xz}]$ and $\boldsymbol{g} = [g \sin \zeta_s, g \cos \zeta_s]$ where $g$ is the magnitude of the gravitational acceleration parallel to the $z$-axis, respectively. As done by Iverson and Denlinger (2001), a local right-handed sign convention is adopted to define the acting direction of the stress and velocity components where the normal stress components (i.e. $\sigma'_{p,xx}$, $\sigma'_{p,zz}$, $\tau_{f,xx}$ and $\tau_{f,zz}$) are positive in compression.

The granular and fluid surfaces can be defined by the functions $F^p(x, z, t) = z - s^p(x, t)$ and $F^f(x, z, t) = z - s^f(x, t)$, respectively, while the basal surface is characterised by $F^b(x, z, t) = z - b(x)$. Hence, the upward pointing normal vector for each surface $\boldsymbol{n}^v = \nabla F^v / |\nabla F^v|$ with $v = p, f, b$. Given that both the granular and fluid phases are constrained by the kinematic condition $F^v(x, t) = 0$ at each of their respective free surfaces, we can expand these conditions to their component form as follows

$$\partial_t(s^p) + u_p \partial_x(s_p) - w_p = 0, \qquad z = s^p(x, t). \qquad (\text{C.15})$$

$$\partial_t(s^f) + u_f \partial_x(s_f) - w_f = 0, \qquad z = s^f(x, t). \qquad (\text{C.16})$$

Similarly, as the model does not consider the erosion of the slope, meaning that $F^b(x) =$

Chapter C: Shallow water model derivation

0, we can also define the following conditions at the basal surface

$$\partial_t(b) + u_p\partial_x(b) - w_p = 0, \qquad z = b(x). \tag{C.17}$$

$$\partial_t(b) + u_f\partial_x(b) - w_f = 0, \qquad z = b(x). \tag{C.18}$$

For the purposes of simplifying the model, it is assumed that the granular phase is always either exactly saturated or undersaturated. This is deemed a reasonable assumption given the relatively large diameters of the particles used to experimentally model the granular phase even though it is likely to be violated by many model solutions. Hence, $s^f \leq s^p$ is always true meaning that in the undersaturated regime, the position of the interface between dry and saturated granular material is located at $s^f$. Given that the position of $s^f$ varies spatially and temporally, the volume fraction of the material crossing $s^f$ would change suddenly. For example, the volume fraction of the fluid jumps from $\phi_f = 0$ above $s^f$ to $\phi_f = 1 - \phi_p$ below $s^f$. As such, we use the mass jump condition presented by Chadwick (1999) to express this behaviour at the interface

$$[[\rho_p\phi_p(\partial_t(s^f) + u_p\partial_x(s^f) - w_p)]] = 0, \qquad z = s^f(x,t), \tag{C.19}$$

where $[[\quad]]$ are jump brackets that designate the variation of the enclosed quantity either side of the discontinuity.

We also assume that both phases are not subjected to external stresses at their free surfaces in either the downslope or slope normal directions

$$-\sigma'_{p,xx}\partial_x(s^p) + \sigma'_{p,xz} = 0, \qquad z = s^p(x,t). \tag{C.20}$$

$$-\sigma'_{p,xz}\partial_x(s^p) + \sigma'_{p,zz} = 0, \qquad z = s^p(x,t). \tag{C.21}$$

$$\phi_f p_f\partial_x(s^f) - \tau_{f,xx}\partial_x(s^f) + \tau_{f,xz} = 0, \qquad z = s^f(x,t). \tag{C.22}$$

$$-\phi_f p_f - \tau_{f,xz}\partial_x(s^f) + \tau_{f,zz} = 0, \qquad z = s^f(x,t). \tag{C.23}$$

Based on the findings of the large-scale chute tests of Iverson (2003), the tangential movement of the granular phase will be constrained by a Coulomb-style basal friction boundary condition in both the downslope and slope normal directions

$$-\sigma'_{p,xx}\partial_x(b) + \sigma'_{p,xz} = -(\boldsymbol{n}^b \cdot \boldsymbol{\sigma}'_p\boldsymbol{n}^b)\left[\frac{u_p^b}{|\boldsymbol{u}_p^b|}\mu_b|\nabla F^b| + \partial_x(b)\right], \qquad z = b(x). \tag{C.24}$$

$$-\sigma'_{p,xz}\partial_x(b) + \sigma'_{p,zz} = -(\boldsymbol{n}^b \cdot \boldsymbol{\sigma}'_p \boldsymbol{n}^b)\left[\frac{w_p^b}{|\boldsymbol{u}_p^b|}\mu_b|\nabla F^b| - 1\right], \qquad z = b(x). \quad \text{(C.25)}$$

where $\mu_b$ is the basal friction coefficient. Similarly, the basal friction boundary conditions for the fluid phase will be modelled utilising the Chézy formula (Chaudhry, 2008).

$$-\tau_{f,xx}\partial_x(b) + \tau_{f,xz} + [\phi_f p_f^b + (\boldsymbol{n}^b \cdot \boldsymbol{\sigma}_f \boldsymbol{n}^b)]\partial_x(b) = \rho_f C_f \bar{u}_f |\bar{\boldsymbol{u}}_f||\nabla F^b|, \qquad z = b(x).$$
$$\text{(C.26)}$$

$$-\tau_{f,xz}\partial_x(b) + \tau_{f,zz} - [\phi_f p_f^b + (\boldsymbol{n}^b \cdot \boldsymbol{\sigma}_f \boldsymbol{n}^b)] = \rho_f C_f \bar{w}_f |\bar{\boldsymbol{u}}_f||\nabla F^b|, \qquad z = b(x). \quad \text{(C.27)}$$

where $C_f$ is the Chézy drag coefficient which accounts for turbulent friction along the horizontal plane, $\bar{\boldsymbol{u}}_f$ is the depth averaged fluid velocity and $\bar{u}_f$ and $\bar{w}_f$ are the $x$ and $z$ components of the depth averaged fluid velocity, respectively.

## C.3  Scaling the system

It is typical for natural scale debris flows to have a characteristic flow depth $H$ that is significantly smaller than their characteristic length $L$ such that their aspect ratio $\epsilon = H/L \ll 1$ (Iverson, 1997). This assumption allows for the development of a more computationally efficient model consisting of a depth averaged system of equations, independent of the slope-normal $z$-direction. To develop this model, it is beneficial to scale the mass and momentum conservation equations to assess the comparative influence of each term on the motion of the flow. To do this, we follow the logic of Meng et al. (2017) and assume that the downslope speed of both phases $U = \sqrt{gH}$ where $L$ and $H$ are the characteristic length scales of the $x$ and $z$ axes, respectively. This suggests that the slope-normal phase velocities can be scaled by $\epsilon U$. Hence, the characteristic timescale of the mass movement is assumed to be $t = L/\sqrt{gH}$ while the granular and fluid stresses are scaled by the expected lithostatic pressure $\rho_p g H$ and the Newtonian fluid rheology defined in Equation (C.8), respectively. We also assume that $C_{dd}$ scales with $\rho_f \sqrt{g/H}$. The full set of scalings for the governing equations and boundary conditions are as follows

$$\left.\begin{aligned}
(x, z, s^f, s^p, b, d_p) &= L(\hat{x}, \epsilon\hat{z}, \epsilon\hat{s}^f, \epsilon\hat{s}^p, \epsilon\hat{b}, \epsilon\hat{d}_p), \qquad t = L/\sqrt{gH}\hat{t}, \\
(u_v, w_v, |\boldsymbol{u}_v|) &= \sqrt{gH}(\hat{u}_v, \epsilon\hat{w}_v, |\hat{\boldsymbol{u}}_v|), \qquad C_{dd} = \rho_f\sqrt{g/H}\hat{C}_{dd}, \\
(\sigma'_{xx}, \sigma'_{zz}, \sigma'_{xz}) &= \rho_p g H(\hat{\sigma}'_{xx}, \hat{\sigma}'_{zz}, \hat{\sigma}'_{xz}), \\
(p_f, \tau_{f,xx}, \tau_{f,zz}, \tau_{f,xz}) &= \rho_f g H(\hat{p}_f, \epsilon\hat{\tau}_{f,xx}, \epsilon\hat{\tau}_{f,zz}, \hat{\tau}_{f,xz}),
\end{aligned}\right\} \quad \text{(C.28)}$$

where the hatted variables are dimensionless. Applying the scalings in Equation (C.28) to Equation (C.2) and Equation (C.13), and removing the common factors, the dimensionless mass and momentum equations for the granular phase are

$$\partial_{\hat{t}}(\phi_p) + \partial_{\hat{x}}(\phi_p \hat{u}_p) + \partial_{\hat{z}}(\phi_p \hat{w}_p) = 0, \tag{C.29}$$

$$\epsilon[\partial_{\hat{t}}(\phi_p \hat{u}_p) + \partial_{\hat{x}}(\phi_p \hat{u}_p \hat{u}_p) + \partial_{\hat{z}}(\phi_p \hat{u}_p \hat{w}_p)] = -\epsilon \partial_{\hat{x}}(\hat{\sigma}'_{p,xx}) - \partial_{\hat{z}}(\hat{\sigma}'_{p,xz}) - \epsilon \gamma^* \partial_{\hat{x}}(\phi_p \hat{p}_f)$$
$$+ \phi_p \sin \zeta_s + \gamma^* \hat{C}_{dd}(\hat{u}_f - \hat{u}_p), \quad \text{(C.30)}$$

$$\epsilon^2[\partial_{\hat{t}}(\phi_p \hat{w}_p) + \partial_{\hat{x}}(\phi_p \hat{u}_p \hat{w}_p) + \partial_{\hat{z}}(\phi_p \hat{w}_p \hat{w}_p)] = -\epsilon \partial_{\hat{x}}(\hat{\sigma}'_{p,xz}) - \partial_{\hat{z}}(\hat{\sigma}'_{p,zz}) - \gamma^* \partial_{\hat{z}}(\phi_p \hat{p}_f)$$
$$- \phi_p \cos \zeta_s + \epsilon \gamma^* \hat{C}_{dd}(\hat{w}_f - \hat{w}_p), \quad \text{(C.31)}$$

where $\gamma^*$ is the density ratio between the two phases such that $\gamma^* = \rho_f / \rho_p$. Similarly, applying the scalings in Equation (C.28) to Equation (C.3) and Equation (C.14), and again removing the common factors, the dimensionless mass and momentum equations for the fluid phase are

$$\partial_{\hat{t}}(\phi_f) + \partial_{\hat{x}}(\phi_f \hat{u}_f) + \partial_{\hat{z}}(\phi_f \hat{w}_f) = 0, \tag{C.32}$$

$$\epsilon[\partial_{\hat{t}}(\phi_f \hat{u}_f) + \partial_{\hat{x}}(\phi_f \hat{u}_f \hat{u}_f) + \partial_{\hat{z}}(\phi_f \hat{u}_f \hat{w}_f)] = \epsilon^2 \partial_{\hat{x}}(\hat{\tau}_{f,xx}) + \partial_{\hat{z}}(\hat{\tau}_{f,xz}) - \epsilon \partial_{\hat{x}}(\phi_f \hat{p}_f)$$
$$+ \phi_f \sin \zeta_s + \hat{C}_{dd}(\hat{u}_p - \hat{u}_f), \quad \text{(C.33)}$$

$$\epsilon^2[\partial_{\hat{t}}(\phi_f \hat{w}_f) + \partial_{\hat{x}}(\phi_f \hat{u}_f \hat{w}_f) + \partial_{\hat{z}}(\phi_f \hat{w}_f \hat{w}_f)] = \epsilon \partial_{\hat{x}}(\hat{\tau}_{f,xz}) + \epsilon \partial_{\hat{z}}(\hat{\tau}_{f,zz}) - \partial_{\hat{z}}(\phi_f \hat{p}_f)$$
$$- \phi_f \cos \zeta_s + \epsilon \hat{C}_{dd}(\hat{w}_p - \hat{w}_f). \quad \text{(C.34)}$$

While the scaling process suggests that any term of $O(\epsilon)$ or higher is negligible and could be discarded, as discussed by Savage and Hutter (1989), removing the longitudinal stress components from the $x$-direction momentum equations would result in an oversimplified model that is incapable of simulating debris flow motion. Hence, $O(\epsilon)$ or higher order terms are only removed from the momentum balances in the $z$-direction.

## C.4  Depth integration

### C.4.1  Mass continuity equations

In order to formulate a depth averaged system, each equation has to be integrated up to the relevant phase's respective flow height $h_v$ using Leibniz's rule (Flanders, 1973) which allows the order of the differentiation and integration operations to be interchanged as follows

$$\int_{z_0}^{z_0+z_1} \partial_x(S)\,\mathrm{d}z = \partial_x\left(\int_{z_0}^{z_0+z_1} S\,\mathrm{d}z\right) - S|_{z_0+z_1}\partial_x(z_0+z_1) + S|_{z_0}\partial_x(z_0), \quad \text{(C.35)}$$

where $z_0$ and $z_1$ are arbitrary surfaces dependent on $z$ and $S$ is an arbitrary scaler quantity. To further simplify the complexity of the modelled flow, as done by many previous authors (e.g. Iverson, 1997; Iverson and Denlinger, 2001; Meng et al., 2022, 2017), we assume that

$$\phi_p = \phi_c, \tag{C.36}$$

where $\phi_c$ is a constant in space and time. While this has been shown to be a reasonable assumption in debris flows whose behaviour are dominated by granular inertia (Iverson and Denlinger, 2001; Meng et al., 2022), as is the case with the current experimental configuration, this approximation inherently assumes a hydrostatic pressure profile. Hence, the model does not consider the influence of excess pore pressures that can arise from the partial, or full, suspension of the granular phase (Kaitna et al., 2016). As such, a spatially and temporally dependent closure equation for $\phi_p$ may need to be considered if the particle size distribution of the debris flow is expected to contain significant amounts of fine granular material (see Iverson and George, 2014; Kowalski and McElwaine, 2013; Pitman and Le, 2005). As it is assumed that the flow is always fully or undersaturated, $\phi_f$ can be described by

$$\phi_f = \begin{cases} 1 - \phi_c, & z \in [b, s^f], \\ 0, & z \in [s^f, s^p]. \end{cases} \tag{C.37}$$

By integrating Equation (C.29) and noting that $\phi_p$ is a constant, we can obtain the depth averaged mass conservation equation for the granular phase

$$\partial_{\hat{t}}(\phi_p\hat{h}_p) + \partial_{\hat{x}}(\phi_p h_p \hat{\bar{u}}_p) + [[\phi_p(\partial_{\hat{t}}(\hat{s}^f) + \hat{u}_p\partial_{\hat{x}}(\hat{s}^f) - \hat{w}_p)]] = 0, \tag{C.38}$$

Chapter C: Shallow water model derivation

where the $[[\phi_p(\partial_{\hat{t}}(\hat{s}^f) + \hat{u}_p\partial_{\hat{x}}(\hat{s}^f) - \hat{w}_p)]]$ describes the difference in the value of the bracketed quantity between $\hat{s}^p$ and the granular-fluid interface in the undersaturated regime at $\hat{s}^f$. Using Equation (C.19) to account for $[[\phi_p(\partial_{\hat{t}}(\hat{s}^f) + \hat{u}_p\partial_{\hat{x}}(\hat{s}^f) - \hat{w}_p)]]$ and rewriting $\phi_p$ using Equation (C.36), we can rewrite the depth averaged mass continuity equation for the granular phase as

$$\partial_{\hat{t}}(\hat{h}_p) + \partial_{\hat{x}}(\hat{h}_p\hat{\bar{u}}_p) = 0. \tag{C.39}$$

Without needing to consider an interfacial surface when integrating up to the fluid free surface, simply integrating Equation (C.32) and applying Equation (C.37) leads to the following dimensionless mass continuity equation for the fluid phase

$$\partial_{\hat{t}}(\hat{h}_f) + \partial_{\hat{x}}(\hat{h}_f\hat{\bar{u}}_f) = 0. \tag{C.40}$$

## C.4.2 Normal components of the momentum continuity equations

By only considering the fluid saturated region of the flow, notice that by applying the limit $\epsilon \to 0$ to Equation (C.34), it can be shown that the fluid is hydrostatic

$$\partial_{\hat{z}}(\hat{p}_f) = -\cos\zeta_s. \tag{C.41}$$

Due to the scaling, velocities in the $z$-momentum equations cancel, which is a key result of the thin/shallow-water flow approximation (Savage and Hutter, 1989). Integrating Equation (C.41) and imposing the free surface boundary condition in Equation (C.23) to leading order accuracy, we obtain

$$\hat{p}_f = \cos\zeta_s(\hat{s}^f - \hat{z}), \qquad \hat{z} \in [\hat{b}, \hat{s}^f]. \tag{C.42}$$

As such, the dimensionless fluid pressure at the basal surface is

$$\hat{p}_f|_{\hat{b}} = \cos\zeta_s\,\hat{h}_f, \qquad \hat{z} = \hat{b}. \tag{C.43}$$

Hence, the depth averaged fluid pressure is

$$\hat{\bar{p}}_f = \frac{1}{\hat{h}_f}\int_{\hat{b}}^{\hat{s}^f} \hat{p}_f\,\mathrm{d}\hat{z} = \frac{1}{2}\cos\zeta_s\,\hat{h}_f. \tag{C.44}$$

153

Writing Equation (C.31) to leading order accuracy, the $z$-momentum balance for the saturated granular material reduces to

$$\partial_{\hat{z}}(\hat{\sigma}'_{p,zz}) = -\phi_c \cos \zeta_s - \gamma^* \phi_c \partial_{\hat{z}}(p_f). \tag{C.45}$$

A similar equation for the dry granular material can be developed given that the contributions of fluid phase would vanish

$$\partial_{\hat{z}}(\hat{\sigma}'_{p,zz}) = -\phi_c \cos \zeta_s. \tag{C.46}$$

Following the logic of Meng et al. (2022), by assuming a continuous velocity profile with depth, there will be no jump in granular effective normal stress across the interfacial surface. Hence, integrating Equations (C.45) and (C.46), imposing the relevant boundary conditions at the free surfaces and applying Equation (C.41), we obtain

$$\hat{\sigma}'_{p,zz} = \begin{cases} \phi_c \cos \zeta_s \left( \hat{s}^p - \hat{z} \right) - \gamma^* \phi_c \cos \zeta_s \left( \hat{s}^f - \hat{z} \right), & \hat{z} \in [\hat{b}, \hat{s}^f], \\ \phi_c \cos \zeta_s \left( \hat{s}^p - \hat{z} \right), & \hat{z} \in [\hat{s}^f, \hat{s}^p]. \end{cases} \tag{C.47}$$

The dimensionless granular normal stress at the basal surface is

$$\hat{\sigma}'_{p,zz}(\hat{b}) = \phi_c \cos \zeta_s \left( \hat{h}_p - \gamma^* \hat{h}_f \right), \qquad \hat{z} = \hat{b}. \tag{C.48}$$

Therefore, the slope normal granular stress is defined as the buoyancy adjusted overburden stress of the granular material (Pitman and Le, 2005). The depth averaged granular stress can then be calculated as

$$\bar{\hat{\sigma}}'_{p,zz} = \frac{1}{\hat{h}_p} \left( \int_{\hat{b}}^{\hat{s}^f} \hat{\sigma}'_{p,zz} \, \mathrm{d}\hat{z} + \int_{\hat{s}^f}^{\hat{s}^p} \hat{\sigma}'_{p,zz} \, \mathrm{d}\hat{z} \right) = \frac{1}{2} \phi_c \cos \zeta_s \hat{h}_p \left[ 1 - \gamma^* \left( \frac{\hat{h}_f}{\hat{h}_p} \right)^2 \right]. \tag{C.49}$$

### C.4.3 Horizontal components of the granular momentum continuity equations

Following the process of many previous authors, we can relate the downslope normal stress $\bar{\hat{\sigma}}_{p,xx}$ to the slope-normal normal stress $\bar{\hat{\sigma}}_{p,zz}$ using a lateral Earth pressure coeffi-

cient $k_{act/pass}$ which can be derived from Coulomb theory

$$\bar{\bar{\sigma}}'_{p,xx} = k_{act/pass}\bar{\bar{\sigma}}'_{p,zz}, \tag{C.50}$$

where the value of $k_{act/pass}$ is dependent on whether the material is contracting ($k_{act/pass} > 1$) or dilating ($k_{act/pass} < 1$). However, we, like previous authors (e.g. Iverson and Denlinger, 2001), choose to assume a statically indeterminate stress state by taking $k_{act/pass}$ to be equal to unity, implying that

$$\bar{\bar{\sigma}}'_{p,xx} = \bar{\bar{\sigma}}'_{p,zz} = \frac{1}{2}\phi_c \cos\zeta_s\, \hat{h}_p \left[ 1 - \gamma^*\left(\frac{\hat{h}_f}{\hat{h}_p}\right)^2 \right]. \tag{C.51}$$

As such, using Equations (C.25) and (C.48), the dimensionless effective granular normal stress at the basal surface can be written as

$$\boldsymbol{n}^b \cdot \hat{\boldsymbol{\sigma}}'_p \boldsymbol{n}^b = \hat{\sigma}'_{p,zz}(\hat{b}) = \phi_c \cos\zeta_s\, \hat{h}_p \left( 1 - \gamma^*\frac{\hat{h}_f}{\hat{h}_p} \right), \qquad \hat{z} = \hat{b}. \tag{C.52}$$

Hence, using the scaling relations in Equation (C.28), a dimensionless version of Equation (C.24) can be written as

$$\begin{aligned}
-\,\hat{\sigma}_{p,xx}(\hat{b})'\partial_{\hat{x}}(\hat{b}) + \hat{\sigma}'_{p,xz}(\hat{b}) = {} \\
-\phi_c \cos\zeta_s\, \hat{h}_p \left( 1 - \gamma^*\frac{\hat{h}_f}{\hat{h}_p} \right)\left( \frac{\hat{u}_p^b}{|\hat{\boldsymbol{u}}_p^b|}\mu_b + \epsilon\partial_{\hat{x}}(\hat{b}) \right), \qquad \hat{z} = \hat{b},
\end{aligned} \tag{C.53}$$

where, for simplicity, it is assumed that $\hat{u}_p^b/|\hat{\boldsymbol{u}}_p^b| \approx \hat{\bar{u}}_p/|\hat{\bar{u}}_p|$ (e.g. Pudasaini, 2012). Given that $\phi_p$ is a constant, The left-hand side of Equation (C.30) can be rewritten as

$$\mathrm{LHS} = \epsilon[\partial_{\hat{t}}(\phi_c\hat{u}_p) + \partial_{\hat{x}}(\phi_c\hat{u}_p\hat{u}_p) + \partial_{\hat{z}}(\phi_c\hat{u}_p\hat{w}_p)]. \tag{C.54}$$

Again, by dividing the integration across the depth of the granular material into two components, based on the location of the interfacial surface, using Leibniz's rule to interchange the order of integration and differentiation operations and applying the kinematic boundary conditions for the granular phase at the basal (Equation C.17) and gran-

ular surfaces (Equation C.15),

$$\int_{\hat{b}}^{\hat{s}^p} \text{LHS} \, d\hat{z} = \int_{\hat{b}}^{\hat{s}^f} \text{LHS} \, d\hat{z} + \int_{\hat{s}^f}^{\hat{s}^p} \text{LHS} \, d\hat{z}$$
$$= \epsilon \partial_{\hat{t}}(\hat{h}_p \phi_c \hat{\bar{u}}_p) + \epsilon \partial_{\hat{x}}(\hat{h}_p \phi_c \overline{(\hat{u}_p)^2})$$
$$+ \epsilon[[\phi_c \hat{u}_p \left( \partial_{\hat{t}}(\hat{s}^f) + \hat{u}_p \partial_{\hat{x}}(\hat{s}^f) - \hat{w}_p \right)]], \tag{C.55}$$

where, similar to Equation (C.38), the term in the jump brackets is equal to 0 provided that the flow velocity profile is continuous across its depth. To simplify the convective term in the momentum equations further, we assume that

$$\overline{(\hat{u}_v)^2} = \frac{1}{\hat{h}_v} \int_{\hat{b}}^{\hat{s}^v} (\hat{u}_v)^2 \, d\hat{z} = (\hat{\bar{u}}_v)^2, \tag{C.56}$$

where $v = f, p$ depending on the phase of interest. It should be noted that, given that we are assuming a simplistic plug flow velocity profile, we have omitted the shape factor from Equation (C.56).

Given that $\phi_p$ is a constant, the right-hand side of Equation (C.30) can also be rewritten

$$\text{RHS} = -\epsilon \partial_{\hat{x}}(\hat{\sigma}'_{p,xx}) - \partial_{\hat{z}}(\hat{\sigma}'_{p,xz}) - \epsilon \gamma^* \partial_{\hat{x}}(\phi_c \hat{p}_f) + \phi_c \sin \zeta_s + \gamma^* \hat{C}_{dd}(\hat{u}_f - \hat{u}_p). \tag{C.57}$$

Similarly, using Leibniz's rule to help integrate across the whole flow depth, noting that the influence of the buoyancy and interphase drag forces are only felt below the fluid free surface, and simplifying the result using Equations (C.15), (C.17) and (C.20)

$$\int_{\hat{b}}^{\hat{s}^p} \text{RHS} \, d\hat{z} = \int_{\hat{b}}^{\hat{s}^f} \text{RHS} \, d\hat{z} + \int_{\hat{s}^f}^{\hat{s}^p} \text{RHS} \, d\hat{z}$$
$$= \hat{h}_p \phi_c \sin \zeta_s - \epsilon \partial_{\hat{x}}(\hat{h}_p \hat{\bar{\sigma}}'_{p,xx}) - \epsilon \gamma^* \partial_{\hat{x}}(\hat{h}_f \phi_c \hat{\bar{p}}_f) - [[\epsilon \hat{\sigma}'_{p,xx} \partial_{\hat{x}}(\hat{s}^f) - \hat{\sigma}'_{p,xz}]]$$
$$- \epsilon \gamma^* \phi_c \hat{p}_f(\hat{b}) \partial_{\hat{x}}(\hat{b}) - [\epsilon \hat{\sigma}'_{p,xx}(\hat{b}) \partial_{\hat{x}}(\hat{b}) - \hat{\sigma}'_{p,xz}(\hat{b})] + \int_{\hat{b}}^{\hat{s}^f} \gamma^* \hat{C}_{dd}(\hat{u}_f - \hat{u}_p) \, d\hat{z}, \tag{C.58}$$

where again, the quantity in the jump bracket is zero provided that the depth profile of the effective granular stress is smooth. For convenience, the interphase coupling term

Chapter C: Shallow water model derivation

will be approximated as

$$\int_{\hat{b}}^{\hat{s}^f} \gamma^* \hat{C}_{dd}(\hat{u}_f - \hat{u}_p)\, \mathrm{d}\hat{z} = \gamma^* \hat{C}_{dd}\min(\hat{h}_f, \hat{h}_p)(\hat{\bar{u}}_f - \hat{\bar{u}}_p). \qquad \text{(C.59)}$$

While the model does assume that the granular phase is never oversaturated, this may not be the case for all numerical solutions. Hence, the inclusion of the min function is worthwhile. By equating Equations (C.56) and (C.58), the depth averaged downslope momentum conservation equation for the granular phase is

$$\begin{aligned}
\epsilon[\partial_{\hat{t}}(\hat{h}_p \phi_c \hat{\bar{u}}_p) + \partial_{\hat{x}}(\hat{h}_p \phi_c \hat{\bar{u}}_p^2)] = {} & -\epsilon\partial_{\hat{x}}(\hat{h}_p \hat{\bar{\sigma}}'_{p,xx}) - \epsilon\gamma^* \partial_{\hat{x}}(\hat{h}_f \phi_c \hat{\bar{p}}_f) \\
& + \hat{h}_p \phi_c \sin\zeta_s - \epsilon\gamma^* \phi_c \hat{p}_f(\hat{b})\partial_{\hat{x}}(\hat{b}) - [\epsilon\hat{\sigma}'_{p,xx}(\hat{b})\partial_{\hat{x}}(\hat{b}) - \hat{\sigma}'_{p,xz}(\hat{b})] \\
& + \gamma^* \hat{C}_{dd}\min(\hat{h}_f, \hat{h}_p)(\hat{\bar{u}}_f - \hat{\bar{u}}_p). \quad \text{(C.60)}
\end{aligned}$$

By, substituting Equations (C.43), (C.44), (C.51) and (C.53) into Equation (C.60) and simplifying, we can obtain the following

$$\begin{aligned}
\epsilon\left[\partial_{\hat{t}}(\hat{h}_p \phi_c \hat{\bar{u}}_p) + \partial_{\hat{x}}\left(\hat{h}_p \phi_c \hat{\bar{u}}_p^2 + \frac{1}{2}\phi_c \cos\zeta_s \,\hat{h}_p^2\right)\right] = {} \\
\underbrace{\hat{h}_p \phi_c \sin\zeta_s}_{\text{Gravity}} - \underbrace{\mu_b \frac{\hat{\bar{u}}_p}{|\hat{\bar{u}}_p|}\hat{h}_p \phi_c \cos\zeta_s\left(1 - \gamma^* \frac{\hat{h}_f}{\hat{h}_p}\right)}_{\text{Basal friction}} + \underbrace{\gamma^* \hat{C}_{dd}\min(\hat{h}_f, \hat{h}_p)(\hat{\bar{u}}_f - \hat{\bar{u}}_p)}_{\text{Darcy drag}} \\
- \underbrace{\epsilon\phi_c \cos\zeta_s \,\hat{h}_p \partial_{\hat{x}}(\hat{b})}_{\text{Topography}}, \quad \text{(C.61)}
\end{aligned}$$

where the gravity, basal friction and darcy drag terms are all $O(1)$ individually, but their sum is $O(\epsilon)$. Hence, Equation (C.61) can be rewritten to leading order accuracy as

$$\partial_{\hat{t}}(\hat{h}_p \phi_c \hat{\bar{u}}_p) + \partial_{\hat{x}}\left(\hat{h}_p \phi_c \hat{\bar{u}}_p^2 + \frac{1}{2}\phi_c \cos\zeta_s \,\hat{h}_p^2\right) = \hat{S}_p, \qquad \text{(C.62)}$$

where $\hat{S}_p$ is the summation of the $O(1)$ source terms such that

$$\epsilon\hat{S}_p = \hat{h}_p \phi_c \sin\zeta_s - \mu_b \frac{\hat{\bar{u}}_p}{|\hat{\bar{u}}_p|}\hat{h}_p \phi_c \cos\zeta_s\left(1 - \gamma^* \frac{\hat{h}_f}{\hat{h}_p}\right) + \gamma^* \hat{C}_{dd}\min(\hat{h}_f, \hat{h}_p)(\hat{\bar{u}}_f - \hat{\bar{u}}_p).$$

$$\text{(C.63)}$$

## C.4.4   Horizontal components of the fluid momentum continuity equations

Using Equation (C.27) and the scaling relations in Equation (C.28), the dimensionless fluid normal stress at the basal surface to $O(1)$ accuracy is

$$(\boldsymbol{n}^b \cdot \hat{\boldsymbol{\sigma}}_f \boldsymbol{n}^b) = -\phi_f \hat{p}_f^b, \qquad \hat{z} = \hat{b}. \tag{C.64}$$

Therefore, a dimensionless version of Equation (C.26) can be rewritten as

$$-\epsilon^2 \hat{\tau}_{f,xx}(\hat{b}) \partial_{\hat{x}}(\hat{b}) + \hat{\tau}_{f,xz}(\hat{b}) = C_f \hat{\bar{u}}_f |\hat{\bar{u}}_f|. \tag{C.65}$$

As was the case for the granular phase, the fluid downslope momentum equation needs to be integrated across the full phase depth. Given that $\phi_f$ is also a constant, the left-hand side of Equation (C.33) becomes

$$\text{LHS}_f = \epsilon\{\partial_{\hat{t}}[(1-\phi_c)\hat{u}_f] + \partial_{\hat{x}}[(1-\phi_c)\hat{u}_f\hat{u}_f] + \partial_{\hat{z}}[(1-\phi_c)\hat{u}_f\hat{w}_f]\}. \tag{C.66}$$

As it is assumed that the granular phase is never oversaturated, this process is simplified as there is no interfacial surface to consider. Again, using Leibniz's rule to swap the order of the integration and differentiation operations, applying the kinematic boundary conditions associated with the fluid phase (Equations C.16 and C.18) and simplifying the result using Equation (C.56)

$$\int_{\hat{b}}^{\hat{s}^f} \text{LHS}_f \, d\hat{z} = \epsilon\{\partial_{\hat{t}}[\hat{h}_f(1-\phi_c)\hat{\bar{u}}_f] + \partial_{\hat{x}}[\hat{h}_f(1-\phi_c)\hat{\bar{u}}_f^2]\}. \tag{C.67}$$

Similarly, the right-hand side of Equation (C.33) can also be rewritten

$$\text{RHS}_f = \epsilon^2 \partial_{\hat{x}}(\hat{\tau}_{f,xx}) + \partial_{\hat{z}}(\hat{\tau}_{f,xz}) - \epsilon \partial_{\hat{x}}[(1-\phi_c)\hat{p}_f] + (1-\phi_c)\sin\zeta_s + \hat{C}_{dd}(\hat{u}_p - \hat{u}_f). \tag{C.68}$$

This can be integrated again using Leibniz's rule and simplified using Equations (C.16), (C.18) and (C.22)

$$\int_{\hat{b}}^{\hat{s}^f} \text{RHS}_f \, d\hat{z} = \hat{h}_f(1-\phi_c)\sin\zeta_s + \epsilon^2 \partial_{\hat{x}}(\hat{h}_f\hat{\bar{\tau}}_{f,xx}) - \epsilon \partial_{\hat{x}}[\hat{h}_f(1-\phi_c)\hat{\bar{p}}_f]$$

$$- \epsilon(1-\phi_c)\hat{p}_f|_{\hat{b}}\partial_{\hat{x}}(\hat{b}) + (\epsilon^2 \tau_{f,xx}|_{\hat{b}}\partial_{\hat{x}}(\hat{b}) - \hat{\tau}_{f,xz}|_{\hat{b}}) + \int_{\hat{b}}^{\hat{s}^f} \hat{C}_{dd}(\hat{u}_p - \hat{u}_f) \, dz. \tag{C.69}$$

Chapter C: Shallow water model derivation

By equating Equations (C.67) and (C.69), rearranging and substituting in Equations (C.43), (C.44), (C.59) and (C.65) we obtain the depth averaged downslope momentum conservation equation for the fluid phase

$$
\epsilon \left\{ \partial_{\hat{t}}[\hat{h}_f(1-\phi_c)\hat{\bar{u}}_f] + \partial_{\hat{x}}\left[\hat{h}_f(1-\phi_c)\hat{\bar{u}}_f^{\,2} + \frac{1}{2}(1-\phi_c)\cos\zeta_s\,\hat{h}_f^2\right]\right\} =
$$

$$
\underbrace{\hat{h}_f(1-\phi_c)\sin\zeta_s}_{\text{Gravity}} - \underbrace{C_f\hat{\bar{u}}_f|\hat{\bar{u}}_f|}_{\text{Chézy drag}} + \underbrace{\hat{C}_{dd}\min(\hat{h}_f,\hat{h}_p)(\hat{\bar{u}}_p - \hat{\bar{u}}_f)}_{\text{Darcy drag}}
$$

$$
- \underbrace{\epsilon(1-\phi_c)\cos\zeta_s\,\hat{h}_f\partial_{\hat{x}}(\hat{b})}_{\text{Topography}} + \underbrace{\epsilon^2\partial_{\hat{x}}(\hat{h}_f\hat{\tau}_{f,xx})}_{\text{Viscous effects}}, \quad \text{(C.70)}
$$

where again the gravity, basal friction and darcy drag terms are all $O(1)$ individually, but their sum is $O(\epsilon)$. Hence, Equation (C.70) can be rewritten to leading order accuracy as

$$
\partial_{\hat{t}}[\hat{h}_f(1-\phi_c)\hat{\bar{u}}_f] + \partial_{\hat{x}}\left[\hat{h}_f(1-\phi_c)\hat{\bar{u}}_f^{\,2} + \frac{1}{2}(1-\phi_c)\cos\zeta_s\,\hat{h}_f^2\right] = \hat{S}_f, \quad \text{(C.71)}
$$

where $\hat{S}_f$ is the summation of the $O(1)$ source terms such that

$$
\epsilon\hat{S}_f = \hat{h}_f(1-\phi_c)\sin\zeta_s - C_f\hat{\bar{u}}_f|\hat{\bar{u}}_f| + \hat{C}_{dd}\min(\hat{h}_f,\hat{h}_p)(\hat{\bar{u}}_p - \hat{\bar{u}}_f). \quad \text{(C.72)}
$$

Note that, with the chosen scaling, the viscous term in Equation (C.70) - the only remaining dependence on the horizontal fluid pressure gradient - is of $O(\epsilon^2)$, and is thus negligible compared with the grain-fluid interaction term. Hence, in our model, the horizontal force balance is dominated by Darcy-type drag between fluid and grains rather than classical fluid forces that would drive the equivalent single-phase flow.

## C.4.5  Depth averaged dimensional system of equations

By discounting the normal component of each phase's momentum continuity equation, a reduced system of equations describing the motion of the depth averaged two-phase flow can be dimensionalised by applying the scalings below

$$
\left.\begin{aligned}
x &= L\hat{x}, & (h_v, s^v, b) &= H(\hat{h}_v, \hat{s}^v, \hat{b}), & t &= L/\sqrt{gH}\hat{t}, \\
u_v &= \sqrt{gH}\hat{u}_v, & S_v &= (gH^2/L)\hat{S}_v, & C_{dd} &= \rho_f\sqrt{g/H}\hat{C}_{dd},
\end{aligned}\right\} \quad \text{(C.73)}
$$

to Equations (C.39), (C.40), (C.62) and (C.71) and obtain

$$\partial_t(h_p) + \partial_x(h_p \bar{u}_p) = 0, \tag{C.74}$$

$$\partial_t(h_f) + \partial_x(h_f \bar{u}_f) = 0, \tag{C.75}$$

$$\partial_t(h_p \bar{u}_p) + \partial_x \left( h_p \bar{u}_p^2 + \frac{1}{2} g \cos \zeta_s \, h_p^2 \right) =$$
$$g \sin \zeta_s \, h_p - \mu_b \frac{\bar{u}_p}{|\bar{u}_p|} g h_p \cos \zeta_s \left( 1 - \gamma^* \frac{h_f}{h_p} \right) + \frac{C_{dd}}{\rho_p \phi_c} \min(h_f, h_p)(\bar{u}_f - \bar{u}_p), \tag{C.76}$$

$$\partial_t(h_f \bar{u}_f) + \partial_x \left( h_f \bar{u}_f^2 + \frac{1}{2} g \cos \zeta_s \, h_f^2 \right) =$$
$$g \sin \zeta_s \, h_f - \frac{C_f \bar{u}_f |\bar{u}_f|}{(1 - \phi_c)} + \frac{C_{dd}}{\rho_f (1 - \phi_c)} \min(h_f, h_p)(\bar{u}_p - \bar{u}_f). \tag{C.77}$$

To leading order accuracy, this system is analogous to the one developed by Meng et al. (2022) when it has been simplified to only consider an undersaturated flow case.

## C.5 Application to fluid-saturated granular column collapse

As our granular-fluid mixture spreads across a horizontal plane (see Figure C.2), we set $\zeta_s$ to 0. Additionally, we assume that fluid basal drag arising from fluid turbulence is negligible by setting $C_f = 0$. This simplification is computationally advantageous, as the fluid basal friction term can become numerically challenging when approximating $\bar{u}_f$ as the ratio between fluid discharge and $h_f$ (Chertock et al., 2015).

Considering the experimental configuration, it is also advantageous to transform the system of Equations (C.74)–(C.77) from a Cartesian to an axisymmetric reference frame. This transformation eliminates the dependence on the polar angle (Alcrudo and Garcia-Navarro, 1993), making the results applicable to flows without lateral boundaries, such as the case of axisymmetric collapses where the flow expands over an open slope, forming a fan. Utilising polar coordinates, we can express each non-conservative flux term $\kappa$ as the summation of a conservative flux term and a source term
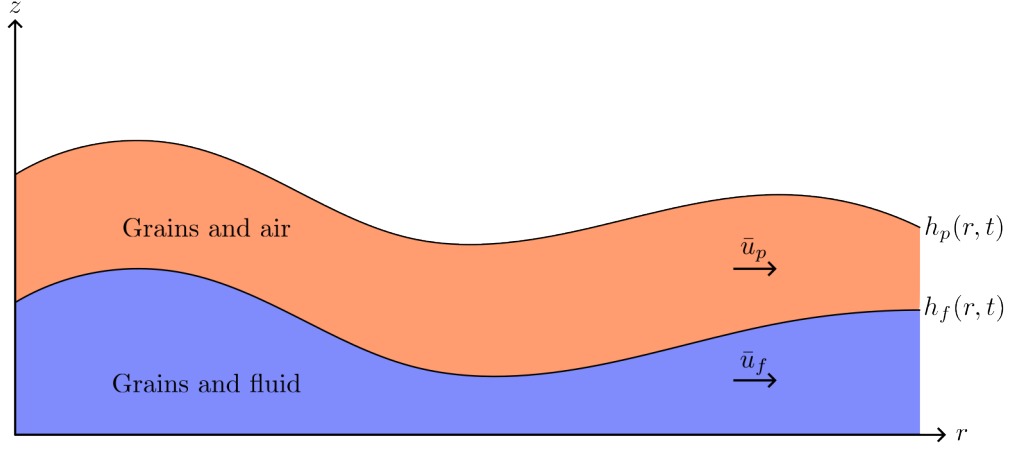
Figure C.2: Sketch of a 2-D slice of an undersaturated granular collapse modelled as two coupled continuum phases.

$$\frac{1}{r}\partial_r[\kappa(r,t)r] = \partial_r[\kappa(r,t)] + \frac{1}{r}\kappa(r,t), \tag{C.78}$$

where $r$ is the radial spatial dimension. Then, the system of Equations (C.74)–(C.77) can be expressed in the following conservative form

$$\partial_t h_p + \partial_r(h_p \bar{u}_p) = -\frac{h_p \bar{u}_p}{r}, \tag{C.79}$$

$$\partial_t h_f + \partial_r(h_f \bar{u}_f) = -\frac{h_f \bar{u}_f}{r}, \tag{C.80}$$

$$\partial_t(h_p \bar{u}_p) + \partial_r\left(h_p \bar{u}_p^2 + \frac{1}{2}g h_p^2\right) =$$
$$-\frac{h_p \bar{u}_p^2}{r} - \mu_b \frac{\bar{u}_p}{|\bar{u}_p|} g h_p \left(1 - \gamma^* \frac{h_f}{h_p}\right) + \frac{\eta_f \phi_f^2}{\rho_p \phi_p k} \min(h_f, h_p)(\bar{u}_f - \bar{u}_p), \tag{C.81}$$

$$\partial_t(h_f \bar{u}_f) + \partial_r\left(h_f \bar{u}_f^2 + \frac{1}{2}g h_f^2\right) = -\frac{h_f \bar{u}_f^2}{r} + \frac{\eta_f \phi_f}{\rho_f k} \min(h_f, h_p)(\bar{u}_p - \bar{u}_f). \tag{C.82}$$

The use of a conservative approach offers several advantages. Firstly, it ensures the accurate preservation of mass and momentum conservation across phase interfaces, enabling the correct representation of jump conditions (Meng et al., 2022). Secondly, from a numerical perspective, employing the conservative formulation proves beneficial, facilitating more efficient and accurate solutions of the system (Kurganov and Tadmor, 2000). The resulting system of Equations (C.79)–(C.82) allows us to predict the be-

haviour of the system in terms of conservative quantities such as $h_v$ and $h_v u_v$ for each phase, respectively.

## C.6  Implementation

The described computational framework was instantiated within Matlab (2020), wherein the spatial discretisation of Equations (C.79)–(C.82) was executed utilising the second-order central-upwind scheme developed by Kurganov and Petrova (2007) for solving the Saint-Venant system of equations. An explicit second-order Runge-Kutta method was employed for the temporal discretisation of the system. The application of this modelling methodology was demonstrated through its utilisation in analysing the collapse of granular-fluid columns subjected to elevated gravitational elevation, as explored in Chapter 5 of this thesis.

Appendix D

# Design of a 2D sloped prototype

## D.1  Introduction

This chapter details the development of a second physical centrifuge model, specifically designed to further investigate the the effects of polydispersity and fluid rheology on granular-fluid flow dynamics. The chapter begins by outlining the key objectives guiding the experimental investigation, followed by an in-depth discussion of the design and methodology underpinning the experimental apparatus. A comprehensive examination of the envisaged parameter space for the study is then presented, along with an evaluation of the strengths and limitations inherent in the chosen approach. The chapter then concludes by outlining the reasons why the model has yet to be used for extensive testing.

## D.2  Modelling objectives

The experimental investigations discussed in this thesis have yielded valuable insights into the impact of grain-fluid interactions on the dynamics of granular-fluid flows. However, it should be acknowledged that the explored parameter space, as outlined in Chapter 7, remains somewhat constrained. Existing evidence suggests a discernible grain size dependence in the evolution of excess pore pressure in geophysical flows (e.g. Mc-Coy et al., 2010). To address this limitation, it would be pertinent to conduct additional centrifuge model experiments that encompass a broader range of particle sizes. This can be achieved by incorporating both a polydispersed inertial particle phase and higher concentrations of kaolin clay suspended within the fluid phase.

Expanding the parameter space not only enhances the comprehensiveness of the study but also offers an opportunity to refine the shallow water model introduced in Chapter 5. Ideally, the new experimental configuration should closely align with the geometric characteristics of geophysical flows, such as the movement of a granular mixture down an inclined slope. Such a configuration would allow the study focus more on the

dynamics of the flow rather than its runout, as was the case for the axisymmetric configuration. Simultaneously, it should facilitate a straightforward definition of the initial geometry of the granular-fluid mixture.

In contrast to the axisymmetric configuration, the new experimental apparatus should feature a flow release mechanism that minimally influences the subsequent flow dynamics. Additionally, careful consideration should be given to mitigating the influence of the Coriolis acceleration direction on flow behaviour. This is crucial for ensuring that the experimental setup can replicate flow conditions consistently, regardless of the radius of the geotechnical centrifuge. In summary, the proposed experiments aim to broaden the scope of the current research, refining both the experimental design and model configuration for a more comprehensive understanding of granular-fluid interactions in geophysical flows.

## D.3   Model apparatus

In this section, we present a comprehensive description of the newly developed experimental apparatus designed for studying unsteady granular-fluid flows down a slope (see Figure D.1). The apparatus is housed within a windproof strong box and can be mounted on to the University of Nottingham's GT50/1.7 geotechnical beam centrifuge, enabling control over the stress-state within the granular-fluid flow.

The orientation of the model can be adjusted to direct the flow towards, away from, or perpendicular to the centrifuge's direction of travel. This adjustment provides control over the Coriolis acceleration's impact on the flow, allowing the user to dictate whether the Coriolis acceleration acts to contract, dilate, or exhibit little volumetric influence on the flow, respectively.

The apparatus, inspired by the work of Cabrera and Wu (2017), consists of two major components within the strong box. The first component is the storage vessel (see Figure D.2), capable of holding a maximum material volume of $8.23 \times 10^{-4}\, \mathrm{m}^3$. Bolted to the strong box's lid, this vessel releases the granular-fluid mixture through a trap door, operated by a release mechanism similar to that used in the axisymmetric column collapse.

The watertight trap door, initially secured by tensioning a steel rod against a forked piece of steel, opens upon triggering an air-powered actuator. A steel wire threaded through the rod allows control over the trap door's opening angle, facilitating a precise and repeatable release. The granular mixture then enters a U-shaped channel and travels

down a 600 mm long slope inclined at 27.5° (see Figure D.3).
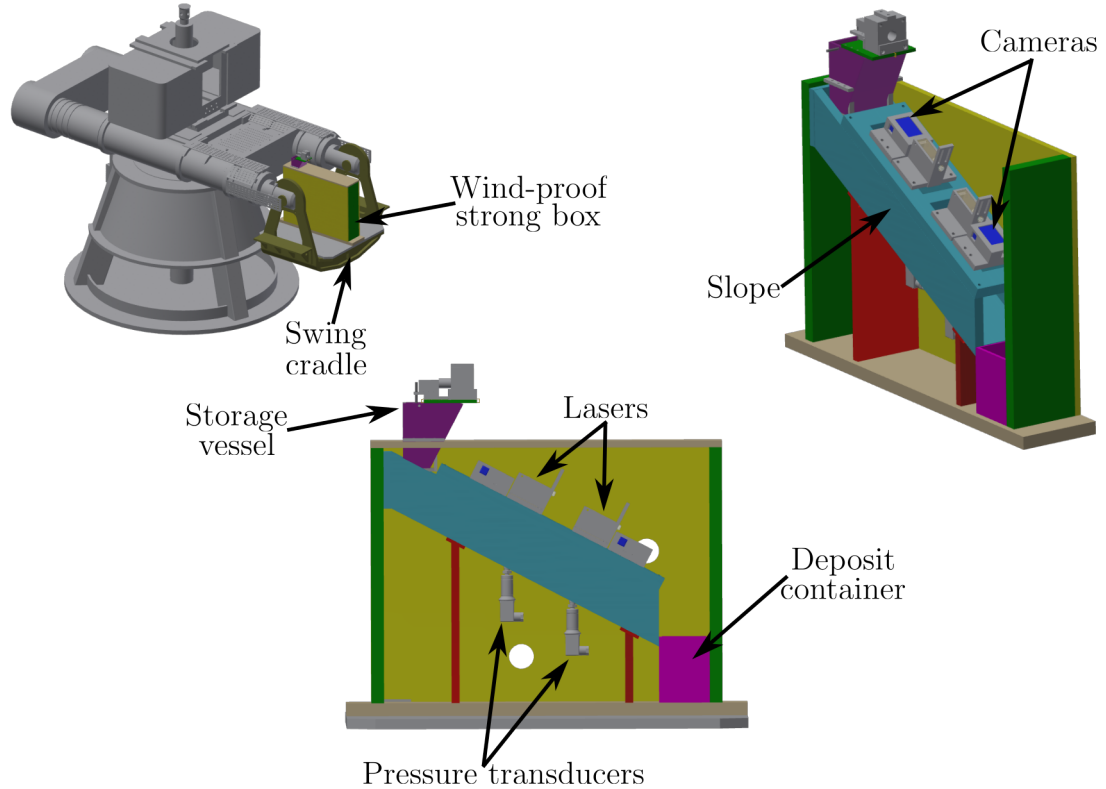


Figure D.1: Schematic of the planar collapse configuration at different angles.

The slope, 100 mm in width (equivalent to 12.5 diameters of the largest inertial particle size), is comprised of smooth sidewalls and a roughened base covered with 4 mm diameter glass spheres. At the slope's lower end, a container captures and stores the granular mixture.

To observe the flowing mixture, two Go-Pro cameras are fixed to the slope's top plate, approximately 115 mm above the surface. Positioned parallel to the slope, these cameras capture the flow's evolution, facilitating subsequent image correction and analysis. Illumination is provided by two 12 V lightsheets installed into the sidewalls, ensuring uniform lighting diffused behind protective plexiglass sheets.

Basal fluid pressure measurements are obtained at two locations using pore pressure transducers capable of recording pressures up to 20 kPa with an accuracy of ±20 Pa at a frequency of 1000 Hz. The transducers are strategically mounted with their diaphragm's axis of deformation perpendicular to the centrifugal field's line of action.

To protect the pressure transducers from damage due to fine kaolin clay particles within the granular mixture, porous discs are mounted above the transducers. These
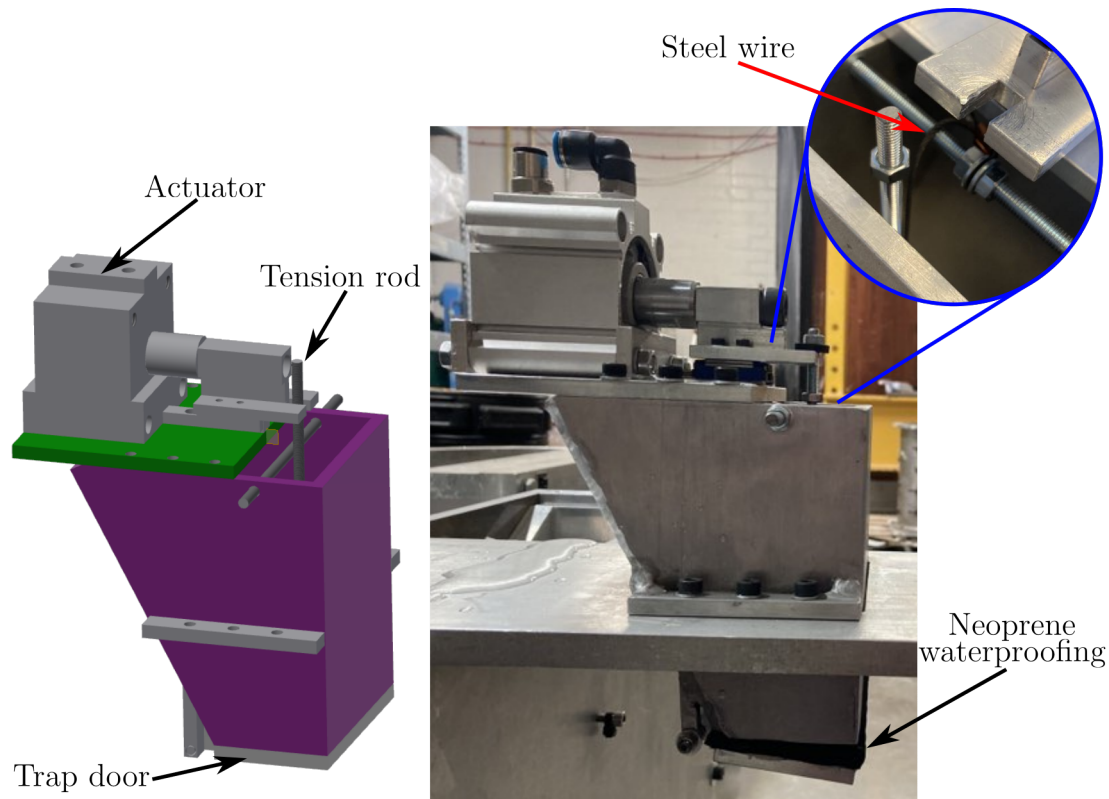
Figure D.2: Schematic (left) and image (right) of the storage vessel where the inset shows a close up view of the tension rod, steel fork, and steel wire.

discs, with sufficient porosity to prevent clay particles passing through them, are fully saturated under vacuum conditions before installation. To maintain saturation during centrifuge spin-up, a rainfall nozzle drizzles water down the slope, ceasing before test initiation. During spin-up the fluid is allowed to drain out of the experimental configuration through an outflow pipe located on the side of the collection container and dumped towards the centrifuge's axis of rotation. Closing the outflow pipe with a solenoid valve prior to the test initiation retains particles and fluid, including fine clays, within the container.

Additionally, two point lasers attached to the slope's top plate record the height of the flow passing below them at a frequency of 1000 Hz. This addition is crucial for obtaining flow height information, which was unavailable in the previous experimental configuration. The lasers are strategically positioned close to the basal fluid pressure measurement locations, avoiding placing the lasers over the porous stones that could distort laser readings due to refraction. This positioning enables the evaluation of excess pore fluid pressures by approximating hydrostatic fluid pressure using flow height and,
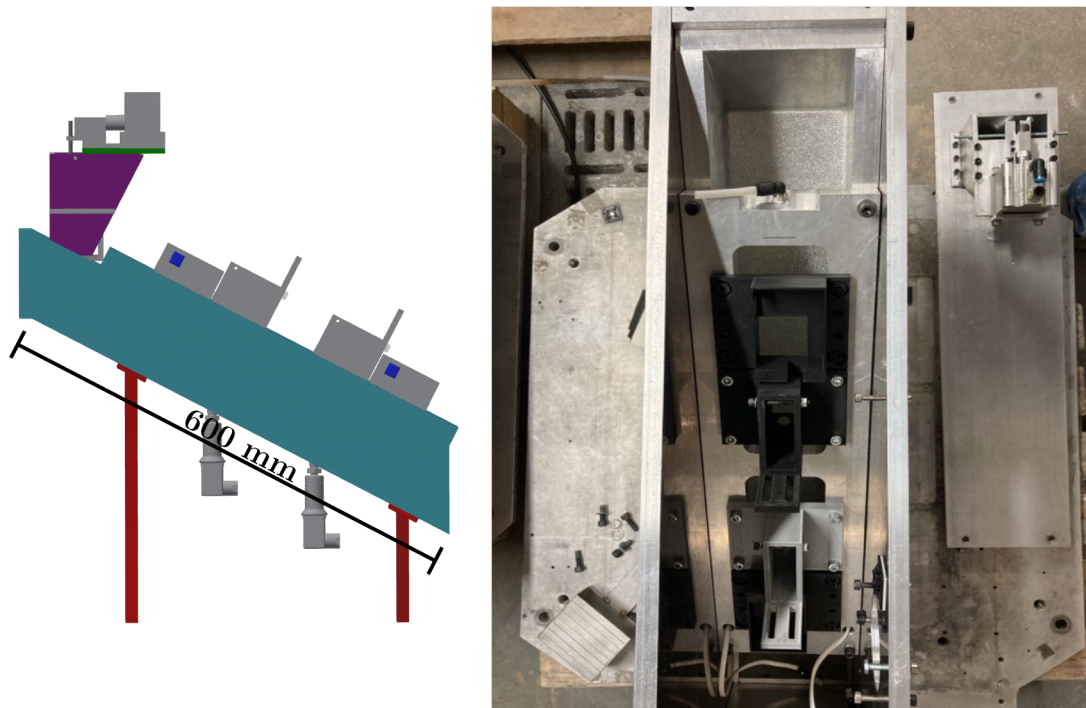
Figure D.3: Schematic (left) and plan view image (right) of the slope and data acquisition systems.

subsequently subtracting this value from the total fluid pressure obtained from the basal fluid pressure sensors (e.g. Kaitna et al., 2016).

## D.4 Parameter space of interest

While the available parameter space for such an investigation is large, as discussed in Section D.1, the primary objective of this study is to enhance our comprehension of the impact of grain-fluid interactions on geophysical flow dynamics. Consequently, the focus should be centred on key variables, namely the particle size distribution of the granular phase, the viscosity of the fluid phase, and the saturation level of the initial configuration.

Among these variables, the primary emphasis lies on variations in the particle size distribution. Preliminary considerations involve a comparative analysis of flow behaviours between monodispersed inertial particle sizes and polydispersed inertial particle sizes. This entails a significant variation in both the concentration and grading of the granular compositions. Additionally, the aim is to explore the influence of fine kaolin particles within the flow composition, with effective kaolin concentrations reach-

ing up to approximately 50% by mass. This approach draws inspiration from the work of Kaitna et al. (2016), who investigated into the role of particle size distribution in the dynamics of steady-state granular-fluid flows.

While a scale analysis akin to the one conducted for the axisymmetric collapse experiments would be beneficial, especially by varying the effective gravitational acceleration imposed on the model by the centrifuge, the majority of tests within the study would aim to replicate geophysically similar stress states. This choice allows the study to focus on understanding the mechanisms behind excess pore pressure generation observed in natural debris flows.

## D.5    Design limitations

While the proposed investigation has the potential to achieve the objectives outlined in Section D.2, the usability of the obtained data is constrained by an incomplete understanding of how centrifuge modelling influences the scaling of grain-fluid interactions (see Chapter 6). There is a possibility that the model's behaviour may deviate from real-world observations.

As discussed in Section 7.2, further numerical modelling is deemed essential to comprehensively understand how the centrifuge modelling environment impacts the behaviour of our laboratory-scale models. Only through such an understanding can we fully appreciate how to relate observations from our experiments to the behaviour observed in geophysical flows and better replicate this behaviour within the models used to predict them.

## D.6    Reasons for non-execution

As of the submission date of this thesis, the planar setup has been constructed, but a detailed testing regimen has yet to commence. The primary impediment to this delay is unforeseen complications during the construction and preliminary testing phases, preventing the extensive testing required for the scheduled analysis in the final months of my PhD. Consequently, an agreement was reached between myself and my supervisors to redirect my time and effort towards developing research articles focusing on the two modelling approaches detailed in Chapters 5 and 6. However, the apparatus is now in a state where preliminary testing can resume, and final adjustments to the model can be made.

# References

Alcrudo, F. and Garcia-Navarro, P. (1993). A high-resolution Godunov-type scheme in finite volumes for the 2D shallow-water equations. *International Journal for Numerical Methods in Fluids*. 16(6):489–505.

Allen, S. K., Rastner, P., Arora, M., Huggel, C., and Stoffel, M. (2016). Lake outburst and debris flow disaster at Kedarnath, June 2013: Hydrometeorological triggering and topographic predisposition. *Landslides*. 13(6):1479–1491.

Artoni, R., Santomaso, A. C., Gabrieli, F., Tono, D., and Cola, S. (2013). Collapse of quasi-two-dimensional wet granular columns. *Physical Review E*. 87(3):032205.

Bagnold, R. A. (1954). Experiments on a gravity-free fispersion of large dolid dpheres in a Newtonian fluid under shear. *Proceedings of the Royal Society of London. Series A, Mathematical and Physical Sciences*. 225(1160):49–63.

Bandis, S., Delmonaco, G., Dutto, F., Margottini, C., Mortara, G., Serafini, S., and Trocciola, A. (1999). Landslides and precipitation: the event of 4–6th November 1994 in the Piemonte region, North Italy. *Floods and Landslides: Integrated Risk Assessment*. Springer:315–326.

Batchelor, G. K. (2000). *An Introduction to Fluid Dynamics*. Cambridge Mathematical Library. Cambridge: Cambridge University Press.

Batra, R. C. (2006). *Elements of Continuum Mechanics*. Aiaa.

Bautista, M. L. P., Delos Reyes, P. J., Santos, E. R. U., Gaurino, W. A., Olfindo, V. S. V., Rivera, D. A. V., Dizon, M. P., Maximo, R. P. R., Ativo, S. C. J., Degones, M. F., Cabaluna, S. B., Babon, L. G. O., Bautista, B. C., Jenkins, S. F., and Solidum, R. U. (2023). Quantitative impact assessment of the 2019 tropical cyclone Kammuri lahars: Mayon volcano, Philippines. *International Journal of Disaster Risk Reduction*. 94:103779.

Berger, C., McArdell, B., and Schlunegger, F. (2011). Direct measurement of channel erosion by debris flows, Illgraben, Switzerland. *Journal of Geophysical Research: Earth Surface*. 116(F1).

Berti, M., Genevois, R., Simoni, A., and Tecca, P. R. (1999). Field observations of a debris flow event in the Dolomites. *Geomorphology*. 29(3):265–274.

# REFERENCES

Berzi, D. and Jenkins, J. T. (2008). A theoretical analysis of free-surface flows of saturated granular–liquid mixtures. *Journal of Fluid Mechanics*. 608:393–410.

Bingham, E. (1922). *Fluidity and Plasticity*. McGraw-Hill Book Company:462.

Blaber, J., Adair, B., and Antoniou, A. (2015). Ncorr: Open-Source 2D Digital Image Correlation Matlab Software. *Experimental Mechanics*. 55(6):1105–1122.

Blajan, M., Umeda, A., and Shimizu, K. (2013). Surface treatment of glass by microplasma. *IEEE Transactions on Industry Applications*. 49(2):714–720.

Bouchut, F., Fernández-Nieto, E. D., Koné, E. H., Mangeney, A., and Narbona-Reina, G. (2017). A two-phase solid-fluid model for dense granular flows including dilatancy effects: comparison with submarine granular collapse experiments. *EPJ Web of Conferences*. 140:09039.

Bouchut, F., Fernandez-Nieto, E. D., Mangeney, A., and Narbona-Reina, G. (2015). A two-phase shallow debris flow model with energy balance. *ESAIM: Mathematical Modelling and Numerical Analysis*. 49(1):101–140.

Bouchut, F., Fernández-Nieto, E. D., Mangeney, A., and Narbona-Reina, G. (2016). A two-phase two-layer model for fluidized granular flows with dilatancy effects. *Journal of Fluid Mechanics*. 801:166–221.

Bougouin, A. and Lacaze, L. (2018). Granular collapse in a fluid: Different flow regimes for an initially dense-packing. *Physical Review Fluids*. 3(6):064305.

Bougouin, A., Lacaze, L., and Bonometti, T. (2019). Collapse of a liquid-saturated granular column on a horizontal plane. *Physical Review Fluids*. 4(12):124306.

Bowman, E. T., Laue, J., Imre, B., and Springman, S. M. (2010). Experimental modelling of debris flow behaviour using a geotechnical centrifuge. *Canadian Geotechnical Journal*. 47(7):742–762.

Bowman, E. T. and Take, W. A. (2015). The runout of chalk cliff collapses in England and France—case studies and physical model experiments. *Landslides*. 12(2):225–239.

Bowman, E., Take, W., Rait, K., and Hann, C. (2012). Physical models of rock avalanche spreading behaviour with dynamic fragmentation. *Canadian Geotechnical Journal*. 49(4):460–476.

Brayshaw, D. and Hassan, M. A. (2009). Debris flow initiation and sediment recharge in gullies. *Geomorphology*. 109(3-4):122–131.

Brucks, A., Arndt, T., Ottino, J. M., and Lueptow, R. M. (2007). Behavior of flowing granular materials under variable g. *Physical Review E*. 75(3):032301.

# REFERENCES

Buckingham, E. (1914). On physically similar systems; illustrations of the use of dimensional equations. *Physical Review*. 4(4):345.

Cabrera, M. (2016). Experimental modelling of granular flows in rotating frames. PhD thesis. University of Natural Resources and Life Sciences, Vienna.

Cabrera, M. and Leonardi, A. (2022). On the scaling principles of kinematic processes in a centrifugal acceleration field. *Proc. of the 10th International Conference on Physical Modelling in Geotechnics*.

Cabrera, M., Mathews, J., and Wu, W. (2016). Granular flows in the centrifuge. *Proceedings of the 3rd European Conference on Physical Modelling in Geotechnics (EUROFUGE 2016)*.

Cabrera, M. and Estrada, N. (2019). Granular column collapse: Analysis of grain-size effects. *Physical Review E*. 99(1):012905.

Cabrera, M., Kailey, P., Bowman, E. T., and Wu, W. (2018). Effects of viscosity in granular flows simulated in a centrifugal acceleration field. *Physical Modelling in Geotechnics, Volume 2*. CRC Press:1075–1080.

Cabrera, M. A., Leonardi, A., and Peng, C. (2020). Granular flow simulation in a centrifugal acceleration field. *Géotechnique*. 70(10):894–905.

Cabrera, M. A. and Wu, W. (2017). Experimental modelling of free-surface dry granular flows under a centrifugal acceleration field. *Granular Matter*. 19(4).

Caicedo, B. and Thorel, L. (2014). Centrifuge modelling of unsaturated soils. *Journal of Geo-Engineering Sciences*. 2(1-2):83–103.

Capart, H. and Young, D. (1998). Formation of a jump by the dam-break wave over a granular bed. *Journal of Fluid Mechanics*. 372:165–187.

Capart, H., Young, D., and Zech, Y. (2002). Voronoï imaging methods for the measurement of granular flows. *Experiments in Fluids*. 32(1):121–135.

Ceccato, F., Leonardi, A., Girardi, V., Simonini, P., and Pirulli, M. (2020). Numerical and experimental investigation of saturated granular column collapse in air. *Soils and Foundations*. 60(3):683–696.

Cesca, M. and D'Agostino, V. (2008). Comparison between FLO-2D and RAMMS in debris-flow modelling: a case study in the Dolomites. *WIT Transactions on Engineering Sciences*. 60:197–206.

Chadwick, P. (1999). *Continuum Mechanics: Concise Theory and Problems*. Courier Corporation.

REFERENCES

Chae, B.-G., Park, H.-J., Catani, F., Simoni, A., and Berti, M. (2017). Landslide prediction, monitoring and early warning: a concise review of state-of-the-art. *Geosciences Journal*. 21:1033–1070.

Chaudhry, M. H. (2008). *Open-Channel Flow*. Vol. 523. Springer.

Chertock, A., Cui, S., Kurganov, A., and Wu, T. (2015). Well-balanced positivity preserving central-upwind scheme for the shallow water system with friction terms. *International Journal for Numerical Methods in Fluids*. 78(6):355–383.

Chiarle, M., Iannotti, S., Mortara, G., and Deline, P. (2007). Recent debris flow occurrences associated with glaciers in the Alps. *Global and Planetary Change*. 56(1-2):123–136.

Choi, C. E., Au-Yeung, S., Ng, C. W. W., and Song, D. (2015). Flume investigation of landslide granular debris and water runup mechanisms. *Géotechnique Letters*. 5(1):28–32.

Christen, M., Kowalski, J., and Bartelt, P. (2010). RAMMS: Numerical simulation of dense snow avalanches in three-dimensional terrain. *Cold Regions Science and Technology*. 63(1-2):1–14.

Contreras, S. M. and Davies, T. R. (2000). Coarse-grained debris-flows: hysteresis and time-dependent rheology. *Journal of Hydraulic Engineering*. 126(12):938–941.

Costa, J. E. (1991). Nature, mechanics, and mitigation of the Val Pola landslide, Valtellina, Italy, 1987-1988. *Zeitschrift für Geomorphologie*. 35(1):15–38.

Coussot, P. (2017). *Mudflow Rheology and Dynamics*. Routledge.

Coussot, P., Laigle, D., Arattano, M., Deganutti, A., and Marchi, L. (1998). Direct determination of rheological characteristics of debris flow. *Journal of Hydraulic Engineering*. 124(8):865–868.

Crosta, G. and Dal Negro, P. (2003). Observations and modelling of soil slip-debris flow initiation processes in pyroclastic deposits: the Sarno 1998 event. *Natural Hazards and Earth System Sciences*. 3(1/2):53–69.

Cui, Y., Choi, C. E., Liu, L. H. D., and Ng, C. W. W. (2018). Effects of particle size of mono-disperse granular flows impacting a rigid barrier. *Natural Hazards*. 91(3):1179–1201.

Cundall, P. A. and Strack, O. D. (1979). A discrete numerical model for granular assemblies. *Géotechnique*. 29(1):47–65.

Dalziel, S. B., Carr, M., Sveen, J. K., and Davies, P. A. (2007). Simultaneous synthetic schlieren and PIV measurements for internal solitary waves. *Measurement Science and Technology*. 18(3):533.

REFERENCES

Davies, T. R. (1988). Debris flow surges: a laboratory investigation. *Mitteilungen der Versuchsanstalt fur Wasserbau, Hydrologie und Glaziologie an der Eidgenossischen Technischen Hochschule Zurich*. 96.

Davies, T. R. (1990). Debris-flow surges—experimental simulation. *Journal of Hydrology (New Zealand)*. 29(1):18–46.

de Boer, R. and Ehlers, W. (1990). The development of the concept of effective stresses. *Acta Mechanica*. 83(1):77–92.

de Bono, J. P. and McDowell, G. R. (2016). Investigating the effects of particle shape on normal compression and overconsolidation using DEM. *Granular Matter*. 18(3):55.

de Haas, T., Braat, L., Leuven, J. R. F. W., Lokhorst, I. R., and Kleinhans, M. G. (2015). Effects of debris flow composition on runout, depositional mechanisms, and deposit morphology in laboratory experiments. *Journal of Geophysical Research: Earth Surface*. 120(9):1949–1972.

de Haas, T., McArdell, B., Nijland, W., Åberg, A., Hirschberg, J., Jong, S. de, and Huguenin, P. (2023). Factors controlling bed and bank erosion in the Illgraben (CH). *E3S Web of Conf.* 415:01004.

Delannay, R., Valance, A., Mangeney, A., Roche, O., and Richard, P. (2017). Granular and particle-laden flows: From laboratory experiments to field observations. *Journal of Physics D-Applied Physics*. 50(5):053001.

Dole, M. (1951). Surface tension measurements. *Physical Methods in Chemical Analysis*. 2:305–332.

Dorbolo, S., Maquet, L., Brandenbourger, M., Ludewig, F., Lumay, G., Caps, H., Vandewalle, N., Rondia, S., Mélard, M., and Loon, J. van (2013). Influence of the gravity on the discharge of a silo. *Granular Matter*. 15:263–273.

Dullien, F. A. (2012). *Porous Media: Fluid Transport and Pore Structure*. San Diego, California: Academic press.

Duncan, J. M., Wright, S. G., and Brandon, T. L. (2014). *Soil Strength and Slope Stability*. John Wiley & Sons.

Ellis, E., Cox, C., Yu, H., Ainsworth, A., and Baker, N. (2006). A new geotechnical centrifuge at the University of Nottingham, UK. *6th International Conference of Physical Modelling in Geotechnics: ICPMG*. 6:129–133.

Fan, Y., Jacob, K. V., Freireich, B., and Lueptow, R. M. (2017). Segregation of granular materials in bounded heap flow: A review. *Powder Technology*. 312:67–88.

REFERENCES

Fang, K., Tang, H., Li, C., Su, X., An, P., and Sun, S. (2022). Centrifuge modelling of landslides and landslide hazard mitigation: A review. *Geoscience Frontiers*. 14(1):101493.

Feng, Y. T., Han, K., and Owen, D. R. J. (2010). Combined three-dimensional lattice Boltzmann method and discrete element method for modelling fluid–particle interactions with experimental assessment. *International Journal for Numerical Methods in Engineering*. 81(2):229–245.

Feng, Z.-G. and Michaelides, E. E. (2004). The immersed boundary-lattice Boltzmann method for solving fluid–particles interaction problems. *Journal of Computational Physics*. 195(2):602–628.

Flanders, H. (1973). Differentiation under the integral sign. *The American Mathematical Monthly*. 80(6):615–627.

Forterre, Y. and Pouliquen, O. (2008). Flows of dense granular media. *Annual Review of Fluid Mechanics*. 40(1):1–24.

Frank, F., McArdell, B. W., Oggier, N., Baer, P., Christen, M., and Vieli, A. (2017). Debris-flow modeling at Meretschibach and Bondasca catchments, Switzerland: sensitivity testing of field-data-based entrainment model. *Natural Hazards and Earth System Sciences*. 17(5):801–815.

Frey, H., Huggel, C., Chisolm, R. E., Baer, P., McArdell, B., Cochachin, A., and Portocarrero, C. (2018). Multi-source glacial lake outburst flood hazard assessment and mapping for Huaraz, Cordillera Blanca, Peru. *Frontiers in Earth Science*. 6:210.

Froude, M. J. and Petley, D. N. (2018). Global fatal landslide occurrence from 2004 to 2016. *Natural Hazards and Earth System Sciences*. 18(8):2161–2181.

Gabet, E. J. and Mudd, S. M. (2006). The mobilization of debris flows from shallow landslides. *Geomorphology*. 74(1-4):207–218.

García-Martínez, R. and López, J. L. (2005). Debris flows of December 1999 in Venezuela. *Debris-Flow Hazards and Related Phenomena*. Berlin, Heidelberg: Springer Berlin Heidelberg:519–538.

Gariano, S. L. and Guzzetti, F. (2016). Landslides in a changing climate. *Earth-Science Reviews*. 162:227–252.

Garnier, J., Gaudin, C., Springman, S. M., Culligan, P., Goodings, D., Konig, D., Kutter, B., Phillips, R., Randolph, M., and Thorel, L. (2007). Catalogue of scaling laws and similitude questions in geotechnical centrifuge modelling. *International Journal of Physical Modelling in Geotechnics*. 7(3):01–23.

REFERENCES

George, D. L. and Iverson, R. M. (2014). A depth-averaged debris-flow model that includes the effects of evolving dilatancy. II. Numerical predictions and experimental tests. *Proceedings of the Royal Society A: Mathematical, Physical and Engineering Sciences*. 470(2170):20130820.

Goharzadeh, A., Khalili, A., and Jørgensen, B. B. (2005). Transition layer thickness at a fluid-porous interface. *Physics of Fluids*. 17(5):057102.

Graf, C. and McArdell, B. W. (2009). Debris-flow monitoring and debris-flow runout modelling before and after construction of mitigation measures: an example from an instable zone in the Southern Swiss Alps. *La géomorphologie alpine: entre patrimoine et contrainte. Actes du colloque de la Société Suisse de Géomorphologie*:3–5.

Gray, J. M. N. T. and Kokelaar, B. P. (2010). Large particle segregation, transport and accumulation in granular free-surface flows. *Journal of Fluid Mechanics*. 652:105–137.

Gray, J. and Edwards, A. (2014). A depth-averaged-rheology for shallow granular free-surface flows. *Journal of Fluid Mechanics*. 755:503–534.

Gray, J., Tai, Y.-C., and Noelle, S. (2003). Shock waves, dead zones and particle-free regions in rapid granular free-surface flows. *Journal of Fluid Mechanics*. 491:161–181.

Gray, J., Wieland, M., and Hutter, K. (1999). Gravity-driven free surface flow of granular avalanches over complex basal topography. *Proceedings of the Royal Society of London. Series A: Mathematical, Physical and Engineering Sciences*. 455(1985):1841–1874.

Gray, J. M. N. T. (2001). Granular flow in partially filled slowly rotating drums. *Journal of Fluid Mechanics*. 441:1–29.

Greve, R. and Hutter, K. (1993). Motion of a granular avalanche in a convex and concave curved chute: experiments and theoretical predictions. *Philosophical Transactions of the Royal Society of London. Series A: Physical and Engineering Sciences*. 342(1666):573–600.

Greve, R., Koch, T., and Hutter, K. (1994). Unconfined flow of granular avalanches along a partly curved surface. I. Theory. *Proceedings of the Royal Society of London. Series A: Mathematical and Physical Sciences*. 445(1924):399–413.

Grimsley, K. J., Rathburn, S. L., Friedman, J. M., and Mangano, J. F. (2016). Debris Flow Occurrence and Sediment Persistence, Upper Colorado River Valley, CO. *Environmental Management*. 58(1):76–92.

REFERENCES

Guadagno, F., Revellino, P., and Grelle, G. (2011). The 1998 Sarno landslides: Conflicting interpretations of a natural event. *International Conference on Debris-Flow Hazards Mitigation: Mechanics, Prediction, and Assessment, Proceedings*.

Guérin, A., Devauchelle, O., and Lajeunesse, E. (2014). Response of a laboratory aquifer to rainfall. *Journal of Fluid Mechanics*. 759.

Guzzetti, F. (2000). Landslide fatalities and the evaluation of landslide risk in Italy. *Engineering Geology*. 58(2):89–107.

Han, K., Feng, Y., and Owen, D. (2007). Coupled lattice Boltzmann and discrete element modelling of fluid–particle interaction problems. *Computers & Structures*. 85(11-14):1080–1088.

Han, Y. and Cundall, P. A. (2011). Lattice Boltzmann modeling of pore-scale fluid flow through idealized porous media. *International Journal for Numerical Methods in Fluids*. 67(11):1720–1734.

Han, Y. and Cundall, P. A. (2013). LBM–DEM modeling of fluid–solid interaction in porous media. *International Journal for Numerical and Analytical Methods in Geomechanics*. 37(10):1391–1407.

Harilal, R. and Ramji, M. (2014). Adaptation of Open Source 2D DIC Software Ncorr for Solid Mechanics Applications. *9th International Symposium on Advanced Science and Technology in Experimental Mechanics*.

He, X. and Luo, L.-S. (1997). Theory of the lattice Boltzmann method: From the Boltzmann equation to the lattice Boltzmann equation. *Physical Review E*. 56(6):6811.

Heller, V. (2011). Scale effects in physical hydraulic engineering models. *Journal of Hydraulic Research*. 49(3):293–306.

Henein, H. (1980). Bed behavior in rotary cylinders with applications to rotary kilns. PhD thesis. University of British Columbia, Canada.

Herrmann, H. J., Andrade, J. S., Araújo, A. D., and Almeida, M. (2007). Particles in fluids. *The European Physical Journal Special Topics*. 143:181–189.

Herschel, W. H. and Bulkley, R. (1926). Consistency measurements of rubber-benzene solutions. *Kolloid-Zeitschrift*. 39(4):291–300.

Hirschberg, J., McArdell, B. W., Badoux, A., and Molnar, P. (2019). Analysis of rainfall and runoff for debris flows at the Illgraben catchment, Switzerland. *Association of Environmental and Engineering Geologists; special publication 28*.

Hu, G., Hu, Z., Jian, B., Liu, L., and Wan, H. (2010). On the determination of the damping voefficient of non-linear spring-dashpot system to model Hertz contact for simu-

lation by Discrete Element Method. *2010 WASE International Conference on Information Engineering*. 3:295–298.

Hu, W., Dong, X., Xu, Q., Wang, G., Van Asch, T., and Hicher, P. (2016). Initiation processes for run-off generated debris flows in the Wenchuan earthquake area of China. *Geomorphology*. 253:468–477.

Huang, Y. and Zhang, B. (2022). Review on key issues in centrifuge modeling of flow-structure interaction. *European Journal of Environmental and Civil Engineering*. 26(6):2354–2370.

Huggel, C., Zgraggen-Oswald, S., Haeberli, W., Kääb, A., Polkvoj, A., Galushkin, I., and Evans, S. G. (2005). The 2002 rock/ice avalanche at Kolka/Karmadon, Russian Caucasus: Assessment of extraordinary avalanche formation and mobility, and application of QuickBird satellite imagery. *Natural Hazards and Earth System Sciences*. 5(2):173–187.

Hungr, O., Evans, S., Bovis, M., and Hutchinson, J. (2002). A review of the classification of landslides of the flow type (vol 7, pg 225, 2001). *Environmental & Engineering Geoscience*. 8(1).

Hungr, O. (2000). Analysis of debris flow surges using the theory of uniformly progressive flow. *Earth Surface Processes and Landforms: The Journal of the British Geomorphological Research Group*. 25(5):483–495.

Hungr, O., Leroueil, S., and Picarelli, L. (2014). The Varnes classification of landslide types, an update. *Landslides*. 11:167–194.

Hussin, H., Quan Luna, B., Van Westen, C., Christen, M., Malet, J.-P., and Van Asch, T. W. (2012). Parameterization of a numerical 2-D debris flow model with entrainment: A case study of the Faucon catchment, Southern French Alps. *Natural Hazards and Earth System Sciences*. 12(10):3075–3090.

Hutchinson, J. (1997). Mass movement. *Encyclopedia of Earth Science*. Berlin, Heidelberg: Springer Berlin Heidelberg:688–696.

Hutter, K. and Koch, T. (1991). Motion of a granular avalanche in an exponentially curved chute: Experiments and theoretical predictions. *Philosophical Transactions of the Royal Society of London. Series A: Physical and Engineering Sciences*. 334(1633):93–138.

Hutter, K., Siegel, M., Savage, S., and Nohguchi, Y. (1993). Two-dimensional spreading of a granular avalanche down an inclined plane Part I. theory. *Acta Mechanica*. 100:37–68.

REFERENCES

Hutter, K., Wang, Y., and Pudasaini, S. P. (2005). The Savage–Hutter avalanche model: How far can it be pushed? *Philosophical Transactions of the Royal Society A: Mathematical, Physical and Engineering Sciences*. 363(1832):1507–1528.

Idinger, G. (2016). Experimental study of failure initiation in partially saturated slopes. PhD thesis. Universität für Bodenkultur, Wien.

Ilea, D. E. and Whelan, P. F. (2011). Image segmentation based on the integration of colour–texture descriptors—A review. *Pattern Recognition*. 44(10-11):2479–2501.

Iverson, N. R., Mann, J. E., and Iverson, R. M. (2010a). Effects of soil aggregates on debris-flow mobilization: Results from ring-shear experiments. *Engineering Geology*. 114(1-2):84–92.

Iverson, R. M. (2003). The debris-flow rheology myth. *Debris-Flow Hazards Mitigation: Mechanics, Prediction, and Assessment*:303–314.

Iverson, R. M., Reid, M. E., Iverson, N. R., LaHusen, R. G., Logan, M., Mann, J. E., and Brien, D. L. (2000). Acute Sensitivity of Landslide Rates to Initial Soil Porosity. *Science*. 290(5491):513–516.

Iverson, R. M. (2014). Debris flows: Behaviour and hazard assessment. *Geology Today*. 30(1):15–20.

Iverson, R. M. (1997). The physics of debris flows. *Reviews of Geophysics*. 35(3):245–296.

Iverson, R. M. (2005). Regulation of landslide motion by dilatancy and pore pressure feedback. *Journal of Geophysical Research: Earth Surface*. 110(F2).

Iverson, R. M. (2015). Scaling and design of landslide and debris-flow experiments. *Geomorphology*. 244:12.

Iverson, R. M. and Denlinger, R. P. (2001). Flow of variably fluidized granular masses across three-dimensional terrain: 1. Coulomb mixture theory. *Journal of Geophysical Research: Solid Earth*. 106(B1):537–552.

Iverson, R. M. and George, D. L. (2014). A depth-averaged debris-flow model that includes the effects of evolving dilatancy. I. Physical basis. *Proceedings of the Royal Society A: Mathematical, Physical and Engineering Sciences*. 470(2170):20130819.

Iverson, R. M., Logan, M., LaHusen, R. G., and Berti, M. (2010b). The perfect debris flow? Aggregated results from 28 large-scale experiments. *Journal of Geophysical Research*. 115(F3):F03005.

Jakob, M., Hungr, O., and Jakob, D. M. (2005). *Debris-Flow Hazards and Related Phenomena*. Vol. 739. Springer.

REFERENCES

Janßen, C. and Krafczyk, M. (2011). Free surface flow simulations on GPGPUs using the LBM. *Computers & Mathematics with Applications*. 61(12):3549–3563.

Ji, S., Wang, S., and Zhou, Z. (2020). Influence of particle shape on mixing rate in rotating drums based on super-quadric DEM simulations. *Advanced Powder Technology*. 31(8):3540–3550.

Jiang, Y.-J., Zhao, Y., Towhata, I., and Liu, D.-X. (2015). Influence of particle characteristics on impact event of dry granular flow. *Powder Technology*. 270:53–67.

Johnson, C. G., Kokelaar, B. P., Iverson, R. M., Logan, M., LaHusen, R. G., and Gray, J. M. N. T. (2012). Grain-size segregation and levee formation in geophysical mass flows. *Journal of Geophysical Research: Earth Surface*. 117(F1):n/a–n/a.

Kaitna, R., Palucis, M. C., Yohannes, B., Hill, K. M., and Dietrich, W. E. (2016). Effects of coarse grain size distribution and fine particle content on pore fluid pressure and shear behavior in experimental debris flows. *Journal of Geophysical Research: Earth Surface*. 121(2):415–441.

Kesseler, M., Heller, V., and Turnbull, B. (2018). A laboratory-numerical approach for modelling scale effects in dry granular slides. *Landslides*. 15(11):2145–2159.

Kesseler, M., Heller, V., and Turnbull, B. (2020). Grain Reynolds number scale effects in dry granular slides. *Journal of Geophysical Research: Earth Surface*. 125(1).

Kowalski, J. and McElwaine, J. N. (2013). Shallow two-component gravity-driven flows with vertical variation. *Journal of Fluid Mechanics*. 714:434–462.

Kurganov, A. and Petrova, G. (2007). A second-order well-balanced positivity preserving central-upwind scheme for the Saint-Venant system. *Communications in Mathematical Sciences*. 5(1):133–160.

Kurganov, A. and Tadmor, E. (2000). New high-resolution central schemes for nonlinear conservation laws and convection–diffusion equations. *Journal of Computational Physics*. 160(1):241–282.

Labuz, J. F. and Zang, A. (2012). Mohr–Coulomb failure criterion. *Rock Mechanics and Rock Engineering*. 45(6):975–979.

Lai, Z., Vallejo, L. E., Zhou, W., Ma, G., Espitia, J. M., Caicedo, B., and Chang, X. (2017). Collapse of granular columns with fractal particle size distribution: Implications for understanding the role of small particles in granular flows. *Geophysical Research Letters*. 44(24):12, 181–12, 189.

Lajeunesse, E., Mangeney-Castelnau, A., and Vilotte, J. P. (2004). Spreading of a granular mass on a horizontal plane. *Physics of Fluids*. 16(7):2371–2381.

## REFERENCES

Lajeunesse, E., Monnier, J. B., and Homsy, G. M. (2005). Granular slumping on a horizontal surface. *Physics of Fluids*. 17(10):103302.

Lam, H. W., Sze, E., Wong, E. K. L., Poudyal, S., Ng, C., Chan, S., and Choi, C. E. (2022). Study of dynamic debris impact load on flexible debris-resisting barriers and the dynamic pressure coefficient. *Canadian Geotechnical Journal*. 59(12):2102–2118.

Lam, H. W. and Wong, A. L. (2021). Experimental and numerical study of dynamic soil debris impact load on reinforced concrete debris-resisting barriers. *Landslides*. 18(3):955–966.

Larrieu, E., Staron, L., and Hinch, E. J. (2006). Raining into shallow water as a description of the collapse of a column of grains. *Journal of Fluid Mechanics*. 554(-1):259.

Law, R. P. H., Choi, C. E., and Ng, C. W. W. (2015). Discrete-element investigation of influence of granular debris flow baffles on rigid barrier impact. *Canadian Geotechnical Journal*. 53(1):179–185.

Legros, F. (2002). The mobility of long-runout landslides. *Engineering Geology*. 63(3-4):301–331.

Lemieux, P.-A. and Durian, D. J. (2000). From avalanches to fluid flow: A continuous picture of grain dynamics down a heap. *Physical Review Letters*. 85(20):4273.

Leonardi, A., Cabrera, M. A., and Pirulli, M. (2021). Coriolis-induced instabilities in centrifuge modeling of granular flow. *Granular Matter*. 23(2):52.

Leonardi, A., Goodwin, S. R., and Pirulli, M. (2019). The force exerted by granular flows on slit dams. *Acta Geotechnica*. 14(6):1949–1963.

Leonardi, A. (2015). Numerical simulation of debris flow and interaction between flow and obstacle via DEM. PhD thesis. ETH Zurich, Zurich.

Leonardi, A., Cabrera, M., Wittel, F. K., Kaitna, R., Mendoza, M., Wu, W., and Herrmann, H. J. (2015). Granular-front formation in free-surface flow of concentrated suspensions. *Physical Review E*. 92(5):052204.

Leonardi, A., Wittel, F. K., Mendoza, M., Vetter, R., and Herrmann, H. J. (2016). Particle–fluid–structure interaction for debris flow impact on flexible barriers. *Computer Aided Civil and Infrastructure Engineering*. 31(5):323–333.

Leonardi, A., Wittel, F. K., Mendoza, M., and Herrmann, H. J. (2014). Coupled DEM-LBM method for the free-surface simulation of heterogeneous suspensions. *Computational Particle Mechanics*. 1(1):3–13.

Li, P., Wang, D., and Niu, Z. (2022). Unchannelized collapse of wet granular columns in the pendular state: Dynamics and morphology scaling. *Physical Review Fluids*. 7(8).

REFERENCES

Lide, D. R. (2004). *CRC Handbook of Chemistry and Physics*. Vol. 85. Boca Raton, Florida: CRC press.

Liu, H., Luo, Q., El Naggar, M. H., Zhang, L., and Wang, T. (2023). Centrifuge modeling of stability of embankment on soft soil improved by rigid columns. *Journal of Geotechnical and Geoenvironmental Engineering*. 149(9):04023069.

Lube, G., Huppert, H. E., Sparks, R. S. J., and Freundt, A. (2005). Collapses of two-dimensional granular columns. *Physical Review E*. 72(4).

Lube, G., Huppert, H. E., Sparks, R. S. J., and Hallworth, M. A. (2004). Axisymmetric collapses of granular columns. *Journal of Fluid Mechanics*. 508:175–199.

Major, J. J. and Pierson, T. C. (1992). Debris flow rheology: Experimental analysis of fine-grained slurries. *Water Resources Research*. 28(3):841–857.

Major, J. J. and Iverson, R. M. (1999). Debris-flow deposition: Effects of pore-fluid pressure and friction concentrated at flow margins. *Geological Society of America Bulletin*. 111(10):1424–1434.

Marchelli, M., Leonardi, A., Pirulli, M., and Scavia, C. (2020). On the efficiency of slit-check dams in retaining granular flows. *Géotechnique*. 70(3):226–237.

Marshall, A., Farrell, R., Klar, A., and Mair, R. (2012). Tunnels in sands: The effect of size, depth and volume loss on greenfield displacements. *Géotechnique*. 62(5):385–399.

Matlab (2020). *version 9.8.0.1451342 (R2020a)*. Natick, Massachusetts: The Math-Works Inc.

McArdell, B. W. (2016). Field measurements of forces in debris flows at the Illgraben: Implications for channel-bed erosion. *International Journal of Erosion Control Engineering*. 9(4):194–198.

McArdell, B. W., Bartelt, P., and Kowalski, J. (2007). Field observations of basal forces and fluid pore pressure in a debris flow. *Geophysical Research Letters*. 34(7).

McCoy, S. W., Kean, J. W., Coe, J. A., Staley, D. M., Wasklewicz, T. A., and Tucker, G. E. (2010). Evolution of a natural debris flow: In situ measurements of flow dynamics, video imagery, and terrestrial laser scanning. *Geology*. 38(8):735–738.

Meng, X., Johnson, C. G., and Gray, J. M. N. T. (2022). Formation of dry granular fronts and watery tails in debris flows. *Journal of Fluid Mechanics*. 943.

Meng, X., Wang, Y., Wang, C., and Fischer, J.-T. (2017). Modeling of unsaturated granular flows by a two-layer approach. *Acta Geotechnica*. 12(3):677–701.

Meyer, H. (2021). Camera Controller for Action Cameras. *MobWheel.com*.

## REFERENCES

MiDi, G. (2004). On dense granular flows. *The European Physical Journal E*. 14:341–365.

Milne, F. D., Brown, M. J., Knappett, J. A., and Davies, M. C. R. (2012). Centrifuge modelling of hillslope debris flow initiation. *CATENA*. 92:162–171.

Mirshekari, M. and Ghayoomi, M. (2017). Centrifuge tests to assess seismic site response of partially saturated sand layers. *Soil Dynamics and Earthquake Engineering*. 94:254–265.

Morland, L. W. (1992). Flow of viscous fluids through a porous deformable matrix. *Surveys in Geophysics*. 13(3):209–268.

Nadim, F., Kjekstad, O., Peduzzi, P., Herold, C., and Jaedicke, C. (2006). Global landslide and avalanche hotspots. *Landslides*. 3(2):159–173.

Ng, C. W. W., Choi, C. E., Koo, R., Goodwin, S., Song, D., and Kwan, J. S. (2018). Dry granular flow interaction with dual-barrier systems. *Géotechnique*. 68(5):386–399.

Oakley, N. S., Cannon, F., Munroe, R., Lancaster, J. T., Gomberg, D., and Ralph, F. M. (2018). Brief communication: Meteorological and climatological conditions associated with the 9 January 2018 post-fire debris flows in Montecito and Carpinteria, California, USA. *Natural Hazards and Earth System Sciences*. 18(11):3037–3043.

Orpe, A. V. and Kudrolli, A. (2007). Velocity correlations in dense granular flows observed with internal imaging. *Physical Review Letters*. 98(23):238001.

Otsu, N. (1979). A Threshold Selection Method from Gray-Level Histograms. *IEEE Transactions on Systems, Man, and Cybernetics*. 9(1):62–66.

Ouriemi, M., Aussillous, P., and Guazzelli, E. (2009). Sediment dynamics. Part 1. Bedload transport by laminar shearing flows. *Journal of Fluid Mechanics*. 636:295–319.

Pacheco-Martinez, H., Van Gerner, H. J., and Ruiz-Suárez, J. (2008). Storage and discharge of a granular fluid. *Physical Review E*. 77(2):021303.

Pailha, M. and Pouliquen, O. (2009). A two-phase flow description of the initiation of underwater granular avalanches. *Journal of Fluid Mechanics*. 633:115–135.

Pasqua, A., Leonardi, A., and Pirulli, M. (2022). Coupling Depth-Averaged and 3D numerical models for the simulation of granular flows. *Computers and Geotechnics*. 149:104879.

Pasqua, A., Leonardi, A., and Pirulli, M. (2023). Coupling Depth-Averaged and 3D numerical models to study debris flow: Saint-Vincent event. *E3S Web of Conferences*. 415. EDP Sciences:02015.

REFERENCES

Pereira, G. G., Dupuy, P. M., Cleary, P. W., and Delaney, G. W. (2012). Comparison of permeability of model porous media between SPH and LB. *Progress in Computational Fluid Dynamics, an International Journal*. 12(2-3):176–186.

Petley, D. (2012). Global patterns of loss of life from landslides. *Geology*. 40(10):927–930.

Petley, D. (2008). The global occurrence of fatal landslides in 2007. *Geophysical Research Abstracts*. 10:3.

Phan, Q. T., Bui, H. H., and Nguyen, G. D. (2022). Modeling submerged granular flow across multiple regimes using the Eulerian–Eulerian approach with shear-induced volumetric behavior. *Physics of Fluids*. 34(6):063308.

Pierson, T. (1986). Flow behavior of channelized debris flows, Mount St. Helens, Washington. *16th Annual Binghamton Symposium*. Hillslope Processes: Allen and Unwin, Winchester, Mass:269–296.

Pierson, T. C. (2005). *Distinguishing between debris flows and floods from field evidence in small watersheds*. Report 2327-6932. US Geological Survey.

Pitman, E. B. and Le, L. (2005). A Two-Fluid Model for Avalanche and Debris Flows. *Philosophical Transactions: Mathematical, Physical and Engineering Sciences*. 363(1832):1573–1601.

Pracht, W. E. (1975). Calculating three-dimensional fluid flows at all speeds with an Eulerian-Lagrangian computing mesh. *Journal of Computational Physics*. 17(2):132–159.

Pudasaini, S. P. and Hutter, K. (2003). Rapid shear flows of dry granular masses down curved and twisted channels. *Journal of Fluid Mechanics*. 495:193–208.

Pudasaini, S. P. and Hutter, K. (2007). *Avalanche Dynamics: Dynamics of Rapid Flows of Dense Granular Avalanches*. Springer Science & Business Media.

Pudasaini, S. P. (2012). A general two-phase debris flow model. *Journal of Geophysical Research: Earth Surface*. 117(F3):n/a–n/a.

Redshaw, P., Boon, D., Campbell, G., Willis, M., Mattai, J., Free, M., Jordan, C., Kemp, S. J., Morley, A., and Thomas, M. (2019). The 2017 Regent Landslide, Freetown Peninsula, Sierra Leone. *Quarterly Journal of Engineering Geology and Hydrogeology*. 52(4):435–444.

Richards, T. W. and Carver, E. K. (1921). A critical study of the capillary rise method of determining surface tension, with data for water, benzene, toluene, chloroform, carbon tetrachloride, ether and dimethyl aniline. *Journal of the American Chemical Society*. 43(4):827–847.

REFERENCES

Rickenmann, D. (1999). Empirical relationships for debris flows. *Natural Hazards*. 19:47–77.

Robinson, M., Ramaioli, M., and Luding, S. (2014). Fluid–particle flow simulations using two-way-coupled mesoscale SPH–DEM and validation. *International Journal of Multiphase Flow*. 59:121–134.

Rodolfo, K. S., Lagmay, A. M. F., Eco, R. C., Herrero, T. M. L., Mendoza, J. E., Minimo, L. G., and Santiago, J. T. (2016). The December 2012 Mayo River debris flow triggered by Super Typhoon Bopha in Mindanao, Philippines: Lessons learned and questions raised. *Natural Hazards and Earth System Sciences*. 16(12):2683–2695.

Roelofs, L., Colucci, P., and Haas, T. (2022). How debris-flow composition affects bed erosion quantity and mechanisms: An experimental assessment. *Earth Surface Processes and Landforms*.

Rondon, L., Pouliquen, O., and Aussillous, P. (2011). Granular collapse in a fluid: Role of the initial volume fraction. *Physics of Fluids*. 23(7):073301.

Rossi, M., Peruccacci, S., Brunetti, M., Marchesini, I., Luciani, S., Ardizzone, F., Balducci, V., Bianchi, C., Cardinali, M., and Fiorucci, F. (2012). SANF: National warning system for rainfall-induced landslides in Italy. *Landslide and Engineered Slopes. Protecting Society through Improved Understanding.* Vol. 2:1895–1899.

Roux, J.-N. and Combe, G. (2002). Quasistatic rheology and the origins of strain. *Comptes Rendus Physique*. 3(2):131–140.

Salciarini, D., Tamagnini, C., and Conversini, P. (2010). Discrete element modeling of debris-avalanche impact on earthfill barriers. *Physics and Chemistry of the Earth, Parts A/B/C*. 35(3):172–181.

Salm, B. (1993). Flow, flow transition and runout distances of flowing avalanches. *Annals of Glaciology*. 18:221–226.

Sanvitale, N. and Bowman, E. T. (2017). Visualization of dominant stress-transfer mechanisms in experimental debris flows of different particle-size distribution. *Canadian Geotechnical Journal*. 54(2):258–269.

Sarlin, W., Morize, C., Sauret, A., and Gondret, P. (2021). Collapse dynamics of dry granular columns: From free-fall to quasistatic flow. *Physical Review E*. 104(6).

Sati, V. P. (2022). Glacier bursts-triggered debris flow and flash flood in Rishi and Dhauli Ganga valleys: A study on its causes and consequences. *Natural Hazards Research*. 2(1):33–40.

REFERENCES

Sattler, K., Keiler, M., Zischg, A., and Schrott, L. (2011). On the connection between debris flow activity and permafrost degradation: A case study from the Schnalstal, South Tyrolean Alps, Italy. *Permafrost and Periglacial Processes*. 22(3):254–265.

Savage, S. B. and Hutter, K. (1989). The motion of a finite mass of granular material down a rough incline. *Journal of Fluid Mechanics*. 199:177–215.

Savage, S. and Lun, C. (1988). Particle size segregation in inclined chute flow of dry cohesionless granular solids. *Journal of Fluid Mechanics*. 189:311–335.

Savage, S. B. (1984). The mechanics of rapid granular flows. *Advances in Applied Mechanics*. 24:289–366.

Savage, S. B. (1979). Gravity flow of cohesionless granular materials in chutes and channels. *Journal of Fluid Mechanics*. 92(1):53–96.

Scaramuzza, D. and Siegwart, R. (2007). A new method and toolbox for easily calibrating omnidirectional cameras. *International Conference on Computer Vision Systems: Proceedings*.

Scheidl, C., Chiari, M., Kaitna, R., Müllegger, M., Krawtschuk, A., Zimmermann, T., and Proske, D. (2013). Analysing debris-flow impact models, based on a small scale modelling approach. *Surveys in Geophysics*. 34:121–140.

Schneider, D., Huggel, C., Cochachin, A., Guillén, S., and García, J. (2014). Mapping hazards from glacier lake outburst floods based on modelling of process cascades at Lake 513, Carhuaz, Peru. *Advances in Geosciences*. 35:145–155.

Schofield, A. N. (1980). Cambridge geotechnical centrifuge operations. *Geotechnique*. 30(3):227–268.

Shiu, W.-J., Lee, C.-F., Chiu, C.-C., Weng, M.-C., Yang, C.-M., Chao, W.-A., Liu, C.-Y., Lin, C.-H., Huang, W.-K., and Group, G. W. (2023). Analyzing landslide-induced debris flow and flow-bridge interaction by using a hybrid model of depth-averaged model and discrete element method. *Landslides*. 20(2):331–349.

Song, D., Choi, C. E., Ng, C. W. W., and Zhou, G. G. D. (2018). Geophysical flows impacting a flexible barrier: Effects of solid-fluid interaction. *Landslides*. 15(1):99–110.

Song, D.-r., Zhou, G. G. D., Choi, C. E., and Zheng, Y. (2019). Debris flow impact on flexible barrier: effects of debris-barrier stiffness and flow aspect ratio. *Journal of Mountain Science*. 16(7):1629–1645.

Song, D. (2016). Mechanisms of debris flow impact on rigid and flexible barriers. PhD thesis. The Hong Kong University of Science and Technology, Hong Kong.

185

REFERENCES

Spielmann, R., Aaron, J., and McArdell, B. W. (2023). Inferring spatial variations in velocity profiles and bed geometry of natural debris flows based on discharge estimates from high-frequency 3D LiDAR point clouds; Illgraben, Switzerland. *E3S Web of Conf.* 415:01024.

Stewart, M. A. and McCartney, J. S. (2014). Centrifuge modeling of soil-structure interaction in energy foundations. *Journal of Geotechnical and Geoenvironmental Engineering.* 140(4):04013044.

Succi, S. (2001). *The lattice Boltzmann equation: For fluid dynamics and beyond.* Oxford university press.

Švec, O., Skoček, J., Stang, H., Geiker, M. R., and Roussel, N. (2012). Free surface flow of a suspension of rigid particles in a non-Newtonian fluid: A lattice Boltzmann approach. *Journal of Non-Newtonian Fluid Mechanics.* 179-180:32–42.

Takahashi, T. (1981). Debris Flow. *Annual Review of Fluid Mechanics.* 13(1):57–77.

Takahashi, T. (2007). *Debris flow: Mechanics, Prediction and Countermeasures.* Taylor & Francis.

Takamura, K., Fischer, H., and Morrow, N. R. (2012). Physical properties of aqueous glycerol solutions. *Journal of Petroleum Science and Engineering.* 98-99:50–60.

Takebayashi, H. and Fujita, M. (2020). Numerical simulation of a debris flow on the basis of a two-dimensional continuum body model. *Geosciences.* 10(2):45.

Taylor, R. N. (1995). *Geotechnical Centrifuge Technology.* New York: Blackie Academic & Professional.

Terzaghi, K. (1943). *Theoretical Soil Mechanics.* Vol. 314. John Wiley and Sons Inc.

Teufelsbauer, H., Wang, Y., Chiou, M. C., and Wu, W. (2009). Flow–obstacle interaction in rapid granular avalanches: DEM simulation and comparison with experiment. *Granular Matter.* 11:209–220.

Thompson, E. L. and Huppert, H. E. (2007). Granular column collapses: Further experimental results. *Journal of Fluid Mechanics.* 575:177–186.

Thornton, C. (2015). Granular dynamics, contact mechanics and particle system simulations. *A DEM study. Particle Technology Series.* 24.

Tierz, P., Woodhouse, M. J., Phillips, J. C., Sandri, L., Selva, J., Marzocchi, W., and Odbert, H. M. (2017). A framework for probabilistic multi-hazard assessment of rain-triggered lahars using Bayesian belief networks. *Frontiers in Earth Science.* 5:73.

Tolomeo, M. and McDowell, G. R. (2023). DEM study of an "avatar" railway ballast with real particle shape, fabric and contact mechanics. *Granular Matter.* 25(2):32.

REFERENCES

Trepanier, M. and Franklin, S. V. (2010). Column collapse of granular rods. *Physical Review E*. 82(1):011308.

Trigila, A. and Iadanza, C. (2008). *Landslides in Italy*. Report. Italian National Institute for Environmental Protection and Research (ISPRA).

Tsai, M., Hsu, Y.-C., Li, H., Shu, H., and Liu, K.-F. (2011). Application of simulation technique on debris flow hazard zone delineation: A case study in the Daniao tribe, Eastern Taiwan. *Natural Hazards and Earth System Sciences*. 11:3053–3062.

Turnbull, B. (2011). Scaling laws for melting ice avalanches. *Physical Review Letters*. 107(25):258001.

Turnbull, B., Bowman, E. T., and McElwaine, J. N. (2015). Debris flows: Experiments and modelling. *Comptes Rendus Physique*. 16(1):86–96.

Valentino, R., Barla, G., and Montrasio, L. (2008). Experimental analysis and micromechanical modelling of dry granular flow and impacts in laboratory flume tests. *Rock Mechanics and Rock Engineering*. 41:153–177.

Vallance, J., Savage, S., Rosato, A., and Blackmore, D. (2000). Particle segregation in granular flows down chutes, *IUTAM Symposium on Segregation in Granular Materials*. Ed. by A. Rosato and D. Blackmore:31–52.

Vallejo, L., Estrada, N., Taboada, A., Caicedo, B., and Silva, J. (2006). Numerical and physical modeling of granular flow. *Physical Modelling in Geotechnics. Proceedings of the Sixth International Conference on Physical Modelling in Geotechnics, 6th ICPMG*. 6.

Varnes, D. J. (1958). Landslide types and processes. *Landslides and engineering practice*. 24:20–47.

Vreugdenhil, C. B. (1994). *Numerical Methods for Shallow-Water Flow*. Vol. 13. Springer Science & Business Media.

Warnett, J., Denissenko, P., Thomas, P., Kiraci, E., and Williams, M. (2014). Scalings of axisymmetric granular column collapse. *Granular Matter*. 16(1):115–124.

Webb, W., Heron, C., and Turnbull, B. (2023a). Fines-controlled drainage in just-saturated, inertial column collapses. *E3S Web of Conferences*. 415:01030.

Webb, W., Heron, C., and Turnbull, B. (2023b). Inertial effects in just-saturated axisymmetric column collapses. *Granular Matter*. 25(2):40.

Webb, W., Turnbull, B., and Johnson, C. G. (2024a). Continuum modelling of a just-saturated inertial column collapse: Capturing fluid-particle interaction. *Granular Matter*. 26(1):21.

REFERENCES

Webb, W., Turnbull, B., and Leonardi, A. (2024b). Performance and limits of a geotechnical centrifuge: DEM-LBM simulations of saturated granular column collapse. *Granular Matter*. 26(2):32.

White, D. J., Take, W. A., and Bolton, M. D. (2003). Soil deformation measurement using particle image velocimetry (PIV) and photogrammetry. *Géotechnique*. 53(7):619–631.

Więckowski, Z. (2004). The material point method in large strain engineering problems. *Computer Methods in Applied Mechanics and Engineering*. 193(39):4417–4438.

Wolf-Gladrow, D. (1995). A lattice Boltzmann equation for diffusion. *Journal of Statistical Physics*. 79:1023–1032.

World Bank (2023). *The World Bank data*. Data retrieved from World Development Indicators, https://data.worldbank.org/indicator/NY.GDP.PCAP.CD?view=chart.

Xiong, Q., Madadi-Kandjani, E., and Lorenzini, G. (2014). A LBM–DEM solver for fast discrete particle simulation of particle–fluid flows. *Continuum Mechanics and Thermodynamics*. 26:907–917.

Yang, F. L. and Hunt, M. L. (2006). Dynamics of particle-particle collisions in a viscous liquid. *Physics of Fluids*. 18(12):121506.

Yuheng, S. and Hao, Y. (2017). Image segmentation algorithms overview. *arXiv preprint arXiv:1707.02051*.

Zhang, B. and Huang, Y. (2022). Impact behavior of superspeed granular flow: Insights from centrifuge modeling and DEM simulation. *Engineering Geology*. 299.

Zhang, B., Li, W., Pu, J., Bi, Y., and Huang, Y. (2023). Dilative and compressive Coriolis effect on granular impact behavior based on centrifuge modeling and DEM simulation. *Engineering Geology*. 323:107232.

Zhang, J., Pu, J., Zhang, M., and Qiu, T. (2001a). Model tests by centrifuge of soil nail reinforcements. *Journal of Testing and Evaluation*. 29(4):315–328.

Zhang, Z., Liu, L., Yuan, Y., and Yu, A. (2001b). A simulation study of the effects of dynamic variables on the packing of spheres. *Powder Technology*. 116(1):23–32.

Zhong, W., Yu, A., Liu, X., Tong, Z., and Zhang, H. (2016). DEM/CFD-DEM modelling of non-spherical particulate systems: Theoretical developments and applications. *Powder Technology*. 302:108–152.

Zhou, Y., Xu, B., Zou, R., Yu, A., and Zulli, P. (2003). Stress distribution in a sandpile formed on a deflected base. *Advanced Powder Technology*. 14(4):401–410.

# REFERENCES

Zou, Z., Tang, H., Xiong, C., Su, A., and Criss, R. E. (2017). Kinetic characteristics of debris flows as exemplified by field investigations and discrete element simulation of the catastrophic Jiweishan rockslide, China. *Geomorphology*. 295:1–15.

Zuiderveld, K. (1994). Contrast Limited Adaptive Histogram Equalization. *Graphics Gems*. IV:474–485.